THE EFFECTS OF NANOPARTICLE PROPERTIES ON BIOLOGICAL IMAGING AND PHOTOTHERMAL CANCER TREATMENT

A Dissertation
Presented to
The Academic Faculty

by

Mena Aioub

In Partial Fulfillment
of the Requirements for the Degree
Doctor of Philosophy in the
School of Chemistry and Biochemistry

Georgia Institute of Technology
August 2017

THE EFFECTS OF NANOPARTICLE PROPERTIES ON BIOLOGICAL IMAGING AND PHOTOTHERMAL CANCER TREATMENT

Approved by:

Dr. Mostafa A. El-Sayed, Advisor
School of Chemistry and Biochemistry
Georgia Institute of Technology

Dr. Bridgette A. Barry
School of Chemistry and Biochemistry
Georgia Institute of Technology

Dr. Christine K. Payne
School of Chemistry and Biochemistry
Georgia Institute of Technology

Dr. Nicholas V. Hud
School of Chemistry and Biochemistry
Georgia Institute of Technology

Dr. Ingeborg Schmidt-Krey
School of Biology
Georgia Institute of Technology

Date Approved: June 14, 2017

ACKNOWLEDGEMENTS

This thesis would not have been possible without the help and support of my friends, family, and coworkers. Specifically, my advisor Dr. Mostafa El-Sayed must be acknowledged for his support during my time at Georgia Tech. His knowledge and passion to never stop asking questions have been invaluable. I would also like to acknowledge my thesis committee members: Dr. Bridgette Barry, Dr. Nicholas Hud, Dr. Christine Payne, and Dr. Ingeborg Schmidt-Krey for their advice, both scientific and career-based, and for their input and feedback throughout my graduate career. An additional thank you must go to the core facilities mangers, Nadia Boguslavsky and Andrew Shaw, whose expertise was crucial to various projects using the instruments under their care.

My research has also been greatly enhanced and aided through collaborations with fellow graduate students, postdocs, and research scientists. I would like to thank my past and present group members for their support and providing a sounding board about life and science. Specifically, I would like to acknowledge Dr. Lauren Austin, Dr. Megan Mackey, Dr. Sajanlal Panikkanvalappil, Dr. Mahmoud Mahmoud, Dr. Bin Kang, Dr. Justin Bordley, Dr. Daniel O'Neil, Dr. Paul Szymanski, Dr. Steven Hira, Dr. Batyr Garlyyev, Dr. Marwa Afifi, Dr. Rachel Near, Dr. Steven Hayden, Dr. Nasrin Hooshmand, Crystal Bell, Samera Ahmed, Hazel Shah, Torus Washington III, Antra Das, and Ashley Allen. They have been a pleasure to work with over the years and have positively contributed to my skills and knowledge as a scientist. I especially thank Dr. Lauren Austin for teaching me the biological techniques I needed to quickly excel in lab,

and Dr. Megan Mackey for teaching me the art of scientific writing. I would also like to thank Mike Riley for keeping the building running and addressing the constant issues that plagued the LDL facilities, and Leslie Dionne-White and Michele Yager for keeping the financial and administrative aspects of the lab functioning.

My friends and family have supported me from the beginning and enabled me to be successful in any avenue I have followed. First and foremost, I thank my wife Allison for her constant and unwavering support and belief in me to excel in whatever interest I pursued. You have taught me the value of planning and a work ethic and I am always grateful to have you to tackle life with me. I also would like to thank my parents for pushing me to always stay in school and learn new things. Likewise, I thank my sisters; you have both done great with your schooling and pushed me to graduate at the same time, even if you both beat me by a hair. Additionally, I thank my in-laws for their constant support of Allison and me as we have stayed professional students for so long. Finally, I thank my friends and family in Atlanta, New Jersey, and across the country that have been there to celebrate the good times and make the bad ones manageable.

TABLE OF CONTENTS

LIST OF TABLES

LIST OF FIGURES

LIST OF SYMBOLS AND ABBREVIATIONS

Å	angstrom
ζ	zeta
λ	wavelength
μ	micro
2D	two dimensional
3D	three dimensional
5-FU	5-fluorouracil
A	adenine
AES	atomic emission spectroscopy
AFM	atomic force microscopy
Ag	silver
$AgNO_3$	silver nitrate
AR	aspect ratio
Au	gold

AuNC	gold nanocages
AuNP	gold nanoparticle
AuNR	gold nanorod
AuNS	gold nanoshells
avg	average
AvN	apoptosis – necrosis
BP	band-pass
C	carbon
C	cytosine
CCD	charge-coupled device
CDE	cell death enhancement
cDMEM	complete medium
cm^{-1}	wavenumber
CO_2	carbon dioxide
CPP	cell-penetrating peptide
CTAB	cetyltrimethylammonium bromide

CTC	ciculating tumor cells
cw	continuous wave
DAPI	4,6 diamidino-2-phenylindole
DCF	2,7-dichlorofluorescein
DCFDA	2,7-dichlorofluorescin diacetate
DI	deionized
DLS	dynamic light scattering
DMEM	Dulbecco's modification of Eagle's medium
DMSO	dimethyl sulfoxide
DNA	deoxyribonucleic acid
DOX	doxorubicin
DPBS	Dulbecco’s phosphate buffered saline
EC_{50}	half-maximal effective concentration
EDTA	ethylenediaminetetraacetic acid
EDX	energy dispersive X-ray spectroscopy
EGF	epidermal growth factor

EGFR	epidermal growth factor receptor
ELISA	enzyme linked immunosorbent assay
EM	electron microscope/microscopy
EPR	enhanced permeability and retention
ET_{50}	half-maximal effective time
eV	electron-volt
f	femto
FBS	fetal bovine serum
FITC	fluorescein isothiocyanate
f-PSA	free prostate specific antigen
G	guanine
g	gram
g	gravity
h	hour
H	hydrogen
H_2DCF	dichlorofluorescin

H_2DCFA	6-carboxy-2', 7'-dichlorofluorescein diacetate
H_2O_2	hydrogen peroxide
HAADF	high-angle annular dark-field
HaCat	human keratinocytes
$HAuCl_4$	gold(III) chloride
HD	hydrodynamic diameter
HER2	Herceptin
HRTEM	high resolution transmission electron microscopy/microscope
HSC-3	human oral squamous carcinoma
IC_{50}	half-maximal inhibitory concentration
ICP	inductively coupled plasma
IgF	immunoglobulin F
IgG	immunoglobulin G
IR	infrared
K_2PtCl_4	potassium tetrachloroplatinate(II)
kcal/mol	kilocalories per mole

L	liter
L	length
LbL	layer by layer
LSPR	localized surface plasmon resonance
M	molar
m	milli
m	meter
min	minute
mPEG-SH5000	methoxy poly(ethylene glycol) thiol
MS	mass spectrometry
N	nitrogen
n	nano
N.A.	numerical aperture
$NaBH_4$	sodium borohydride
NaH_2PO_4	sodium phosphate

NaOH	sodium hydroxide
NIR	near-infrared
NLS	nuclear localizing signal/sequence
nm	nanometer
NR	nanorod
NT-	nuclear-targeted-
O	oxygen
OD	optical density
OES	optical emission spectroscopy
PA	photoacoustic
PAT	photoacoustic tomography
PBS	phosphate buffered saline
PCR	polymerase chain reaction
PDT	photodynamic therapy
PEG	poly (ethylene glycol)
PEI	poly (ethylenimine)

PERSIS	plasmonically-enhanced Rayleigh scattering imaging spectroscopy
Phe	phenylalanine
PI	propidium iodide
PLGA	poly (lactic-co-glycolic acid)
PPT	photothermal therapy
PPTT	photothermal therapy
Pt	platinum
PtAuNR	platinum-coated gold nanorod
PVP	poly (vinyl pyrrolidone)
RGD	arginine-glycine-aspartic acid
RIA	radioimmunoassay
RNA	ribonucleic acid
ROS	reactive oxygen species
rpm	revolutions per minute
S	sulfur
s	second

s.d.	standard deviation
s.e.m.	standard error of the mean
sAuNP	small AuNP
SAXS	small angle X-ray scattering
SCCHN	squamous cell carcinoma of the head and neck
ScFv	single chain variable fragment
SEM	scanning electron microscope/microscopy
SERS	surface-enhanced Raman spectroscopy
SPR	surface plasmon resonance
STEM	scanning transmission electron microscope/microscopy
T	thymine
TEM	transmission electron microscope/microscopy
TNF-α	tumor necrosis factor alpha
T-PESCIS	targeted plasmonically enhanced single cell imaging spectroscopy
TR-SERS	time-resolved surface-enhanced Raman spectroscopy
Tyr	tyrosine

UV	ultraviolet
V	volt
Vis	visible
W	watt
W	width
XRD	X-ray ray diffraction
XTT	(2,3-Bis-(2-Methoxy-4-Nitro-5-Sulfophenyl)-2*H*-Tetrazolium-5-Carboxanilide)

SUMMARY

Over the past two decades, gold nanoparticles (AuNPs) have emerged as promising tools for biomedical applications. Their unique optical properties enable sensitive detection and effective treatment strategies. Additionally, the expanding toolkit of AuNP colloidal synthesis, combined with their straightforward surface functionalization, allowing for their conjugation with a variety of targeting and / or therapeutic ligands, contribute to their increasing use. This thesis explores the effects of nanoparticle size, shape, composition, and surface chemistry in the design and application of AuNPs for biological imaging and cancer treatment applications.

The 1st chapter introduces various AuNP synthesis, characterization, and conjugation strategies, and presents an overview of their tunable optical properties. Recent AuNP applications such as biological imaging, diagnostics, and cancer treatments (**Chapter 1**) are reviewed to prepare the reader for the remaining chapters. Then, **Chapter 2** discusses the effect of varying surface chemistries on nanoparticle localization within living cells. Using different targeting ligands, a dynamic profile of AuNP localization was obtained. Cellular localization was found to critically affect AuNP scattering properties, a crucial component of biological imaging. Increased subcellular targeting was found to result in greater and more rapid localization, resulting in increased light scattering and enhanced imaging (**Chapter 2**). Subsequently, the nuclear-targeted AuNPs (NT-AuNPs) previously found to give the greatest imaging enhancement were employed as probes to increase the inherent light scattering from cells. **Chapter 3** describes a technique to use these NT-AuNPs to compare the relative efficacies of three

clinically relevant chemotherapeutic drugs. This allows the use of a single sample of cells in real-time using inexpensive lab equipment, saving time and material costs while imparting the potential to rapidly screen drugs or analogs to determine the most effective option.

The remainder of this thesis focuses on plasmonic photothermal therapy (PPT), an emerging treatment where AuNPs convert light into heat, causing cell death specifically in the vicinity of the targeted AuNPs. **Chapter 4** discusses the use of NT-AuNPs to induce PPT cell death while simultaneously serving as scattering probes to monitor the associated molecular changes through time-dependent surface-enhanced Raman spectroscopy of single cells. The same molecular changes were observed using different AuNP sizes, concentrations, and laser intensities, indicating the consistency mechanism of action of PPT. Finally, the use of platinum-coated gold nanorods (PtAuNRs) is introduced in **Chapter 5** to mitigate the side effects of PPT. Platinum, commonly used for oxygen reduction in catalysis, is incorporated to scavenge reactive oxygen species (ROS), allowing the decoupling of thermal and chemical effects during PPT. The PtAuNRs protected untreated cells from the ROS byproducts of PPT, making them ideal candidates to advance the treatment while reducing deleterious side effects. This thesis presents a fundamental investigation of the influence of AuNP properties on imaging and cancer treatment, which can be used to continue advancing their utility and applications.

CHAPTER 1. INTRODUCTION [1]

(This chapter was published in Aioub, M.; Austin, L. A.; El-Sayed, M. A., Gold Nanoparticles for Cancer Diagnostics, Spectroscopic Imaging, Drug Delivery, and Plasmonic Photothermal Therapy. In *Inorganic Frameworks as Smart Nanomedicines*, Vol. 7, Grumezescu, A. M., Copyright Elsevier (2017).)

As a noble metal, gold has been highly valued for over 5000 years due its scarcity, malleability, and stability, being easy to work but remaining inert under most conditions. In particular, the use of colloidal gold, or gold nanoparticles (AuNPs) dispersed in a solution or medium, also dates back over thousand years. It was first used as an additive to color glass or ceramics and later to treat various diseases in the Middle Ages. One of the earliest and most famous examples of the use of colloidal gold is the Roman Lycurgus cup dating back to the 4th century. The cup appears red when light is viewed transmitted through the cup, or green when the reflected light is observed.[2-3] While the presence of AuNPs may not have been known or understood in these early times, the first scientific report of the synthesis and optical properties of colloidal gold is generally attributed to Michael Faraday, who reported the synthesis of red solutions of colloidal gold through a two-phase approach. He then created thin films of AuNPs and observed the color change of the films at different interparticle separation distances by mechanically compressing the films.[4] These represent some of the first investigations into the optical properties of AuNPs.

More recently, the advent of the electron microscope, enabling the direct observation of nanomaterials, and a growing understanding of the electronic and chemical properties of materials on the nanoscale has led to the emergence of many new

fields of study. In particular, AuNPs have served a key role in the emergence of nanotechnology for biological, medical, and pharmaceutical applications over the last 20-30 years.[5-14] Some of the most common uses of AuNPs include as diagnostic probes, allowing for enhanced spectroscopic signals for the detection of biological processes.[10] AuNPs have also historically been used as imaging tags in electron microscopy due to the high contrast afforded by the strong scattering gold lattice (for immunostaining),[15-16] and as probes for cellular[8, 17] or photoacoustic imaging.[6, 17] Additionally, assays using AuNPs as colorimetric, fluorometric, or electrochemical sensors are used daily for applications ranging from pregnancy tests to the detection of biological threats.[18-20] Furthermore, the small size of nanomaterials has led to their widespread use as drug delivery vehicles, capable of releasing high local drug payloads.[21-22] Recently, combined therapeutic treatments utilizing multiple AuNP properties, such as plasmonic photothermal therapy (PPT) where the nanoparticles convert light to heat into induce hyperthermia, or photodynamic therapy, which often combines the AuNP photothermal properties with their drug delivery capabilities, have emerged.[17-18] **Table 1.1** below outlines some AuNP properties and several of their common biomedical applications.

Table 1.1 Typical AuNP properties needed for common biomedical applications

	Optical Imaging	Photo-acoustic Imaging	Diagnostics / Sensing	Drug Delivery	PPT	PDT
Biocompatibility	X	X	X	X	X	X
Surface Modification	X	X	X	X	X	X
Stability	X	X	X	X	X	X
Absorption		X			X	
Scattering	X		X			X

The range of applications for AuNPs has been aided by the expanding methodology for the wet-chemical synthesis of various nanoparticle sizes and shapes, as well as increasing techniques for their biochemical conjugation and surface modifications.[22-23] This chapter will discuss the synthesis, characterization, and modification of AuNPs. Their optical properties and some emerging biomedical applications in cellular and spectroscopic imaging, diagnostics, and cancer treatment will also be discussed.

1.1 Gold Nanoparticle (AuNP) Synthesis, Conjugation, Characterization

1.1.1 Synthesis

The desire for well-defined AuNP shapes and sizes has led to significant interest in various synthetic techniques, including wet-chemical or colloidal synthesis, electrochemical techniques, photolithography and electron beam lithography. Lithographic techniques serve as excellent methods for the production of 2 dimensional arrays through the vapor deposition of gold onto a prefabricated support, followed by chemical etching of the support matrix. Large arrays of nanostructures can be obtained with precise control over the AuNP geometry, size, and interparticle separation distances[10, 18]. However, these methods are time consuming and generally not amenable for *in vivo* or *in vitro* biological applications due to the extra steps required for washing the AuNPs and transferring them from the solid substrate into a biocompatible solution for their functionalization and application.

Among the traditional AuNP synthetic strategies, the reduction of gold (III) salts remains the most popular due to its scalability for producing large amounts of material,

ease of tuning the nanoparticle size, shape, and surface chemistry, and the relative monodispersity of the synthesized AuNPs. The first structural study of AuNP synthesis was reported by Turkevich *et al.* in 1951, using various synthetic conditions including altering ascorbic acid and sodium citrate concentrations to reduce the gold salt, and using UV irradiation.[25] Subsequently, Frens performed a systematic study of Turkevich's citrate reduction method to improve the procedure, yielding spherical AuNPs with diameters of ~ 10 – 150 nm[26] (**Figure 1.1A**), although in practice, size and shape control suffer for particle diameters larger than ~50 nm.

While these approaches are still the most commonly used techniques for spherical AuNP synthesis, numerous other methods and modifications have been introduced in recent years, including the reverse addition method,[27] the Brust-Schiffrin method,[28] biological approaches using plant extracts or enzymes,[29] and seeded growth methods.[30-31] As implied by the name, the reverse addition method reverses the traditional citrate reduction technique by adding the gold salt into a citrate solution while heating (instead of adding citrate to reduce a hot solution of aqueous gold salt), resulting in monodisperse gold nanospheres with 5 – 10 nm diameters.[27] These smaller AuNPs possess the desirable attributes of those synthesized using the standard citrate reduction technique, namely biocompatibility and ease of surface modification. They are also capable of passing through the nuclear pore complex which has a diameter of ~ 10 nm but can expand to a maximum of ~38 nm.[32] This size regime allows for the targeting of cell nuclei for drug or gene delivery applications as well as their use as seeds[33] for further AuNP growth. The Brust-Schiffrin method allows for the formation of even smaller AuNPs of 1.5 – 5.2 nm diameter, using a two-phase synthesis and organothiol stabilization, resulting in air- and

temperature-stable nanoparticles.[28] Although the biological syntheses of AuNPs are an emerging field, existing methods do not exhibit the same size control or surface functionality as the citrate reduction technique and are therefore not widely used.[29]

For the synthesis of larger nanospheres, desirable for imaging applications, seed mediated approaches are commonly used and fall into two general categories, kinetically controlled growth or chemically controlled growth. Under kinetically controlled growth conditions, seeds are formed using the standard citrate reduction technique. The reaction solution is then cooled below 90°C and excess gold and citrate are added. At that temperature, the citrate cannot reduce the gold salt to form new particles so the gold ions deposit onto the existing seeds, forming larger, spherical AuNPs.[30] For chemically controlled growth, small seed particles are either made through the citrate reduction method or using stronger reducing agents, most often sodium borohydride ($NaBH_4$), and a surfactant capping agent, hexadecyltrimethylammonium bromide (CTAB). These CTAB-capped seed particles can then be grown iteratively into larger AuNPs, with controlled diameters of 5 – 150 nm showing excellent monodispersity.[34] However, the CTAB used as a capping agent for these AuNPs is a cationic detergent, inducing cytotoxicity if it is not properly removed from the nanoparticle surface before biological applications. Other chemically controlled methods using citrate capped seeds have shown promise for the synthesis of large, more biocompatible AuNPs. These often use hydroxylamine[35] or hydroquinone[31] as the reducing agent and involve the room temperature reduction of the gold salt onto the seeds while using citrate as a biocompatible capping agent to passivate and stabilize the AuNP surface (**Figure 1.1B**).

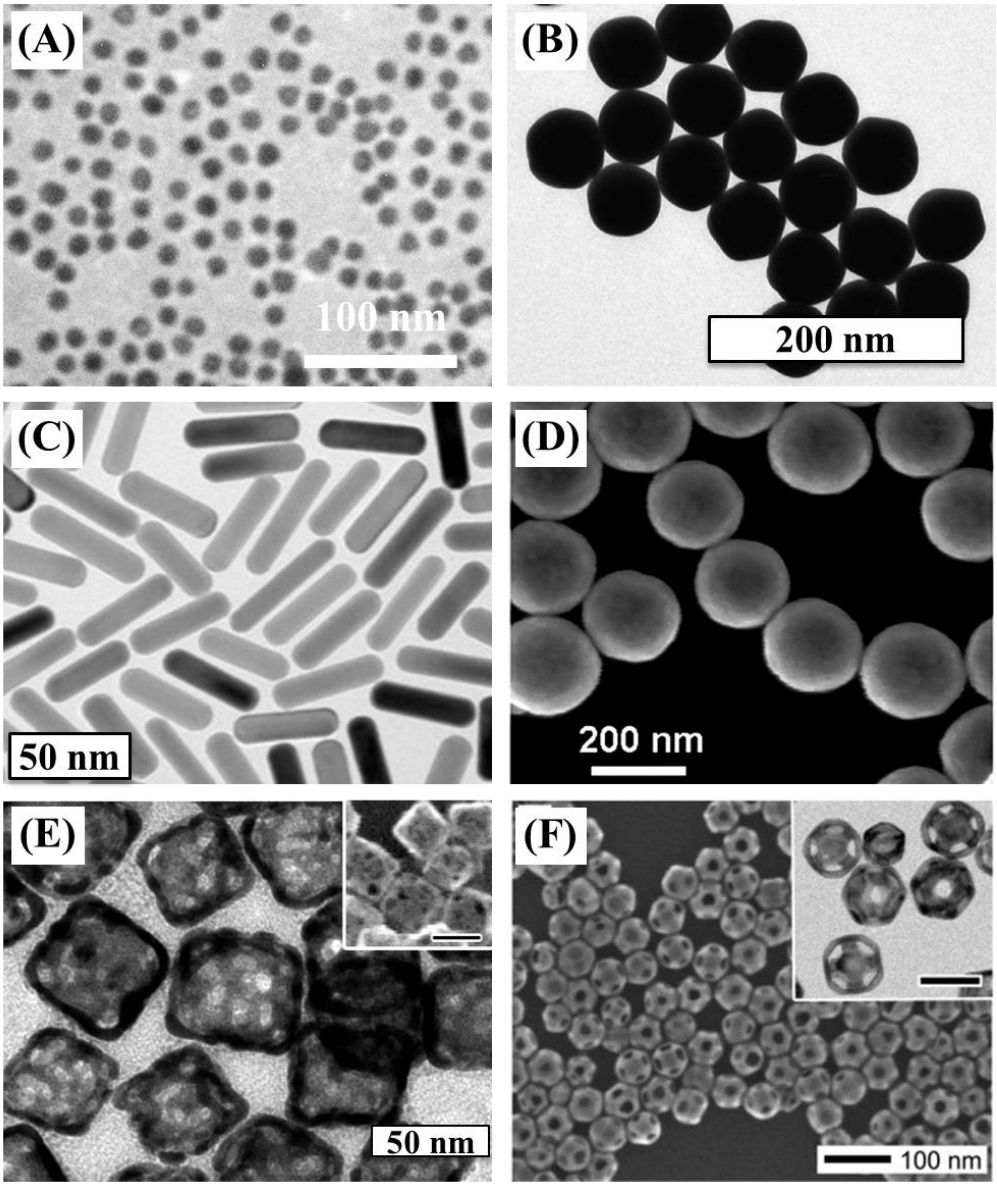

Figure 1.1 EM images of different AuNP sizes and shapes used in biomedical. (A) TEM of small, 15 nm nanospheres synthesized using the citrate reduction method, (B) TEM of large, 150 nm spheres synthesized via a seeded growth method, (C) nanorods, (D) SEM of nanoshells, (E) TEM of cubic nanocages with a 50 nm edge length, 5 nm wall thickness, and SEM inset, and (F) SEM of truncated nanocages with a 30 nm edge length and a high magnification TEM inset. (A) Adapted with permission from ([220]). Copyright (2016) American Chemical Society. (B) Adapted with permission from ([221]). Copyright (2011) American Chemical Society. (C) Adapted with permission from ([122]). Copyright (2014) American Chemical Society. (D) Adapted with permission from ([14]). Copyright (2007) American Chemical Society. (E) Adapted with permission from ([41]). Copyright (2007) American Chemical Society. (F) Reprinted with permission from ([222]). Copyright (2010) Elsevier.

While significant efforts have gone into the synthesis of novel AuNP geometries, the most common solid, nonspherical AuNP geometry used for biomedical applications is the nanorod. Nanorods are generally made through seed mediated growth methods by synthesizing the seeds as described above, using $NaBH_4$ to reduce the gold salt and CTAB to cap and stabilize the particles. The CTAB capped seeds were first used for nanorod synthesis by Nikoobakht and El-Sayed[36] as well as Murphy *et al*.[37] This method yielded gold nanorods (AuNRs) in relatively high yield by adding the seeds into an aqueous growth solution containing CTAB, gold chloride, silver nitrate, and ascorbic acid (**Figure 1.1C**). This is still the most widely used method for AuNR synthesis due to the yield and tunability of the nanorod aspect ratio (length : width ratio), which is achieved by simply adjusting the seed / gold salt ratio or the silver concentration. Other common nanostructures used in biomedical applications, include nanoshells and hollow nanocages. The use of gold nanoshells (AuNSs) was pioneered by the Halas group, who deposited small AuNPs onto a silica core (**Figure 1.1D**). The nanoshells were then generated through the chemical reduction of additional gold ions onto the particles using a mild reducing agent, resulting in the coalescence of the initially deposited small AuNPs and the generation of a uniform gold nanoshell on the surface of the silica core.[14, 38-39] In contrast to nanorods and nanoshells, gold nanocages (AuNCs) are formed through a templated reaction introduced by Xia and coworkers.[13, 40-41] In this method, silver nanocubes are first synthesized and then coated with a layer of gold. The silver core is then hollowed out by a galvanic replacement reaction, where 3 silver atoms are oxidized to silver (I) ions and a gold (III) ion is reduced to a gold atom due to the difference in their electrochemical potential. The etching of silver from the interior of the cube and

deposition of gold proceeds until the majority of the silver is consumed,[41] resulting in a hollow frame or cage structure with a tunable size and thickness (**Figure 1.1E and 1.1F**). Additional AuNP geometries used for biomedical applications include nanoplates,[42-43] nanoprisms,[44-46] and branched nanostructures[43, 47-50] (**Table 1.2**).

Table 1.2 Synthesis and LSPR properties of AuNPs

AuNP	LSPR peak	Typical size range	Synthetic methods	References
Spheres	510 – 575 nm	5 – 150 nm	Citrate reduction, Brust method, seeded growth	25-26, 28, 30-31, 33
Nanorods	600 – 1200 nm (longitudinal)	20 – 400 nm (long axis) x 5 – 50 nm (short axis)	Seed mediated growth, seedless, electrochemical	36-37, 224-225
Nanoshells	520 – 1000 nm	60 – 250 nm (10 – 200 nm shell thickness)	Templated	14, 38-39
Nanocages	520 – 1000 nm	30 – 200 nm (edge length)	Galvanic replacement	13, 40-41, 123, 222
Nanoprisms and nanodisks	650 – 1300 nm	40 – 400 nm (edge length) x 5 – 20 nm (thickness)	Electrochemical reduction, photochemical reaction,	42-46
Branched nanostructures	600 – 750 nm	40 – 300 nm	Seed mediated, direct (one pot)	43, 47-50

1.1.2 Conjugation

For biological applications, the surface chemistry of nanoparticles plays a crucial role in determining their targeting, uptake and clearance, stability, toxicity and

biocompatibility, and recognition by and interaction with biomolecules.[51-58] Thus, specific passivating groups, typically polymers,[59-62] or targeting moieties, such as peptides,[63-65] proteins,[66-68] DNA or RNA,[63, 69-70] and small molecules,[71-72] are often desired to promote uptake into specific cells or tissues, or to prevent uptake and increase circulation. Various conjugation strategies have been used to attach these ligands, through noncovalent interactions such as electrostatic adsorption or layer by layer (LbL) assembly, and covalent attachments (**Table 1.3**).

Table 1.3 Summary of AuNP surface modifications

Surface Chemistry	Common ligands	Application	Conjugation technique	References
Citrate	Citrate	Uptake	AuNPs as synthesized	25-26
CTAB	CTAB	Uptake	AuNPs as synthesized	34, 36-37, 217
Polymer	PEG, poly(vinyl pyrrolidone) (PVP), poly(ethylenimine) (PEI), poly(lactic-co-glycolic acid) (PLGA)	Biocompatibility, increased circulatory half-life, gene delivery passive targeting	AuNPs as synthesized, Covalent, electrostatic, LbL	54, 62, 79, 105, 224, 226-228
Peptide	RGD, NLS, TAT, ScFv(s)	Targeting	Covalent, amide coupling	63, 65, 229-230
Antibody	EGFR, HER2, transferrin, TNF-α	Imaging, PPT, therapeutic	Electrostatic, LbL, amide coupling	66, 68, 126, 185, 231-233
Nucleotide	DNA, RNA	RNA interference, targeting, gene regulation	Covalent, electrostatic	48, 63, 70, 199, 212, 227, 234
Small molecule	Folic acid, hormones, photosensitizer	Targeting, PDT	Covalent	71, 83, 212, 235-236
Drugs	Doxorubicin, docetaxel, platinum complexes	Therapeutic	Covalent, electrostatic, LbL, pH or heat labile linkers	187, 196, 199-200, 237-238

During electrostatic adsorption, antibodies are bound to the AuNP surface by adjusting the solution pH around the isoelectric point of the protein to impart a slight positive or negative charge to that protein, allowing for conjugation to the charged AuNPs through electrostatic interactions.[67] Electrostatic adsorption to AuNPs has also been extended to DNA.[73] While a relatively straightforward conjugation technique, the primary drawbacks of electrostatic adsorption are denaturation of the protein upon binding, which can result in a decrease or loss of targeting due to the proteins' conformational change, and the relative weakness of the interaction, which can result in desorption of the proteins or DNA under physiological conditions. To circumvent the electrostatic limitations, LbL assemblies can be used.[59] These involve the encapsulation of the AuNPs by the adsorption of multiple polymer layers with alternating positive and negative charges[52] (for example, CTAB capped nanorods would be coated with a negatively charged poly (styrene sulfonate) to allow for electrostatic coating, followed by a layer of positively charged poly (ethylene imine)[74]). LbL coatings allow for tunable AuNP surface charge, which can be used for electrostatic protein adsorption[75] or gene delivery[74]. They can also be designed to incorporate hydrophobic and hydrophilic regions in the various layers and programmed to release them slowly.[21, 76] This is a highly desirable characteristic for the delivery of therapeutic drugs with limited solubility or high clearance.

Despite the inert nature of gold, it is known for the ability to form a relatively strong gold-thiol bond (Au-S) with molecules containing terminal thiols or disulfide bonds, often thought of as covalent or semi-covalent linkages.[77] These attachments have

been investigated extensively in the context of self-assembled monolayers (SAMs), where thiolated molecules form a highly ordered monolayer on the gold surface. Accordingly, the strength of the gold-thiol bond (~ 45 kcal / mol; as a reference, disulfides, with bond energies of ~ 60 kcal / mol, stabilize proteins and help impart tertiary structure)[77] has been widely used to functionalize AuNP surfaces. Thiolated polymers, most commonly poly (ethylene glycol) (PEG), are used to impart stability, hydrophilicity, and biocompatibility to AuNPs, while minimizing nanoparticle uptake and clearance, and preventing nonspecific protein adsorption.[62, 78-80] Additionally, varying the terminal functional groups allows for the attachment of many different biological molecules, including antibodies,[81] targeting peptides,[82] and hormones[83] to name a few. Heterobifunctional PEG thiol molecules, with terminal amine or carboxyl groups, are commonly used as a handle to attach proteins or peptides to AuNPs through carbodiimide coupling reactions, covalently linking the PEG functional group to the protein or peptide of interest. Alkyne or azide terminated PEG thiol molecules have also been adsorbed to gold and used to functionalize the AuNP surface through "click" chemistry reactions.[84-85] Nucleic acids have also been attached to AuNPs by modifying the 3' or 5' ends with thiolated PEG linkers and used to promote cellular targeting and uptake, to generate 3D assemblies through hybridization of complementary strands,[86-88] for regulating gene expression,[89] and as sensors for various proteins, target RNA strands, and heavy metal ions[85, 90-91].

1.1.3 Characterization

Multiple techniques are often used in parallel to characterize the size, shape, surface chemistry, aggregation state, and optical properties of AuNPs. Among the most

important methods is transmission electron microscopy (TEM) or scanning electron microscopy (SEM), which both allow for the direct observation of the size and shape of colloidal or substrate stabilized nanoparticles. While TEM and high resolution TEM (HRTEM) provide detailed information on nanoparticle size and crystal structure, SEM is often preferred to characterize non-spherical AuNPs due to the increased shape resolution provided by the scanning electron beam, allowing for an extra dimension (relative to the 2D TEM) in the micrograph. The wider field of view during SEM measurements is also advantageous for analyzing images containing more AuNPs, providing greater insight into the monodispersity of the sample.[23-24]

While electron microscopy involves the use of samples dried onto an appropriate electron microscopy (EM) grid and imaged under vacuum, dynamic light scattering (DLS) is often used in tandem to characterize AuNPs in solution. DLS measures fluctuations in scattered light intensity due to Brownian (i.e. random) motion of the particles in solution, which is then used to determine their diffusion coefficient and then related to the hydrodynamic radius of a sphere through the Stokes-Einstein relationship. DLS can generally be used in the pico- to nanomolar concentration range and for particles ranging from below 1 nm up to 10 μm. [92-94] However, the analysis becomes less reliable and more complex at higher concentrations or for non-spherical shapes due to multiple scattering events, where the incident photons are scattered multiple times before detection, and the varied scattering angles based on the orientation of the nanostructure. For these reasons, DLS is generally used as a complimentary method instead of a qualitative one, with an increase in hydrodynamic size indicating successful conjugation of a ligand or protein of interest. Nanoparticle surface chemistry is also measured in

solution to monitor colloidal stability or successful conjugation through ζ-potential measurements. Although the ζ-potential of colloids is not directly measurable, in practice it is calculated based on the electrophoretic mobility of the nanoparticles in solutions, or their ability to conduct an electrical charge on their surface. Accordingly, a change in ζ-potential (the scale and magnitude of which depends on the initial surface chemistry of the AuNP and the molecule being conjugated) is indicative of successful conjugation due to the change in surface chemistry of the particles. For example, AuNPs made through the citrate reduction method have negative ζ-potentials upon synthesis (typically −30 mV to −50 mV), which become less negative or positive upon conjugation with PEG or targeting peptides. [80, 95]

Extinction spectroscopy is also used extensively to characterize the AuNPs optical response in the UV-Vis-NIR regions of the electromagnetic spectrum due to their characteristic LSPR band, which is sensitive to the nanoparticle size, concentration, morphology, aggregation state, and the quality of the colloidal dispersion (see *1.2 AuNP Optical Properties*). The absorption of colloidal gold solutions at 400 nm, arising from atomic gold (i.e. Au^0), has also been used to estimate AuNP concentration based on Beer's Law and EM information about the particle size and shape.[96-97] The number of atoms per AuNP can be estimated using its size and shape, and accounting for the crystal structure of gold, and then used to calculate the AuNP concentration in solution based on absorbance. A more accurate, albeit more expensive and time consuming, method for calculating AuNP concentration is through inductively coupled plasma (ICP), which is coupled with detection techniques such as mass spectrometry (ICP-MS), optical emission spectroscopy (ICP-OES), or atomic emission spectroscopy (ICP-AES). These techniques

involve the digestion of a AuNP solution with a known extinction, using concentrated aqua regia, which results in the dissolution of the nanoparticle into individual gold chloride ions. The gold concentration is then determined using ICP and correlated to AuNP size and shape through EM measurements to calculate the number of nanoparticles in solution. Thus, an extinction coefficient can be determined for a particular size and shape of AuNPs and used to rapidly calculate the colloidal concentration.[67, 97-98]

Other techniques used to characterize AuNPs, although less common, include atomic force microscopy (AFM), [99-101] small angle X-ray scattering (SAXS), [102-104] energy dispersive X-ray spectroscopy (EDX), [105-108] and X-ray ray diffraction (XRD) [40, 109] (see **Table 1.4** below). EDX is often used in conjunction with TEM or SEM to confirm the elemental composition of the nanostructure, which is particularly useful for core shell particles such as nanoshells, and bimetallic particles such as nanocages. [105-108] For smaller AuNPs (< 5 nm), which can be challenging to accurately size using EM, SAXS is often used in conjunction with electron microscopy to confirm AuNP size. An added benefit of SAXS measurements is the ability to be performed in situ, which allows for the evolution of nanoparticle growth to be monitored during synthesis.[102-104] XRD can also be used as an elemental analysis technique to determine the metal content of bimetallic nanostructures and to approximate AuNP size by analyzing the broadening of the diffraction peaks using the Scherrer Equation. Although XRD can resolve size differences of ~ 1 - 2 nm, EM techniques have generally replaced XRD for AuNP size characterizations due to the significantly lower sample volumes needed for EM imaging and the ease of sample preparation, which often consists of simple drop casting of a few microliters of the colloidal AuNPs. It is however still commonly used to characterize

nanostructure crystallinity, which can have a significant effect on their optical response. In contrast to EM methods which must be used under vacuum, AFM is a scanning probe microscopy technique that can be used to analyze wet or dry samples, in addition to soft materials, and particles assembled into films or 3D structures. Although AFM has significantly lower lateral resolution than EM techniques (~ 20 – 30 nm for AFM and < 1 nm for EM) due to convolution from the tip, AFM has excellent vertical resolution, often below 1 nm, which has been used to map the ligands on a nanoparticle surface and to monitor bioconjugation (for a detailed overview of AFM for bioconjugation applications, see the review by Tessmer *et al*. [110]).

Table 1.4 Summary of AuNP characterization techniques

Technique	Output	Common uses	Advantages	Dis-advantages	Refer-ences
TEM (most commonly used)	Electron micrograph	Size and shape characterization	Detailed analysis of AuNP size and morphology, single particle analysis	Samples must be dried, small field of view limits number of NPs analyzed, relatively expensive	Nearly all AuNP literature
SEM	Electron micrograph	Size and shape characterization	Detailed analysis of AuNP shape, wide field of view, single particle analysis	Samples must be dried, generally lower magnification than TEM, relatively expensive	14, 222, 239
DLS	Hydro-dynamic size	Measuring AuNP size and monodispersity, confirming conjugation, diagnostics	Nondestructive, rapid, measured in solution, sensitive to aggregation	Assumes spherical shape, biased by larger particles, not ideal for polydisperse samples, requires filtration	92-94

Table 1.4 (continued)

ζ-potential	Surface potential	Confirm AuNP conjugation, compare stability	Measures particle stability and surface charge	May induce aggregation	80, 95
UV-Vis-NIR spectro-scopy (most commonly used)	Extinction spectra	Characterizing optical properties and concentration	Simple, rapid, nondestructive	Ensemble measurement, does not provide definitive information	Nearly all AuNP literature
ICP	Metal ion concent-ration	Determining concentration	Sensitive, straightforward sample preparation, precise characterization of AuNP uptake	Must be used in tandem with EM to determine concentration, requires AuNP digestion with concentrated acids	67, 97-98
AFM	Surface topography	Characterizing AuNP arrays and biomolecular interactions	3D mapping of sample on substrate, applicable for wet surfaces,	Slow scan time / small viewing area, sample must be stabilized by a substrate, requires optimization	99-101
SAXS	Structural information	Analysis of AuNP size (< 5 – 10 nm), shape	Detailed size and shape (crystal facet) information	Requires complex sample preparation (thin films), complex data analysis	102-104
EDX	Elemental analysis	Elemental mapping for bimetallic nanostructures	Provides elemental information	Generally must be combined with EM techniques, complex analysis	105-108
XRD	Structural information	Crystallinity characterization	Detailed crystal structure analysis, crystal facet size can be extracted	Requires complex sample preparation (thin films or large volumes)	40, 109

1.2 AuNP Optical Properties

Gold nanoparticles have been used since ancient times due to their strong interactions with light, resulting in enhanced scattering and absorption properties.[3] These properties are apparent in the distinct colors exhibited by colloidal gold solutions and arise from their localized surface plasmon resonance (LSPR). The LSPR results from the coherent oscillation of conduction band electrons through the metal nanoparticle, in resonance with incident light (Error! Reference source not found.). The frequency of the scillation depends on the size and shape of the AuNP, along with its composition (specifically the dielectric constant of the metal), the refractive index of the surrounding media, and coupling interactions between nanoparticles in close proximity.[111] The excited LSPR of AuNPs can decay radiatively, in the form of light scattered by the nanoparticle at the same incident frequency. This enhanced electromagnetic field at the AuNP surface forms the basis of many optical and spectroscopic imaging applications. If the incident photon is instead absorbed, the plasmon decays non-radiatively through collisions between the excited electrons and metal lattice,[112] resulting in heating of the solution surrounding the AuNP, which forms the basis of plasmonic photothermal therapy.

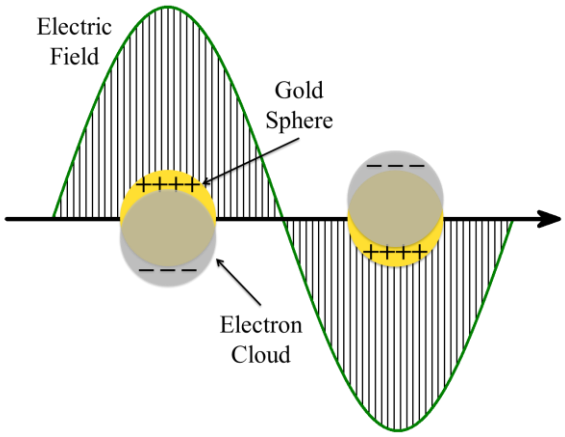

Figure 1.2 Schematic illustration of the LSPR, arising from the coherent oscillation of the AuNP conduction band electrons in resonance with incident light.

1.2.1 Scattering

The AuNP plasmon resonance leads to enhanced electromagnetic fields at the nanoparticle surface, resulting in immense scattering cross sections which can serve as powerful tools for imaging. The scattering by AuNPs is predicted by Mie theory, Gustav Mie's solution to Maxwell's equations for the scattering of light by spherical particles (with a diameter significantly smaller than the wavelength of incident light).[113] The scattering by a single AuNP is 4 – 6 orders of magnitude larger than the emission from a typical organic dye or fluorescent protein, which allows for single particle imaging.[114] An added benefit of AuNPs is their photostability; they do not bleach which allows for longer imaging time and greater excitation energy, simplifying some imaging applications.[7]

When light is scattered by a AuNP, it is emitted from the particle surface with the same energy as the incident excitation photon. This elastically scattered light forms the basis of optical imaging applications and is used extensively in dark-field microscopy.[7, 58] Dark-field imaging is commonly used because it is a sensitive, high contrast imaging modality but does not require expensive instrumentation or intensive sample preparation, simply a standard optical microscope equipped with a dark-field condenser. Broad, white light sources are used for excitation and the condenser ensures that the light is incident to the sample at high angles such that only light scattered by the sample is collected through the objective while the remaining excitation light passes undetected. While biological samples only weakly scatter white light, AuNPs strongly scatter light that coincides to their LSPR wavelength. Thus, the nanoparticles are seen as bright, colored spots (with a color corresponding to their LSPR wavelength) that contrast with the dark sample background (see *1.3.1 Optical Imaging* for recent applications in bioimaging).

While AuNPs scatter light with the same energy as the excitation photons, molecules in the nanoparticle vicinity interact with that elastically scattered light, leading to inelastic or Raman scattering. Raman scattering occurs when a molecule absorbs a photon, which is then emitted with a different energy. The difference in energy between the excitation photon and the emitted one is characteristic of a specific bond within the molecule. Thus, Raman spectroscopy presents a unique fingerprint of the bonds (specifically the vibrations of those bonds) within the molecule being studied. While Raman spectroscopy is highly suited for biological applications due to negligible interference from water, the main disadvantage is that Raman is an inherently weak spectroscopic imaging technique (~ 1 in 10 million photons is inelastically scattered);

therefore, high concentrations of the analyte being studied and / or high excitation laser intensities are typically required. However, the AuNPs can greatly enhance Raman signals due to their enhanced electromagnetic field in an effect termed surface enhanced Raman spectroscopy (SERS). For ensemble measurements, SERS typically achieves enhancements of 6 orders of magnitude relative to traditional Raman measurements, and the SERS enhancement has been estimated to reach as high as 10^{14} – 10^{15} in some experiments, which has allowed for single particle and single molecule imaging. For recent applications of SERS in diagnostics, see *1.4.3 Surface enhanced Raman Spectroscopy (SERS)*, or refer to the recent review by Lane *et al.*[10] for a more comprehensive discussion of SERS.

1.2.2 Absorption

In addition to scattered light, the AuNP may absorb the photon which results in the non-radiative decay of the plasmon resonance through collisions between the excited electrons (electron-electron interactions), between electrons and the metal lattice (electron-phonon interactions), and finally through collisions within the lattice (phonon-phonon interactions). The collision of phonons, or oscillations within the metal lattice, generates heat surrounding the nanoparticle which can significantly increase the temperature of the surrounding medium. The photothermal conversion of light to heat by AuNPs is useful for biomedical applications, as it only occurs in the nanoparticle vicinity.[115] Through rational design of the AuNP optical properties and surface chemistry, hyperthermia can be induced in selectively targeted cell populations without adversely affecting nearby untargeted tissues (see *1.3.2 Photoacoustic Imaging* and *1.5.3 Plasmonic*

Photothermal Therapy (PPT) for recent applications in biomedical imaging and cancer treatment).

1.2.3 Tuning AuNP Optical Response

One of the most valuable properties of AuNPs is the tunability of their optical response, namely their scattering properties, absorption properties, and the frequency of their LSPR bands. The LSPR peak can be red-shifted to longer wavelengths, with a corresponding increase in intensity, by increasing the AuNP size. For example, a spherical 15 nm AuNP exhibits a plasmon resonance at ~ 518 nm, which shifts to ~ 530 nm for a 30 nm particle, ~ 540 nm for a 60 nm AuNP (**Figure 1.3**), and the extinction coefficient for the particles increases by a factor of ~ 8 – 10 for both cases.[97] Additionally, the AuNP scattering and absorption properties can be tuned by adjusting the nanoparticle size. For particle diameters below 20 nm, the total light extinction is due almost entirely to absorption and the scattering contribution is negligible. As the AuNP size increases, the scattering to absorption ratio increases; while the total extinction for a 20 nm AuNP is > 95% absorption, the total extinction from an 80 nm AuNP is ~ 50% absorption and ~ 50% scattering.[116] These properties allow for the rational design of AuNPs for specific biomedical applications. For absorption based applications, such as photothermal therapy or photoacoustic imaging, smaller nanoparticles are preferred due to their greater light absorption efficiency, while for imaging, larger AuNPs are desirable for their increased scattering properties.

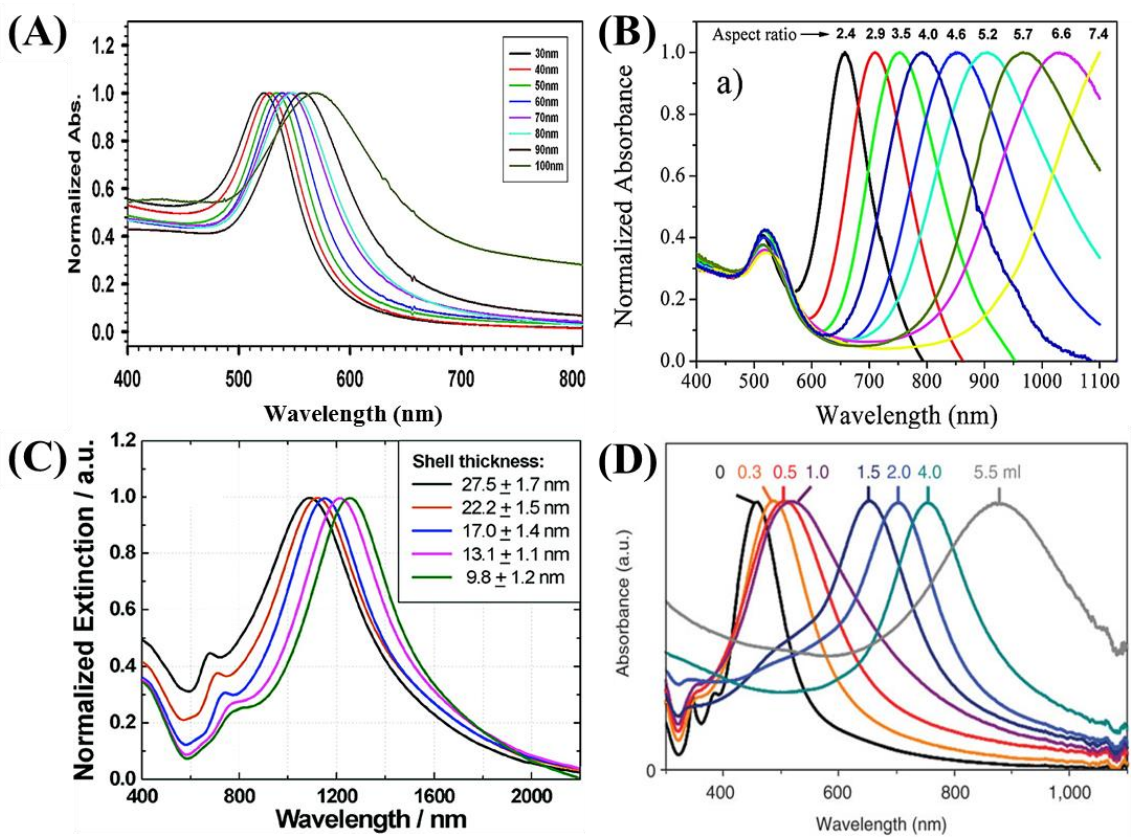

Figure 1.3 Size, shape, and structure tunability of AuNPs optical properties. (A) Red-shift of LSPR frequency with increasing AuNP size. (B) Tuning longitudinal LSPR of AuNRs with increasing aspect ratio. (C) Red-shift of LSPR frequency with decreasing nanoshell thickness. (D) Tuning LSPR frequency of nanocages with increasing gold concentrations during synthesis. (A) Adapted with permission from (223). Copyright 2007 American Chemical Society. (B) Reprinted with permission from (8). Copyright 2008 American Chemical Society. (C) Reprinted with permission from (14). Copyright (2007) American Chemical Society. (D) Reprinted with permission from (123). Copyright 2007 Nature Publishing Group.

In practice, tuning the LSPR frequency of spherical AuNPs is limited to ~ 50 nm because AuNPs with diameters above ~ 100 – 150 nm suffer from decreased stability, lower rates of cellular uptake, and increased dephasing of the plasmon as the particle size approaches that of the wavelength of light. Alternatively, the LSPR can be tuned by modifying the surface chemistry of AuNPs to assemble into 3D structures, often using

DNA templates, or to promote cellular uptake and aggregation into tightly packed vesicles (e.g. lysosomes, endosomes, etc.). When multiple AuNPs come into close proximity of each other, in 3D structures or in vesicles, the electromagnetic plasmon fields on adjacent nanoparticles couple together. This plasmon coupling results in a red-shift of the LSPR frequency to longer wavelengths and a simultaneous increase in scattering intensity, relative to a single AuNP.[58] Additionally, the coupled plasmon of AuNPs in close proximity is highly sensitive to separation distance, such that the observed LSPR shift of nanoparticle dimers has been used to measure nanometer separation distances. The 'plasmon ruler', first introduced by Alivisatos and coworkers,[117] has recently been refined to measure distances as small as 5Å (0.5 nm),[118] and used to investigate molecular binding events,[119] monitor drug response,[120] and to measure enzyme activity,[119] and a 3D plasmon ruler has recently been reported.[121] Larger AuNP aggregates, such as those found in vesicles, are typically more difficult to analyze quantitatively due to their complex, dynamic structure but have shown imaging utility (see *1.3 Imaging*).

Additionally, the LSPR of AuNPs can be tuned by controlling the shape and structure of the nanoparticle. Considering non-spherical nanoparticles, AuNRs are among the most studied. By breaking the nanoparticle symmetry and elongating it into a rod, the AuNR conduction band electrons are able to oscillate in two directions, along the short axis and along the long axis of the nanorod, respectively. These two distinct electron oscillations result in two plasmon modes (i.e. LSPR bands). The transverse plasmon mode arises from electron oscillation along the short nanorod axis and the corresponding LSPR band appears at a similar frequency to a nanosphere with the same diameter. The

longitudinal mode, arising from electron oscillation along the long axis of the nanorod, results in the appearance of the second LSPR band at a longer wavelength.[112] The frequency of the longitudinal mode is highly sensitive to the nanorod aspect ratio (length : width ratio), and the LSPR band can easily be tuned from ~ 650 nm to > 1100 nm simply by increasing the AuNR aspect ratio (**Figure 1.3B**).[122]

Variations in AuNP structure, such as the nanoshell or nanocage, are also used to tune AuNP optical properties. In the case of nanoshells, introduced by Halas and coworkers, small AuNPs are deposited on a silica core and serve as seeds for the growth of the nanoshell. It was found that decreasing the shell thickness resulted in a red-shift in the LSPR band due to hybridization of the plasmon modes on the interior and exterior of the gold layer.[14] Using the same 60 nm core size, decreasing the AuNS thickness from 20 nm to 5 nm resulted in a ~ 300 nm red-shift in the LSPR band (**Figure 1.3C**). More recently, Xia and coworkers developed gold nanocages, hollow or porous nanostructures synthesized through the galvanic replacement of a silver nanocube with gold ions. The size and shape of the AuNCs were dictated by the silver nanoparticles used as templates in the synthesis. The thickness of the cage walls as well as the LSPR frequency was tuned by modifying the amount of gold added during synthesis (**Figure 1.3D**).[123]

1.3 Imaging

Gold nanoparticles are used extensively in bio-imaging applications due to their strong, tunable optical properties, described previously. The intense scattering properties exhibited by AuNPs, with diameters typically in the 30 – 80 nm range for imaging, are readily detected and easily quantified using standard optical microscopes. Additionally,

modifying the AuNP size and shape allows for tuning of the LSPR wavelength within the "biological window" (650 – 1100 nm) where there is minimal attenuation by blood (specifically hemoglobin) and tissue, and imparts control over the scattering and absorption properties.[124-125] This allows for both optical imaging using elastically scattered light, spectroscopic imaging using inelastically scattered light, and photoacoustic imaging using absorbed light. The tunable scattering and absorption properties of AuNPs, combined with their excellent photostability, have led to their use as powerful probes for cellular imaging, both *in vitro* and *in vivo*.

1.3.1 Optical Imaging

Bioconjugated AuNPs were first shown to distinguish between healthy and cancer cells in 2003 by Sokolov et al. through the use of laser scanning confocal reflectance microscopy.[126] In this work, the authors utilized anti-EGFR antibody functionalized AuNPs that bind to EGFR, a transmembrane glycoprotein that is overexpressed in epithelial cancers,[127] to selectively identify cancer cells. Seeing this work and knowing the strong light scattering properties of AuNPs, El-Sayed and co-workers set out to achieve the same outcome using a different imaging technique, dark-field microscopy (**Figure 1.4A**).[68] Dark-field microscopy utilizes a white light source and a condenser that prevents centered light rays from reaching the sample of interest. This results in only scattered light entering the objective. The microscope can then be coupled to a color-CCD camera for simple image collection. Through the addition of human anti-EGFR antibody conjugated spherical AuNPs, El-Sayed and co-workers were able to successfully distinguish between cancerous and noncancerous cells (**Figure 1.4B**). The authors confirmed their microscopy results with SPR absorption spectroscopy, which

showed an increase at 543 nm for cancerous cells due to the binding of AuNPs to the cancer cell surface. Antibody functionalized gold nanorods (AuNRs) and gold nanoshells (AuNSs) have also been utilized in dark-field microscopy assays.[128-129] By switching to AuNRs or AuNSs, there is an added benefit that once identified, cells with increased nanoparticle binding can be irradiated with near-IR light resulting in their selective photothermal destruction. While the studies highlighted here focused on oral and breast cancer cells, this diagnostic imaging platform is extremely versatile and can be expanded to identify many other cancer cell types and cellular biomarkers.

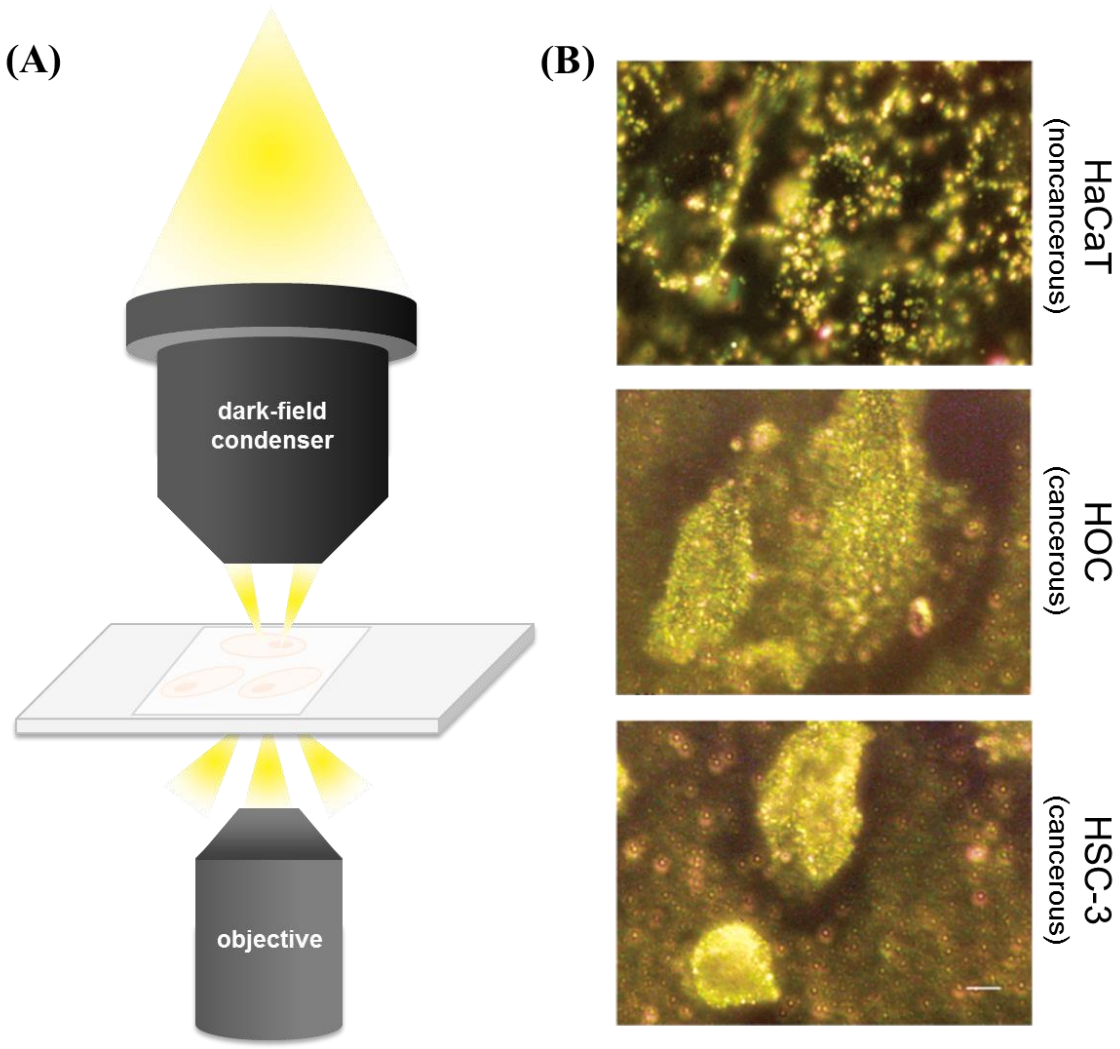

Figure 1.4 (A) Schematic diagram of the main optical components for dark-field microscopy. (B) Dark-field images of cancerous and noncancerous cells treated with human anti-EGFR antibody conjugated spherical AuNPs. Cancerous cells showed increased AuNP light scattering intensities compared to noncancerous cells. Adapted with permission from (68). Copyright (2005) American Chemical Society.

In addition to conventional dark-field microscopy, the simultaneous visualization and quantification of cell surface biomarkers could be achieved by coupling dark-field microscopy and colorimetric analysis of the AuNP scattered light in the acquired images. Recently, live cell dark-field microscopy has been used to monitor nano-bio interactions

in real-time. By modifying the traditional optical microscope to incorporate a temperature and atmosphere controlled incubator and using an angled incident white light source in place of a dark-field condenser, El-Sayed and coworkers designed a system to image the cellular interactions of AuNPs in real-time. Spherical AuNPs were conjugated with different ratios of RGD, a cell penetrating peptide, and a nuclear localizing sequence (NLS) peptide, and changes in scattering intensity and wavelength were monitored during cellular uptake and localization of the nanoparticles. The AuNPs with the highest ratio of NLS peptides (i.e. the most highly targeted particles) displayed the largest red-shift in scattering wavelength and the greatest scattering intensity, which was attributed to the formation of denser nanoparticle clusters. The increased scattering indicated that highly targeted AuNPs would be ideal probes for cellular imaging.[58] Nuclear targeted AuNPs were then used as scattering probes to compare the efficacies of three commonly prescribed anticancer drugs, cisplatin, 5-fluorouracil (5FU), and camptothecin, which induce apoptotic cell death. Some characteristic morphological changes of apoptotic death include shrinking of the cell, membrane blebbing, and increased white light scattering. However, monitoring the scattering increase due to cell death, without the use of exogenous probes, was not a reliable method to compare drug efficacy. The addition of AuNPs, at a sufficiently low concentration that normal cell function was not perturbed, led to a significant increase in scattering upon cell death. Following the scattering increase over time yielded a profile of drug efficacy similar to that determined using a commercially available cell viability kit.[130] The ability to monitor nanoparticle-cell interactions in real-time using inexpensive equipment, or to use AuNPs as probes to monitor cell processes with minimal perturbation, will likely lead to significant

advancements in the pharmaceutical field and increased biological applications of nanotechnology.

1.3.2 Photoacoustic Imaging

Photoacoustic (PA) imaging offers a proven *in* vivo imaging technique with high spatial resolution. In contrast to optical or spectroscopic imaging which use scattered light, PA imaging uses light that is absorbed by AuNPs. The absorbed energy is then converted to heat through electron-electron (~ 100 fs), electron-phonon (~ 1 ps), and phonon-phonon oscillations (~ 100 ps) within the AuNP.[112] This relaxation process occurs very rapidly and results in intense heating at the nanoparticle surface. When the local nanoparticle environment is rapidly heated and the heat cannot dissipate quickly enough, a thermal expansion occurs. This expansion quickly collapses on itself and generates a photoacoustic (PA) wave, which is detected using an ultrasonic transducer and converted into an image.[124] Photoacoustic signals are inherently weak, relegating the use of PA imaging to vascular structures due to the strong absorption of hemoglobin. Although tumor angiogenesis results in differing vasculature from healthy tissue,[131] PA imaging does not possess sufficient contrast to distinguish between healthy and malignant vasculature. Thus, exogenous agents, such as AuNPs, are needed to increase the absorption, and therefore PA contrast, for tumor imaging applications. This was first reported by Oraevsky and coworkers, who assessed the contrast enhancement of 40 nm AuNPs conjugated with Herceptin to selectively target breast cancer cells and were able to detect nanoparticle concentrations as low as ~ 1 pM at depths up to 6 cm.[132] This technique was later termed photoacoustic tomography (PAT) and used to successfully image malignant populations using AuNCs, resulting in a 63% contrast enhancement, and

AuNSs that achieved an 81% contrast enhancement. More recently, a combination magnetic resonance imaging (MRI), PAT contrast, Raman imaging nanoparticle was used to image brain tumors *in vivo*. Using a spherical AuNP core (for PAT contrast enhancement), coated with a Raman active layer and surrounded by a gadolinium shell (for MRI), the probe was developed to combine the benefits of all three imaging techniques into a single, multimodal nanoparticle probe while enhancing the stability of each individual method.[133] Other AuNP geometries have also been used as PAT contrast agents, including nanorods,[134-136] nanoshells,[137] nanocages,[138], nanostars,[139] hollow nanospheres,[140-141] and hybrid magnetic core shell particles (gold / iron oxide).[142-143]

1.4 Diagnostics

As with many diseases, the development of earlier, more accurate, and cost effective detection assays is crucial for increasing cancer patient survival. With their unique optical and physical properties as well as relatively straightforward syntheses, AuNPs offer a promising alternative to traditional fluorescence and radiolabeled assays. Their strong light scattering allows for greater simplicity in assay designs while still maintaining, or even lowering, the detection limit for the analyte of interest. While these AuNP properties should be leveraged in developed countries to expedite disease detection, AuNP diagnostic assays may see the greatest clinical impact in regions with limited healthcare availability and where point-of-care diagnostics are required.

1.4.1 Colorimetric Assays

Colorimetric based assays are regarded as having a relatively simplistic, high-throughput, and cost effective design. They are based on the color change of a solution,

which can often be seen by the naked eye, resulting from the aggregation of bioconjugated AuNPs after the introduction of a target analyte **(Figure 1.5)**. Normally AuNPs exhibit a red wine color when in solution. However, when triggered, AuNPs can aggregate and undergo interparticle plasmonic coupling that causes their LSPR band to red-shift to longer wavelengths, leading to the adoption of a purple color in solution. This assay format was first described by Chad Mirkin and co-workers in 1997 when they utilized mercaptoalkyloligonucleotide modified AuNPs for the selective detection of polynucleotides via hybridization.[144] Since this initial demonstration, the derivatization of this assay for the detection of disease relevant oligonucleotides and oligonucleotide mutations has been a popular research focus.[73, 145-149] One such derivative has been described for the detection of bladder cancer through telomerase quantification.[150] Telomerase is a reverse transcriptase that is responsible for protecting chromosomes from DNA damage by adding a TTAGGG sequence to the end of telomeres.[151] However, cancer cells have exploited this enzyme to evade cell death, and thus exhibit increased levels. In this work, AuNPs were conjugated to a telomerase primer as well as a reporter probe. If telomerase is present, primer elongation occurs resulting in the primers ability to bind to reporter probes on neighboring AuNPs. Absorbance ratios of 650 nm (aggregated)/520 nm (single AuNPs) were successfully utilized to classify 18 patients as those who were healthy vs. those that had bladder cancer. Furthermore, this assay provided a simplified experimental strategy for telomerase quantification compared to the traditional PCR-based TRAP method, which could potentially be translated to a point-of-care assay employed in developing regions.

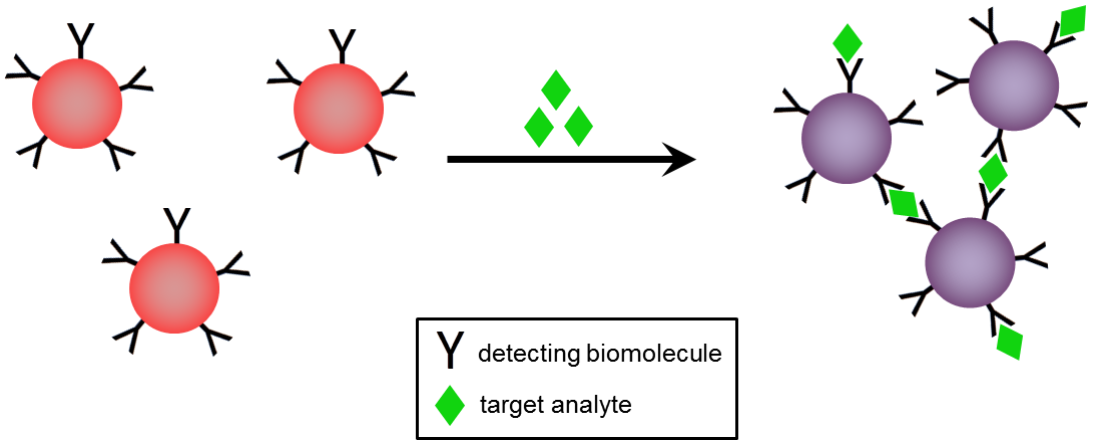

Figure 1.5 Schematic representation of the colorimetric assay format utilized to quantify cancer biomarkers. Biofunctionalized AuNPs are exposed to a target analyte that induces AuNP aggregation. Aggregation is detected by the red-shift in the AuNP's LSPR. A color change in the AuNP solution from red to purple can also be observed, usually by the naked eye.

Aptamer functionalized AuNPs have also been heavily utilized in colorimetric assays to detect the presence of cancer cells using both direct and indirect strategies.[152-155] Direct cancer cell detection was demonstrated by Medley et al. in 2008.[152] T-cell human acute lymphoblastic leukemia and B cell human Burkitt's lymphoma cells were mixed with AuNPs functionalized with aptamers specific for each cell type. Only when aptamer-AuNPs were added to their targeted cell solution did the red-shifted (aggregated) absorbance of the cell solution increase. The absorbance increased linearly with increasing cell concentration. In this proof-of-concept study, it was also determined that 20 nm AuNPs exhibited the highest assay sensitivity when compared to 5, 50 and 100 nm AuNPs. The direct detection of breast cancer cells has also been demonstrated using a similar colorimetric assay strategy and two-photon light scattering detection.[155] Indirect detection assays generally involve the incubation of a target aptamer solution with cancer

cells of interest and then the subsequent removal of unbound target aptamers. The unbound aptamers are then quantified by their ability to either hybridize and aggregate complementary aptamer-functionalized AuNPs or prevent aggregation of bare AuNPs in high salt solutions by providing particle stabilization. Recently, detection limits of 4-10 cells were reported with both approaches when assaying in physiological buffers.[153-154] The true impact and utility of these platforms will be tested when these proof-of-concept studies expand into clinical samples, namely blood, where the biological matrix becomes increasingly more complex. If successful, these assays could see utility in circulating tumor cell detection.

1.4.2 Dynamic Light Scattering (DLS)

Coupling AuNPs and dynamic light scattering (DLS) can also result in simple, low-cost, and highly sensitive diagnostic biomarker assays. DLS was first introduced in the 1970s for polymer particle size analysis, and has since been expanded to monitor aggregated states of bioconjugated nanoparticles upon addition of a target analyte.[156] In 2008, Huo and co-workers demonstrated the utility of combing antibody functionalized AuNPs and DLS in the detection of free prostate specific antigen (f-PSA).[94] Prostate cancer is responsible for ~30,000 deaths in the United States. Early detection, when the disease is at a localized stage improves the five-year survival rate to 100% from a devastating 28% when the disease is found in a distant, metastatic state. [157] [156] The combined analysis of f-PSA and total PSA has been researched as a promising metric for prostate cancer detection.[158] The authors utilized detector and capture anti-PSA antibodies conjugated to spherical AuNPs and AuNRs, respectively. This assay format achieved a detection limit of 0.1 ng/mL. In follow up work by the same group, citrate

stabilized AuNPs were incubated with human serum samples and then exposed to rabbit anti-human IgG antibodies **(Figure 1.6B)**.[159] Serum samples that were from patients with prostate cancer showed increased hydrodynamic diameters after the addition of the rabbit anti-human IgG antibodies when compared to samples from healthy individuals. The increased diameter was attributed to the increased level of tumor-specific autoantibodies that were able to bind to the surface of the AuNPs. This work shows promising clinical impact, especially in resource sparce regions, as it is cost-effective, required only drops of blood, and the results are ready within minutes. While the direct clinical utility of this technique for cancer diagnostics has focused on antibody and protein biomarker detection, it has also been successful at detecting oligionucleotides, aptamers, and single and double stranded DNA in other proof-of-concept studies. [92, 160-162]

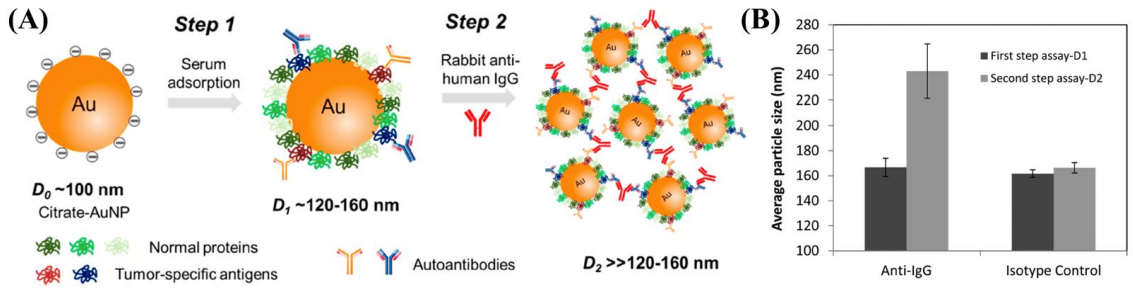

Figure 1.6 (A) Schematic diagram depicting the two-step assay procedure to quantify the presence of tumor-specific autoantibodies. Citrate stabilized AuNPs were exposed to patient serum samples and then introduced to rabbit anti-human IgF antibodies. (B) Patient samples with increased levels of tumor-specific autoantibodies showed increased hydrodynamic diameters after the addition of rabbit anti-human IgG antibodies that bind to the patient's autoantibodies. Adapted with permission from ([159]). Copyright (2015) American Chemical Society

1.4.3 Surface enhanced Raman Spectroscopy (SERS)

Surface enhanced Raman spectroscopy (SERS) is a powerful technique that can provide rich spectroscopic information in the biological fingerprint region (600-1500 cm^{-1}) and has been employed in numerous *in vitro* and *in vivo* cancer diagnostic applications.[10] Spontaneous Raman scattering is generally regarded as a very weak process with 1 in every 10^7 photons being scattered. This rare event results in a weak signal and hinders its use in complex biological environments. However, when a molecule is close to the surface of a metal nanoparticle, a 10^4-10^6 signal enhancement is observed. The mechanism behind this enhancement is attributed to both electromagnetic and chemical effects.[10, 163]

Biomarker detection using SERS has been readily demonstrated in the literature.[10, 164] AuNPs conjugated to mouse anti-human PSA antibodies and a Raman report, a molecule with a distinct, strong Raman signal, were used in conjunction with a gold film modified to contain mouse anti-human f-PSA antibodies for the detection of f-PSA in human serum.[165] The SERS sandwich assay provided a detection limit of ~1 pg/mL. A similar strategy was also employed for the detection of MUC4 in human serum samples with implications in pancreatic cancer detection.[166] As MUC4 has not been able to be quantified using traditional enzyme linked immunosorbent assay (ELISA) and radioimmunoassay (RIA) assays, this work provided a huge step forward in MUC4's potential use as a pancreatic cancer biomarker. Detection of circulating tumor cells (CTCs) was also shown to be possible with SERS.[167] AuNPs were conjugated to an epidermal growth factor (EGF) peptide that can bind to EGFRs overexpressed on CTCs. The assay was first validated in squamous cell carcinoma of the head and neck (SCCHN)

cancer cells, Tu212 cells, spiked into mouse WBC samples. Patient samples were also evaluated, and 17 of 19 positive patient samples were identified using SERS. Multiplexed SERS assays are also possible by conjugating different Raman reporters to gold nanoparticles functionalized with different detecting biomolecules. This multiplex strategy has been employed for lung,[168] breast,[169-171] and liver[172] cancer detection.

Unlike the diagnostic strategies described previously, SERS also allows for *in vivo* cancer detection, and has shown potential intraoperative utility in tumor resections.[10, 164] AuNPs are compatible with near-IR excitation sources that are necessary for *in vivo* imaging. The near-IR region is commonly referred to as the therapeutic window as tissue components (i.e. water and blood) have minimal absorption allowing maximum light penetration. One of the first demonstrations of utilizing SERS for *in vivo* tumor detection used AuNPs conjugated to single-chain variable fragment (ScFv) antibodies that can bind to EGFRs, and a Raman reporter, malachite green.[173] The overexpression of EGFR on epithelial tumor cells provides the distinguishing component between diseased and healthy tissues. Mice treated with targeted AuNPs showed Raman signatures at the tumor site while mice treated with pegylated AuNPs showed Raman scattering in the liver. HER-2 positive tumors were also successfully imaged *in vivo* using ScFv-conjugated CyNAMLA-381 AuNPs in SKBR-3 nude mice xenograph models.[174] Administration of the functionalized AuNPs in a HER-2 negative xenograph model did not result in a detectable SERS signal demonstrating this method's selectively.

For surgical intervention to be successful a tumor must be fully resected and therefore clean margins must be achieved. Distinguishing between cancerous and noncancerous tissue in surgery can be difficult often leading to excess tissue being

removed or residual cancer tissues remaining. In an effort to bring real-time, sensitive feedback into the operating room some groups have focused on the use of AuNPs to amplify SERS signals at the tumor margins as well as combining SERS with other sensitive techniques including photoacoustic imaging and MRI to create surgical plans. In 2012 Gambhir and co-workers reported the use of this strategy for successful SERS guided tumor resection of brain and ovarian tumors in mouse models.[133, 135] AuNPs were administered intravenously and accumulated at the tumor site due to the enhanced permeability and retention (EPR) effect. Upon accumulation, SERS signals of chosen Raman reporters were detected and used to fine-tune tumor resection removing cancerous foci that were invisible to the naked eye, but were later confirmed through histology. Additionally, silica coated Raman active AuNPs and SERS were used for breast cancer tumor detection and phenotyping.[175] In this work, the authors performed multiplexed SERS analysis on tumors by topically applying AuNPs that were labeled with EGFR, HER2 and isotype antibodies. The ratio of EGFR/isotype and HER2/isotype SERS signals allowed for the rapid (<15 min) quantitative molecular phenotyping of tumors. The authors suggest that this strategy could readily be employed intraoperative for breast cancer lumpectomies.

Time resolved SERS (TR-SERS) has also shown potential utility for improving our understanding and evaluation of cancer cells. By using a live-cell imaging chamber that is compatible with a Raman microscope, it is possible to investigate important cellular processes, including cell cycle progression and cell death. PEGylated AuNPs equipped with RGD and nuclear localizing sequence (NLS) peptides to enhance cellular uptake and nuclear localization, respectively, were used to track a cell's progression

throughout the cell cycle and identify Raman signatures that were correlated to each phase of the cell cycle.[176] Raman signatures of cell cycle progression corresponded to the different production times of proteins and DNA. Apoptotic molecular events can also be distinguished using this methodology.[177] In this work, El-Sayed and co-workers treated human oral squamous cell carcinoma (HSC-3) cells with 100 μM of H_2O_2 to induce apoptosis and monitored the time dependent changes in SERS spectra. Tracking SERS signals over time as well as correlating these signal changes to *in situ* SERS experiments, a real-time sequence of apoptotic molecular events was obtained. Protein disulfide bond breakage along with DNA fragmentation was shown to occur first followed by the exposure of hydrophobic amino acids and the peptide backbone (loss of tertiary structure). Lastly, denatured proteins underwent peptide bond hydrolysis. While these studies demonstrate the usefulness of TR-SERS in mechanistic studies, TR-SERS's greatest impact will most likely come from its ability to evaluate drug efficacy and delivery as these strategies could be readily adopted into high-throughput assays that could help identify promising cancer therapeutic candidates.[178-179] By employing nuclear-targeted AuNPs, TR-SERS was able to determine the relative efficacy of cisplatin and 5-fluoruracil (5-FU) quicker than that of the traditional XTT cell viability assay **(Figure 1.7)**. In this work, SERS "death bands" were identified as their relative change over time resulted in an ET_{50} value that could be used as a comparison factor between the chosen chemotherapeutics. The SERS "death bands", 1000 cm^{-1} and 1585 cm^{-1}, were later associated with the amino acid phenylalanine and the DNA bases arginine and guanine, respectively.[177] Real-time tracking of drug delivery was also shown with this technique through the exploitation of the nanoparticle plasmon effect.[178] In this study, doxorubicin

(DOX) was covalently attached to the surface of nuclear-targeted AuNPs through a pH sensitive linker. When DOX was attached to AuNPs, its fluorescence was quenched, but its Raman signals were enhanced. Once the AuNPs were internalized within the cell and sequestered in the lysosome (pH 5), the pH sensitive linker was cleaved, releasing DOX. The release restored DOX's fluorescence and eliminated the ability to detect is Raman vibrations. The inverse relationship between Raman and fluorescence at the surface of AuNPs was shown to be an effective mode of following drug delivery. Although the studies highlighted here utilized nuclear-targeted AuNPs, other organelle targeted AuNPs have been coupled with live-cell SERS expanding the platform for real-time cell studies.[180]

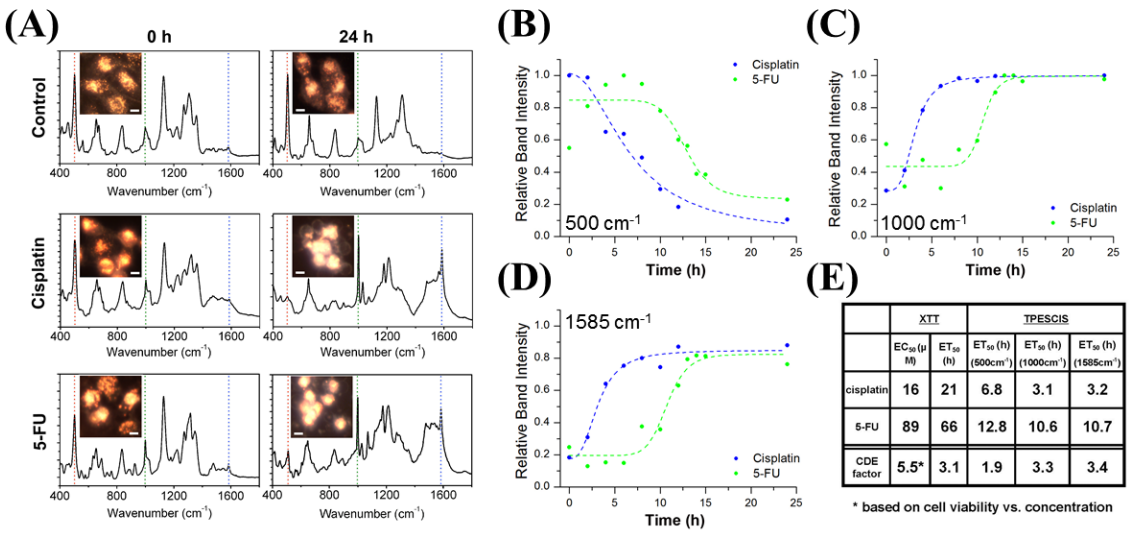

Figure 1.7 (A) Representative dark-field and TR-SERS spectra of HSC-3 cells treated with cisplatin and 5-FU. SERS "death bands" are highlighted by the dotted colored lines – 500 cm^{-1}, red; 1000 cm^{-1}, green; 1585 cm^{-1}, blue. The SERS "death band" intensities – (B) 500 cm^{-1}, (C) 1000 cm^{-1}, and (D) 1585 cm^{-1} – over time utilized to calculate the (E) ET_{50} of cisplatin and 5-FU for comparison of the TR-SERS method to the traditional XTT cell viability assay. Adapted with permission from ([178]). Copyright (2013) American Chemical Society.

1.5 Cancer Treatment

For the successful implementation of AuNPs as a therapeutic treatment for malignancy, the nanostructures must be biocompatible (to minimize off target effects or systematic toxicity) and exhibit preferential targeting of malignancy over healthy tissue. Multiple strategies are used to selectively target AuNPs to malignant cells or tumors for use as drug delivery vectors. Additional strategies involve the use of AuNPs as direct therapeutic agents to induce photothermal therapy, which encompasses cell death due to protein denaturation or membrane disruption, or photodynamic therapy, during which cytotoxicity in induced through the production of reactive oxygen species (ROS).

1.5.1 Tumor Targeting

For effective cancer treatment, AuNPs must be designed to selectively target malignant cells and minimize off target effects toward healthy tissue. Several approaches are used to promote tumor targeting and / or cellular uptake for efficient cancer therapy, and are generally divided into two categories: (1) passive targeting and (2) active targeting. Passive targeting relies on the passive accumulation of nanoparticles within the tumor microenvironment due to the enhanced permeability and retention (EPR) effect.[181] While the vasculature supporting healthy tissues have tight junctions between endothelial cells, the angiogenesis associated with the rapid growth of malignancies results in leakier blood vessel walls with large fenestrations.[131] This leakiness is the basis of the EPR effect, allowing nanostructures to pass through the porous blood vessels and accumulate within the tumor environment. Thus, nanoparticle size is a crucial factor in determining uptake via passive tumor targeting, with structures in the 30 – 200 nm size range displaying the best tumor retention.[181] For the design of passively targeted particles, surface modifications such as PEG are often used for decreasing protein adsorption to the particles to shield the nanostructures from immune recognition and increase circulatory half-life.[78, 182-183] Early investigations by Chan and coworkers used 20 – 100 nm PEG conjugated spherical AuNPs and found that 60 nm particles showed the greatest accumulation within tumors.[184-185]

Various ligands have been used in attempts to improve tumor targeting through specific molecular interactions (i.e., active targeting) including peptides,[186] antibodies,[66, 187] nucleic acids,[188-189] hormones,[190] and small molecules.[72, 105] In general, these methods rely on the interaction between the nanoparticle surface ligand and a recognition element

expressed by the cancer cells. The active targeting ligands are used to target specific cell types, or specific organelles or proteins within those cells, with the hope of increasing local site accumulation. However, the enhancement in tumor accumulation provided by active targeting ligands is still the subject of debate due to the differences in size, shape, and surface chemistry of the nanostructures used, variations of targeting ligands and their coverage density, and the heterogeneity of tumor models studied.[12, 17]

1.5.2 Drug Delivery

The high surface area to volume ratio and facile surface chemistry of AuNPs make them ideal candidates as drug delivery vehicles that are easily loaded with large numbers of drug molecules. The concentration of a desired drug can be greatly increased within the tumor microenvironments through the use of passively and actively targeted AuNPs due to the high local concentration of the drug on the nanoparticle surface.[191] In early applications, AuNPs served solely as carriers for therapeutic drugs. Paciotti *et al*. reported the first use of AuNPs as drug delivery vehicles, by covalently attaching tumor necrosis factor to the surface of 30 nm particles [192]. These nanoparticle conjugates exhibited minimal systemic toxicity while showing enhanced efficacy at a lower concentration than the free drug. Many other cancer drugs have since been attached to AuNP delivery vectors and have shown increased efficacy relative to the free drugs, including doxorubicin,[189, 193], tamoxifen,[83] cisplatin,[194] oxaliplatin,[195] paclitaxel,[141] and XAV939[196]. Drug-AuNP conjugates have also shown promise in overcoming drug resistance by using doxorubicin conjugates to increase intracellular concentration of the therapeutic agent [197-198].

While early examples of AuNPs as drug carriers showed promise, recent applications often involve the controlled release of the drugs at target sites. Thus, drug delivery can now be broken down into two components, drug loading to the nanostructure and delivery or release at the target site. A variety of covalent linkages, electrostatic adsorption, and hydrophobic / hydrophilic interactions (layer by layer assembly) have been used to conjugate AuNPs with the desired therapeutic agent (see *1.1.2 Conjugation* for an overview of the chemistries involved). Various strategies are commonly used to control release of the drug, including thermally activated,[199] pH responsive,[200] light activated,[199, 201] and timed release linkers[187].

1.5.3 Plasmonic Photothermal Therapy (PPT)

Photothermal therapy involves the conversion of light to heat for the purpose of inducing hyperthermia in malignant cells, which occurs when cells are exposed to temperatures >42°C for several minutes, resulting in death from irreversible damage to protein and membrane structures. AuNPs serve as excellent probes for PPT due to their strong absorption that can be tuned to NIR wavelengths to minimize tissue attenuation during treatment. AuNSs, first developed by Halas and coworkers, were among the first nanostructures to be used for PPT.[39] Using PEG conjugated nanoshells under 820 nm laser irradiation at 35 W/cm^2 for 7 min, they observed significant cell death in the irradiated area, which was not observed for control cells without AuNSs. The nanoshells were then directly injected into tumors and cell death was again observed (820 nm laser irradiation at 4 W/cm^2, 6 min).[39] Subsequently, selective photothermal cell death was shown using anti-HER2 conjugated AuNSs to target HER2-positive SK-BR-3 breast cancer cells.[129] El-Sayed and coworkers then demonstrated selective PPT using AuNRs

conjugated with EGFR antibodies. Under 800 nm continuous wave (cw) laser irradiation, the AuNRs induced cell death at laser powers as low as 10 W/cm^2,[128] significantly lower than the initial in vitro experiments using AuNSs. Xia and coworkers then introduced AuNCs as PPT agents, inducing cell death at even lower laser intensities (808 nm, 0.7 W/cm^2), although with a longer 10 min irradiation.[202] Other AuNP geometries with tunable optical properties that have also been used for PPT include nanoplates, nanoprisms, and branched nanoparticles. Current research is focused on optimizing the AuNP size and shape to increase the tumor accumulation and photothermal conversion efficiency of the particles so that lower laser powers are required for PPT. Additionally, identifying the specific mechanisms involved in cell death from PPT treatment is a key focus due to the conflicting reports of apoptotic and necrotic cell death present in the literature.[202-206] These differences are likely due to variations in the nanoparticle targeting strategies, physical properties such as the particle absorption cross sections, and overlap between AuNP LSPR band with the treatment laser, and the duration and intensity of laser exposure.

1.5.3.1 Photodynamic Therapy (PDT)

In photodynamic therapy, a molecule or nanoparticle (i.e. a photosensitizer) is used to transfer energy from light to oxygen, converting it from the triplet ground state to the singlet state, a form of highly reactive oxygen species (ROS). This species reacts with cellular components such as DNA or proteins, causing irreversible changes in structure or function to induce cell death. The photosensitizer is only active when illuminated with light, affording selectivity in treatment location and duration. While organic dye molecules (e.g. cyanines or porphyrins) were traditionally used for PDT, they generally

suffer from nonspecific targeting and poor hydrophilicity which complicates delivery.[207] Thus, AuNPs are highly desirable as PDT agents due to their surface chemistry which can be modified to carry photosensitizers and improve hydrophilicity and tumor targeting. Russel and coworkers reported the use of AuNPs for PDT by stabilizing small 2 – 4 nm gold particles with a photosensitizing phthalocyanine dye. These AuNP conjugates exhibited greater solubility, a ~50% increase in the quantum yield of singlet oxygen, and ~ 2.5 times greater tumor accumulation compared to the free dye.[208-209] More recent research has focused on combining PDT with PPT[210-213] for a multimodal approach to cancer treatment.

Although organic PDT agents generally require UV or visible light to generate ROS, NIR light activation is highly desirable for its greater penetration depth. The tunability of AuNP optical properties, combined with their greater stability (organic PDT agents often exhibit poor water solubility and can decompose upon light exposure[214]), make them excellent candidates for PDT using NIR light. The use of AuNPs as direct photosensitizers capable of producing singlet oxygen upon light exposure (without additional photosensitizing agents) has recently been demonstrated under NIR exposure using nanocages,[215] nanoshells, nanorods,[216-218] and aggregated nanospheres[219] to produce various ROS including singlet oxygen, superoxide anions, and hydroxyl radicals.

1.6 Conclusion

The emergence of nanotechnology has resulted in the development of many new biomedical platforms with significant promise for the pharmaceutical industry. AuNPs have become promising candidates due to their well-established colloidal synthetic

routes, low cytotoxicity, straightforward surface modification with a variety of targeting or therapeutic ligands, and tunable optical properties. Specifically, AuNPs have been utilized in optical and photoacoustic imaging, diagnostic applications, as drug delivery platforms, and in direct cancer therapeutic applications such as plasmonic photothermal therapy or photodynamic therapy. Recent pharmaceutical applications of AuNPs increasingly combine several of these properties into single, multimodal platforms for theranostic functions. The increasing selectivity and efficacy of these multimodal platforms hold significant promise for the successful translation from the lab into clinical applications.

1.7 References

(1) Aioub, M.; Austin, L. A.; El-Sayed, M. A., Gold Nanoparticles for Cancer Diagnostics, Spectroscopic Imaging, Drug Delivery, and Plasmonic Photothermal Therapy. In *Inorganic Frameworks as Smart Nanomedicines*, Vol. 7, Grumezescu, A. M., Elsevier (2017).

(2) Wagner, F. E.; Haslbeck, S.; Stievano, L.; Calogero, S.; Pankhurst, Q. A.; Martinek, P. Before Striking Gold in Gold-Ruby Glass. *Nature* **2000,** *407*, 691-692.

(3) Daniel, M. C.; Astruc, D. Gold Nanoparticles: Assembly, Supramolecular Chemistry, Quantum-Size-Related Properties, and Applications toward Biology, Catalysis, and Nanotechnology. *Chem. Rev.* **2004,** *104*, 293-346.

(4) Faraday, M. The Bakerian Lecture: Experimental Relations of Gold (and Other Metals) to Light. *Philosophical Transactions of the Royal Society of London* **1857,** *147*, 145-181.

(5) Alkilany, A. M.; Thompson, L. B.; Boulos, S. P.; Sisco, P. N.; Murphy, C. J. Gold Nanorods: Their Potential for Photothermal Therapeutics and Drug Delivery, Tempered by the Complexity of Their Biological Interactions. *Adv. Drug Delivery Rev.* **2012,** *64*, 190-199.

(6) Dreaden, E. C.; Alkilany, A. M.; Huang, X. H.; Murphy, C. J.; El-Sayed, M. A. The Golden Age: Gold Nanoparticles for Biomedicine. *Chem. Soc. Rev.* **2012,** *41*, 2740-2779.

(7) Huang, X.; El-Sayed, I. H.; El-Sayed, M. A. Applications of Gold Nanorods for Cancer Imaging and Photothermal Therapy. *Methods Mol. Biol.* **2010,** *624*, 343-357.

(8) Jain, P. K.; Huang, X. H.; El-Sayed, I. H.; El-Sayed, M. A. Noble Metals on the Nanoscale: Optical and Photothermal Properties and Some Applications in Imaging, Sensing, Biology, and Medicine. *Acc. Chem. Res.* **2008,** *41*, 1578-1586.

(9) Lal, S.; Clare, S. E.; Halas, N. J. Nanoshell-Enabled Photothermal Cancer Therapy: Impending Clinical Impact. *Acc. Chem. Res.* **2008,** *41*, 1842-1851.

(10) Lane, L. A.; Qian, X.; Nie, S. Sers Nanoparticles in Medicine: From Label-Free Detection to Spectroscopic Tagging. *Chem. Rev.* **2015,** *115*, 10489-10529.

(11) Link, S.; El-Sayed, M. A. Shape and Size Dependence of Radiative, Non-Radiative and Photothermal Properties of Gold Nanocrystals. *Int. Rev. Phys. Chem.* **2000,** *19*, 409-453.

(12) Nie, S. M. Understanding and Overcoming Major Barriers in Cancer Nanomedicine. *Nanomedicine* **2010,** *5*, 523-528.

(13) Skrabalak, S. E.; Chen, J. Y.; Sun, Y. G.; Lu, X. M.; Au, L.; Cobley, C. M.; Xia, Y. N. Gold Nanocages: Synthesis, Properties, and Applications. *Acc. Chem. Res.* **2008,** *41*, 1587-1595.

(14) Wang, H.; Brandl, D. W.; Nordlander, P.; Halas, N. J. Plasmonic Nanostructures: Artificial Molecules. *Acc. Chem. Res.* **2007,** *40*, 53-62.

(15) Faulk, W. P.; Taylor, G. M. An Immunocolloid Method for the Electron Microscope. *Immunochemistry* **1971,** *8*, 1081-1083.

(16) Sperling, R. A.; Rivera Gil, P.; Zhang, F.; Zanella, M.; Parak, W. J. Biological Applications of Gold Nanoparticles. *Chem. Soc. Rev.* **2008,** *37*, 1896-1908.

(17) Yang, X.; Yang, M. X.; Pang, B.; Vara, M.; Xia, Y. N. Gold Nanomaterials at Work in Biomedicine. *Chem. Rev.* **2015,** *115*, 10410-10488.

(18) Chen, G. Y.; Roy, I.; Yang, C. H.; Prasad, P. N. Nanochemistry and Nanomedicine for Nanoparticle-Based Diagnostics and Therapy. *Chem. Rev.* **2016,** *116*, 2826-2885.

(19) Saha, K.; Agasti, S. S.; Kim, C.; Li, X. N.; Rotello, V. M. Gold Nanoparticles in Chemical and Biological Sensing. *Chem. Rev.* **2012,** *112*, 2739-2779.

(20) Jans, H.; Huo, Q. Gold Nanoparticle-Enabled Biological and Chemical Detection and Analysis. *Chem. Soc. Rev.* **2012,** *41*, 2849-2866.

(21) Ghosh, P.; Han, G.; De, M.; Kim, C. K.; Rotello, V. M. Gold Nanoparticles in Delivery Applications. *Adv. Drug Delivery Rev.* **2008,** *60*, 1307-1315.

(22) Vigderman, L.; Zubarev, E. R. Therapeutic Platforms Based on Gold Nanoparticles and Their Covalent Conjugates with Drug Molecules. *Adv. Drug Delivery Rev.* **2013,** *65*, 663-676.

(23) Hu, M.; Chen, J. Y.; Li, Z. Y.; Au, L.; Hartland, G. V.; Li, X. D.; Marquez, M.; Xia, Y. N. Gold Nanostructures: Engineering Their Plasmonic Properties for Biomedical Applications. *Chem. Soc. Rev.* **2006,** *35*, 1084-1094.

(24) Sapsford, K. E.; Tyner, K. M.; Dair, B. J.; Deschamps, J. R.; Medintz, I. L. Analyzing Nanomaterial Bioconjugates: A Review of Current and Emerging Purification and Characterization Techniques. *Anal. Chem.* **2011,** *83*, 4453-4488.

(25) Turkevich, J.; Stevenson, P. C.; Hillier, J. A Study of the Nucleation and Growth Processes in the Synthesis of Colloidal Gold. *Discuss Faraday Soc.* **1951**, 55-75.

(26) Frens, G. Controlled Nucleation for Regulation of Particle-Size in Monodisperse Gold Suspensions. *Nat., Phys. Sci.* **1973,** *241*, 20-22.

(27) Sivaraman, S. K.; Kumar, S.; Santhanam, V. Monodisperse Sub-10 Nm Gold Nanoparticles by Reversing the Order of Addition in Turkevich Method - the Role of Chloroauric Acid. *J Colloid Interf. Sci.* **2011,** *361*, 543-547.

(28) Brust, M.; Walker, M.; Bethell, D.; Schiffrin, D. J.; Whyman, R. Synthesis of Thiol-Derivatized Gold Nanoparticles in a 2-Phase Liquid-Liquid System. *J. Chem. Soc., Chem. Comm.* **1994**, 801-802.

(29) Mittal, A. K.; Chisti, Y.; Banerjee, U. C. Synthesis of Metallic Nanoparticles Using Plant Extracts. *Biotechnol. Adv.* **2013,** *31*, 346-356.

(30) Bastus, N. G.; Comenge, J.; Puntes, V. Kinetically Controlled Seeded Growth Synthesis of Citrate-Stabilized Gold Nanoparticles of up to 200 Nm: Size Focusing Versus Ostwald Ripening. *Langmuir* **2011,** *27*, 11098-11105.

(31) Perrault, S. D.; Chan, W. C. W. Synthesis and Surface Modification of Highly Monodispersed, Spherical Gold Nanoparticles of 50-200 Nm. *J. Am. Chem. Soc.* **2009,** *131*, 17042-17043.

(32) Alber, F.; Dokudovskaya, S.; Veenhoff, L. M.; Zhang, W. H.; Kipper, J.; Devos, D.; Suprapto, A.; Karni-Schmidt, O.; Williams, R.; Chait, B. T.; Sali, A.; Rout, M. P. The Molecular Architecture of the Nuclear Pore Complex. *Nature* **2007,** *450*, 695-701.

(33) Piella, J.; Bastus, N. G.; Puntes, V. Size-Controlled Synthesis of Sub-10-Nanometer Citrate-Stabilized Gold Nanoparticles and Related Optical Properties. *Chem. Mater.* **2016,** *28*, 1066-1075.

(34) Zheng, Y. Q.; Zhong, X. L.; Li, Z. Y.; Xia, Y. N. Successive, Seed-Mediated Growth for the Synthesis of Single-Crystal Gold Nanospheres with Uniform Diameters Controlled in the Range of 5-150 Nm. *Part. Part. Syst. Char.* **2014,** *31*, 266-273.

(35) Brown, K. R.; Natan, M. J. Hydroxylamine Seeding of Colloidal Au Nanoparticles in Solution and on Surfaces. *Langmuir* **1998,** *14*, 726-728.

(36) Nikoobakht, B.; El-Sayed, M. A. Preparation and Growth Mechanism of Gold Nanorods (Nrs) Using Seed-Mediated Growth Method. *Chem. Mater.* **2003,** *15*, 1957-1962.

(37) Jana, N. R.; Gearheart, L.; Murphy, C. J. Wet Chemical Synthesis of High Aspect Ratio Cylindrical Gold Nanorods. *J. Phys. Chem. B* **2001,** *105*, 4065-4067.

(38) Oldenburg, S. J.; Averitt, R. D.; Westcott, S. L.; Halas, N. J. Nanoengineering of Optical Resonances. *Chem. Phys. Lett.* **1998,** *288*, 243-247.

(39) Hirsch, L. R.; Stafford, R. J.; Bankson, J. A.; Sershen, S. R.; Rivera, B.; Price, R. E.; Hazle, J. D.; Halas, N. J.; West, J. L. Nanoshell-Mediated Near-Infrared Thermal Therapy of Tumors under Magnetic Resonance Guidance. *Proc. Natl. Acad. Sci. U.S.A.* **2003,** *100*, 13549-13554.

(40) Sun, Y. G.; Xia, Y. N. Shape-Controlled Synthesis of Gold and Silver Nanoparticles. *Science* **2002,** *298*, 2176-2179.

(41) Lu, X. M.; Au, L.; McLellan, J.; Li, Z. Y.; Marquez, M.; Xia, Y. N. Fabrication of Cubic Nanocages and Nanoframes by Dealloying Au/Ag Alloy Nanoboxes with an Aqueous Etchant Based on Fe(No3)(3) or Nh4oh. *Nano Lett.* **2007,** *7*, 1764-1769.

(42) Chen, L.; Ji, F.; Xu, Y.; He, L.; Mi, Y. F.; Bao, F.; Sun, B. Q.; Zhang, X. H.; Zhang, Q. High-Yield Seedless Synthesis of Triangular Gold Nanoplates through Oxidative Etching. *Nano Lett.* **2014,** *14*, 7201-7206.

(43) Sau, T. K.; Murphy, C. J. Room Temperature, High-Yield Synthesis of Multiple Shapes of Gold Nanoparticles in Aqueous Solution. *J. Am. Chem. Soc.* **2004,** *126*, 8648-8649.

(44) Millstone, J. E.; Park, S.; Shuford, K. L.; Qin, L. D.; Schatz, G. C.; Mirkin, C. A. Observation of a Quadrupole Plasmon Mode for a Colloidal Solution of Gold Nanoprisms. *J. Am. Chem. Soc.* **2005,** *127*, 5312-5313.

(45) Ha, T. H.; Koo, H. J.; Chung, B. H. Shape-Controlled Syntheses of Gold Nanoprisms and Nanorods Influenced by Specific Adsorption of Halide Ions. *J. Phys. Chem. C* **2007,** *111*, 1123-1130.

(46) Millstone, J. E.; Hurst, S. J.; Metraux, G. S.; Cutler, J. I.; Mirkin, C. A. Colloidal Gold and Silver Triangular Nanoprisms. *Small* **2009,** *5*, 646-664.

(47) Hao, E.; Bailey, R. C.; Schatz, G. C.; Hupp, J. T.; Li, S. Y. Synthesis and Optical Properties of "Branched" Gold Nanocrystals. *Nano Lett.* **2004,** *4*, 327-330.

(48) Dam, D. H. M.; Culver, K. S. B.; Odom, T. W. Grafting Aptamers onto Gold Nanostars Increases in Vitro Efficacy in a Wide Range of Cancer Cell Types. *Mol Pharmaceut.* **2014,** *11*, 580-587.

(49) Khoury, C. G.; Vo-Dinh, T. Gold Nanostars for Surface-Enhanced Raman Scattering: Synthesis, Characterization and Optimization. *J. Phys. Chem. C* **2008,** *112*, 18849-18859.

(50) Kumar, P. S.; Pastoriza-Santos, I.; Rodriguez-Gonzalez, B.; Garcia de Abajo, F. J.; Liz-Marzan, L. M. High-Yield Synthesis and Optical Response of Gold Nanostars. *Nanotechnology* **2008,** *19*.

(51) Hauck, T. S.; Ghazani, A. A.; Chan, W. C. W. Assessing the Effect of Surface Chemistry on Gold Nanorod Uptake, Toxicity, and Gene Expression in Mammalian Cells. *Small* **2008,** *4*, 153-159.

(52) Alkilany, A. M.; Nagaria, P. K.; Hexel, C. R.; Shaw, T. J.; Murphy, C. J.; Wyatt, M. D. Cellular Uptake and Cytotoxicity of Gold Nanorods: Molecular Origin of Cytotoxicity and Surface Effects. *Small* **2009,** *5*, 701-708.

(53) Albanese, A.; Tang, P. S.; Chan, W. C. W. The Effect of Nanoparticle Size, Shape, and Surface Chemistry on Biological Systems. *Annu. Rev. Biomed. Eng.* **2012,** *14*, 1-16.

(54) Walkey, C. D.; Olsen, J. B.; Guo, H. B.; Emili, A.; Chan, W. C. W. Nanoparticle Size and Surface Chemistry Determine Serum Protein Adsorption and Macrophage Uptake. *J. Am. Chem. Soc.* **2012,** *134*, 2139-2147.

(55) Chithrani, B. D.; Chan, W. C. W. Elucidating the Mechanism of Cellular Uptake and Removal of Protein-Coated Gold Nanoparticles of Different Sizes and Shapes. *Nano Lett.* **2007,** *7*, 1542-1550.

(56) Nativo, P.; Prior, I. A.; Brust, M. Uptake and Intracellular Fate of Surface-Modified Gold Nanoparticles. *ACS Nano* **2008,** *2*, 1639-1644.

(57) Yang, J. A.; Lohse, S. E.; Murphy, C. J. Tuning Cellular Response to Nanoparticles Via Surface Chemistry and Aggregation. *Small* **2014,** *10*, 1642-1651.

(58) Aioub, M.; Kang, B.; Mackey, M. A.; El-Sayed, M. A. Biological Targeting of Plasmonic Nanoparticles Improves Cellular Imaging via the Enhanced Scattering in the Aggregates Formed. *J. Phys. Chem. Lett.* **2014,** *5*, 2555-2561.

(59) Elbakry, A.; Zaky, A.; Liebkl, R.; Rachel, R.; Goepferich, A.; Breunig, M. Layer-by-Layer Assembled Gold Nanoparticles for Sirna Delivery. *Nano Lett.* **2009,** *9*, 2059-2064.

(60) Deng, Z. J.; Liang, M. T.; Toth, I.; Monteiro, M. J.; Minchin, R. F. Molecular Interaction of Poly(Acrylic Acid) Gold Nanoparticles with Human Fibrinogen. *ACS Nano* **2012,** *6*, 8962-8969.

(61) Brandenberger, C.; Muhlfeld, C.; Ali, Z.; Lenz, A. G.; Schmid, O.; Parak, W. J.; Gehr, P.; Rothen-Rutishauser, B. Quantitative Evaluation of Cellular Uptake and Trafficking of Plain and Polyethylene Glycol-Coated Gold Nanoparticles. *Small* **2010,** *6*, 1669-1678.

(62) Jokerst, J. V.; Lobovkina, T.; Zare, R. N.; Gambhir, S. S. Nanoparticle Pegylation for Imaging and Therapy. *Nanomedicine* **2011,** *6*, 715-728.

(63) Patel, P. C.; Giljohann, D. A.; Seferos, D. S.; Mirkin, C. A. Peptide Antisense Nanoparticles. *Proc. Natl. Acad. Sci. U.S.A.* **2008,** *105*, 17222-17226.

(64) Mackey, M. A.; Saira, F.; Mahmoud, M. A.; El-Sayed, M. A. Inducing Cancer Cell Death by Targeting Its Nucleus: Solid Gold Nanospheres Versus Hollow Gold Nanocages. *Bioconjugate Chem.* **2013,** *24*, 897-906.

(65) Tkachenko, A. G.; Xie, H.; Liu, Y. L.; Coleman, D.; Ryan, J.; Glomm, W. R.; Shipton, M. K.; Franzen, S.; Feldheim, D. L. Cellular Trajectories of Peptide-Modified Gold Particle Complexes: Comparison of Nuclear Localization Signals and Peptide Transduction Domains. *Bioconjugate Chem.* **2004,** *15*, 482-490.

(66) Choi, C. H. J.; Alabi, C. A.; Webster, P.; Davis, M. E. Mechanism of Active Targeting in Solid Tumors with Transferrin-Containing Gold Nanoparticles. *Proc. Natl. Acad. Sci. U.S.A.* **2010,** *107*, 1235-1240.

(67) Chithrani, B. D.; Ghazani, A. A.; Chan, W. C. W. Determining the Size and Shape Dependence of Gold Nanoparticle Uptake into Mammalian Cells. *Nano Lett.* **2006,** *6*, 662-668.

(68) El-Sayed, I. H.; Huang, X.; El-Sayed, M. A. Surface Plasmon Resonance Scattering and Absorption of Anti-EGFR Antibody Conjugated Gold Nanoparticles in Cancer Diagnostics: Applications in Oral Cancer. *Nano Lett.* **2005,** *5*, 829-834.

(69) Li, Z.; Jin, R. C.; Mirkin, C. A.; Letsinger, R. L. Multiple Thiol-Anchor Capped DNA-Gold Nanoparticle Conjugates. *Nucleic Acids Res.* **2002,** *30*, 1558-1562.

(70) Rosi, N. L.; Giljohann, D. A.; Thaxton, C. S.; Lytton-Jean, A. K. R.; Han, M. S.; Mirkin, C. A. Oligonucleotide-Modified Gold Nanoparticles for Intracellular Gene Regulation. *Science* **2006,** *312*, 1027-1030.

(71) Dreaden, E. C.; Gryder, B. E.; Austin, L. A.; Defo, B. A. T.; Hayden, S. C.; Pi, M.; Quarles, L. D.; Oyelere, A. K.; El-Sayed, M. A. Antiandrogen Gold Nanoparticles Dual-Target and Overcome Treatment Resistance in Hormone-Insensitive Prostate Cancer Cells. *Bioconjugate Chem.* **2012,** *23*, 1507-1512.

(72) Wang, H.; Zheng, L. F.; Peng, C.; Shen, M. W.; Shi, X. Y.; Zhang, G. X. Folic Acid-Modified Dendrimer-Entrapped Gold Nanoparticles as Nanoprobes for Targeted Ct Imaging of Human Lung Adencarcinoma. *Biomaterials* **2013,** *34*, 470-480.

(73) Li, H.; Rothberg, L. Colorimetric Detection of DNA Sequences Based on Electrostatic Interactions with Unmodified Gold Nanoparticles. *Proc. Natl. Acad. Sci. U.S.A.* **2004,** *101*, 14036-14039.

(74) Guo, S. T.; Huang, Y. Y.; Jiang, Q. A.; Sun, Y.; Deng, L. D.; Liang, Z. C.; Du, Q. A.; Xing, J. F.; Zhao, Y. L.; Wang, P. C.; Dong, A. J.; Liang, X. J. Enhanced Gene Delivery and Sirna Silencing by Gold Nanoparticles Coated with Charge-Reversal Polyelectrolyte. *ACS Nano* **2010,** *4*, 5505-5511.

(75) Qi, Z. M.; Honma, I.; Ichihara, M.; Zhou, H. S. Layer-by-Layer Fabrication and Characterization of Gold-Nanoparticle/Myoglobin Nanocomposite Films. *Adv. Funct. Mater.* **2006,** *16*, 377-386.

(76) Angelatos, A. S.; Katagiri, K.; Caruso, F. Bioinspired Colloidal Systems Via Layer-by-Layer Assembly. *Soft Matter* **2006,** *2*, 18-23.

(77) Love, J. C.; Estroff, L. A.; Kriebel, J. K.; Nuzzo, R. G.; Whitesides, G. M. Self-Assembled Monolayers of Thiolates on Metals as a Form of Nanotechnology. *Chem. Rev.* **2005,** *105*, 1103-1169.

(78) Akiyama, Y.; Mori, T.; Katayama, Y.; Niidome, T. The Effects of Peg Grafting Level and Injection Dose on Gold Nanorod Biodistribution in the Tumor-Bearing Mice. *J. Controlled Rel.* **2009,** *139*, 81-84.

(79) Otsuka, H.; Nagasaki, Y.; Kataoka, K. Pegylated Nanoparticles for Biological and Pharmaceutical Applications. *Adv. Drug Delivery Rev.* **2003,** *55*, 403-419.

(80) Rahme, K.; Chen, L.; Hobbs, R. G.; Morris, M. A.; O'Driscoll, C.; Holmes, J. D. Pegylated Gold Nanoparticles: Polymer Quantification as a Function of Peg Lengths and Nanoparticle Dimensions. *Rsc Advances* **2013,** *3*, 6085-6094.

(81) Popovtzer, R.; Agrawal, A.; Kotov, N. A.; Popovtzer, A.; Balter, J.; Carey, T. E.; Kopelman, R. Targeted Gold Nanoparticles Enable Molecular Ct Imaging of Cancer. *Nano Lett.* **2008,** *8*, 4593-4596.

(82) Kumar, S.; Aaron, J.; Sokolov, K. Directional Conjugation of Antibodies to Nanoparticles for Synthesis of Multiplexed Optical Contrast Agents with Both Delivery and Targeting Moieties. *Nat. Protoc.* **2008,** *3*, 314-320.

(83) Dreaden, E. C.; Mwakwari, S. C.; Sodji, Q. H.; Oyelere, A. K.; El-Sayed, M. A. Tamoxifen-Poly(Ethylene Glycol)-Thiol Gold Nanoparticle Conjugates: Enhanced Potency and Selective Delivery for Breast Cancer Treatment. *Bioconjugate Chem.* **2009,** *20*, 2247-2253.

(84) Presolski, S. I.; Hong, V. P.; Finn, M. G. Copper-Catalyzed Azide-Alkyne Click Chemistry for Bioconjugation. *Curr Protoc Chem Biol* **2011,** *3*, 153-162.

(85) Xu, X. Y.; Daniel, W. L.; Wei, W.; Mirkin, C. A. Colorimetric Cu2+ Detection Using DNA-Modified Gold-Nanoparticle Aggregates as Probes and Click Chemistry. *Small* **2010,** *6*, 623-626.

(86) Wen, Y. Q.; McLaughlin, C. K.; Lo, P. K.; Yang, H.; Sleiman, H. F. Stable Gold Nanoparticle Conjugation to Internal DNA Positions: Facile Generation of Discrete Gold Nanoparticle-DNA Assemblies. *Bioconjugate Chem.* **2010,** *21*, 1413-1416.

(87) Lee, K.; Drachev, V. P.; Irudayaraj, J. DNA-Gold Nanoparticle Reversible Networks Grown on Cell Surface Marker Sites: Application in Diagnostics. *ACS Nano* **2011,** *5*, 2109-2117.

(88) Shen, X. B.; Song, C.; Wang, J. Y.; Shi, D. W.; Wang, Z. A.; Liu, N.; Ding, B. Q. Rolling up Gold Nanoparticle-Dressed DNA Origami into Three-Dimensional Plasmonic Chiral Nanostructures. *J. Am. Chem. Soc.* **2012,** *134*, 146-149.

(89) Park, S.; Hamad-Schifferli, K. Enhancement of in Vitro Translation by Gold Nanoparticle-DNA Conjugates. *ACS Nano* **2010,** *4*, 2555-2560.

(90) Li, M.; Wang, Q. Y.; Shi, X. D.; Hornak, L. A.; Wu, N. Q. Detection of Mercury(Ii) by Quantum Dot/DNA/Gold Nanoparticle Ensemble Based Nanosensor Via Nanometal Surface Energy Transfer. *Anal. Chem.* **2011,** *83*, 7061-7065.

(91) Xia, F.; Zuo, X. L.; Yang, R. Q.; Xiao, Y.; Kang, D.; Vallee-Belisle, A.; Gong, X.; Yuen, J. D.; Hsu, B. B. Y.; Heeger, A. J.; Plaxco, K. W. Colorimetric Detection of DNA, Small Molecules, Proteins, and Ions Using Unmodified Gold Nanoparticles and Conjugated Polyelectrolytes. *Proc. Natl. Acad. Sci. U.S.A.* **2010,** *107*, 10837-10841.

(92) Aaryasomayajula, V. S. R.; Severs, T.; Ghosh, K.; DeLong, R.; Zhang, X.; Talapatra, S.; Wanekaya, A. K. Assembly of a Dual Aptamer Gold Nanoparticle

Conjugate Ensemble in the Specific Detection of Thrombin When Coupled with Dynamic Light Scattering Spectroscopy. *J. Nanomed. Nanotechnol.* **2014,** *2014*.

(93) Jans, H.; Liu, X.; Austin, L.; Maes, G.; Huo, Q. Dynamic Light Scattering as a Powerful Tool for Gold Nanoparticle Bioconjugation and Biomolecular Binding Studies. *Anal. Chem.* **2009,** *81*, 9425-9432.

(94) Liu, X.; Dai, Q.; Austin, L.; Coutts, J.; Knowles, G.; Zou, J.; Chen, H.; Huo, Q. A One-Step Homogeneous Immunoassay for Cancer Biomarker Detection Using Gold Nanoparticle Probes Coupled with Dynamic Light Scattering. *J. Am. Chem. Soc.* **2008,** *130*, 2780-2782.

(95) Kim, C. S.; Mout, R.; Zhao, Y. L.; Yeh, Y. C.; Tang, R.; Jeong, Y.; Duncan, B.; Hardy, J. A.; Rotello, V. M. Co-Delivery of Protein and Small Molecule Therapeutics Using Nanoparticle-Stabilized Nanocapsules. *Bioconjugate Chem.* **2015,** *26*, 950-954.

(96) Haiss, W.; Thanh, N. T. K.; Aveyard, J.; Fernig, D. G. Determination of Size and Concentration of Gold Nanoparticles from UV-Vis Spectra. *Anal. Chem.* **2007,** *79*, 4215-4221.

(97) Near, R. D.; Hayden, S. C.; Hunter, R. E.; Thackston, D.; El-Sayed, M. A. Rapid and Efficient Prediction of Optical Extinction Coefficients for Gold Nanospheres and Gold Nanorods. *J. Phys. Chem. C* **2013,** *117*, 23950-23955.

(98) O'Brien, M. N.; Jones, M. R.; Brown, K. A.; Mirkin, C. A. Universal Noble Metal Nanoparticle Seeds Realized through Iterative Reductive Growth and Oxidative Dissolution Reactions. *J. Am. Chem. Soc.* **2014,** *136*, 7603-7606.

(99) Irrgang, J.; Ksienczyk, J.; Lapiene, V.; Niemeyer, C. M. Analysis of Non-Covalent Bioconjugation of Colloidal Nanoparticles by Means of Atomic Force Microscopy and Data Clustering. *Chemphyschem* **2009,** *10*, 1483-1491.

(100) Gomes, I.; Santos, N. C.; Oliveira, L. M. A.; Quintas, A.; Eaton, P.; Pereira, E.; Franco, R. Probing Surface Properties of Cytochrome C at Au Bionanoconjugates. *J. Phys. Chem. C* **2008,** *112*, 16340-16347.

(101) Shukla, R.; Bansal, V.; Chaudhary, M.; Basu, A.; Bhonde, R. R.; Sastry, M. Biocompatibility of Gold Nanoparticles and Their Endocytotic Fate inside the Cellular Compartment: A Microscopic Overview. *Langmuir* **2005,** *21*, 10644-10654.

(102) Koerner, H.; MacCuspie, R. I.; Park, K.; Vaia, R. A. In Situ UV/Vis, Saxs, and Tem Study of Single-Phase Gold Nanoparticle Growth. *Chem. Mater.* **2012,** *24*, 981-995.

(103) Park, S. Y.; Lytton-Jean, A. K. R.; Lee, B.; Weigand, S.; Schatz, G. C.; Mirkin, C. A. DNA-Programmable Nanoparticle Crystallization. *Nature* **2008,** *451*, 553-556.

(104) McKenzie, L. C.; Haben, P. M.; Kevan, S. D.; Hutchison, J. E. Determining Nanoparticle Size in Real Time by Small-Angle X-Ray Scattering in a Microscale Flow System. *J. Phys. Chem. C* **2010,** *114*, 22055-22063.

(105) Topete, A.; Alatorre-Meda, M.; Iglesias, P.; Villar-Alvarez, E. M.; Barbosa, S.; Costoya, J. A.; Taboada, P.; Mosquera, V. Fluorescent Drug-Loaded, Polymeric-Based, Branched Gold Nanoshells for Localized Multimodal Therapy and Imaging of Tumoral Cells. *ACS Nano* **2014,** *8*, 2725-2738.

(106) Sanchez-Gaytan, B. L.; Swanglap, P.; Lamkin, T. J.; Hickey, R. J.; Fakhraai, Z.; Link, S.; Park, S. J. Spiky Gold Nanoshells: Synthesis and Enhanced Scattering Properties. *J. Phys. Chem. C* **2012,** *116*, 10318-10324.

(107) Kim, J.; Park, J.; Kim, H.; Singha, K.; Kim, W. J. Transfection and Intracellular Trafficking Properties of Carbon Dot-Gold Nanoparticle Molecular Assembly Conjugated with Pei-Pdna. *Biomaterials* **2013,** *34*, 7168-7180.

(108) Grzelczak, M.; Perez-Juste, J.; Rodriguez-Gonzalez, B.; Liz-Marzan, L. M. Influence of Silver Ions on the Growth Mode of Platinum on Gold Nanorods. *J. Mater. Chem.* **2006,** *16*, 3946-3951.

(109) Yan, W. F.; Petkov, V.; Mahurin, S. M.; Overbury, S. H.; Dai, S. Powder Xrd Analysis and Catalysis Characterization of Ultra-Small Gold Nanoparticles Deposited on Titania-Modified Sba-15. *Catal. Commun.* **2005,** *6*, 404-408.

(110) Tessmer, I.; Kaur, P.; Lin, J. G.; Wang, H. Investigating Bioconjugation by Atomic Force Microscopy. *J Nanobiotechnol.* **2013,** *11*.

(111) Kelly, K. L.; Coronado, E.; Zhao, L. L.; Schatz, G. C. The Optical Properties of Metal Nanoparticles: The Influence of Size, Shape, and Dielectric Environment. *J. Phys. Chem. B* **2003,** *107*, 668-677.

(112) Link, S.; El-Sayed, M. A. Spectral Properties and Relaxation Dynamics of Surface Plasmon Electronic Oscillations in Gold and Silver Nanodots and Nanorods. *J. Phys. Chem. B* **1999,** *103*, 8410-8426.

(113) Mie, G. Articles on the Optical Characteristics of Turbid Tubes, Especially Colloidal Metal Solutions. *Ann Phys-Berlin* **1908,** *25*, 377-445.

(114) Nie, S. M.; Emory, S. R. Probing Single Molecules and Single Nanoparticles by Surface-Enhanced Raman Scattering. *Science* **1997,** *275*, 1102-1106.

(115) Abadeer, N. S.; Murphy, C. J. Recent Progress in Cancer Thermal Therapy Using Gold Nanoparticles. *J. Phys. Chem. C* **2016,** *120*, 4691-4716.

(116) Jain, P. K.; Lee, K. S.; El-Sayed, I. H.; El-Sayed, M. A. Calculated Absorption and Scattering Properties of Gold Nanoparticles of Different Size, Shape, and Composition: Applications in Biological Imaging and Biomedicine. *J. Phys. Chem. B* **2006,** *110*, 7238-7248.

(117) Sonnichsen, C.; Reinhard, B. M.; Liphardt, J.; Alivisatos, A. P. A Molecular Ruler Based on Plasmon Coupling of Single Gold and Silver Nanoparticles. *Nat. Biotechnol.* **2005,** *23*, 741-745.

(118) Hill, R. T.; Mock, J. J.; Hucknall, A.; Wolter, S. D.; Jokerst, N. M.; Smith, D. R.; Chilkoti, A. Plasmon Ruler with Angstrom Length Resolution. *ACS Nano* **2012,** *6*, 9237-9246.

(119) Lee, S. E.; Chen, Q.; Bhat, R.; Petkiewicz, S.; Smith, J. M.; Ferry, V. E.; Correia, A. L.; Alivisatos, A. P.; Bissell, M. J. Reversible Aptamer-Au Plasmon Rulers for Secreted Single Molecules. *Nano Lett.* **2015,** *15*, 4564-4570.

(120) Tajon, C. A.; Seo, D.; Asmussen, J.; Shah, N.; Jun, Y. W.; Craik, C. S. Sensitive and Selective Plasmon Ruler Nanosensors for Monitoring the Apoptotic Drug Response in Leukemia. *ACS Nano* **2014,** *8*, 9199-9208.

(121) Liu, N.; Hentschel, M.; Weiss, T.; Alivisatos, A. P.; Giessen, H. Three-Dimensional Plasmon Rulers. *Science* **2011,** *332*, 1407-1410.

(122) Abadeer, N. S.; Brennan, M. R.; Wilson, W. L.; Murphy, C. J. Distance and Plasmon Wavelength Dependent Fluorescence of Molecules Bound to Silica-Coated Gold Nanorods. *ACS Nano* **2014,** *8*, 8392-8406.

(123) Skrabalak, S. E.; Au, L.; Li, X. D.; Xia, Y. N. Facile Synthesis of Ag Nanocubes and Au Nanocages. *Nat. Protoc.* **2007,** *2*, 2182-2190.

(124) Li, W. W.; Chen, X. Y. Gold Nanoparticles for Photoacoustic Imaging. *Nanomedicine* **2015,** *10*, 299-320.

(125) Mallidi, S.; Larson, T.; Tam, J.; Joshi, P. P.; Karpiouk, A.; Sokolov, K.; Emelianov, S. Multiwavelength Photoacoustic Imaging and Plasmon Resonance Coupling of Gold Nanoparticles for Selective Detection of Cancer. *Nano Lett.* **2009,** *9*, 2825-2831.

(126) Sokolov, K.; Follen, M.; Aaron, J.; Pavlova, I.; Malpica, A.; Lotan, R.; Richards-Kortum, R. Real-Time Vital Optical Imaging of Precancer Using Anti-Epidermal Growth Factor Receptor Antibodies Conjugated to Gold Nanoparticles. *Cancer Res.* **2003,** *63*, 1999-2004.

(127) Herbst, R. S. Review of Epidermal Growth Factor Receptor Biology. *Inter. J. Radiat. 59*, S21-S26.

(128) Huang, X.; El-Sayed, I. H.; Qian, W.; El-Sayed, M. A. Cancer Cell Imaging and Photothermal Therapy in the near-Infrared Region by Using Gold Nanorods. *Journal of the American Chemical Society* **2006,** *128*, 2115-2120.

(129) Loo, C.; Lowery, A.; Halas, N.; West, J.; Drezek, R. Immunotargeted Nanoshells for Integrated Cancer Imaging and Therapy. *Nano Lett.* **2005,** *5*, 709-711.

(130) Aioub, M.; Austin, L. A.; El-Sayed, M. A. Determining Drug Efficacy Using Plasmonically Enhanced Imaging of the Morphological Changes of Cells Upon Death. *J. Phys. Chem. Lett.* **2014,** *5*, 3514-3518.

(131) Weis, S. M.; Cheresh, D. A. Tumor Angiogenesis: Molecular Pathways and Therapeutic Targets. *Nat. Med.* **2011,** *17*, 1359-1370.

(132) Copland, J. A.; Eghtedari, M.; Popov, V. L.; Kotov, N.; Mamedova, N.; Motamedi, M.; Oraevsky, A. A. Bioconjugated Gold Nanoparticles as a Molecular Based Contrast Agent: Implications for Imaging of Deep Tumors Using Optoacoustic Tomography. *Mol. Imaging. Biol.* **2004,** *6*, 341-349.

(133) Kircher, M. F.; De La Zerda, A.; Jokerst, J. V.; Zavaleta, C. L.; Kempen, P. J.; Mittra, E.; Pitter, K.; Huang, R.; Campos, C.; Habte, F. A Brain Tumor Molecular Imaging Strategy Using a New Triple-Modality Mri-Photoacoustic-Raman Nanoparticle. *Nat. Med.* **2012,** *18*, 829-834.

(134) Comenge, J.; Fragueiro, O.; Sharkey, J.; Taylor, A.; Held, M.; Burton, N. C.; Park, B. K.; Wilm, B.; Murray, P.; Brust, M.; Levy, R. Preventing Plasmon Coupling between Gold Nanorods Improves the Sensitivity of Photoacoustic Detection of Labeled Stem Cells in Vivo. *ACS Nano* **2016,** *10*, 7106-7116.

(135) Jokerst, J. V.; Cole, A. J.; Van de Sompel, D.; Gambhir, S. S. Gold Nanorods for Ovarian Cancer Detection with Photoacoustic Imaging and Resection Guidance Via Raman Imaging in Living Mice. *ACS nano* **2012,** *6*, 10366-10377.

(136) Yang, H. W.; Liu, H. L.; Li, M. L.; Hsi, I. W.; Fan, C. T.; Huang, C. Y.; Lu, Y. J.; Hua, M. Y.; Chou, H. Y.; Liaw, J. W.; Ma, C. C. M.; Wei, K. C. Magnetic Gold-Nanorod/Pnipaamma Nanoparticles for Dual Magnetic Resonance and Photoacoustic Imaging and Targeted Photothermal Therapy. *Biomaterials* **2013,** *34*, 5651-5660.

(137) Wang, Y. W.; Xie, X. Y.; Wang, X. D.; Ku, G.; Gill, K. L.; O'Neal, D. P.; Stoica, G.; Wang, L. V. Photoacoustic Tomography of a Nanoshell Contrast Agent in the in Vivo Rat Brain. *Nano Lett.* **2004,** *4*, 1689-1692.

(138) Yang, X. M.; Skrabalak, S. E.; Li, Z. Y.; Xia, Y. N.; Wang, L. H. V. Photoacoustic Tomography of a Rat Cerebral Cortex in Vivo with Au Nanocages as an Optical Contrast Agent. *Nano Lett.* **2007,** *7*, 3798-3802.

(139) Raghavan, V.; Subhash, H.; Breathnach, A.; Leahy, M.; Dockery, P.; Olivo, M. Dual Plasmonic Gold Nanoparticles for Multispectral Photoacoustic Imaging Application. *Proc Spie* **2014,** *8943*.

(140) Lu, W.; Huang, Q.; Geng, K. B.; Wen, X. X.; Zhou, M.; Guzatov, D.; Brecht, P.; Su, R.; Oraevsky, A.; Wang, L. V.; Li, C. Photoacoustic Imaging of Living Mouse Brain Vasculature Using Hollow Gold Nanospheres. *Biomaterials* **2010,** *31*, 2617-2626.

(141) Manivasagan, P.; Bharathiraja, S.; Bui, N. Q.; Lim, I. G.; Oh, J. Paclitaxel-Loaded Chitosan Oligosaccharide-Stabilized Gold Nanoparticles as Novel Agents for Drug Delivery and Photoacoustic Imaging of Cancer Cells. *Int. J. Pharmaceut.* **2016,** *511*, 367-379.

(142) Truby, R. L.; Emelianov, S. Y.; Homan, K. A. Ligand-Mediated Self-Assembly of Hybrid Plasmonic and Superparamagnetic Nanostructures. *Langmuir* **2013,** *29*, 2465-2470.

(143) Song, J.; Kim, J.; Hwang, S.; Jeon, M.; Jeong, S.; Kim, C.; Kim, S. "Smart" Gold Nanoparticles for Photoacoustic Imaging: An Imaging Contrast Agent Responsive to the Cancer Microenvironment and Signal Amplification Via Ph-Induced Aggregation. *Chem Commun* **2016,** *52*, 8287-8290.

(144) Elghanian, R.; Storhoff, J. J.; Mucic, R. C.; Letsinger, R. L.; Mirkin, C. A. Selective Colorimetric Detection of Polynucleotides Based on the Distance-Dependent Optical Properties of Gold Nanoparticles. *Science* **1997,** *277*, 1078-1081.

(145) Valentini, P.; Fiammengo, R.; Sabella, S.; Gariboldi, M.; Maiorano, G.; Cingolani, R.; Pompa, P. P. Gold-Nanoparticle-Based Colorimetric Discrimination of Cancer-Related Point Mutations with Picomolar Sensitivity. *ACS Nano* **2013,** *7*, 5530-5538.

(146) Xia, F.; Zuo, X.; Yang, R.; Xiao, Y.; Kang, D.; Vallée-Bélisle, A.; Gong, X.; Yuen, J. D.; Hsu, B. B. Y.; Heeger, A. J.; Plaxco, K. W. Colorimetric Detection of DNA, Small Molecules, Proteins, and Ions Using Unmodified Gold Nanoparticles and Conjugated Polyelectrolytes. *Proc. Natl. Acad. Sci. U.S.A.* **2010,** *107*, 10837-10841.

(147) Javier, D. J.; Castellanos-Gonzalez, A.; Weigum, S. E.; White, A. C.; Richards-Kortum, R. Oligonucleotide-Gold Nanoparticle Networks for Detection of Cryptosporidium Parvum Heat Shock Protein 70 Mrna. *J. Clin. Microbiol.* **2009,** *47*, 4060-4066.

(148) Storhoff, J. J.; Lucas, A. D.; Garimella, V.; Bao, Y. P.; Muller, U. R. Homogeneous Detection of Unamplified Genomic DNA Sequences Based on Colorimetric Scatter of Gold Nanoparticle Probes. *Nat. Biotechnol.* **2004,** *22*, 883-887.

(149) Reynolds, R. A.; Mirkin, C. A.; Letsinger, R. L. Homogeneous, Nanoparticle-Based Quantitative Colorimetric Detection of Oligonucleotides. *J. Am. Chem. Soc.* **2000,** *122*, 3795-3796.

(150) Duan, R.; Wang, B.; Zhang, T.; Zhang, Z.; Xu, S.; Chen, Z.; Lou, X.; Xia, F. Sensitive and Bidirectional Detection of Urine Telomerase Based on the Four Detection-Color States of Difunctional Gold Nanoparticle Probe. *Anal. Chem.* **2014,** *86*, 9781-9785.

(151) Gomez, D. E.; Armando, R. G.; Farina, H. G.; Menna, P. L.; Cerrudo, C. S.; Ghiringhelli, P. D.; Alonso, D. F. Telomere Structure and Telomerase in Health and Disease. *Int. J. Oncol.* **2012,** *41*, 1561-1569.

(152) Medley, C. D.; Smith, J. E.; Tang, Z.; Wu, Y.; Bamrungsap, S.; Tan, W. Gold Nanoparticle-Based Colorimetric Assay for the Direct Detection of Cancerous Cells. *Anal. Chem.* **2008,** *80*, 1067-1072.

(153) Borghei, Y.-S.; Hosseini, M.; Dadmehr, M.; Hosseinkhani, S.; Ganjali, M. R.; Sheikhnejad, R. Visual Detection of Cancer Cells by Colorimetric Aptasensor Based on Aggregation of Gold Nanoparticles Induced by DNA Hybridization. *Anal. Chim. Acta* **2016,** *904*, 92-97.

(154) Yu, T.; Dai, P.-P.; Xu, J.-J.; Chen, H.-Y. Highly Sensitive Colorimetric Cancer Cell Detection Based on Dual Signal Amplification. *ACS Appl. Mater. Inter.* **2016,** *8*, 4434-4441.

(155) Lu, W.; Arumugam, S. R.; Senapati, D.; Singh, A. K.; Arbneshi, T.; Khan, S. A.; Yu, H.; Ray, P. C. Multifunctional Oval-Shaped Gold-Nanoparticle-Based Selective Detection of Breast Cancer Cells Using Simple Colorimetric and Highly Sensitive Two-Photon Scattering Assay. *ACS Nano* **2010,** *4*, 1739-1749.

(156) Pierre-Pierre, N.; Huo, Q., Dynamic Light Scattering Coupled with Gold Nanoparticle Probes as a Powerful Sensing Technique for Chemical and Biological Target Detection. In *Recent Progress in Colloid and Surface Chemistry with Biological Applications*, American Chemical Society: 2015; Vol. 1215, pp 157-179.

(157) *Cancer Facts & Figures 2016.*; American Cancer Society: Atlanta, GA, 2016.

(158) Ankerst, D. P.; Gelfond, J.; Goros, M.; Herrera, J.; Strobl, A.; Thompson, I. M., Jr.; Hernandez, J.; Leach, R. J. Serial Percent Free Prostate Specific Antigen in Combination with Prostate Specific Antigen for Population Based Early Detection of Prostate Cancer. *J. Urol. 196*, 355-360.

(159) Zheng, T.; Pierre-Pierre, N.; Yan, X.; Huo, Q.; Almodovar, A. J. O.; Valerio, F.; Rivera-Ramirez, I.; Griffith, E.; Decker, D. D.; Chen, S.; Zhu, N. Gold Nanoparticle-Enabled Blood Test for Early Stage Cancer Detection and Risk Assessment. *ACS Appl. Mater. Inter.* **2015,** *7*, 6819-6827.

(160) Pylaev, T. E.; Khanadeev, V. A.; Khlebtsov, B. N.; Dykman, L. A.; Bogatyrev, V. A.; Khlebtsov, N. G. Colorimetric and Dynamic Light Scattering Detection of DNA Sequences by Using Positively Charged Gold Nanospheres: A comparative Study with Gold Nanorods. *Nanotechnology* **2011,** *22*, 285501.

(161) Miao, X.-M.; Xiong, C.; Wang, W.-W.; Ling, L.-S.; Shuai, X.-T. Dynamic-Light-Scattering-Based Sequence-Specific Recognition of Double-Stranded DNA with Oligonucleotide-Functionalized Gold Nanoparticles. *Chemistry – A European Journal* **2011,** *17*, 11230-11236.

(162) Seow, N.; Tan, Y. N.; Yung, L.-Y. L. Gold Nanoparticle–Dynamic Light Scattering Tandem for the Rapid and Quantitative Detection of the Let7 Microrna Family. *Part. Part. Syst. Char.* **2014,** *31*, 1260-1268.

(163) Stiles, P. L.; Dieringer, J. A.; Shah, N. C.; Van Duyne, R. P. Surface-Enhanced Raman Spectroscopy. *Annu. Rev. Anal. Chem.* **2008,** *1*, 601-626.

(164) Vendrell, M.; Maiti, K. K.; Dhaliwal, K.; Chang, Y.-T. Surface-Enhanced Raman Scattering in Cancer Detection and Imaging. *Trends Biotechnol.* **2013,** *31*, 249-257.

(165) Grubisha, D. S.; Lipert, R. J.; Park, H.-Y.; Driskell, J.; Porter, M. D. Femtomolar Detection of Prostate-Specific Antigen: An Immunoassay Based on Surface-Enhanced Raman Scattering and Immunogold Labels. *Anal. Chem.* **2003,** *75*, 5936-5943.

(166) Wang, G.; Lipert, R. J.; Jain, M.; Kaur, S.; Chakraboty, S.; Torres, M. P.; Batra, S. K.; Brand, R. E.; Porter, M. D. Detection of the Potential Pancreatic Cancer Marker Muc4 in Serum Using Surface-Enhanced Raman Scattering. *Anal. Chem.* **2011,** *83*, 2554-2561.

(167) Wang, X.; Qian, X.; Beitler, J. J.; Chen, Z. G.; Khuri, F. R.; Lewis, M. M.; Shin, H. J. C.; Nie, S.; Shin, D. M. Detection of Circulating Tumor Cells in Human Peripheral Blood Using Surface-Enhanced Raman Scattering Nanoparticles. *Cancer Res.* **2011,** *71*, 1526-1532.

(168) Chon, H.; Lee, S.; Yoon, S.-Y.; Chang, S.-I.; Lim, D. W.; Choo, J. Simultaneous Immunoassay for the Detection of Two Lung Cancer Markers Using Functionalized Sers Nanoprobes. *Chem Commun* **2011,** *47*, 12515-12517.

(169) Wang, H.-N.; Crawford, B. M.; Fales, A. M.; Bowie, M. L.; Seewaldt, V. L.; Vo-Dinh, T. Multiplexed Detection of Microrna Biomarkers Using Sers-Based Inverse Molecular Sentinel (Ims) Nanoprobes. *J. Phys. Chem. C* **2016,** *120*, 21047-21055.

(170) Sun, L.; Yu, C.; Irudayaraj, J. Raman Multiplexers for Alternative Gene Splicing. *Anal. Chem.* **2008,** *80*, 3342-3349.

(171) Li, M.; Kang, J. W.; Sukumar, S.; Dasari, R. R.; Barman, I. Multiplexed Detection of Serological Cancer Markers with Plasmon-Enhanced Raman Spectro-Immunoassay. *Chem. Sci.* **2015,** *6*, 3906-3914.

(172) Dinish, U.; Balasundaram, G.; Chang, Y. T.; Olivo, M. Sensitive Multiplex Detection of Serological Liver Cancer Biomarkers Using Sers-Active Photonic Crystal Fiber Probe. *J. Biophoton.* **2014,** *7*, 956-965.

(173) Qian, X.; Peng, X.-H.; Ansari, D. O.; Yin-Goen, Q.; Chen, G. Z.; Shin, D. M.; Yang, L.; Young, A. N.; Wang, M. D.; Nie, S. In Vivo Tumor Targeting and Spectroscopic Detection with Surface-Enhanced Raman Nanoparticle Tags. *Nat. Biotechnol.* **2008,** *26*, 83-90.

(174) Samanta, A.; Maiti, K. K.; Soh, K.-S.; Liao, X.; Vendrell, M.; Dinish, U. S.; Yun, S.-W.; Bhuvaneswari, R.; Kim, H.; Rautela, S.; Chung, J.; Olivo, M.; Chang, Y.-T. Ultrasensitive near-Infrared Raman Reporters for Sers-Based in Vivo Cancer Detection. *Angew. Chem., Int. Ed.* **2011,** *50*, 6089-6092.

(175) Wang, Y.; Kang, S.; Khan, A.; Ruttner, G.; Leigh, S. Y.; Murray, M.; Abeytunge, S.; Peterson, G.; Rajadhyaksha, M.; Dintzis, S.; Javid, S.; Liu, J. T. C. Quantitative

Molecular Phenotyping with Topically Applied Sers Nanoparticles for Intraoperative Guidance of Breast Cancer Lumpectomy. *Sci. Rep.* **2016,** *6*, 21242.

(176) Kang, B.; Austin, L. A.; El-Sayed, M. A. Real-Time Molecular Imaging Throughout the Entire Cell Cycle by Targeted Plasmonic-Enhanced Rayleigh/Raman Spectroscopy. *Nano Letters* **2012,** *12*, 5369-5375.

(177) Kang, B.; Austin, L. A.; El-Sayed, M. A. Observing Real-Time Molecular Event Dynamics of Apoptosis in Living Cancer Cells Using Nuclear-Targeted Plasmonically Enhanced Raman Nanoprobes. *ACS Nano* **2014,** *8*, 4883-4892.

(178) Kang, B.; Afifi, M. M.; Austin, L. A.; El-Sayed, M. A. Exploiting the Nanoparticle Plasmon Effect: Observing Drug Delivery Dynamics in Single Cells Via Raman/Fluorescence Imaging Spectroscopy. *ACS Nano* **2013,** *7*, 7420-7427.

(179) Austin, L. A.; Kang, B.; El-Sayed, M. A. A New Nanotechnology Technique for Determining Drug Efficacy Using Targeted Plasmonically Enhanced Single Cell Imaging Spectroscopy. *J. Am. Chem. Soc.* **2013,** *135*, 4688-4691.

(180) Kang, J. W.; So, P. T. C.; Dasari, R. R.; Lim, D.-K. High Resolution Live Cell Raman Imaging Using Subcellular Organelle-Targeting Sers-Sensitive Gold Nanoparticles with Highly Narrow Intra-Nanogap. *Nano Lett.* **2015,** *15*, 1766-1772.

(181) Jain, R. K.; Stylianopoulos, T. Delivering Nanomedicine to Solid Tumors. *Nat. Rev. Clin. Oncol.* **2010,** *7*, 653-664.

(182) Yoo, J. W.; Chambers, E.; Mitragotri, S. Factors That Control the Circulation Time of Nanoparticles in Blood: Challenges, Solutions and Future Prospects. *Curr. Pharm. Design* **2010,** *16*, 2298-2307.

(183) Zhang, X. D.; Wu, D.; Shen, X.; Liu, P. X.; Fan, F. Y.; Fan, S. J. In Vivo Renal Clearance, Biodistribution, Toxicity of Gold Nanoclusters. *Biomaterials* **2012,** *33*, 4628-4638.

(184) Perrault, S. D.; Walkey, C.; Jennings, T.; Fischer, H. C.; Chan, W. C. W. Mediating Tumor Targeting Efficiency of Nanoparticles through Design. *Nano Lett.* **2009,** *9*, 1909-1915.

(185) Jiang, W.; Kim, B. Y. S.; Rutka, J. T.; Chan, W. C. W. Nanoparticle-Mediated Cellular Response Is Size-Dependent. *Nat. Nanotechnol.* **2008,** *3*, 145-150.

(186) Huang, X. H.; Peng, X. H.; Wang, Y. Q.; Wang, Y. X.; Shin, D. M.; El-Sayed, M. A.; Nie, S. M. A Reexamination of Active and Passive Tumor Targeting by Using Rod-Shaped Gold Nanocrystals and Covalently Conjugated Peptide Ligands. *ACS Nano* **2010,** *4*, 5887-5896.

(187) Liu, H. Y.; Liu, T. L.; Wu, X. L.; Li, L. L.; Tan, L. F.; Chen, D.; Tang, F. Q. Targeting Gold Nanoshells on Silica Nanorattles: A Drug Cocktail to Fight Breast Tumors via a Single Irradiation with near-Infrared Laser Light. *Adv. Mater.* **2012,** *24*, 755-761.

(188) Chiu, T. C.; Huang, C. C. Aptamer-Functionalized Nano-Biosensors. *Sensors* **2009,** *9*, 10356-10388.

(189) Kim, D.; Jeong, Y. Y.; Jon, S. A Drug-Loaded Aptamer-Gold Nanoparticle Bioconjugate for Combined Ct Imaging and Therapy of Prostate Cancer. *ACS Nano* **2010,** *4*, 3689-3696.

(190) Lu, W.; Xiong, C. Y.; Zhang, G. D.; Huang, Q.; Zhang, R.; Zhang, J. Z.; Li, C. Targeted Photothermal Ablation of Murine Melanomas with Melanocyte-Stimulating Hormone Analog-Conjugated Hollow Gold Nanospheres. *Clin. Cancer Res.* **2009,** *15*, 876-886.

(191) Duncan, B.; Kim, C.; Rotello, V. M. Gold Nanoparticle Platforms as Drug and Biomacromolecule Delivery Systems. *J. Controlled Rel.* **2010,** *148*, 122-127.

(192) Paciotti, G. F.; Myer, L.; Weinreich, D.; Goia, D.; Pavel, N.; McLaughlin, R. E.; Tamarkin, L. Colloidal Gold: A Novel Nanoparticle Vector for Tumor Directed Drug Delivery. *Drug Deliv.* **2004,** *11*, 169-183.

(193) Manivasagan, P.; Bharathiraja, S.; Bui, N. Q.; Jang, B.; Oh, Y. O.; Lim, I. G.; Oh, J. Doxorubicin-Loaded Fucoidan Capped Gold Nanoparticles for Drug Delivery and Photoacoustic Imaging. *Int. J. Biol. Macromol.* **2016,** *91*, 578-588.

(194) Shi, Y.; Goodisman, J.; Dabrowiak, J. C. Cyclodextrin Capped Gold Nanoparticles as a Delivery Vehicle for a Prodrug of Cisplatin. *Inorg. Chem.* **2013,** *52*, 9418-9426.

(195) Brown, S. D.; Nativo, P.; Smith, J. A.; Stirling, D.; Edwards, P. R.; Venugopal, B.; Flint, D. J.; Plumb, J. A.; Graham, D.; Wheate, N. J. Gold Nanoparticles for the Improved Anticancer Drug Delivery of the Active Component of Oxaliplatin. *J. Am. Chem. Soc.* **2010,** *132*, 4678-4684.

(196) Afifi, M. M.; Austin, L. A.; Mackey, M. A.; El-Sayed, M. A. Xav939: From a Small Inhibitor to a Potent Drug Bioconjugate When Delivered by Gold Nanoparticles. *Bioconjug Chem* **2014,** *25*, 207-215.

(197) Wang, F.; Wang, Y. C.; Dou, S.; Xiong, M. H.; Sun, T. M.; Wang, J. Doxorubicin-Tethered Responsive Gold Nanoparticles Facilitate Intracellular Drug Delivery for Overcoming Multidrug Resistance in Cancer Cells. *ACS Nano* **2011,** *5*, 3679-3692.

(198) Pan, L. M.; Liu, J. A.; He, Q. J.; Wang, L. J.; Shi, J. L. Overcoming Multidrug Resistance of Cancer Cells by Direct Intranuclear Drug Delivery Using Tat-Conjugated Mesoporous Silica Nanoparticles. *Biomaterials* **2013,** *34*, 2719-2730.

(199) Yang, X. J.; Liu, X.; Liu, Z.; Pu, F.; Ren, J. S.; Qu, X. G. Near-Infrared Light-Triggered, Targeted Drug Delivery to Cancer Cells by Aptamer Gated Nanovehicles. *Adv. Mater.* **2012,** *24*, 2890-2895.

(200) Shi, P.; Qu, K. G.; Wang, J. S.; Li, M.; Ren, J. S.; Qu, X. G. Ph-Responsive NIR Enhanced Drug Release from Gold Nanocages Possesses High Potency against Cancer Cells. *Chem Commun* **2012,** *48*, 7640-7642.

(201) Niikura, K.; Iyo, N.; Matsuo, Y.; Mitomo, H.; Ijiro, K. Sub-100 Nm Gold Nanoparticle Vesicles as a Drug Delivery Carrier Enabling Rapid Drug Release Upon Light Irradiation. *ACS Appl. Mater. Inter.* **2013,** *5*, 3900-3907.

(202) Chen, J. Y.; Glaus, C.; Laforest, R.; Zhang, Q.; Yang, M. X.; Gidding, M.; Welch, M. J.; Xia, Y. N. Gold Nanocages as Photothermal Transducers for Cancer Treatment. *Small* **2010,** *6*, 811-817.

(203) Perez-Hernandez, M.; del Pino, P.; Mitchell, S. G.; Moros, M.; Stepien, G.; Pelaz, B.; Parak, W. J.; Galvez, E. M.; Pardo, J.; de la Fuente, J. M. Dissecting the Molecular Mechanism of Apoptosis During Photothermal Therapy Using Gold Nanoprisms. *ACS Nano* **2015,** *9*, 52-61.

(204) Huang, X. H.; Kang, B.; Qian, W.; Mackey, M. A.; Chen, P. C.; Oyelere, A. K.; El-Sayed, I. H.; El-Sayed, M. A. Comparative Study of Photothermolysis of Cancer Cells with Nuclear-Targeted or Cytoplasm-Targeted Gold Nanospheres: Continuous Wave or Pulsed Lasers. *J. Biomed. Opt.* **2010,** *15*, 058002.

(205) Rengan, A. K.; Bukhari, A. B.; Pradhan, A.; Malhotra, R.; Banerjee, R.; Srivastava, R.; De, A. In Vivo Analysis of Biodegradable Liposome Gold Nanoparticles as Efficient Agents for Photothermal Therapy of Cancer. *Nano Lett.* **2015,** *15*, 842-848.

(206) Burke, A. R.; Singh, R. N.; Carroll, D. L.; Wood, J. C. S.; D'Agostino, R. B.; Ajayan, P. M.; Torti, F. M.; Torti, S. V. The Resistance of Breast Cancer Stem Cells to Conventional Hyperthermia and Their Sensitivity to Nanoparticle-Mediated Photothermal Therapy. *Biomaterials* **2012,** *33*, 2961-2970.

(207) Kamkaew, A.; Lim, S. H.; Lee, H. B.; Kiew, L. V.; Chung, L. Y.; Burgess, K. Bodipy Dyes in Photodynamic Therapy. *Chem. Soc. Rev.* **2013,** *42*, 77-88.

(208) Hone, D. C.; Walker, P. I.; Evans-Gowing, R.; FitzGerald, S.; Beeby, A.; Chambrier, I.; Cook, M. J.; Russell, D. A. Generation of Cytotoxic Singlet Oxygen Via Phthalocyanine-Stabilized Gold Nanoparticles: A Potential Delivery Vehicle for Photodynamic Therapy. *Langmuir* **2002,** *18*, 2985-2987.

(209) Camerin, M.; Magaraggia, M.; Soncin, M.; Jori, G.; Moreno, M.; Chambrier, I.; Cook, M. J.; Russell, D. A. The in Vivo Efficacy of Phthalocyanine-Nanoparticle Conjugates for the Photodynamic Therapy of Amelanotic Melanoma. *Eur. J. Cancer* **2010,** *46*, 1910-1918.

(210) Fan, Z.; Dai, X. M.; Lu, Y. F.; Yu, E.; Brahmbatt, N.; Carter, N.; Tchouwou, C.; Singh, A. K.; Jones, Y.; Yu, H. T.; Ray, P. C. Enhancing Targeted Tumor Treatment by near IR Light-Activatable Photodynamic-Photothermal Synergistic Therapy. *Mol Pharmaceut.* **2014,** *11*, 1109-1116.

(211) Vijayaraghavan, P.; Liu, C. H.; Vankayala, R.; Chiang, C. S.; Hwang, K. C. Designing Multi-Branched Gold Nanoechinus for NIR Light Activated Dual Modal Photodynamic and Photothermal Therapy in the Second Biological Window. *Adv. Mater.* **2014,** *26*, 6689-6695.

(212) Wang, J.; Zhu, G. Z.; You, M. X.; Song, E. Q.; Shukoor, M. I.; Zhang, K. J.; Altman, M. B.; Chen, Y.; Zhu, Z.; Huang, C. Z.; Tan, W. H. Assembly of Aptamer Switch Probes and Photosensitizer on Gold Nanorods for Targeted Photothermal and Photodynamic Cancer Therapy. *ACS Nano* **2012,** *6*, 5070-5077.

(213) Lin, J.; Wang, S. J.; Huang, P.; Wang, Z.; Chen, S. H.; Niu, G.; Li, W. W.; He, J.; Cui, D. X.; Lu, G. M.; Chen, X. Y.; Nie, Z. H. Photosensitizer-Loaded Gold Vesicles with Strong Plasmonic Coupling Effect for Imaging-Guided Photothermal/Photodynamic Therapy. *ACS Nano* **2013,** *7*, 5320-5329.

(214) MacDonald, I. J.; Dougherty, T. J. Basic Principles of Photodynamic Therapy. *J. Porphyr. Phthalocya.* **2001,** *5*, 105-129.

(215) Gao, H.; Liu, R.; Gao, F. P.; Wang, Y. L.; Jiang, X. L.; Gao, X. Y. Plasmon-Mediated Generation of Reactive Oxygen Species from near-Infrared Light Excited Gold Nanocages for Photodynamic Therapy in Vitro. *ACS Nano* **2014,** *8*, 7260-7271.

(216) Zhao, T. T.; Shen, X. Q.; Li, L.; Guan, Z. P.; Gao, N. Y.; Yuan, P. Y.; Yao, S. Q.; Xu, Q. H.; Xu, G. Q. Gold Nanorods as Dual Photo-Sensitizing and Imaging Agents for Two-Photon Photodynamic Therapy. *Nanoscale* **2012,** *4*, 7712-7719.

(217) Vankayala, R.; Huang, Y. K.; Kalluru, P.; Chiang, C. S.; Hwang, K. C. First Demonstration of Gold Nanorods-Mediated Photodynamic Therapeutic Destruction of Tumors Via near Infra-Red Light Activation. *Small* **2014,** *10*, 1612-1622.

(218) Labouret, T.; Audibert, J. F.; Pansu, R. B.; Palpant, B. Plasmon-Assisted Production of Reactive Oxygen Species by Single Gold Nanorods. *Small* **2015,** *11*, 4475-4479.

(219) Jiang, C. F.; Zhao, T. T.; Yuan, P. Y.; Gao, N. Y.; Pan, Y. L.; Guan, Z. P.; Zhou, N.; Xu, Q. H. Two-Photon Induced Photoluminescence and Singlet Oxygen Generation from Aggregated Gold Nanoparticles. *ACS Appl. Mater. Inter.* **2013,** *5*, 4972-4977.

(220) Aioub, M.; El-Sayed, M. A. A Real-Time Surface Enhanced Raman Spectroscopy Study of Plasmonic Photothermal Cell Death Using Targeted Gold Nanoparticles. *J. Am. Chem. Soc.* **2016,** *138*, 1258-1264.

(221) Ziegler, C.; Eychmuller, A. Seeded Growth Synthesis of Uniform Gold Nanoparticles with Diameters of 15-300 Nm. *J. Phys. Chem. C* **2011,** *115*, 4502-4506.

(222) Cobley, C. M.; Xia, Y. N. Engineering the Properties of Metal Nanostructures Via Galvanic Replacement Reactions. *Mat. Sci. Eng. Rep.* **2010,** *70*, 44-62.

(223) Njoki, P. N.; Lim, I. I. S.; Mott, D.; Park, H. Y.; Khan, B.; Mishra, S.; Sujakumar, R.; Luo, J.; Zhong, C. J. Size Correlation of Optical and Spectroscopic Properties for Gold Nanoparticles. *J. Phys. Chem. C* **2007,** *111*, 14664-14669.

(224) van der Zande, B. M. I.; Bohmer, M. R.; Fokkink, L. G. J.; Schonenberger, C. Colloidal Dispersions of Gold Rods: Synthesis and Optical Properties. *Langmuir* **2000,** *16*, 451-458.

(225) Yu, Y. Y.; Chang, S. S.; Lee, C. L.; Wang, C. R. C. Gold Nanorods: Electrochemical Synthesis and Optical Properties. *J. Phys. Chem. B* **1997,** *101*, 6661-6664.

(226) Xiong, Y. J.; Washio, I.; Chen, J. Y.; Cai, H. G.; Li, Z. Y.; Xia, Y. N. Poly(Vinyl Pyrrolidone): A Dual Functional Reductant and Stabilizer for the Facile Synthesis of Noble Metal Nanoplates in Aqueous Solutions. *Langmuir* **2006,** *22*, 8563-8570.

(227) Han, L.; Zhao, J.; Zhang, X.; Cao, W. P.; Hu, X. X.; Zou, G. Z.; Duan, X. L.; Liang, X. J. Enhanced Sirna Delivery and Silencing Gold-Chitosan Nanosystem with Surface Charge-Reversal Polymer Assembly and Good Biocompatibility. *ACS Nano* **2012,** *6*, 7340-7351.

(228) Lee, S. K.; Han, M. S.; Asokan, S.; Tung, C. H. Effective Gene Silencing by Multilayered Sirna-Coated Gold Nanoparticles. *Small* **2011,** *7*, 364-370.

(229) Tkachenko, A. G.; Xie, H.; Coleman, D.; Glomm, W.; Ryan, J.; Anderson, M. F.; Franzen, S.; Feldheim, D. L. Multifunctional Gold Nanoparticle-Peptide Complexes for Nuclear Targeting. *J. Am. Chem. Soc.* **2003,** *125*, 4700-4701.

(230) Qian, X. M.; Peng, X. H.; Ansari, D. O.; Yin-Goen, Q.; Chen, G. Z.; Shin, D. M.; Yang, L.; Young, A. N.; Wang, M. D.; Nie, S. M. In Vivo Tumor Targeting and Spectroscopic Detection with Surface-Enhanced Raman Nanoparticle Tags. *Nat. Biotechnol.* **2008,** *26*, 83-90.

(231) Chattopadhyay, N.; Cai, Z. L.; Pignol, J. P.; Keller, B.; Lechtman, E.; Bendayan, R.; Reilly, R. M. Design and Characterization of Her-2-Targeted Gold Nanoparticles for Enhanced X-Radiation Treatment of Locally Advanced Breast Cancer. *Mol. Pharmaceut.* **2010,** *7*, 2194-2206.

(232) Shenoi, M. M.; Iltis, I.; Choi, J.; Koonce, N. A.; Metzger, G. J.; Griffin, R. J.; Bischof, J. C. Nanoparticle Delivered Vascular Disrupting Agents (Vdas): Use of Tnf-Alpha Conjugated Gold Nanoparticles for Multimodal Cancer Therapy. *Mol. Pharmaceut.* **2013,** *10*, 1683-1694.

(233) Goel, R.; Shah, N.; Visaria, R.; Paciotti, G. F.; Bischof, J. C. Biodistribution of Tnf-Alpha-Coated Gold Nanoparticles in an in Vivo Model System. *Nanomedicine* **2009,** *4*, 401-410.

(234) Prigodich, A. E.; Seferos, D. S.; Massich, M. D.; Giljohann, D. A.; Lane, B. C.; Mirkin, C. A. Nano-Flares for Mrna Regulation and Detection. *ACS Nano* **2009,** *3*, 2147-2152.

(235) Dixit, V.; Van den Bossche, J.; Sherman, D. M.; Thompson, D. H.; Andres, R. P. Synthesis and Grafting of Thioctic Acid-Peg-Folate Conjugates onto Au Nanoparticles for Selective Targeting of Folate Receptor-Positive Tumor Cells. *Bioconjugate Chem.* **2006,** *17*, 603-609.

(236) Cheng, Y.; Meyers, J. D.; Broome, A. M.; Kenney, M. E.; Basilion, J. P.; Burda, C. Deep Penetration of a PDT Drug into Tumors by Noncovalent Drug-Gold Nanoparticle Conjugates. *J. Am. Chem. Soc.* **2011,** *133*, 2583-2591.

(237) Agarwal, A.; Mackey, M. A.; El-Sayed, M. A.; Bellamkonda, R. V. Remote Triggered Release of Doxorubicin in Tumors by Synergistic Application of Thermosensitive Liposomes and Gold Nanorods. *ACS Nano* **2011,** *5*, 4919-4926.

(238) Dhar, S.; Daniel, W. L.; Giljohann, D. A.; Mirkin, C. A.; Lippard, S. J. Polyvalent Oligonucleotide Gold Nanoparticle Conjugates as Delivery Vehicles for Platinum(Iv) Warheads. *J. Am. Chem. Soc.* **2009,** *131*, 14652-14653.

(239) Peckys, D. B.; de Jonge, N. Visualizing Gold Nanoparticle Uptake in Live Cells with Liquid Scanning Transmission Electron Microscopy. *Nano Lett.* **2011,** *11*, 1733-1738.

CHAPTER 2. BIOLOGICAL TARGETING OF PLASMONIC NANOPARTICLES IMPROVES CELLULAR IMAGING VIA THE ENHANCED SCATTERING IN THE AGGREGATES FORMED [1]

(Adapted with permission from Aioub, M.; Kang, B.; Mackey, M. A.; El-Sayed, M. A. Biological Targeting of Plasmonic Nanoparticles Improves Cellular Imaging via the Enhanced Scattering in the Aggregates Formed. *J. Phys. Chem. Lett.* **2014,** *5*, 2555-2561.

Gold nanoparticles (AuNPs) demonstrate great promise in biomedical applications due to their plasmonically enhanced imaging properties. When in close proximity, AuNPs plasmonic fields couple together, increasing their scattering cross-section due to the formation of hot spots, improving their imaging utility. In the present study, we modified the AuNPs surface with different peptides to target the nucleus and/or the cell as a whole, resulting in similar cellular uptake but different scattering intensities. Nuclear-targeted AuNPs showed the greatest scattering due to the formation of denser nanoparticle clusters (i.e., increased localization). We also obtained a dynamic profile of AuNP localization in living cells, indicating that nuclear localization is directly related to the number of nuclear-targeting peptides on the AuNP surface. Increased localization led to increased plasmonic field coupling, resulting in significantly higher scattering intensity. Thus, biochemical targeting of plasmonic nanoparticles to subcellular components is expected to lead to more resolved imaging of cellular processes.

2.1 Introduction

In recent years, the use of nanoparticles in the biomedical field has increased greatly due to their small size and unique physical, optical, and chemical properties.[2-5] In particular, gold and silver metallic nanoparticles have been extensively studied due to their unique interaction with electromagnetic radiation, owing to their characteristic localized surface plasmon resonance (LSPR).[6-9] The LSPR arises from the coherent oscillation of conduction band electrons, in resonance with the incident light of a particular frequency, which depends on the dielectric function of the metal, that of the medium, as well as the size, shape, and composition of the nanoparticle.[6, 10] The LSPR results in a remarkably strong enhancement of the electromagnetic field localized at the nanoparticle surface, which is utilized in surface enhanced spectroscopy[11] and solar energy applications.[12-14] Additionally, the enhanced electric field (plasmonic field) of one nanoparticle can interact with that of an adjacent nanoparticle in close proximity, resulting in plasmon coupling.[15-18] The interparticle coupling leads to an intense enhancement of the plasmonic field relative to that of a single nanoparticle.[18-19] The LSPR of the coupled nanoparticles is red-shifted to longer wavelengths from the LSPR of a single nanoparticle, with a magnitude that depends on the proximity of the nanoparticles. Thus, the plasmon shift gives a measure of the distance between nanoparticles.[15-16, 20-21]

Gold nanoparticles (AuNPs) in particular have been increasingly utilized in a variety of biomedical fields, such as cellular imaging,[22] drug delivery,[23] and photothermal cancer therapy,[24] due not only to their plasmonic properties, but also to their relatively low toxicity and facile surface chemistry.[3] For many of these biomedical applications,

gold nanoparticles often need to be delivered intracellularly, and their nanoscale size allows AuNPs to be internalized by various types of cells through several endocytic processes.[25-27] This can be achieved by chemical modification of the AuNP surface with targeting ligands, such as the cancer cell membrane targeting peptide (RGD), to selectively deliver AuNPs into cancer cells through receptor-mediated endocytosis.[25, 28-29] Also, chemical modification with a nuclear localization sequence (NLS) peptide can selectively deliver AuNPs to the cell nucleus.[26, 30-33] Once AuNPs are internalized by cells, they are transported through subcellular vesicles and may accumulate in endosomes or lysosomes near the nucleus. During intracellular transport and localization, nanoparticles accumulate in subcellular components at different concentrations, which may depend on the size, shape, and most importantly, the surface chemistry of the nanoparticle. Therefore, understanding the localization of nanoparticles is critical to understanding their fundamental interactions within cells and improving their design for biomedical applications. To this end, the accumulation of AuNPs in endosomes and lysosomes has been observed by cryo-TEM,[34-35] but the direct observation of the dynamics of nanoparticle localization in living cells still remains a challenge. Our group has previously observed the cellular uptake of gold nanoparticles by live-cell plasmonically enhanced Rayleigh scattering imaging techniques, which take advantage of the subcellular localization of AuNPs, resulting in the enhancement of AuNP Rayleigh scattering,[36-39] but the dynamics of this AuNP localization remains unknown.

In the present work, we have built a novel instrument and studied the cellular uptake and subcellular localization of AuNPs within living cells, in real-time, via single-cell plasmonically-enhanced Rayleigh-scattering imaging spectroscopy (PERSIS). This

approach takes advantage of the characteristic optical properties of plasmonic AuNPs, namely, their ability to strongly scatter light, and the coupling of their plasmonic fields when particles come into close proximity. By monitoring the enhanced Rayleigh (elastic) scattering of different surface-modified AuNPs, the subcellular localization dynamics can be studied in real time. We have shown that the localization of AuNPs is dependent on the specific surface modification of the nanoparticles. Varying the amounts of the RGD and NLS peptides on the AuNP surface did not lead to a significant difference in the number of AuNPs internalized by the cancer cells, but large differences in the scattering intensity were observed due to the different surface modifications causing changes in AuNP localization within cells. Targeting AuNPs to the nucleus of cells increased the level of aggregation, leading to an increase in the total light scattered and a redshift to longer wavelengths, indicating enhanced coupling of the plasmonic fields due to decreased interparticle separation. Increasing the amount of NLS also caused the AuNPs to localize more rapidly, indicating that nuclear-targeted AuNPs may be more effective as imaging agents for biomedical applications, due to their greater light scattering ability and faster subcellular localization. This suggests that targeting subcellular components leads to greater localization, which offers an effective method of enhanced imaging using plasmonic nanoparticles.

2.2 Methods

2.2.1 AuNP Synthesis

For these studies, Citrate-stabilized AuNPs with an average diameter of 31 nm were synthesized by the reduction of chloroauric acid via sodium citrate.[40] Briefly, 490

mL of a 0.6 mM aqueous solution of chloroauric acid (Sigma-Aldrich) was heated in a 1 L Erlenmeyer flask, with stirring. When the solution reached boiling, 10 mL of a 180 mM trisodium citrate (Sigma-Aldrich) in water solution was immediately added. Stirring and heating were discontinued when the solution became a red-wine color and it was allowed to cool to room temperature. TEM images (**Figure 2.1**) were taken on a JEOL 100CX-2 transmission electron microscope and the average particle diameter was found to be 31 nm using ImageJ software. UV–Vis spectroscopy showed a surface plasmon resonance peak at 533 nm (Figure 2.1).

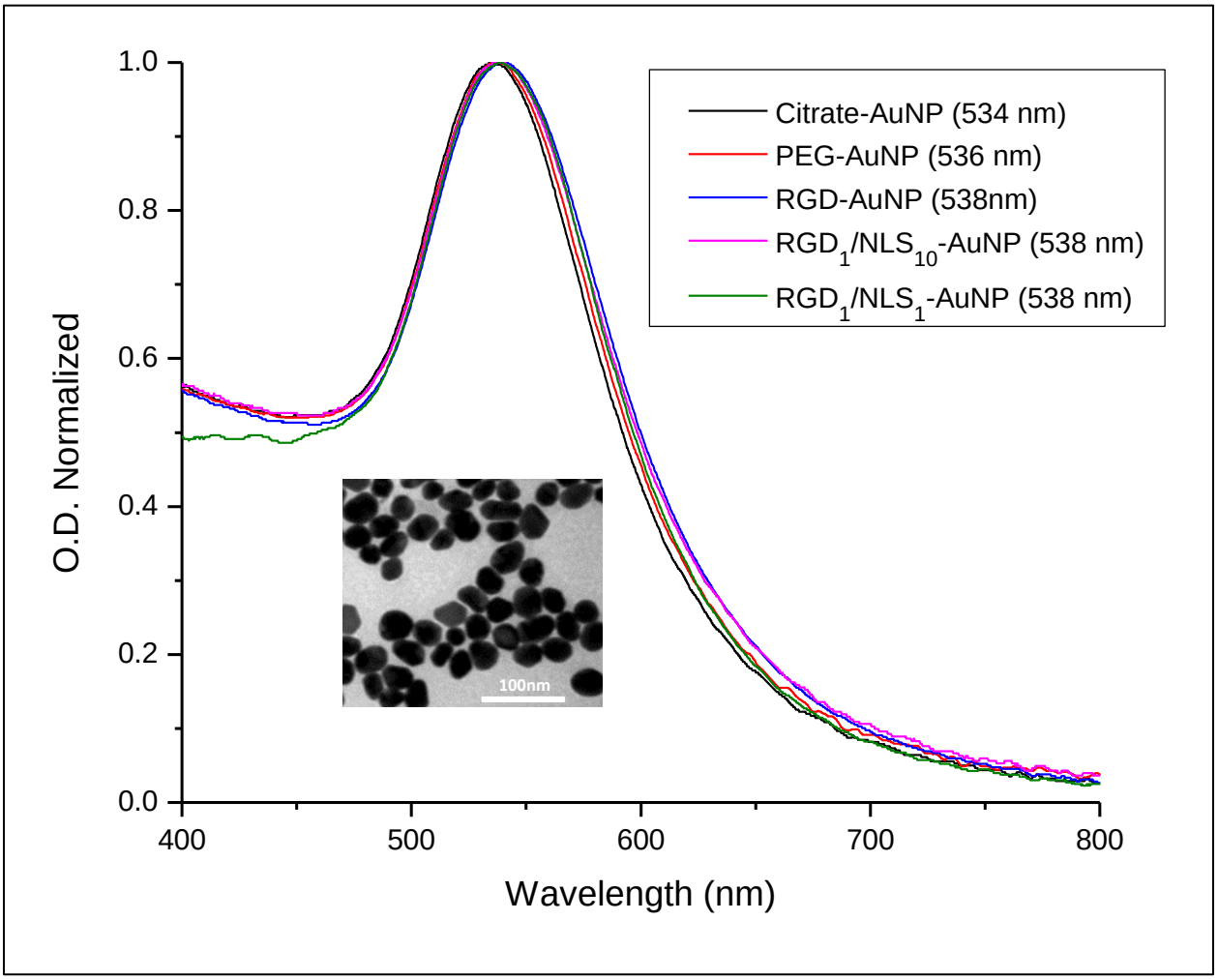

Figure 2.1 Characterization of targeted AuNPs. UV–Vis spectrum of AuNPs before (black) and after conjugation with mPEG-SH_{5000} (red), and varying molar ratios of RGD and NLS peptides (blue, pink, and green) in aqueous solution. There was a slight red shift in the plasmon peak indicating successful conjugation. The inset shows a TEM micrograph of 31 ± 4 nm citrate-capped AuNPs.

2.2.2 AuNP Functionalization

The citrate-capped AuNPs were stabilized with polyethylene glycol thiol (mPEG-SH_{5k}) to prevent nonspecific interactions under physiological conditions.[29] A 1.0 mM solution of mPEG-SH (MW 5000, Lysan Bio, Inc.) in deionized (DI) water was added to achieve a ~30% surface coverage. The PEG-AuNP solution was shaken overnight at room

temperature and unbound PEG was removed by centrifugation (6000 rpm, 14 min). Washed PEG-AuNPs were redispersed in DI water and characterized by UV–Vis spectroscopy (**Figure 2.1**). The PEG-AuNPs were then modified with RGD (arginine−glycine−aspartic acid) and NLS (nuclear localization signal) peptides. The RGD peptide allows for receptor-mediated endocytosis of AuNPs by targeting αvβ6 integrins, which are overexpressed on the surface of human oral squamous carcinoma (HSC-3) cells.[29] The NLS peptide has a characteristic KKKRK (lysine−lysine−lysine−arginine−lysine) sequence, which binds importins in the cytoplasm of the cell, allowing for translocation of AuNPs to the nucleus.[26, 30-31] Peptide conjugation was utilized to design three different surface-modified AuNPs: RGD-AuNPs, RGD_1/NLS_1-AuNPs having equal amounts of RGD and NLS peptides, and RGD_1/NLS_{10}-AuNPs with RGD_1/NLS_{10}-AuNPs containing 10 times the NLS content of RGD_1/NLS_1-AuNPs. Previous work has shown that both RGD and NLS peptides indeed promote cellular uptake and localization of AuNPs at the nucleus, respectively.[39, 41-42] Briefly, 5.0 mM solutions of NLS (CGGPKKKKRKVGG) in DI water and / or RGD (CGPDGRDGRDGRDGR) in DI water were added to the PEG-AuNPs. A total of 4,000 peptides per PEG-AuNP were added in equal molar amounts of RGD and NLS for RGD_1/NLS_1-AuNPs, a 10:1 ratio of NLS/RGD for RGD_1/NLS_{10}-AuNPs, and only RGD was added for RGD-AuNPs. The peptide-nanoparticle solutions were allowed to shake overnight at room temperature and excess peptides removed by centrifugation (6000 rpm, 14 min). The desired concentration of 0.4 nM AuNPs was achieved by diluting stock AuNPs in cell culture medium.

2.2.3 Cell Culture

Human oral squamous carcinoma (HSC-3) cells, a malignant epithelial cell line expressing $\alpha_v\beta_6$ integrins on the cell membrane, were chosen as our cancer cell model.[2] The cells were cultured in Dulbecco's modification of Eagle's medium (DMEM, Mediatech) supplemented with 4.5 g/L glucose, L-glutamine, and sodium pyruvate, 10% v/v Fetal Bovine Serum (Mediatech), and 1% v/v antimycotic solution (Mediatech). Cell cultures were kept in a humidified 37°C incubator with an atmosphere of 5% CO_2.

2.2.4 Cell Viability Assay

To assess the viability of HSC-3 cells treated with targeted AuNPs, cells were grown in 96-well plates overnight. The growth medium was then removed and replaced with culture medium containing 0.4 nM AuNPs. After 24 hour incubation, the AuNP containing culture medium was replaced with an XTT solution (Biotium, Inc.) in DMEM. Cells were then incubated with the XTT solution for 4 h and absorbance measurements were taken at 450 nm and 690 nm on a Biotek Synergy H4 Multi-Mode Plate Reader. Cell viabilities are shown as the mean ± s.e.m. of three independent.

2.2.5 AuNP Uptake

The percentage of AuNPs taken up by HSC-3 cells was determined using a previously established spectroscopic technique.[1] Briefly, cells were grown in 96-well tissue culture plates overnight. The growth media was then replaced with medium containing 0.4 nM AuNPs. After 24 h incubation with AuNPs, the nanoparticle containing culture medium was moved to a new 96-well culture plate. The optical density

was measured at a wavelength of 538 nm (Biotek Synergy H4 Multimode Plate Reader). To determine AuNP uptake, the measured optical density of culture medium without AuNPs was subtracted from the optical density of the AuNP containing treatment medium. This AuNP optical density was then converted to a percentage of that initially added to the cell culture.

2.2.6 PERSIS Technique

The PERSIS system is composed of a home-made live cell incubator, a spectrometer (USB2000+, Ocean Optics), and a dark-field microscope. To obtain scattering spectra, cells were grown overnight on a glass-bottom culture dish (MatTek) in DMEM. The growth medium was then removed and the cells treated with solutions of 0.4 nM AuNPs in DMEM and immediately moved to the PERSIS live-cell incubator located on the microscope stage. The incubator maintained the cells at 37°C in a humidified atmosphere containing 5% CO_2. The PERSIS system angled a beam of white light onto the sample such that incident light passed through the sample and only scattered light was collected into the 40X microscope objective. The collection area was controlled by a 0.6 mm pinhole and the magnification of the objective, with an absolute collection area of roughly 3 μm x 3 μm (~10 μm^2 collection area), allowing for single cell resolution. A CCD camera was used to capture the true-color Rayleigh scattering images from the cells and spectral signals were coupled into an optical fiber and recorded.

2.2.7 Spectral Analysis

Scattering spectra were collected and averaged from 10 different cells and all experiments were performed in triplicate. Reference spectra were taken immediately

upon addition of AuNP to cells and subtracted from subsequent time points to remove any scattering from cells or the AuNP/culture medium background. Spectra were then deconvoluted into three Gaussians using OriginPro 9.0 software (Origin Lab, Corp.). The first Gaussian was fixed at 538 nm to correspond to the plasmon peak of single AuNPs (**Figure 2.1**). The peaks due to small and larger AuNP clusters were centered between 636 – 646 nm and 740 – 750 nm, respectively, and the best fit integrated to give intensities of the Rayleigh scattered bands. Scattering intensities were fit to a sigmoidal growth curve using a logistic response function with OriginPro 9.0 software. Initial and final scattering values were used to generate the scattering half-times, defined as the time required to reach the median of the fit between these values. The power of the logistic fitting function was assumed to be non-negative and the curve fit was optimized using the Levenberg Marquardt algorithm.

2.2.8 Statistical Analysis

Results are expressed as the mean ± s.e.m. of three independent experiments. Changes in scattering intensity were compared using a linear regression analysis calculator and the changes were not considered statistically significant ($p = 0.1388$). Statistical significance of AuNP uptake was calculated using unpaired *t*-tests (GraphPad Software, Inc.), and the difference in uptake between the AuNPs studied was not found to be statistically significant. The viability of cells treated with targeted AuNPs were also compared to untreated controls using unpaired *t*-tests (GraphPad Software, Inc.), and differences between the AuNPs studied were not found to be statistically significant.

2.3 Results and Discussion

2.3.1 PERSIS Design and Technique

Since the endocytosis of AuNPs results in specific subcellular localization, we can observe the plasmonic coupling of single particles as they are internalized and come in proximity with other AuNPs.[43-44] As represented by **Figure 2.2A**, the degree of AuNP localization within cells can vary. At the early stages of cellular uptake, the nanoparticles bind to receptors on the cell surface and are internalized into the cytoplasm to form small clusters of particles.[45] This results in a redshift in the surface plasmon band from the single nanoparticle wavelength (538 nm) to longer wavelengths (641 nm), due to coupling of the plasmonic fields between AuNPs as they localize and aggregate.[45-46] Subsequently, the AuNPs begin to form larger clusters as they accumulate in the endosomes or lysosomes and localize at the perinuclear region,[44-45] causing a further shift in the plasmon band to even longer wavelengths (745 nm).[47] By monitoring the coupling of the plasmon bands, observed as a redshift in the LSPR, the dynamics of nanoparticle uptake and localization in single living cells can be followed in real time with our single-cell plasmon-enhanced Rayleigh scattering imaging spectroscopy (PERSIS) technique. Additionally, the Rayleigh scattering spectra from cells without AuNP treatment do not show any significant changes over time (**Figure 2.3**), indicating that the observed changes are due to AuNP uptake and localization. Shown in **Figure 2.2**, our PERSIS system is composed of a homemade live cell incubator, a spectrometer to collect Rayleigh scattering spectra, and a dark-field microscope with an attached CCD camera to record the Rayleigh scattering images. This allows for the real-time monitoring of AuNP

uptake and localization in living cells, by analyzing the scattering intensity in dark-field images and the plasmon band redshift of the Rayleigh scattering spectra over time.

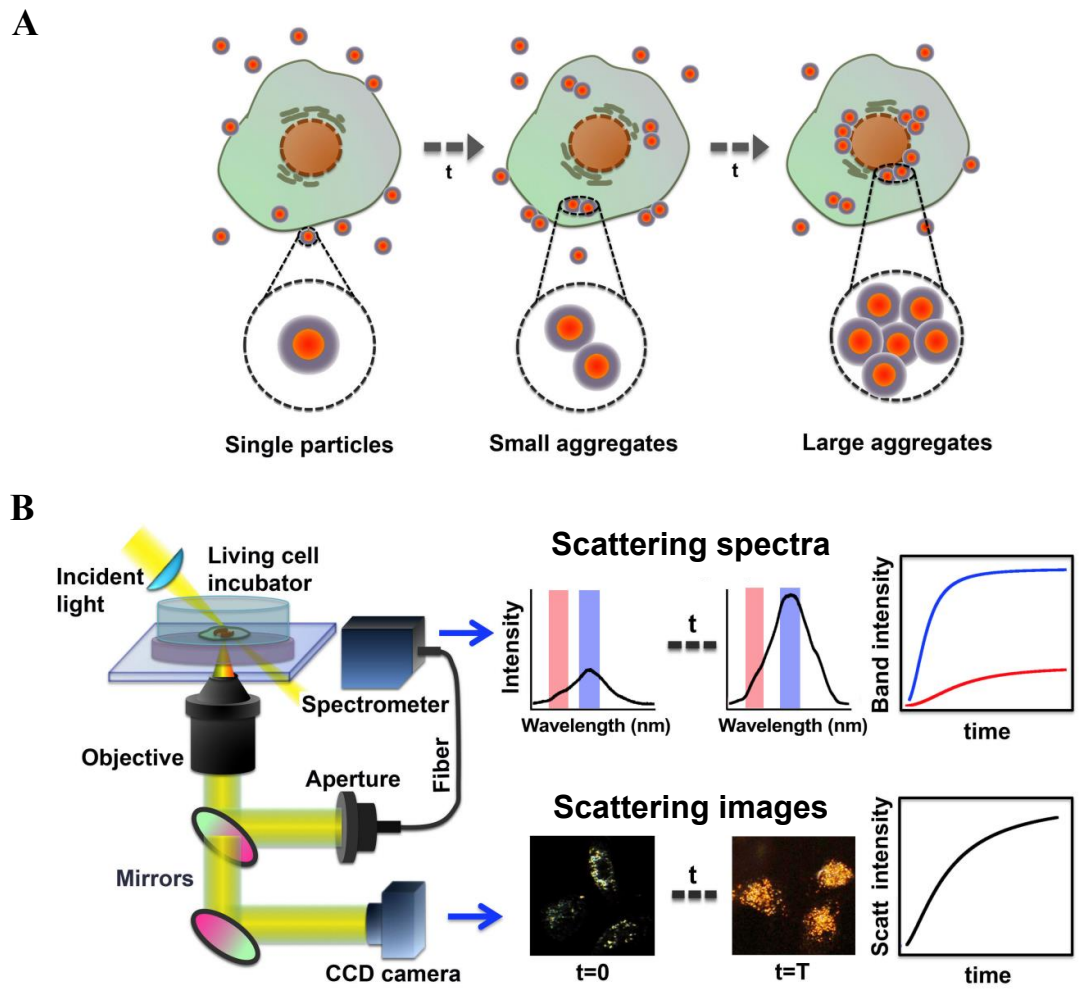

Figure 2.2 Schematic of nanoparticle localization by the PERSIS system. (A) Schematic representation of gold nanoparticle localization within cells during the process of cellular uptake; (B) Diagram of the experimental setup and the measurement of nanoparticle localization dynamics by PERSIS.

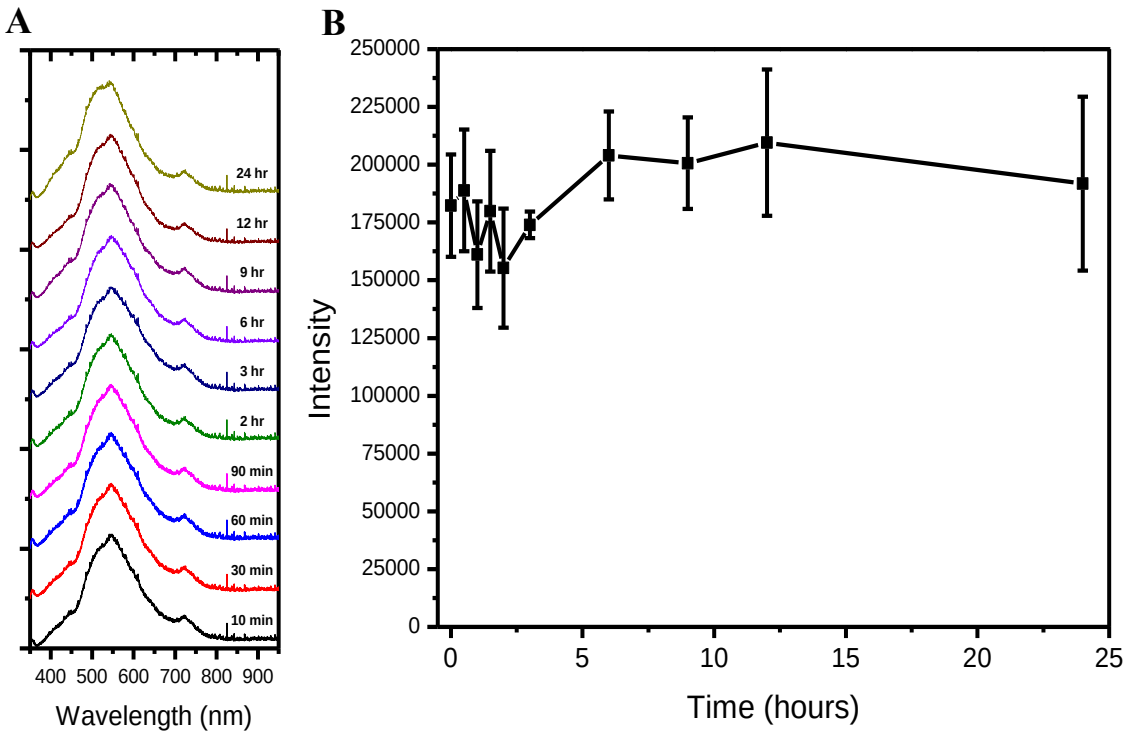

Figure 2.3 (A) Rayleigh scattering spectra of HSC-3 cells without AuNP treatment show no change with time. (B) Scattering intensity of untreated cells does not change significantly with time ($p = 0.139$).

2.3.2 Localization kinetics using Plasmonically-Enhanced Rayleigh Scattering

To ensure that changes in the observed scattering intensity were due to AuNP uptake (and not influenced by cell death), a treatment concentration of 0.4 nM AuNP in culture media was chosen for these studies. After 24 h, the viability of treated cells was measured using an XTT cell viability assay, and no significant cell death was observed from the three AuNP designs studied (**Figure 2.4**). Due to the αβ integrin targeting ability of RGD, all three AuNP samples studied also demonstrated similar levels of overall uptake (~30%, **Figure 2.5**). However, the intracellular localization of the different

AuNPs varied based on the AuNP surface modification. As suggested by the live-cell Rayleigh-scattering dark field images in **Figure 2.6**, the AuNPs containing NLS peptide (**Figure 2.6**, middle and bottom) show higher AuNP localization at the nucleus compared to AuNPs without NLS (**Figure 2.6**, top). Additionally, an increase in NLS peptide content (RGD_1/NLS_{10}-AuNPs) results in a more rapid localization rate of AuNPs at the nucleus (**Figure 2.6**, bottom).

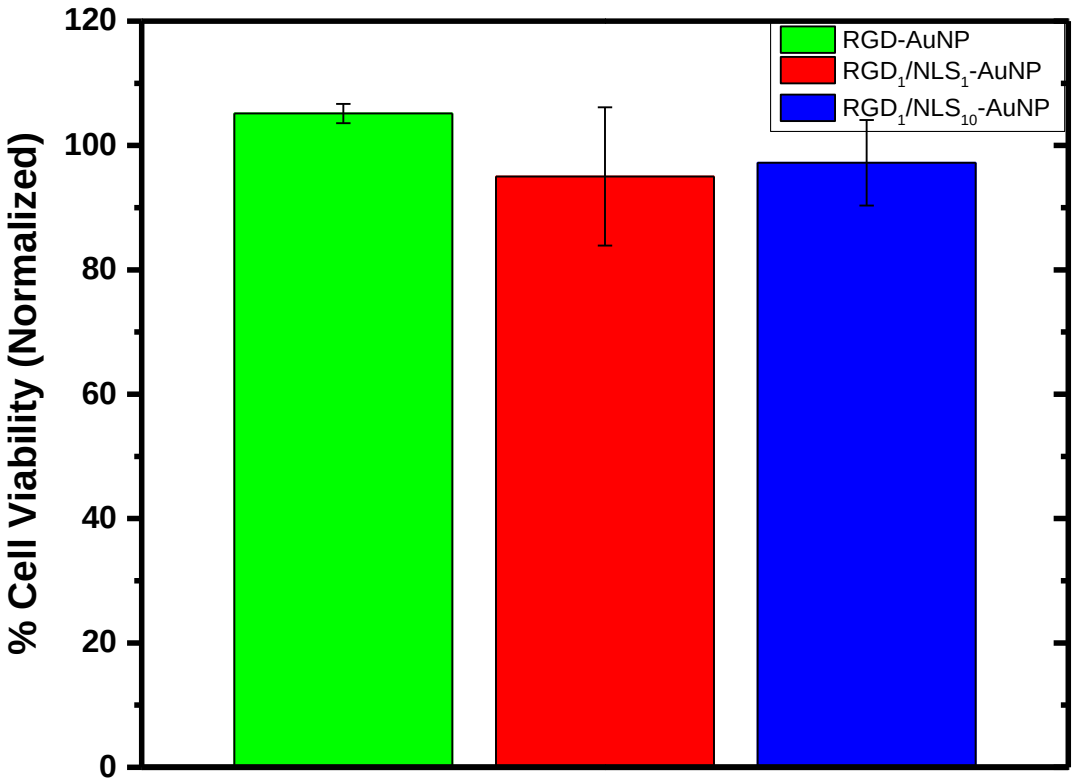

Figure 2.4 Viability of HSC-3 cells after 24 h of incubation with targeted AuNPs. No statistically significant cell death was observed from treatment with the three AuNP designs.

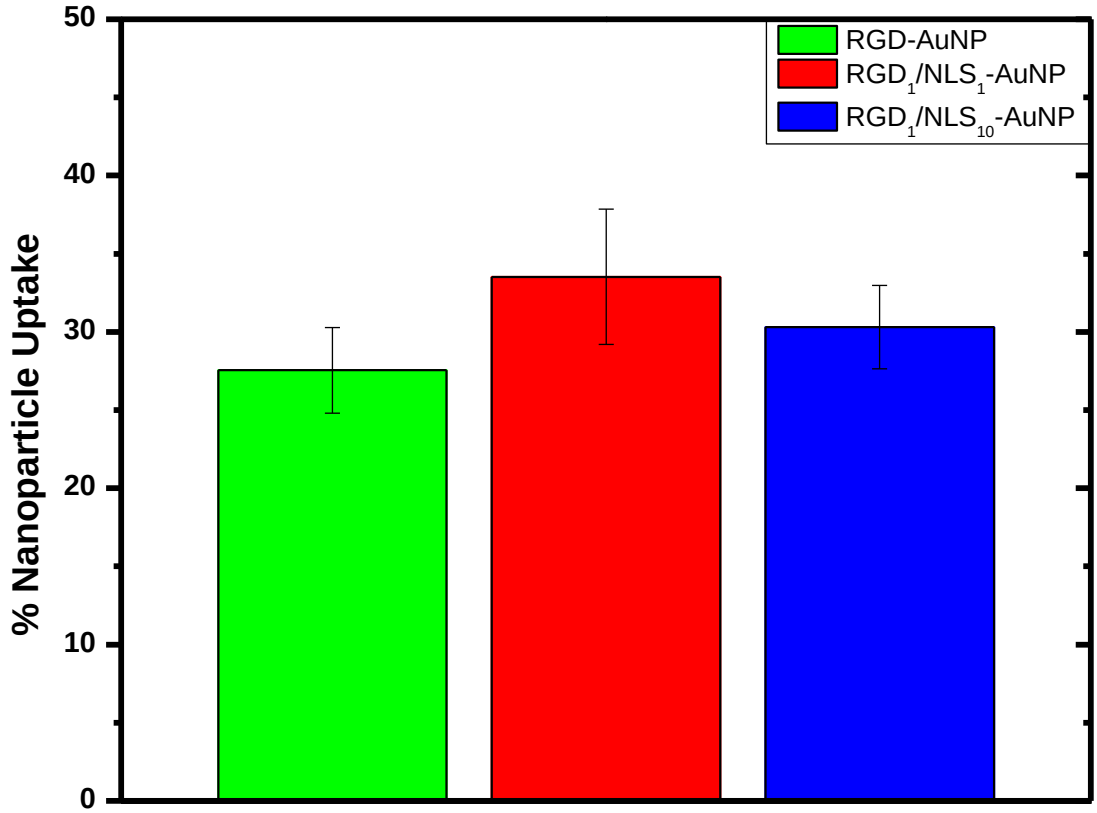

Figure 2.5 Cellular uptake of targeted AuNPs by HSC cells after 24 hours, shown as percentage of AuNPs taken up ± s.e.m. No statistically significant difference in uptake was observed for the three AuNP designs.

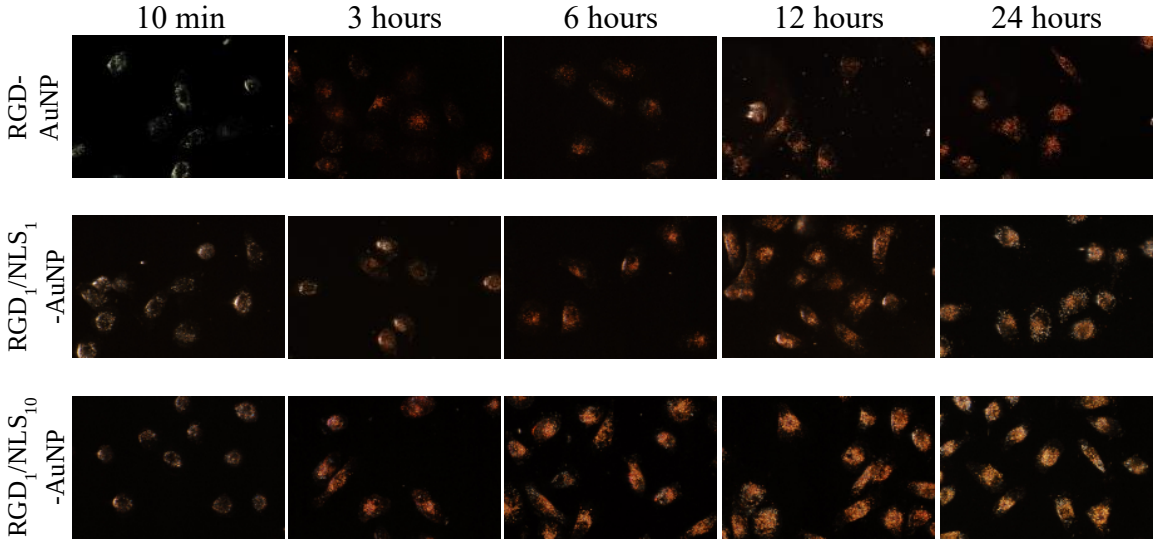

Figure 2.6 Real-time Rayleigh scattering dark-field images of cellular uptake of gold nanoparticles with different surface modifications: (top) RGD-AuNPs, (middle) RGD_1/NLS_1-AuNPs, (bottom) RGD_1/NLS_{10}-AuNPs. Scale bar: 10 μm.

From these Rayleigh scattering dark-field images, our PERSIS technique allows us to obtain Rayleigh scattering spectra of AuNPs in living cells. Accordingly, spectra were collected for the various AuNPs tested over a 24 h period as shown in **Figure 2.7**. The entire spectrum obtained at each time point was integrated to give the total scattering intensity for each different surface modified AuNP, and is shown in **Figure 2.8**. From these integrated scattering intensities, a scattering half-time (see *2.2.7 Spectral Analysis*) for each different surface-modified AuNP to estimate the rate at which the AuNPs localize within cells. RGD-AuNPs were found to have a scattering half-time of 11.4 h, while RGD_1/NLS_1-AuNPs exhibited a faster scattering half-time of 6.7 h. RGD_1/NLS_{10}-AuNPs had the fastest scattering half-time of just 2.9 h. In addition to the faster half-time, indicating more rapid AuNP localization within cells, the RGD_1/NLS_{10}-AuNPs exhibit a significantly higher overall scattering intensity after 24 h, compared to that of RGD-

AuNPs and RGD_1/NLS_1-AuNPs. This indicates that higher concentrations of NLS on the AuNP surface leads to an increased concentration of localized AuNPs at the perinuclear region, as evidenced by their more rapid increase in scattering, greater scattering intensity, and greater interparticle coupling of the plasmonic fields (i.e., greater intensity of the red-shifted plasmon peaks).

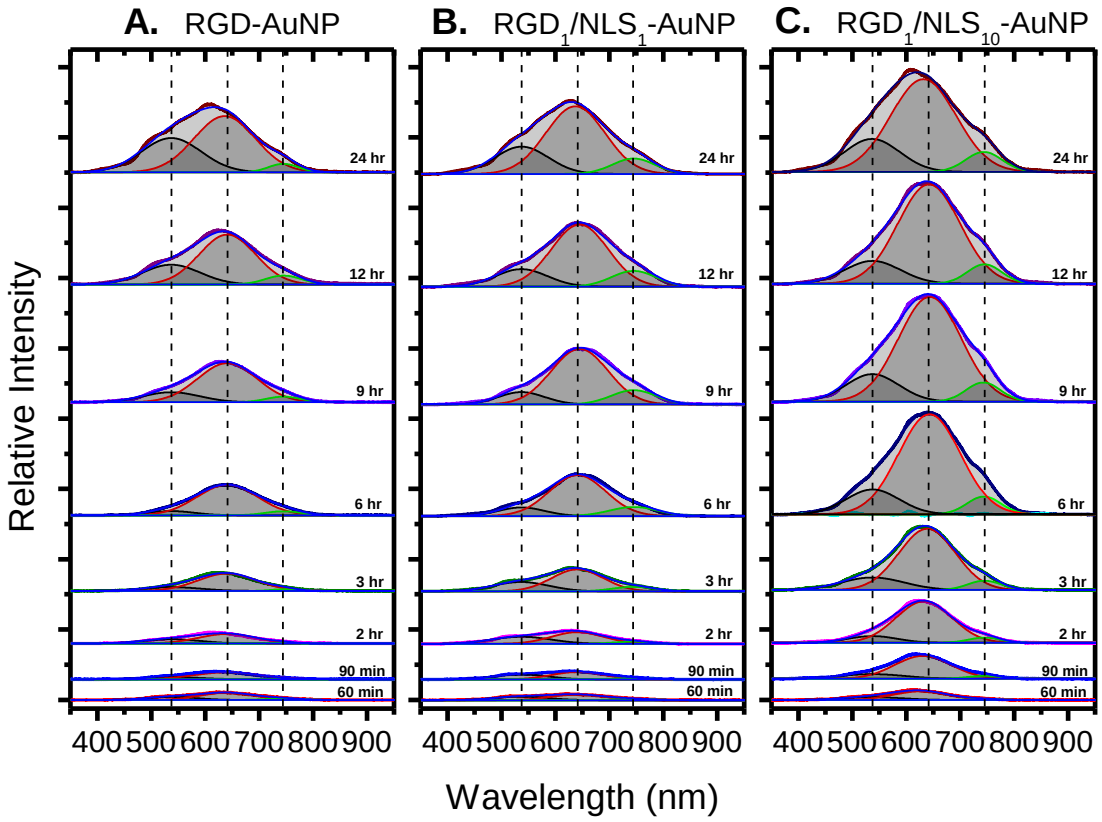

Figure 2.7 Real-time Rayleigh scattering spectra of AuNP uptake and localization within living cells for (A) RGD-AuNPs, (B) RGD_1/NLS_1-AuNPs, and (C) RGD_1/NLS_{10}-AuNPs. The deconvoluted peaks show the plasmonic scattering bands of single nanoparticles (538 nm), small AuNP clusters (641 nm), and large AuNP clusters (745 nm) and the center of the Gaussian fits are denoted by dashed lines.

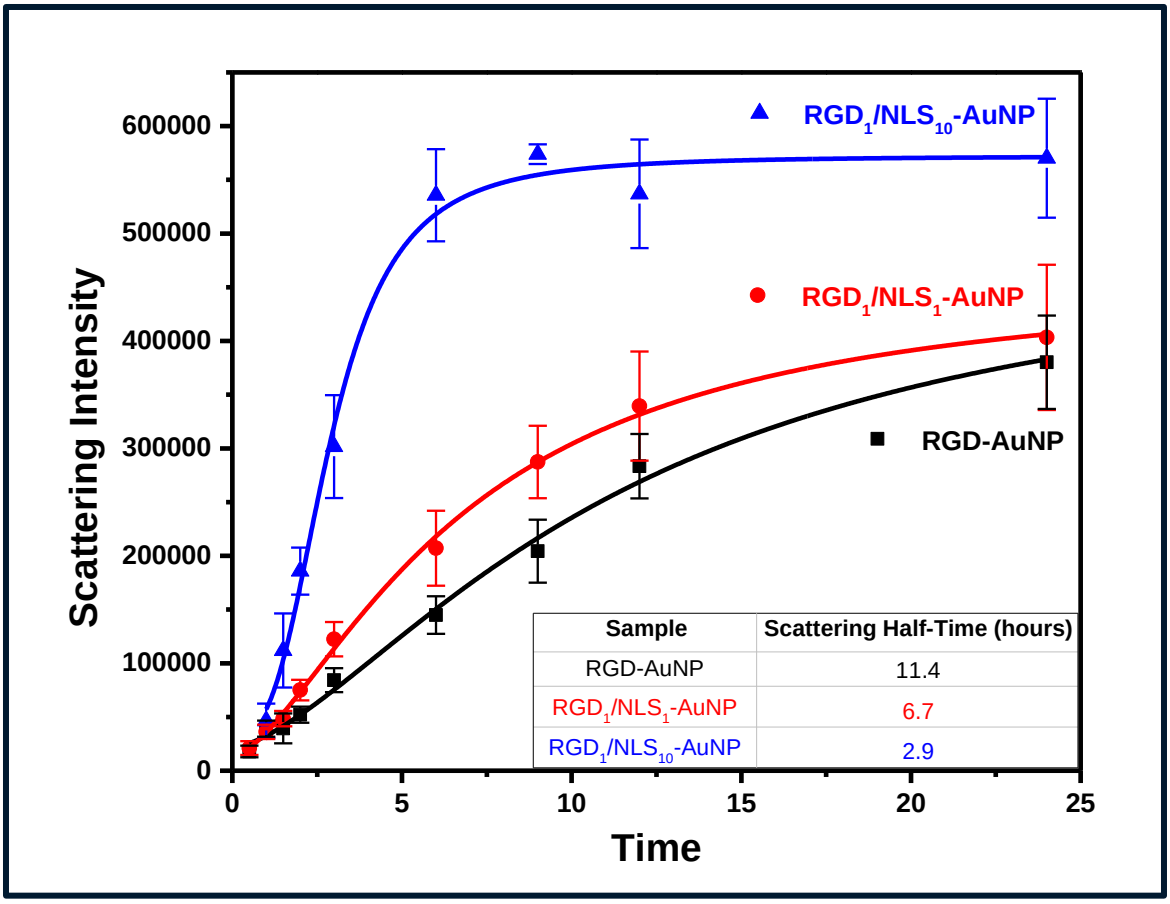

Figure 2.8 Dependence of the rate of increase of the scattered light intensity on the type of nanoparticle surface capping material, shown as the mean ± s.e.m. of three independent experiments. This figure shows that the higher the concentration of NLS (the nuclear localization sequence), the higher the observed rate of the scattered light intensity increases. The calculated scattering half-times are given above for RGD-AuNPs (black, R^2 = 0.993), RGD_1/NLS_1-AuNPs (red, R^2 = 0.997), and RGD_1/NLS_{10}-AuNPs (blue, R^2 = 0.989).

2.3.3 AuNP Localization Dynamics

The overall scattering spectrum shown in **Figure 2.8** not only describes the total amount of light scattered by the different AuNPs in cells over time, but it can also provide a detailed dynamic profile of AuNP aggregation and localization. This subcellular localization results in the formation of AuNP clusters with smaller

interparticle separations, leading to stronger coupling of their plasmonic fields and therefore, large red-shifted plasmon peaks. Thus, the total scattering spectrum obtained was fit to multiple Gaussians, allowing its deconvolution into three components: (1) AuNP monomers indicated by the plasmon band at 538 nm, (2) small AuNP clusters (with higher local concentrations of AuNPs, relative to AuNP monomers, which do not have interacting plasmonic fields), having a plasmon band at 641 nm, and (3) larger clusters of AuNPs (with the highest local AuNP concentration, indicating even greater coupling between the plasmonic fields of AuNPs in close proximity) give scattering at the longest wavelength of the 745 nm plasmon band (all are denoted with the dashed lines in **Figure 2.7**). Although the spectrum for each different AuNP contains these three components, the bands vary significantly based on the AuNP surface modification, indicating varying degrees of localization (i.e., different local concentrations of AuNPs within cells). In order to compare these bands for the different surface modified AuNPs and obtain detailed information on their degree of localization, the small (641 nm) and large (745 nm) AuNP cluster bands were integrated to give their total scattering intensities, as shown in **Figure 2.9A** and **2.9B**, respectively. From these integrated scattering intensities, we again calculated a scattering half-time for each different surface modified AuNP tested, to give a measure of how quickly the different AuNPs with different surface biochemical capping become localized.

During the formation of smaller AuNP clusters (**Figure 2.9A**), RGD-AuNPs and RGD_1/NLS_1-AuNPs showed similar scattering intensities after 24 h. However, RGD_1/NLS_1-AuNPs had a shorter small cluster half-time of 5.4 h, compared to 6.4 h for the AuNPs without the NLS peptide. The RGD_1/NLS_{10}-AuNPs were found to have the

shortest small cluster half-time of 2.7 h, while showing a scattering intensity almost twice as large as that of the small cluster. This suggests that the increased amount of NLS peptides enhanced the rate of formation of small AuNP clusters at the perinuclear region.

During the formation of the larger AuNP clusters (**Figure 2.9B**), NLS-modified particles (RGD1/NLS_{10}-AuNPs and RGD_1/NLS_1-AuNPs) showed similar scattering intensities after 24 h. However, the AuNPs containing more NLS peptides (RGD_1/NLS_{10}-AuNPs) exhibited a shorter large cluster half-time of 3.3 h, compared to the 7.4 h for AuNPs containing less NLS peptide. Again, we attribute the shorter half-time to the increase in NLS peptides on the AuNP surface, enhancing the rate of nanoparticle localization at the nucleus or the nuclear membrane. The RGD-AuNPs were found to have the longest large cluster half-time of 8.1 h, while demonstrating a large aggregate scattering intensity almost five times smaller than the AuNPs bound to the NLS peptides. These results suggest that nuclear-targeted AuNPs tend to form more dense clusters having larger scattering cross sections, as they are bound to the small perinuclear region, than those not targeted to subcellular regions.

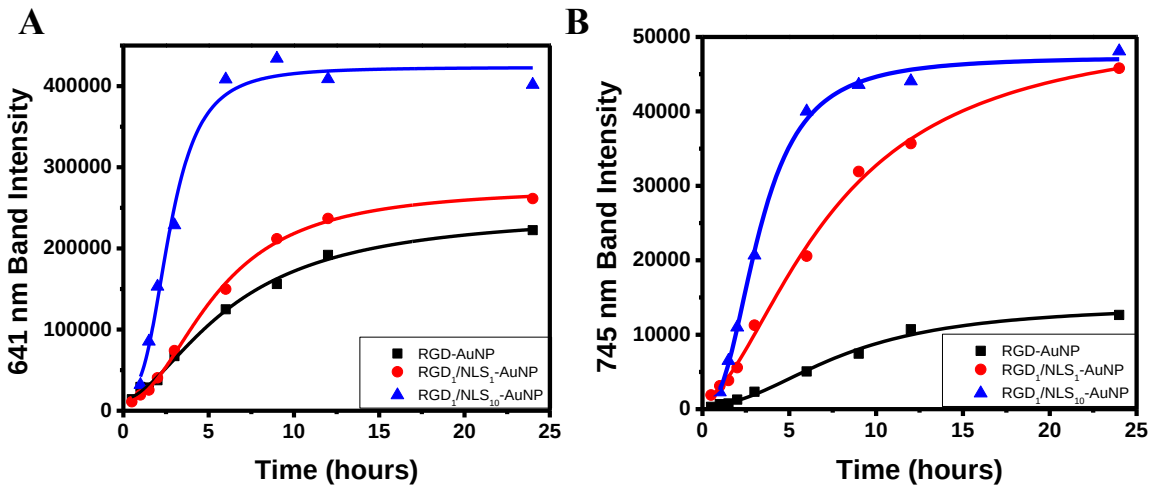

Figure 2.9 Dynamics of scattered light intensity for bands of (A) small AuNP clusters at 641 nm and (B) large AuNP clusters at 745 nm. Localization half-times of small AuNP clusters were calculated to be 6.4 h for RGD-AuNPs (black, R^2 = 0.995), 5.4 h for RGD_1/NLS_1-AuNPs (red, R^2 = 0.997), and 2.7 h for RGD_1/NLS_{10}-AuNPs (blue, R^2 = 0.979). Localization half-times of large AuNP clusters were calculated to be 8.1 h for RGD-AuNPs black, R^2 = 0.989), 7.4 h for RGD_1/NLS_1-AuNPs (red, R^2 = 0.996), and 3.3 h for RGD_1/NLS_{10}-AuNPs (blue, R^2 = 0.996).

2.4 Conclusion

In conclusion, we have developed an instrument and demonstrated its use of PERSIS to monitor the dynamics of AuNP uptake, localization and aggregation of plasmonic nanoparticles with different capping materials. The AuNP surface modification greatly affected their localization and led to decreased interparticle separation between AuNPs, causing great enhancement of the scattered light and a red-shift in their observed plasmonic spectral peak to longer wavelengths. Nuclear-targeted AuNPs, directed to the smaller volume of the nucleus, were found to localize more rapidly than those not targeted to the nucleus of the cancer cells. This also leads to the formation of more dense clusters having more hot spots between the nanoparticles. Hot

spots are known to have much more enhanced plasmonic fields leading to stronger scattering and thus better imaging of the region targeted by the nanoparticles. Increasing the concentration of the NLS peptides on the AuNP surface increased the localization rate and the concentration of the plasmonic nanoparticles at the NLS target in the cell. It is clear that this technique is not limited to studying the nuclear region. Various peptides are known to target different cellular components and the addition of a terminal thiol group would make it possible to conjugate the AuNPs for enhanced imaging at the selected location in the cell.

2.5 References

(1) Aioub, M.; Kang, B.; Mackey, M. A.; El-Sayed, M. A. Biological Targeting of Plasmonic Nanoparticles Improves Cellular Imaging via the Enhanced Scattering in the Aggregates Formed. *J. Phys. Chem. Lett.* **2014,** *5*, 2555-2561.

(2) Jain, P. K.; Huang, X. H.; El-Sayed, I. H.; El-Sayed, M. A. Noble Metals on the Nanoscale: Optical and Photothermal Properties and Some Applications in Imaging, Sensing, Biology, and Medicine. *Acc. Chem. Res.* **2008,** *41*, 1578-1586.

(3) Dreaden, E. C.; Alkilany, A. M.; Huang, X. H.; Murphy, C. J.; El-Sayed, M. A. The Golden Age: Gold Nanoparticles for Biomedicine. *Chem. Soc. Rev.* **2012,** *41*, 2740-2779.

(4) Burda, C.; Chen, X. B.; Narayanan, R.; El-Sayed, M. A. Chemistry and Properties of Nanocrystals of Different Shapes. *Chem. Rev.* **2005,** *105*, 1025-1102.

(5) Kelly, K. L.; Coronado, E.; Zhao, L. L.; Schatz, G. C. The Optical Properties of Metal Nanoparticles: The Influence of Size, Shape, and Dielectric Environment. *J. Phys. Chem. B* **2003,** *107*, 668-677.

(6) Link, S.; El-Sayed, M. A. Spectral Properties and Relaxation Dynamics of Surface Plasmon Electronic Oscillations in Gold and Silver Nanodots and Nanorods. *J. Phys. Chem. B* **1999,** *103*, 8410-8426.

(7) Reinhard, B. M.; Sheikholeslami, S.; Mastroianni, A.; Alivisatos, A. P.; Liphardt, J. Use of Plasmon Coupling to Reveal the Dynamics of DNA Bending and Cleavage by Single EcoRV Restriction Enzymes. *Proc. Natl. Acad. Sci. U.S.A.* **2007,** *104*, 2667-2672.

(8) Rong, G. X.; Wang, H. Y.; Skewis, L. R.; Reinhard, B. M. Resolving Sub-Diffraction Limit Encounters in Nanoparticle Tracking Using Live Cell Plasmon Coupling Microscopy. *Nano Lett.* **2008,** *8*, 3386-3393.

(9) Aaron, J.; Travis, K.; Harrison, N.; Sokolov, K. Dynamic Imaging of Molecular Assemblies in Live Cells Based on Nanoparticle Plasmon Resonance Coupling. *Nano Lett.* **2009,** *9*, 3612-3618.

(10) El-Sayed, M. A. Some Interesting Properties of Metals Confined in Time and Nanometer Space of Different Shapes. *Acc. Chem. Res.* **2001,** *34*, 257-264.

(11) Schatz, G. C. Theoretical-Studies of Surface Enhanced Raman-Scattering. *Acc. Chem. Res.* **1984,** *17*, 370-376.

(12) Kamat, P. V. Meeting the Clean Energy Demand: Nanostructure Architectures for Solar Energy Conversion. *J. Phys. Chem. C* **2007,** *111*, 2834-2860.

(13) Standridge, S. D.; Schatz, G. C.; Hupp, J. T. Distance Dependence of Plasmon-Enhanced Photocurrent in Dye-Sensitized Solar Cells. *J. Am. Chem. Soc.* **2009,** *131*, 8407-8409.

(14) Knight, M. W.; Wang, Y. M.; Urban, A. S.; Sobhani, A.; Zheng, B. Y.; Nordander, P.; Halas, N. J. Embedding Plasmonic Nanostructure Diodes Enhances Hot Electron Emission. *Nano Lett.* **2013,** *13*, 1687-1692.

(15) Jain, P. K.; El-Sayed, M. A. Surface Plasmon Coupling and Its Universal Size Scaling in Metal Nanostructures of Complex Geometry: Elongated Particle Pairs and Nanosphere Trimers. *J. Phys. Chem. C* **2008,** *112*, 4954-4960.

(16) Jain, P. K.; Huang, W. Y.; El-Sayed, M. A. On the Universal Scaling Behavior of the Distance Decay of Plasmon Coupling in Metal Nanoparticle Pairs: A Plasmon Ruler Equation. *Nano Lett.* **2007,** *7*, 2080-2088.

(17) Lin, S.; Li, M.; Dujardin, E.; Girard, C.; Mann, S. One-Dimensional Plasmon Coupling by Facile Self-Assembly of Gold Nanoparticles into Branched Chain Networks. *Adv. Mater.* **2005,** *17*, 2553-2559.

(18) Gunnarsson, L.; Rindzevicius, T.; Prikulis, J.; Kasemo, B.; Kall, M.; Zou, S. L.; Schatz, G. C. Confined Plasmons in Nanofabricated Single Silver Particle Pairs: Experimental Observations of Strong Interparticle Interactions. *J. Phys. Chem. B* **2005,** *109*, 1079-1087.

(19) Slaughter, L. S.; Wu, Y. P.; Willingham, B. A.; Nordlander, P.; Link, S. Effects of Symmetry Breaking and Conductive Contact on the Plasmon Coupling in Gold Nanorod Dimers. *ACS Nano* **2010,** *4*, 4657-4666.

(20) Sonnichsen, C.; Reinhard, B. M.; Liphardt, J.; Alivisatos, A. P. A Molecular Ruler Based on Plasmon Coupling of Single Gold and Silver Nanoparticles. *Nat. Biotechnol.* **2005,** *23*, 741-745.

(21) Reinhard, B. M.; Siu, M.; Agarwal, H.; Alivisatos, A. P.; Liphardt, J. Calibration of Dynamic Molecular Ruler Based on Plasmon Coupling between Gold Nanoparticles. *Nano Lett.* **2005,** *5*, 2246-2252.

(22) Loo, C.; Lowery, A.; Halas, N.; West, J.; Drezek, R. Immunotargeted Nanoshells for Integrated Cancer Imaging and Therapy. *Nano Lett.* **2005,** *5*, 709-711.

(23) Kang, B.; Afifi, M. M.; Austin, L. A.; El-Sayed, M. A. Exploiting the Nanoparticle Plasmon Effect: Observing Drug Delivery Dynamics in Single Cells via Raman/Fluorescence Imaging Spectroscopy. *ACS Nano* **2013,** *7*, 7420-7427.

(24) Hirsch, L. R.; Stafford, R. J.; Bankson, J. A.; Sershen, S. R.; Rivera, B.; Price, R. E.; Hazle, J. D.; Halas, N. J.; West, J. L. Nanoshell-Mediated Near-Infrared Thermal Therapy of Tumors under Magnetic Resonance Guidance. *Proc. Natl. Acad. Sci. U.S.A.* **2003,** *100*, 13549-13554.

(25) Castel, S.; Pagan, R.; Mitjans, F.; Piulats, J.; Goodman, S.; Jonczyk, A.; Huber, F.; Vilaro, S.; Reina, M. RGD Peptides and Monoclonal Antibodies, Antagonists of αv-Integrin, Enter the Cells by Independent Endocytic Pathways. *Lab. Invest.* **2001,** *81*, 1615-1626.

(26) Tkachenko, A. G.; Xie, H.; Liu, Y. L.; Coleman, D.; Ryan, J.; Glomm, W. R.; Shipton, M. K.; Franzen, S.; Feldheim, D. L. Cellular Trajectories of Peptide-Modified Gold Particle Complexes: Comparison of Nuclear Localization Signals and Peptide Transduction Domains. *Bioconjugate Chem.* **2004,** *15*, 482-490.

(27) Gao, H.; Shi, W.; Freund, L. B. Mechanics of Receptor-Mediated Endocytosis. *Proc. Natl. Acad. Sci. U.S.A.* **2005,** *102*, 9469-9474.

(28) Zitzmann, S.; Ehemann, V.; Schwab, M. Arginine–Glycine–Aspartic Acid (RGD)-Peptide Binds to Both Tumor and Tumor-Endothelial Cells in Vivo. *Cancer Res.* **2002,** *62*, 5139-5143.

(29) Xue, H.; Atakilit, A.; Zhu, W. M.; Li, X. W.; Ramos, D. M.; Pytela, R. Role of the αvβ6 Integrin in Human Oral Squamous Cell Carcinoma Growth in Vivo and in Vitro. *Biochem. Biophys. Res. Commun.* **2001,** *288*, 610-618.

(30) Tkachenko, A. G.; Xie, H.; Coleman, D.; Glomm, W.; Ryan, J.; Anderson, M. F.; Franzen, S.; Feldheim, D. L. Multifunctional Gold Nanoparticle–Peptide Complexes for Nuclear Targeting. *J. Am. Chem. Soc.* **2003,** *125*, 4700-4701.

(31) Escriou, V.; Carriere, M.; Scherman, D.; Wils, P. NLS Bioconjugates for Targeting Therapeutic Genes to the Nucleus. *Adv. Drug Delivery Rev.* **2003,** *55*, 295-306.

(32) Feldherr, C. M.; Akin, D. Regulation of Nuclear Transport in Proliferating and Quiescent Cells. *Exp. Cell. Res.* **1993,** *205*, 179-186.

(33) Nakielny, S.; Dreyfuss, G. Transport of Proteins and RNAs in and out of the Nucleus. *Cell* **1999,** *99*, 677-690.

(34) Jiang, W.; Kim, B. Y. S.; Rutka, J. T.; Chan, W. C. W. Nanoparticle-Mediated Cellular Response Is Size-Dependent. *Nat. Nanotechnol.* **2008,** *3*, 145-150.

(35) Chithrani, B. D.; Ghazani, A. A.; Chan, W. C. W. Determining the Size and Shape Dependence of Gold Nanoparticle Uptake into Mammalian Cells. *Nano Lett.* **2006,** *6*, 662-668.

(36) Austin, L. A.; Kang, B.; El-Sayed, M. A. A New Nanotechnology Technique for Determining Drug Efficacy Using Targeted Plasmonically Enhanced Single Cell Imaging Spectroscopy. *J. Am. Chem. Soc.* **2013,** *135*, 4688-4691.

(37) El-Sayed, I. H.; Huang, X.; El-Sayed, M. A. Surface Plasmon Resonance Scattering and Absorption of Anti-EGFR Antibody Conjugated Gold Nanoparticles in Cancer Diagnostics: Applications in Oral Cancer. *Nano Lett.* **2005,** *5*, 829-834.

(38) Huang, X.; El-Sayed, I. H.; El-Sayed, M. A. Applications of Gold Nanorods for Cancer Imaging and Photothermal Therapy. *Methods Mol. Biol.* **2010,** *624*, 343-357.

(39) Kang, B.; Mackey, M. A.; El-Sayed, M. A. Nuclear Targeting of Gold Nanoparticles in Cancer Cells Induces DNA Damage, Causing Cytokinesis Arrest and Apoptosis. *J. Am. Chem. Soc.* **2010,** *132*, 1517-1519.

(40) Frens, G. Controlled Nucleation for Regulation of Particle-Size in Monodisperse Gold Suspensions. *Nat., Phys. Sci.* **1973,** *241*, 20-22.

(41) Austin, L. A.; Kang, B.; Yen, C. W.; El-Sayed, M. A. Plasmonic Imaging of Human Oral Cancer Cell Communities During Programmed Cell Death by Nuclear-Targeting Silver Nanoparticles. *J. Am. Chem. Soc.* **2011,** *133*, 17594-17597.

(42) Mackey, M. A.; Saira, F.; Mahmoud, M. A.; El-Sayed, M. A. Inducing Cancer Cell Death by Targeting Its Nucleus: Solid Gold Nanospheres Versus Hollow Gold Nanocages. *Bioconjugate Chem.* **2013,** *24*, 897-906.

(43) Kang, B.; Austin, L. A.; El-Sayed, M. A. Real-Time Molecular Imaging Throughout the Entire Cell Cycle by Targeted Plasmonic-Enhanced Rayleigh/Raman Spectroscopy. *Nano Lett.* **2012,** *12*, 5369-5375.

(44) Chithrani, B. D.; Chan, W. C. W. Elucidating the Mechanism of Cellular Uptake and Removal of Protein-Coated Gold Nanoparticles of Different Sizes and Shapes. *Nano Lett.* **2007,** *7*, 1542-1550.

(45) Nativo, P.; Prior, I. A.; Brust, M. Uptake and Intracellular Fate of Surface-Modified Gold Nanoparticles. *ACS Nano* **2008,** *2*, 1639-1644.

(46) Storhoff, J. J.; Lazarides, A. A.; Mucic, R. C.; Mirkin, C. A.; Letsinger, R. L.; Schatz, G. C. What Controls the Optical Properties of DNA-Linked Gold Nanoparticle Assemblies. *J. Am. Chem. Soc.* **2000,** *122*, 4640-4650.

(47) Su, K. H.; Wei, Q. H.; Zhang, X.; Mock, J. J.; Smith, D. R.; Schultz, S. Interparticle Coupling Effects on Plasmon Resonances of Nanogold Particles. *Nano Lett.* **2003,** *3*, 1087-1090.

CHAPTER 3. DETERMINING DRUG EFFICACY USING PLASMONICALLY-ENHANCED IMAGING OF THE MORPHOLOGICAL CHANGES OF CELLS UPON DEATH [1]

(Adapted with permission from Aioub, M.; Austin, L. A.; El-Sayed, M. A. Determining Drug Efficacy Using Plasmonically Enhanced Imaging of the Morphological Changes of Cells Upon Death. *J. Phys. Chem. Lett.* **2014,** *5*, 3514-3518.

Recently, we utilized the optical properties of gold nanoparticles (AuNPs) for plasmonically enhanced Rayleigh scattering imaging spectroscopy (PERSIS), a new technique that enabled the direct observation of AuNP localization. In this study, we employ PERSIS by using AuNPs as light-scattering probes to compare the relative efficacy of three chemotherapeutic drugs on human oral squamous carcinoma cells. Although the drugs induced apoptotic cell death through differing mechanisms, morphological changes including cell membrane blebbing and shrinkage, accompanied by an increase in white light scattering, were visually evident. By utilizing the AuNPs to increase the cells' inherent Rayleigh scattering, we have obtained the time profile of cell death from the anticancer drugs using a single sample of cells in real time, using inexpensive equipment available in any lab. From this time profile, we calculated cell death enhancement factors to compare the relative efficacies of the different drugs using our technique, which corresponded to those calculated from the commonly used XTT cell viability assay. Although this technique does not impart molecular insights into cell death, the ability to quantitatively correlate cell death to morphological changes suggests

the potential use of this technique for the rapid screening of drug analogues to determine the most effective structure against a disease or cell line.

3.1 Introduction

Plasmonic nanoparticles have been heavily utilized in the biomedical field due to their small size and unique physical, optical, and chemical properties.[2-5] In particular, the plasmonically enhanced scattering of gold nanoparticles (AuNPs) has been used in cellular imaging applications to differentiate cancerous from noncancerous cells[6] and in surface-enhanced Raman spectroscopy to observe the molecular dynamics of apoptosis[7] and to detect biomarkers in complex physiological environments.[8] We recently developed a new technique, plasmonically enhanced Rayleigh scattering imaging spectroscopy (PERSIS), which enabled cellular imaging and the observation of AuNP localization. The AuNP localization caused a change in the intensity and the wavelength of light scattered by the nanoparticles as they came into close proximity.[9] Here, we utilize this technique, specifically the change in scattering intensity, to study the relative efficacy of three anticancer drugs (cisplatin, camptothecin, and 5-fluorouracil (5-FU)) in human oral squamous carcinoma (HSC-3) cells. This technique is validated against a commercially available XTT cell viability assay.

Normal progression through the cell cycle plays a critical role in the health and proliferation of living cells. Perturbations in this cycle can cause the loss of essential cellular functions or unwanted mutations, necessitating safeguards such as apoptosis, which results in the programmed death of cells that have mutated (i.e., become malignant) or lost vital functions.[10] Not surprisingly, many anticancer drugs attempt to

induce apoptosis in these malignancies, often by disrupting DNA synthesis or replication.[11-13] However, the precise mechanism of action differs between drugs, leading to fluctuations in efficacy based on the cells' current phase in their replication cycles. For example, camptothecin inhibits DNA topoisomerase I, making it most effective during the S-phase,[14] whereas cisplatin forms DNA cross-link adducts leading to increased cellular sensitivity in the G1-phase,[15] and 5-FU blocks DNA synthesis by inhibiting thymidylate synthase and incorporation into RNA, causing G1/S-phase arrest.[16] Despite the differing mechanisms of action for these drugs, the morphological characteristics of apoptotic cell death are retained, specifically cell shrinkage, membrane blebbing, and enhanced white light scattering due to the aggregation of cellular components.[13]

3.2 Methods

3.2.1 AuNP Synthesis

Citrate–capped AuNPs with an average diameter of 31 nm were synthesized by the sodium citrate mediated reduction of chloroauric acid.[1] Briefly, 98 mL of a 0.6 mM solution of aqueous chloroauric acid (Sigma-Aldrich) was heated, with stirring, in a 250 mL Erlenmeyer flask. When the solution boiled, a 2 mL aqueous solution of 180 mM trisodium citrate (Sigma-Aldrich) was immediately added. When the solution became a wine-red color, stirring and heating were discontinued, and the solution was allowed to cool to room temperature. TEM images (**Figure 3.1**) were taken with a JEOL 100CX-2 transmission electron microscope and the average particle diameter was found to be 31 ± 4 nm using ImageJ software. UV–Vis spectroscopy showed a surface plasmon resonance peak at 534 nm (**Figure 3.1**).

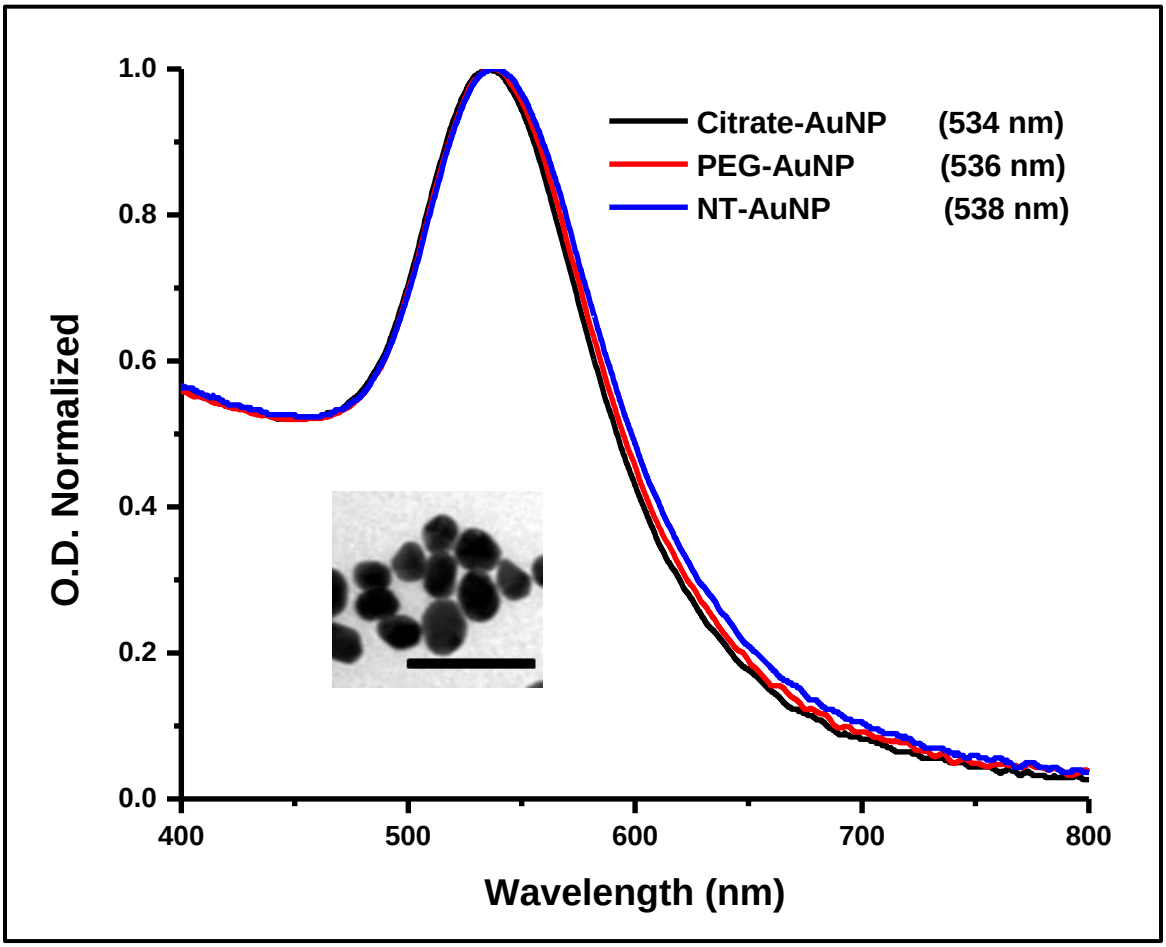

Figure 3.1 Characterization of nuclear-targeted AuNPs (NT-AuNPs). UV–Vis spectrum of AuNPs before (black) and after conjugation with mPEG-SH_{5000} (red), and RGD and NLS peptides (blue) in aqueous solution. There was a red shift in the plasmon peak indicating successful conjugation. The inset shows a TEM micrograph of 31 nm citrate-stabilized AuNPs (scale bar is 100 nm).

3.2.2 AuNP Functionalization

Before peptide functionalization, the citrate-stabilized AuNPs were coated with polyethylene glycol (PEG) to prevent nonspecific interactions in the physiological environment.[2] A 1.0 mM solution of mPEG-SH (MW 5000, Lysan Bio, Inc.) in deionized (DI) water was added for a ~30% surface coverage. The PEG-AuNP solution was left

shaking overnight at room temperature and unbound PEG was removed by centrifugation (6000 rpm, 14 min). PEG-AuNPs were redispersed in DI water and characterized via UV–Vis spectroscopy (**Figure 3.1**).

Nuclear-targeted AuNPs (NT-AuNPs) were then functionalized by adding RGD and nuclear localization sequence (NLS) peptides to the PEG-AuNPs following a previously established method.[3] Briefly, 5.0 mM solutions of NLS (CGGPKKKKRKVGG) in DI water and RGD (CGPDGRDGRDGRDGR) in DI water were added to the PEG-AuNPs. A total of 4,000 peptides per PEG-AuNP were added at a 10:1 molar ratio of NLS/RGD peptides. The NT-AuNP solution was shaken overnight at room temperature and excess peptides removed by centrifugation (6000 rpm, 14 min). The desired AuNP concentration was achieved by diluting stock NT-AuNPs in cell culture medium.

3.2.3 Cell Culture

Human oral squamous carcinoma (HSC-3) cells, a malignant epithelial cell line with $\alpha_v\beta_6$ integrins overexpressed on the cell membrane, were chosen as our cancer cell model.[4] The cells were cultured in Dulbecco's modification of Eagle's medium (DMEM, Mediatech) supplemented with 10% v/v fetal bovine serum (Mediatech), 1% v/v antimycotic solution (Mediatech), and 4.5 g/L glucose, L-glutamine, and sodium pyruvate. Cell cultures were kept in a 37°C incubator with a humidified atmosphere of 5% CO_2.

3.2.4 Cell Cycle Analysis

Cells were grown in culture medium for 24 h and then incubated with 0.1 nM or 0.2 nM solutions of NT-AuNPs in DMEM. After 24 h of incubation, cells were fixed with cold ethanol (-20°C, 95%) until analysis. For flow cytometric analysis, suspensions of fixed cells were centrifuged for 10 min at 2000 rpm and redispersed in PBS. Cells were then incubated with 200 μg/mL RNAse (Sigma-Aldrich) at 37°C for 30 min. Propidium iodide (100 μg/mL, Sigma-Aldrich) was used to stain DNA for 15 min at room temperature. A BD LSR II (BD Biosciences) flow cytometer was used for analysis with a 488 nm excitation laser and fluorescence intensity detected in the PE channel. The cell cycle data was analyzed using FlowJo software (Tree Star, Inc.).

3.2.5 Cell Viability Assays

To determine the cell viability, HSC-3 cells were grown in 96-well plates for 24 h and then pretreated with 0.1 nM NT-AuNPs in DMEM. The AuNP solutions were then replaced with 100 μM solutions in DMEM of cisplatin (Sigma-Aldrich), camptothecin (Sigma-Aldrich), or 5-fluorouracil (5-FU, Sigma-Aldrich). After the desired treatment times of 0, 12, 24, 48, and 72 h, the drug solutions were replaced with an XTT solution (Biotium, Inc.) in DMEM. Cell viabilities were measured after 4 h on a Biotek Synergy H4 Multi-Mode Plate Reader. Absorbance measurements were taken at 450 nm and 690 nm. To determine the time profile for each drug, the cell viabilities from 3 independent experiments were averaged and fit to an exponential function. The ET_{50} values were generated from the fits using OriginPro 9.0 software (Origin Lab, Corp.) and the quality of fit for the cisplatin, camptothecin, and 5-FU curves were $R^2 = 0.976$, $R^2 = 0.977$, and

R^2 = 0.981, respectively. The CDE factors are given as the ratios of the ET_{50} values of camptothecin or 5-FU, relative to cisplatin.

3.2.6 PERSIS Technique and Anti-Cancer Drug Treatment

The PERSIS system is composed of a home-made live cell incubator, a dark-field microscope, and a spectrometer (USB2000+, Ocean Optics). To obtain Rayleigh scattering spectra, cells were grown overnight on a glass-bottom culture dish (MatTek) in DMEM. The growth media was then removed and the cells pretreated for 24 h with a solution of 0.1 nM NT-AuNPs in DMEM. The AuNP solution was then replaced with 100 μM solutions of the anti-cancer drugs in DMEM and the samples immediately moved to the PERSIS live-cell incubator, located on the microscope stage. The incubator maintained the cells at 37°C in a humidified atmosphere of 5% CO_2. The PERSIS system was designed with an angled beam of white light that reached the sample such that incident light passed through undetected, and only scattered light was collected into the long-distance 40X microscope objective, which allowed for a ~10 μm^2 collection area resulting in single cell resolution. The spectral signals from the cells were coupled into an optical fiber and recorded, and a CCD camera was used to capture the Rayleigh scattering images.

3.2.7 Spectral Analysis

Scattering spectra were collected and averaged from 10 individual cells at each time point, and all experiments were performed in triplicate. Reference scattering spectra were taken from a dark area without cells, and subtracted from the Rayleigh scattering spectra of treated cells to remove any scattering from the drug/culture medium

background. Spectra were then integrated to give the total Rayleigh scattering intensities, which were plotted temporally using OriginPro 9.0 software (Origin Lab, Corp.). The intensities were fit to a sigmoidal growth curve using a logistic response function, and scattering half-times generated from the fit using OriginPro 9.0 software. The quality of fit for the cisplatin, camptothecin, and 5-FU curves were R^2 = 0.98, R^2 = 0.97, and R^2 = 0.93, respectively. The CDE factors using this method are given as the ratios of the scattering half-times of camptothecin or 5-FU, relative to cisplatin.

3.2.8 Statistical Analysis

All results are expressed as the mean ± s.e.m. of three independent experiments. Changes in scattering intensity were compared using a linear regression analysis calculator, and the changes were not considered statistically significant (p = 0.2546, GraphPad Software, Inc.). Cell cycle changes were compared using unpaired t-tests (GraphPad Software, Inc.) and no statistically significant difference was found between NT-AuNP treated HSC-3 cells and untreated control cells.

3.3 Results and discussion

To monitor the light scattering and morphology of treated cells, AuNPs were used as light-scattering probes to enhance the cells' inherent Rayleigh scattering, allowing for greater differentiation between living and dead cells based on their scattering intensities. Cells without nanoparticle pretreatment displayed significantly lower scattering intensities, leading to diminished differentiation between living and dead cells, and a less accurate comparison of drug efficacies. PERSIS experiments were conducted in a live-cell chamber (**Figure 3.2A**) to obtain both Rayleigh scattering dark-field images and

Rayleigh scattering spectra from single cells incubated with AuNPs. The temporal effect of drug treatment was monitored via changes in the scattering spectra following drug administration. We have previously shown that the surface chemistry of AuNPs dictates their localization within cells and, consequently, is responsible for their observed strong light-scattering properties.[9] Thus, we used nuclear-targeted AuNPs (NT-AuNPs, **Figure 3.1**), for their greater light-scattering abilities. Citrate-capped AuNPs were synthesized, and their surfaces were modified to contain polyethylene glycol (PEG) to increase biocompatibility and prevent nonspecific interactions under physiological conditions.[17-18] After PEGylation, arginine-glycine-aspartic acid (RGD) and nuclear localizing sequence (NLS) peptides were bioconjugated to the AuNPs' surfaces (**Figure 3.2B**). RGD was used to increase nanoparticle endocytosis by targeting αβ integrins on the cell membrane,[19-20] while NLS was used to selectively target the AuNPs at the cell nuclei[21-22] and to increase scattering by localizing the plasmonic nanoparticles. HSC-3 cells were chosen as the model cell line due to the overexpression of αvβ6 integrins on their membrane.[23] To validate our technique, we calculated the time required to reach a half-maximal increase in scattering intensity, which is indicative of apoptosis. The relative drug efficacies obtained using our technique compared favorably to those obtained using the commercial XTT cell viability assay.

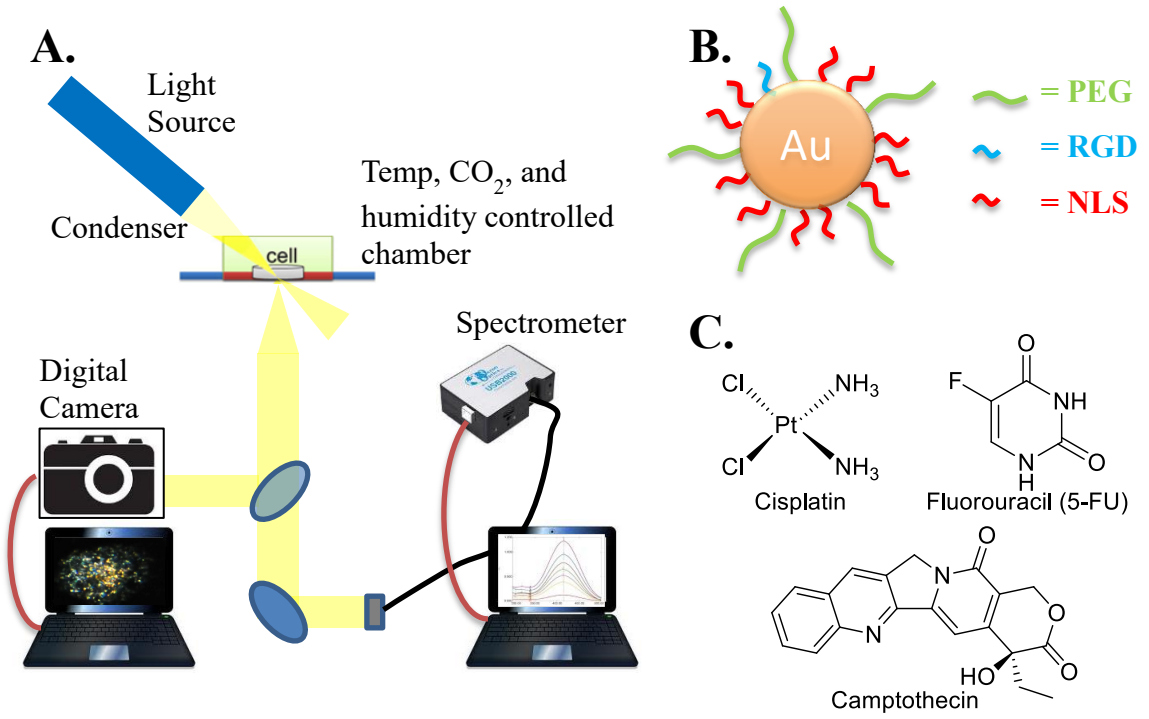

Figure 3.2 (A) Schematic of the PERSIS instrument used to monitor drug efficacy. (B) Illustration of the NT-AuNPs used to enhance the Rayleigh scattering. (C) Chemical structure of the anticancer drugs used.

3.3.1 Determining Nanoprobe Pretreatment

The life cycle of a dividing cell has been extensively characterized from the G1-phase, which includes cell growth and preparation for DNA replication in the forthcoming S-phase, through the G2-phase, which comprises the preparation for mitosis and the birth of two daughter cells in the M-phase.[24] To effectively compare the relative efficacy of several anticancer drugs, the concentration of AuNP scattering probes must be chosen to enhance scattering without affecting normal cellular function (e.g., altering the cell cycle) or inducing cell death. Accordingly, flow cytommetry was used to evaluate the effect of AuNP pretreatment on the distribution of cells throughout various stages of the

cell cycle. As shown in **Figure 3.3**, no significant changes were observed in the cell cycle upon treatment with low concentrations of NT-AuNPs (0.1 and 0.2 nM) relative to the untreated control cells. Thus, pretreatment with low concentrations of NT-AuNPs is not expected to affect anticancer drug treatment, allowing AuNPs to be used as scattering probes for the effective evaluation of relative drug efficacies. Both 0.1 and 0.2 nM NT-AuNPs gave similar scattering enhancement upon cell death (~50%); therefore, 0.1 nM was used for the remaining experiments.

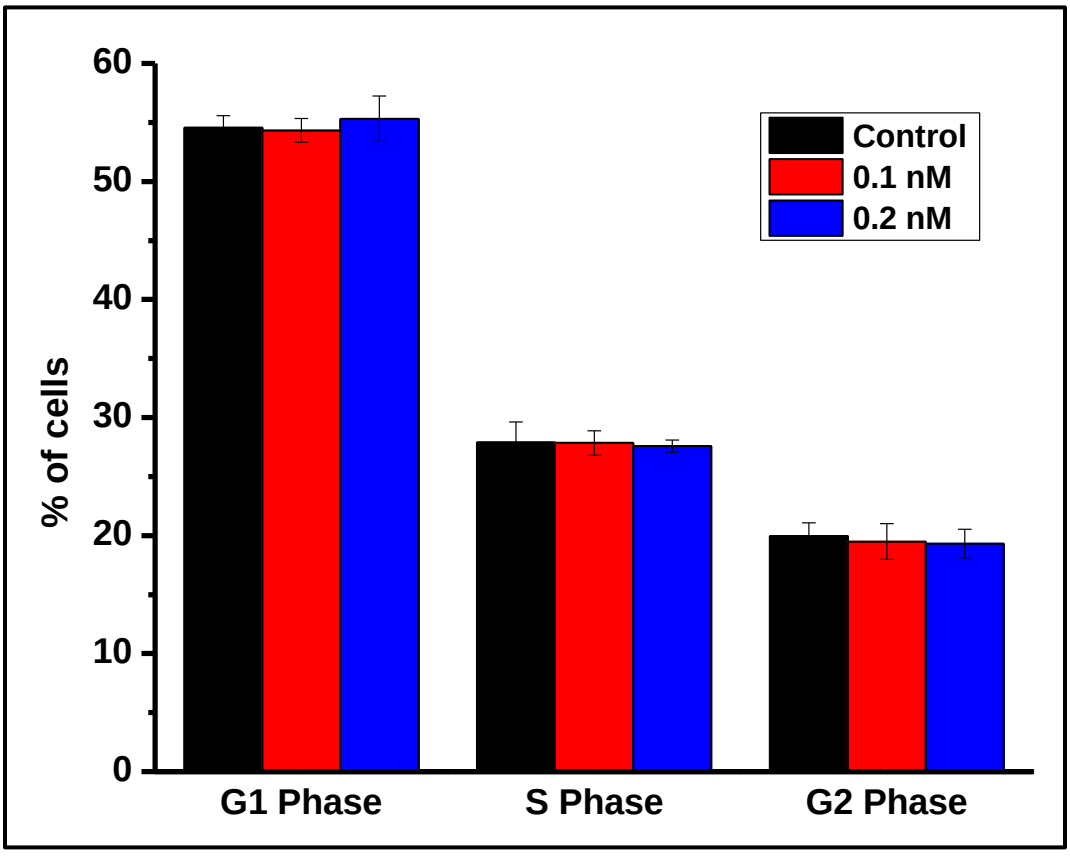

Figure 3.3 Cell cycle analysis of HSC-3 cancer cells treated with 0.1 nM (red) and 0.2 nM (blue) NT-AuNPs for 24 hours. There was no significant difference in the cell cycle between the treated cancer cells and the untreated control cells (black).

3.3.2 Drug Efficacy via Cell Viability Assays

In order to assess the validity of our PERSIS technique to the current assay standard, the efficacies of three popular anticancer drugs, cisplatin, camptothecin, and 5-FU **(Figure 3.2C)**, were first determined. Efficacy was expressed as the effective time needed to induce 50% cell death (ET50) following treatment with the anticancer drugs. To mimic the conditions of the PERSIS experiments, cells were first pretreated with 0.1 nM NT-AuNPs in culture media for 24 h. The AuNP solutions were then replaced with 100 μM solutions of the anticancer drugs for the desired treatment times. We obtained the temporal response of cancer cell viability to anticancer drug treatment over 72 h using an XTT cell viability assay **(Figure 3.4)**. These time profiles showed the enhanced efficacy of cisplatin (ET_{50} = 16 ± 1 h) relative to camptothecin and 5-FU, which had ET_{50} values of 52 ± 3 and 67 ± 2 h, respectively. For a simpler comparison between the drugs, we used the previously established cell death enhancement (CDE) factor,[25] which is defined as the ratio of the ET_{50} values of camptothecin or 5-FU relative to cisplatin. Using the ET_{50} values extracted from the curve fits of the cell death time profiles in **Figure 3.4**, CDE factors were calculated to be 3.3 for camptothecin and 4.2 for 5-FU. Additionally, treatment with NT-AuNPs alone did not induce any significant cell death **(Figure 3.4)**, further indicating that the low concentration of AuNPs served only to enhance Rayleigh scattering from the cells, allowing for greater differentiation between dead cells and living cells, without affecting cellular function or drug treatment.

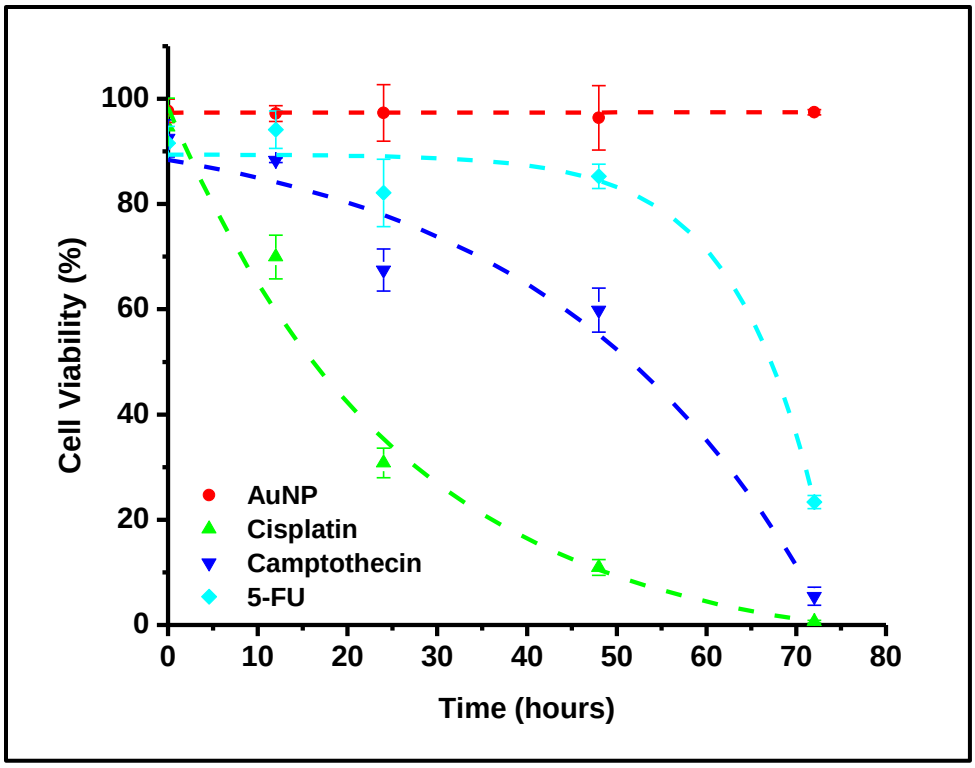

Figure 3.4 Time profile of HSC-3 cells treated with 100 μM cisplatin (green), camptothecin (blue), and 5-FU (teal), shown as the average cell viability ± s.e.m. from three independent experiments. ET_{50} values were calculated to be 16 ± 1 h for cisplatin (R^2 = 0.976), 52 ± 3 h for camptothecin (R^2 = 0.977), and 67 ± 2 h for 5-FU (R^2 = 0.981), giving CDE factors of 3.3 and 4.2 for camptothecin and 5-FU, respectively. Control cells treated with AuNPs alone (red) did not have a significant decrease in viability.

3.3.3 Drug Efficacy via PERSIS Technique

To compare drug efficacies using our PERSIS technique, cells were pretreated with 0.10 nM NT-AuNPs for 24 h to enhance their Rayleigh scattering. The AuNP solutions were then replaced with 100 μM solutions of the anticancer drugs, and cellular morphology and light scattering were monitored from 10 different cells for 24 h via Rayleigh scattering spectra **(Figure 3.5)** and dark-field images. After drug administration, the Rayleigh scattering spectra initially remained constant but increased

over time as cell death progressed. As seen in **Figure 3.5**, cisplatin induced the quickest increase in Rayleigh scattering, while 5-FU treatment displayed the slowest scattering increase. These trends correlate well with that previously observed using XTT cell viability assays. Complete cell death was signified when the spectra remained constant and changes were no longer observed. Dark-field images were also taken for the control cells that did not receive drug treatment, and cells treated with cisplatin, camptothecin, and 5-FU, which allowed the cell death to be observed visually. Upon drug treatment, the initially viable cells were seen to first shrink and lose mobility, indicative of apoptosis,[13] and then showed a large increase in light scattering due to having more nanoparticles in close proximity.[26-27] Thus, the number of nanoparticles with optimal interparticle separation distances increased within the shrunken cells, resulting in greater scattering intensities. Eventually, the cell morphology remained constant, and the treated cells ceased all movement. It should be noted that the number of visible cells decreased as some of the dead cells floated off of the culture dish and out of the focal plane of the microscope. HSC-3 cells that did not receive anticancer drug treatment did not exhibit these visual or spectral changes (Figure 3.6) and were seen to increase in number due to cell cycle proliferation.

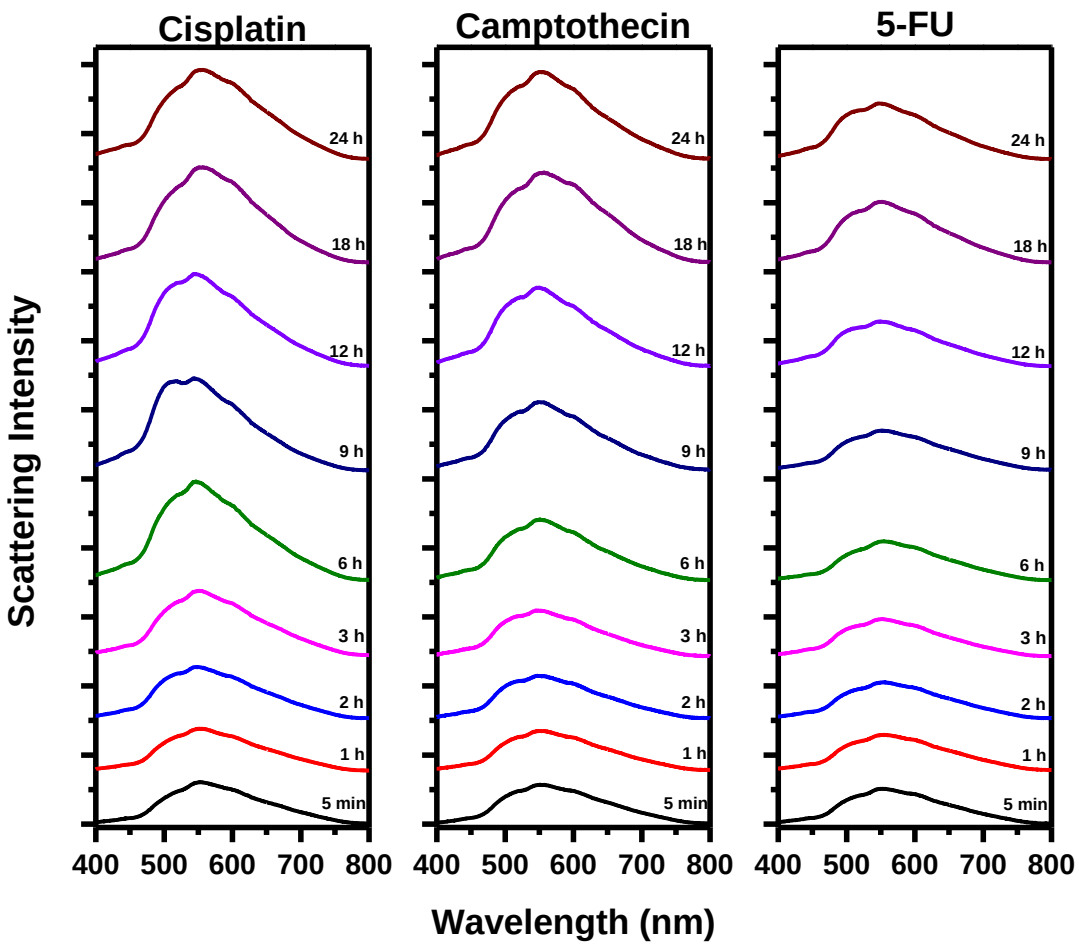

Figure 3.5 Real-time Rayleigh scattering spectra of HSC-3 cells treated for 24 h with 100 μM cisplatin, camptothecin, and 5-FU, shown as the mean ± s.e.m. of three independent experiments (n = 10 cells).

To quantitatively compare the relative efficacy of the anticancer drugs using the PERSIS technique, the time profile of cell death was obtained to correlate the observed visual changes and increased light scattering to the biochemically determined cell death parameters. The Rayleigh scattering spectra in **Figure 3.5** were integrated to obtain the total scattering intensity. These intensities, shown in **Figure 3.7**, were plotted temporally to obtain a time profile of cell death based on the increased light scattering from the cells

upon drug treatment. The plasmonically enhanced Rayleigh scattering was found to initially remain constant for all of the samples, before a large increase due to cell death. However, the scattering profiles changed at different rates, which correlated with the differences observed in the ET_{50} values obtained using the XTT cell viability assay. Additionally, NT-AuNP incubated cells that were not treated with anticancer drugs did not display any significant changes in scattering over 24 h, as seen in **Figure 3.6**. To effectively compare these changes, scattering half-times, defined as the time required to achieve the half-maximal increase in scattering intensity, were calculated for each drug. Cisplatin had the fastest scattering half-time of 2.9 ± 0.2 h, followed by camptothecin and 5-FU with scattering half-times of 8.6 ± 1.6 and 12 ± 0.8 h, respectively (**Figure 3.7**). These scattering half-times are again similar to the trends observed from the biochemically determined drug efficacies (**Figure 3.5**). To directly compare drug efficacies as well as compare our PERSIS technique with traditional cell viability assays, we calculated CDE factors for the anticancer drugs using the ratio between the scattering half-times of camptothecin or 5-FU relative to cisplatin. As shown in

Table 3.1, the CDE factors for camptothecin (3.0) and 5-FU (4.1) calculated using the PERSIS technique compared favorably to those obtained using the XTT cell viability assay (3.3 and 4.2, respectively), indicating the ability of PERSIS to accurately assess drug efficacy. Moreover, the PERSIS technique, including nanoparticle pretreatment, decreased the time required to obtain ET_{50} values by 24 h.

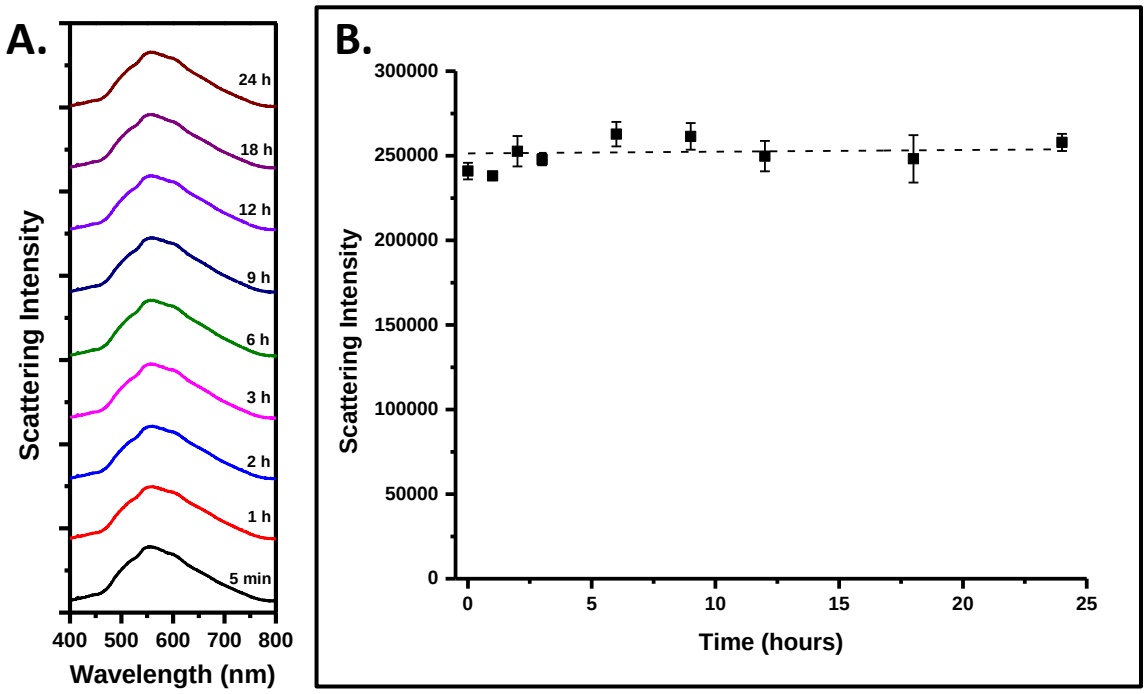

Figure 3.6 (A) Rayleigh scattering spectra of untreated HSC-3 cells after 24 h incubation with NT-AuNPs show no change with time. (B) Total Rayleigh scattering intensity of untreated HSC cells after 24 h incubation with NT-AuNPs show no statistically significant change with time.

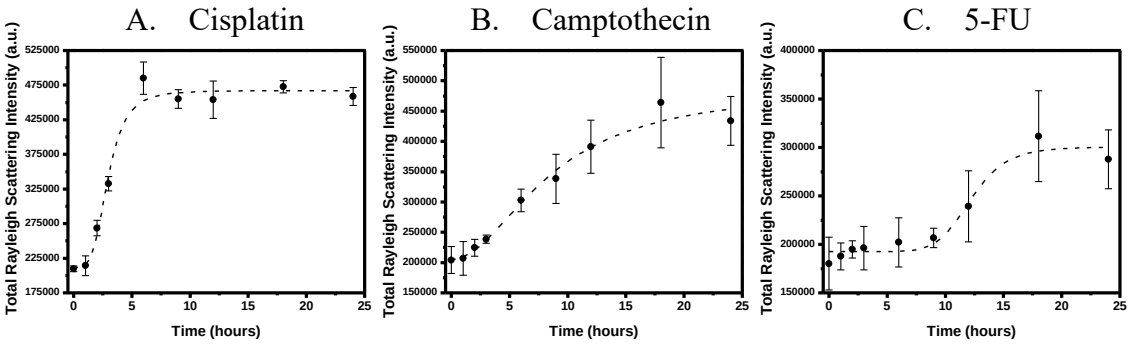

Figure 3.7 Rayleigh scattering intensity time profiles of HSC-3 cells treated with 100 μM cisplatin, camptothecin, and 5-FU, shown as the average intensity ± s.e.m. from three independent experiments. Scattering half-times were calculated to be 2.9 h for cisplatin (A, R^2 = 0.982), 8.6 h for camptothecin (B, R^2 = 0.976), and 12 h for 5-FU (C, R^2 = 0.928), giving CDE factors of 3.0 and 4.1, respectively.

Table 3.1 CDE Factors Obtained Using the PERSIS Technique, Comparable to Those Obtained Using a Standard XTT Cell Viability Assay.

drug	XTT ET_{50} (h)	PERSIS ET_{50} (h)	CDE factor (XTT)	CDE factor (PERSIS)
cisplatin	16 ± 1	2.9 ± 0.2		
camptothecin	52 ± 3	8.6 ± 1.6	3.3	3.0
5-FU	67 ± 2	12 ± 0.8	4.2	4.1

3.4 Conclusion

In conclusion, we have demonstrated the accuracy of our PERSIS technique for determining relative drug efficacies using NT-AuNPs as scattering enhancement probes. The model cell line, HSC-3, was pretreated with a low concentration of AuNPs to enhance their Rayleigh scattering without affecting normal cellular function or inducing cell death. The relative drug efficacies obtained with our technique correspond favorably to those obtained using a standard cell viability assay. The PERSIS technique presents a novel system for studying the effects of drug treatment based on the morphological changes and increase in scattered light observed upon cell death. This represents a continuous assay capable of monitoring a single sample of living cells in real time, without the need for expensive instrumentation. Furthermore, this home-built system has the potential to be engineered into a multicomponent assay capable of screening multiple samples simultaneously, which could allow for the rapid comparison of various drugs, or drug analogues, against a particular disease or cell line.

3.5 References

(1) Aioub, M.; Austin, L. A.; El-Sayed, M. A. Determining Drug Efficacy Using Plasmonically Enhanced Imaging of the Morphological Changes of Cells Upon Death. *J. Phys. Chem. Lett.* **2014,** *5*, 3514-3518.

(2) Dreaden, E. C.; Alkilany, A. M.; Huang, X. H.; Murphy, C. J.; El-Sayed, M. A. The Golden Age: Gold Nanoparticles for Biomedicine. *Chem. Soc. Rev.* **2012,** *41*, 2740-2779.

(3) Jain, P. K.; Huang, X. H.; El-Sayed, I. H.; El-Sayed, M. A. Noble Metals on the Nanoscale: Optical and Photothermal Properties and Some Applications in Imaging, Sensing, Biology, and Medicine. *Acc. Chem. Res.* **2008,** *41*, 1578-1586.

(4) Daniel, M. C.; Astruc, D. Gold Nanoparticles: Assembly, Supramolecular Chemistry, Quantum-Size-Related Properties, and Applications toward Biology, Catalysis, and Nanotechnology. *Chem. Rev.* **2004,** *104*, 293-346.

(5) Giljohann, D. A.; Seferos, D. S.; Daniel, W. L.; Massich, M. D.; Patel, P. C.; Mirkin, C. A. Gold Nanoparticles for Biology and Medicine. *Angew. Chem., Int. Ed.* **2010,** *49*, 3280-3294.

(6) El-Sayed, I. H.; Huang, X.; El-Sayed, M. A. Surface Plasmon Resonance Scattering and Absorption of Anti-EGFR Antibody Conjugated Gold Nanoparticles in Cancer Diagnostics: Applications in Oral Cancer. *Nano Lett.* **2005,** *5*, 829-834.

(7) Kang, B.; Austin, L. A.; El-Sayed, M. A. Observing Real-Time Molecular Event Dynamics of Apoptosis in Living Cancer Cells Using Nuclear-Targeted Plasmonically Enhanced Raman Nanoprobes. *ACS Nano* **2014,** *8*, 4883-4892.

(8) Liu, X.; Dai, Q.; Austin, L.; Coutts, J.; Knowles, G.; Zou, J. H.; Chen, H.; Huo, Q. A One-Step Homogeneous Immunoassay for Cancer Biomarker Detection Using Gold Nanoparticle Probes Coupled with Dynamic Light Scattering. *J. Am. Chem. Soc.* **2008,** *130*, 2780-2782.

(9) Aioub, M.; Kang, B.; Mackey, M. A.; El-Sayed, M. A. Biological Targeting of Plasmonic Nanoparticles Improves Cellular Imaging via the Enhanced Scattering in the Aggregates Formed. *J. Phys. Chem. Lett.* **2014,** *5*, 2555-2561.

(10) Evan, G.; Littlewood, T. A Matter of Life and Cell Death. *Science* **1998,** *281*, 1317-1322.

(11) Holohan, C.; Van Schaeybroeck, S.; Longley, D. B.; Johnston, P. G. Cancer Drug Resistance: An Evolving Paradigm. *Nat. Rev. Cancer* **2013,** *13*, 714-726.

(12) Brown, J. M.; Attardi, L. D. The Role of Apoptosis in Cancer Development and Treatment Response. *Nat. Rev. Cancer* **2005,** *5*, 231-237.

(13) Fesik, S. W. Promoting Apoptosis as a Strategy for Cancer Drug Discovery. *Nat. Rev. Cancer* **2005,** *5*, 876-885.

(14) Hsiang, Y. H.; Liu, L. F. Identification of Mammalian DNA Topoisomerase-I as an Intracellular Target of the Anticancer Drug Camptothecin. *Cancer Res.* **1988,** *48*, 1722-1726.

(15) Siddik, Z. H. Cisplatin: Mode of Cytotoxic Action and Molecular Basis of Resistance. *Oncogene* **2003,** *22*, 7265-7279.

(16) Li, M. H.; Ito, D.; Sanada, M.; Odani, T.; Hatori, M.; Iwase, M.; Nagumo, M. Effect of 5-Fluorouracil on G1 Phase Cell Cycle Regulation in Oral Cancer Cell Lines. *Oral Oncol.* **2003,** *40*, 63-70.

(17) Otsuka, H.; Nagasaki, Y.; Kataoka, K. Pegylated Nanoparticles for Biological and Pharmaceutical Applications. *Adv. Drug Delivery Rev.* **2003,** *55*, 403-419.

(18) Ghosh, P.; Han, G.; De, M.; Kim, C. K.; Rotello, V. M. Gold Nanoparticles in Delivery Applications. *Adv. Drug Delivery Rev.* **2008,** *60*, 1307-1315.

(19) Castel, S.; Pagan, R.; Mitjans, F.; Piulats, J.; Goodman, S.; Jonczyk, A.; Huber, F.; Vilaro, S.; Reina, M. RGD Peptides and Monoclonal Antibodies, Antagonists of αv-Integrin, Enter the Cells by Independent Endocytic Pathways. *Lab. Invest.* **2001,** *81*, 1615-1626.

(20) Zitzmann, S.; Ehemann, V.; Schwab, M. Arginine–Glycine–Aspartic Acid (RGD)-Peptide Binds to Both Tumor and Tumor-Endothelial Cells in Vivo. *Cancer Res.* **2002,** *62*, 5139-5143.

(21) Escriou, V.; Carriere, M.; Scherman, D.; Wils, P. NLS Bioconjugates for Targeting Therapeutic Genes to the Nucleus. *Adv. Drug Delivery Rev.* **2003,** *55*, 295-306.

(22) Tkachenko, A. G.; Xie, H.; Liu, Y. L.; Coleman, D.; Ryan, J.; Glomm, W. R.; Shipton, M. K.; Franzen, S.; Feldheim, D. L. Cellular Trajectories of Peptide-Modified Gold Particle Complexes: Comparison of Nuclear Localization Signals and Peptide Transduction Domains. *Bioconjugate Chem.* **2004,** *15*, 482-490.

(23) Xue, H.; Atakilit, A.; Zhu, W. M.; Li, X. W.; Ramos, D. M.; Pytela, R. Role of the αvβ6 Integrin in Human Oral Squamous Cell Carcinoma Growth in Vivo and in Vitro. *Biochem. Biophys. Res. Commun.* **2001,** *288*, 610-618.

(24) Voet, D.; Voet, J. G.; Pratt, C. W., *Fundamentals of Biochemistry : Life at the Molecular Level*. 4th ed.; Wiley: Hoboken, NJ, 2012.

(25) Austin, L. A.; Kang, B.; El-Sayed, M. A. A New Nanotechnology Technique for Determining Drug Efficacy Using Targeted Plasmonically Enhanced Single Cell Imaging Spectroscopy. *J. Am. Chem. Soc.* **2013,** *135*, 4688-4691.

(26) Jain, P. K.; Huang, W. Y.; El-Sayed, M. A. On the Universal Scaling Behavior of the Distance Decay of Plasmon Coupling in Metal Nanoparticle Pairs: A Plasmon Ruler Equation. *Nano Lett.* **2007,** *7*, 2080-2088.

(27) Reinhard, B. M.; Siu, M.; Agarwal, H.; Alivisatos, A. P.; Liphardt, J. Calibration of Dynamic Molecular Ruler Based on Plasmon Coupling between Gold Nanoparticles. *Nano Lett.* **2005,** *5*, 2246-2252.

CHAPTER 4. A REAL-TIME SURFACE ENHANCED RAMAN SPECTROSCOPY STUDY OF PLASMONIC PHOTOTHERMAL CELL DEATH USING TARGETED GOLD NANOPARTICLES [1]

(Adapted with permission from Aioub, M.; El-Sayed, M. A. A Real-Time Surface Enhanced Raman Spectroscopy Study of Plasmonic Photothermal Cell Death Using Targeted Gold Nanoparticles. *J. Am. Chem. Soc.* **2016,** *138*, 1258-1264. Copyright 2016 American Chemical Society.)

Plasmonic nanoparticles are increasingly utilized in biomedical applications including imaging, diagnostics, drug delivery, and plasmonic photothermal therapy (PPT). PPT involves the rapid conversion of light into heat by plasmonic nanoparticles targeted to a tumor, causing hyperthermia-induced cell death. These nanoparticles can be passively targeted utilizing the enhanced permeability and retention effect, or actively targeted using proteins, peptides, or other small molecules. Here, we report the use of actively targeted spherical gold nanoparticles (AuNPs), both to induce PPT cell death, and to monitor the associated molecular changes through time-dependent surface enhanced Raman spectroscopy within a single cell. We monitored these changes in real-time and found that heat generated from the aggregated nanoparticles absorbing near-infrared (NIR) laser light of sufficient powers caused modifications in the protein and lipid structures within the cell and ultimately led to cell death. The same molecular changes were observed using different nanoparticle sizes and laser intensities, indicating the consistency of the molecular changes throughout PPT-induced cell death from actively targeted AuNPs. We also confirmed these observations by comparing them to reference spectra obtained by cell death induced by oven heating at 100°C. The ability to

monitor PPT-induced cell death in real-time will help understand the changes on a molecular level and offers us a basis to understand the molecular mechanisms involved in photothermal cancer cell death.

4.1 Introduction

The use of nanoparticles in biomedical applications has increased tremendously in recent years due to their biologically relevant size and the unique chemical, physical, and optical properties that arise on the nanoscale. Metallic nanoparticles have been heavily used in particular, due to the growing ease of their colloidal synthetic strategies, precise control over their size and shape, facile surface chemistry, and tunable optical properties.[2-6] Gold nanoparticles (AuNPs) exhibit these properties, along with low inherent toxicity, an essential requirement for biological applications.[7] They also display intense optical properties arising from their localized surface plasmon resonance (LSPR).[8] The LSPR arises from the coherent oscillation of electrons in the conduction band, in resonance with light of a particular frequency. The observed LSPR peak depends on the dielectric function of the metal nanoparticle and surrounding media, as well as the size and shape of the nanoparticle.[8,9] Therefore, the LSPR can easily be tuned for biological applications by adjusting the size and shape of the nanoparticles to control the observed wavelength and relative scattering/absorption properties.[9,10] This has led to the widespread use of AuNPs in cellular imaging (including both surface enhanced Raman scattering (SERS) for molecular fingerprinting and Rayleigh scattering for traditional imaging),[11,12] drug delivery/photodynamic therapy,[13-15] and plasmonic photothermal therapy (PPT).[16,17]

PPT is a promising cancer treatment where plasmonic nanoparticles rapidly convert NIR light to heat through the nonradiative relaxation of the excited LSPR

through electron–electron, electron–phonon, and phonon–phonon collisions. These interactions generate an intense heating of the gold nanoparticle, leading to the hyperthermia induced death of cells in close proximity to the nanoparticles.[10,16,18] Therefore, PPT relies on the accumulation of plasmonic nanoparticles in or around the cells of interest, which can be achieved through passive- or active-targeting.[19] AuNPs can be passively targeted to tumors through the enhanced permeability and retention (EPR) effect, which occurs due to the abnormal vasculature that results from tumor angiogenesis and results in the accumulation of nanoparticles and small molecules at the tumor site.[20] Nanoparticles can also be actively targeted to cancer cells using proteins, peptides, or small molecules, such as antiepidermal growth factor receptor or herceptin proteins, or RGD peptides, which target overexpressed receptors on the cancer cell surface.[21] Significant research efforts have gone into characterizing cell death resulting from PPT treatment, and investigating specific proteins and signaling molecules, as well as the mechanisms underlying cell death (i.e., apoptosis or necrosis).[16,18,22,23] However, there have been many literature reports of both apoptotic[18,22] and necrotic[22,24-27] cell death resulting from PPT. These conflicting reports are most likely due to differences in the nanoparticle targeting (passive or active), physical properties (e.g., size, shape, absorption cross section, etc.) that dictate the absorption cross section, spectral overlap between the plasmon band and the laser used for PPT, and the intensity and duration of the laser exposure.

In the present work, we exploit the enhanced optical properties of AuNPs, namely, their strong absorption properties to induce PPT cell death, and their intense scattering to monitor the molecular changes that occur in real-time using SERS. While

Raman scattering is a relatively old technique, the advent of enhanced Raman spectroscopies, such as SERS, has resulted in incredible enhancement factors of up to 10^{14}, making single molecule and single cell spectroscopies achievable.[28,29] Here, we have used actively targeted AuNPs and SERS to study PPT-induced cell death in real-time, as a function of both nanoparticle concentration and laser intensity. Because SERS enhancement is only observed in the AuNP microenvironment, we are able to follow the molecular changes that occur around the nanoparticles as heat is generated in real-time. We found a minimum threshold of laser intensity/nanoparticle concentration, below which heat dissipation outpaces heat generation and no cell death is observed. When above this threshold, the heat generated causes perturbations to lipid and protein structure, ultimately resulting in cell death. Increasing laser intensity leads to more rapid cell death, but the same biochemical changes are observed.

4.2 Methods

4.2.1 Materials

Tetrachloroauric acid trihydrate ($HAuCl_4 \cdot 3H_2O$) and trisodium citrate were purchased from Sigma-Aldrich. Methoxy-poly(ethylene glycol)-thiol (mPEG-SH, MW 5000) was obtained from Laysan Bio, Inc. Custom RGD (RGDRGDRGDRGDPGC) and NLS (CGGGPKKKRKVGG) peptides were purchased from GenScript, Inc. Dulbecco's phosphate buffered saline (PBS), Dulbecco's modified Eagle's medium (DMEM), antibiotic solution, fetal bovine serum (FBS), 0.25% trypsin/2.2 mM EDTA, and propidium iodide (PI) were purchased from VWR. Annexin-V binding buffer was obtained from Invitrogen, Inc., and Annexin-V FITC was purchased from Biolegend.

4.2.2 Instrumentation

Transmission electron microscope (TEM) images were taken using a JEOL 100CX-2 microscope. Average nanoparticle particle diameter was measured using ImageJ software. UV–vis spectra were collected using an Ocean Optics HR4000CG-UV-NIR spectrometer. Dark-field images and SERS spectra were collected using a Renishaw InVia Raman microscope coupled with a Leica optical microscope and 785 nm diode Raman excitation laser. Flow cytometry experiments were performed using a BD LSR II Flow Cytometer (BD Biosciences).

4.2.3 Larger AuNP (30 nm) Synthesis and Functionalization

Citrate-capped gold nanoparticles (AuNPs) were prepared following the Turkevich/Frens citrate reduction technique.[30,31] A 100 mL aqueous solution of 0.60 mM chloroauric acid was heated with stirring. Just before the solution reached boiling, 1 mL of 90 mM sodium citrate was added. Stirring and heating were discontinued and the solution was allowed to cool to room temperature when a red-wine color was observed.

The citrate-stabilized AuNPs were first cleaned by centrifugation at 4000*g* for 15 min and redispersed in deionized (DI) water. The AuNPs were then conjugated with PEG to increase stability, enhance biocompatibility, and prevent nonspecific interactions in physiological environments.[21] A 1.0 mM solution of mPEG-SH in DI water was added to achieve a ~20% surface coverage. The PEG-AuNP solution was shaken at room temperature overnight and unbound ligands removed by centrifugation (12000*g*, 7 min). PEG-AuNPs were again dispersed in DI water, followed by conjugation with a 1:10 ratio of RGD and NLS peptides to fill remaining surface sites. The AuNPs were centrifuged

(12000*g*, 7 min) to remove unbound peptides and dispersed in DI water to yield nuclear targeted gold nanoparticles (NT-AuNPs).

4.2.4 Smaller AuNP (sAuNP) Synthesis and Functionalization

Smaller citrate-capped gold nanoparticles (sAuNPs) were also prepared following the Turkevich/Frens citrate reduction technique. A 100 mL aqueous solution of 0.25 mM chloroauric acid was heated with stirring. Just before the solution reached boiling, 2 mL of 65 mM trisodium citrate was added. Stirring and heating were discontinued and the solution was allowed to cool to room temperature when a red-wine color was observed.

The sAuNPs were first cleaned by centrifugation at 9500*g* for 15 min and redispersed in deionized (DI) water. The AuNPs were then conjugated with PEG to increase stability, enhance biocompatibility, and prevent nonspecific interactions in physiological environments. A 1.0 mM solution of mPEG-SH in deionized (DI) water was added to achieve a ~20% surface coverage. The PEG-AuNP solution was shaken at room temperature overnight and unbound ligands removed by centrifugation (12500*g*, 10 min). PEG-sAuNPs were again dispersed in DI water, followed by conjugation with a 1:10 ratio of RGD and NLS peptides to fill remaining surface sites. The AuNPs were again centrifuged (12500*g*, 10 min) to remove unbound peptides and dispersed in DI water to yield the smaller nuclear targeted gold nanoparticles (NT-sAuNPs).

4.2.5 Cell Culture

Human oral squamous carcinoma (HSC-3) cells, an epithelial cell line expressing αβ integrins on the cellular membrane,[32] were used as our cancer model. The cells were

cultured in DMEM supplemented with 10% v/v FBS and 1% v/v antibiotic. Cell cultures were maintained in a 5% CO_2 atmosphere in a humidified 37°C incubator.

4.2.6 Apoptosis–Necrosis Assay

Cells were seeded in culture medium for a 70% final confluence and allowed to adhere overnight. The growth media was then removed and the cells were incubated with 0.10 nM NT-AuNPs in DMEM for 24 h. After nanoparticle incubation, the NT-AuNP solution was replaced with DMEM and cells to be heated were placed in a 100°C oven for 7 min to induce cell death. For flow cytometric analysis, cells were trypsinized for 7 min and collected via centrifugation (7 min, 250*g*). Cells were washed twice with cold PBS and redispersed in 500µl Annexin V binding buffer. Cells were then incubated with 5 µl of Annexin V-FITC and 2 µl of PI (100µg/ml) for 15 min at room temperature. Following incubation, 493 µl of Annexin V binding buffer was added and the samples were immediately analyzed via flow cytometry. Fluorophores were excited with a 488 nm laser and detected by a 525/30 BP filter for FITC and a 575/30 BP filter for PI. Sample populations consisted of at least 10000 events and results were analyzed using FlowJo software (TreeStar, Inc.).

4.2.7 SERS Measurements

For SERS studies, cells were seeded on round glass coverslips for a 70% final confluence. After cells were allowed to adhere overnight, the cells were incubated with NT-AuNPs diluted to the specified concentrations in complete DMEM for 24 h. NT-AuNP concentrations were specifically chosen to avoid toxicity or perturbing the cell cycle.[33]

Following nanoparticle incubation, single cells were irradiated for 2 h using the 785 nm diode laser at the indicated intensities. Time-dependent SERS spectra were recorded throughout the laser exposure to monitor the molecular changes upon photothermal heating of the NT-AuNPs. These spectra were collected from the area within the cell that displayed the most scattering due to nanoparticle localization, corresponding to the areas with the greatest enhancement of Raman vibrations from molecules in the nanoparticle microenvironment. The laser was directed into the microscope and focused on the sample by a 50×/0.75 N.A. objective, leading to a ~1–2 μm spot size and resulting in single cell irradiation/resolution. For oven heating experiments, SERS spectra were obtained and averaged from 10 individual cells before and after heating. All SERS measurements were obtained in supplemented DMEM without phenol red. SERS spectra were measured in backscattering geometry using a 1200 lines/mm grating and collected by a CCD detector in the 400–1800 cm^{-1} range with a 10 s integration time. Spectra were background corrected using a cubic spline interpolation for the baseline fit by manually selecting points representative of the background. Dark-field images were collected using a Lumenera infinity2 CCD camera.

4.3 Results and Discussion

Plasmonic photothermal therapy (PPT) is increasingly being investigated as a cancer therapy using gold nanoparticles (AuNPs) to absorb NIR light and rapidly produce heat, causing hyperthermia in the nanoparticle vicinity. However, differences in the size and shape of the nanoparticles lead to different absorption and scattering properties,[9,10] impacting the amount of heat generated and influencing the mechanism of cell death. Active nanoparticle targeting with proteins or cell-penetrating peptides (CPPs) and

passive-targeting through the EPR effect results in nanoparticle accumulation (and therefore heat generation) either within individual cells, or within the tumor microenvironment, respectively. For this study, we have used actively targeted AuNPs due to their strong absorption properties leading to PPT-induced cell death, and their intense plasmonic field, allowing the monitoring of the SERS spectra for biochemical changes of the nanoparticle environment throughout the laser treatment and accompanying cell death.

Nearly spherical AuNPs were synthesized following the Turkevich/Frens citrate reduction method, where the gold salt precursor is reduced via sodium citrate, which also acts as the capping agent to complete nanocrystal growth. The AuNPs were characterized by TEM (**Figure 4.1B**) and found to have a ~29±3 nm diameter and an LSPR peak at 529 nm. The citrate-capped AuNPs were then conjugated with mPEG-SH to increase their stability and biocompatibility, and with RGD and NLS peptides, to promote cellular uptake[34] and localization at the nuclear region,[35] respectively. Successful conjugation is evident in the red-shift of the plasmon peak to longer wavelengths, from 529 nm for the as-synthesized AuNPs to 531 nm for PEG-AuNPs, and finally to 533 nm for the NT-AuNPs (**Figure 4.2A**). Cancer cells were then incubated with NT-AuNPs for 24 h to allow for uptake into the cells and localization at the nuclear region, which was confirmed through dark-field microscopy (**Figure 4.1C**). Localization of the AuNPs was critical, as it has been widely shown that having multiple AuNPs in close proximity shifts the observed LSPR peak to longer wavelengths due to coupling of their plasmonic fields.[11,36,37] This plasmonic coupling allows for the overlap with the 785 nm laser used for PPT heating and SERS measurements in this study. The AuNP treatment

concentration (0.2 nM) was specifically chosen to allow for significant heat generation, resulting in PPT-induced cell death, while simultaneously monitoring the SERS spectra to identify the biochemical changes resulting from PPT. Following AuNP incubation, SERS spectra were collected from single cells for 2 h during continuous laser irradiation, leading to significant biochemical changes observed in the spectra and eventual cell death.

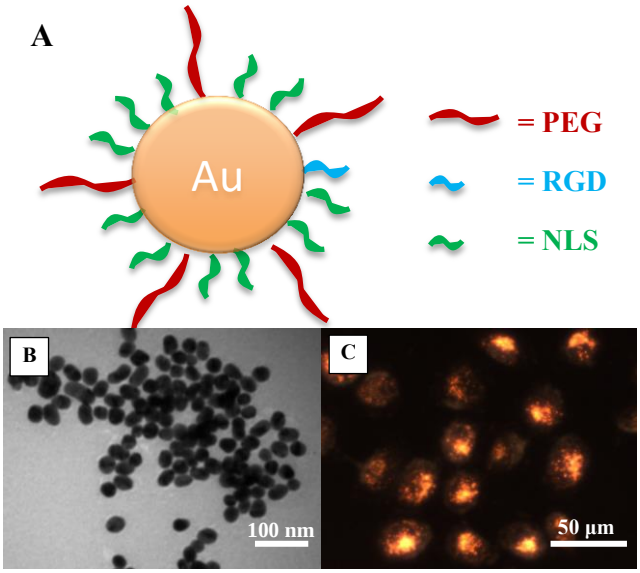

Figure 4.1 (A) Schematic showing nuclear-targeted AuNPs (NT-AuNPs) used in this study. (B) TEM micrograph of 29 nm citrate stabilized AuNPs. (C) Dark-field image of HSC-3 cells incubated with NT-AuNPs, showing the nanoparticles primarily localized at the perinuclear region.

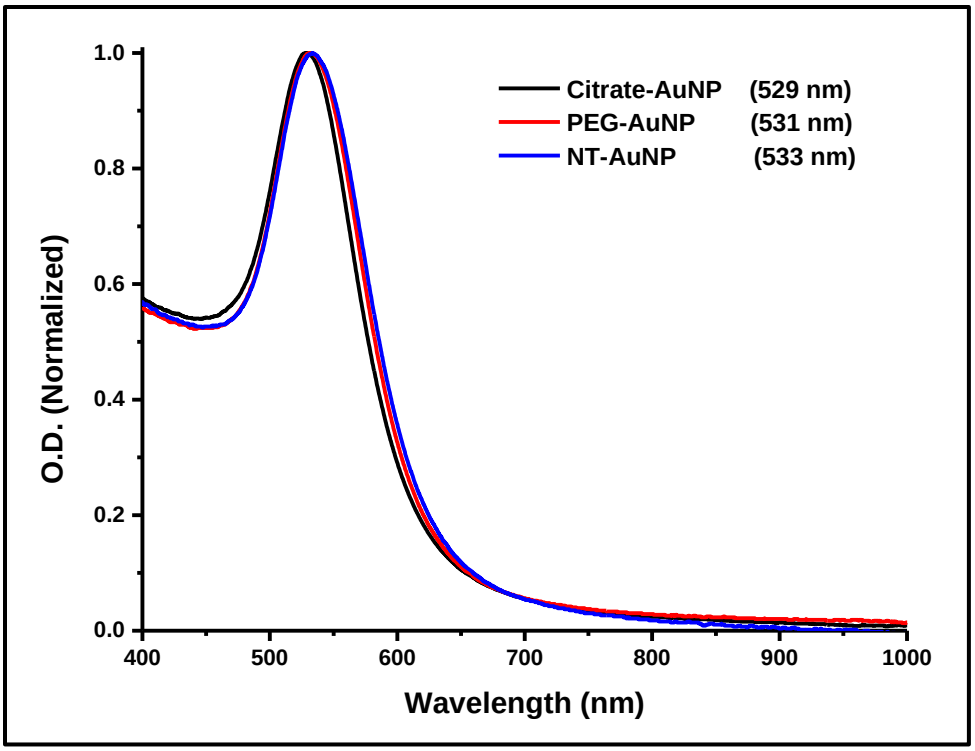

Figure 4.2 Characterization of nuclear-targeted AuNPs (NT-AuNPs). UV-Vis extinction spectrum of AuNPs before (black) and after conjugation with PEG (red), and RGD and NLS peptides (blue) in aqueous solution. The red shift in the plasmon peak indicates successful conjugation.

Initially, SERS bands appeared at ~500 and 654 cm^{-1} (**Figure 4.3**) primarily corresponding to –S–S– and –C–S– vibrations, respectively, from sulfur containing amino acids in proteins surrounding the AuNPs.[38,39] During 6.2 mW laser exposure, the –S-S- band disappeared almost entirely, indicating the likely rupture of disulfide bonds,[40] a critical component of protein structure, around the AuNPs due to PPT heating. By comparison, the intensity of –C–S– vibration band remained relatively unchanged, indicating the continued presence of sulfur containing amino acids in the AuNP microenvironment. The slight changes in –C–S– vibration intensity could potentially be attributed to fluctuations in the interactions of the sulfur containing amino acids and the

AuNP plasmonic field, and modifications in their dihedral angles as the amino acids would be more flexible following the loss of protein tertiary structure.[38,41]

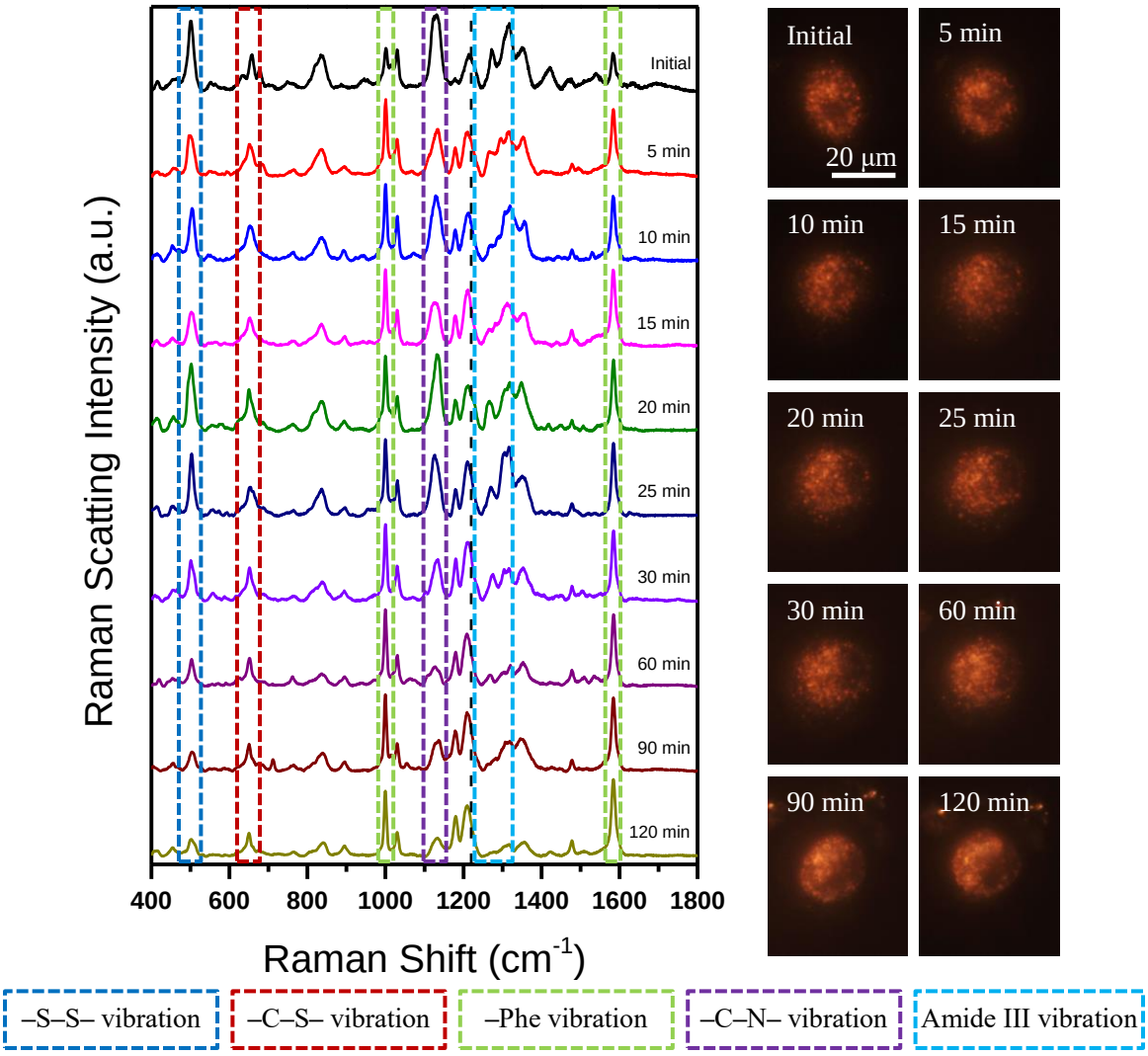

Figure 4.3 Time-dependent SERS spectra collected from a single HSC-3 cell during PPT cell death induced by continuous laser exposure at lower power (6.2 mW). The vertical line at 1225 cm^{-1} serves as a visual guide to highlight the shift in this vibrational peak from the amide III β-confirmation at 1225 cm^{-1} to the aromatic amino acid residue peaks at 1209 cm^{-1}, which in conjunction with the disappearance of additional vibrations around 500 cm^{-1} and in the 1250 cm–1350 cm^{-1} range signals cell death. Corresponding dark-field images for each spectrum are shown.

Additionally, the Raman band observed at 1225 cm^{-1} in the initial spectra is mainly attributed to the amide III vibration of the β-sheet conformation of the proteins.[42,43] Upon laser exposure, this band shifted toward 1209 cm^{-1}, which is primarily due to the C_6H_5–C stretch of phenylalanine (with some contribution from tyrosine).[44] This was accompanied by the enhancement of the intensity of the 1180, 1001, and 1584 cm^{-1} bands, which are attributed to the in-plane CH bend,[44-46] ring breathing,[44,45,47] and in-plane CH stretching vibrations corresponding to phenylalanine moieties,[44,45,48] respectively. While fairly weak in the initial SERS spectra, these bands were seen to grow progressively stronger in intensity, eventually dominating the spectra along with the 1209 cm^{-1} vibration. Furthermore, additional spectral bands were seen at ~835 cm^{-1} due to symmetric lipid–O–C–C–N– stretches and tyrosine,[49,50] and at 1130 cm^{-1}, due to lipid *trans*-confirmations and the C–N backbone of proteins,[51-53] respectively. Additional vibrations are also observed in the 1275–1350 cm^{-1} region, attributed to the amide III vibrations of α-helix and random coil structures in the surrounding proteins,[53-55] as well as the $–CH_2$ twist in lipids.[50,53,56] Upon PPT heating, these protein and lipid structural vibrations disappeared, further supporting the hypothesis that, during laser exposure, actively targeted AuNPs generate intense amounts of local heat within the cell, disrupting lipid and protein structure and ultimately resulting in hyperthermia-induced cell death. Since the targeting peptides conjugated to the AuNPs do not contain phenylalanine, tryptophan, or tyrosine, the observed spectral features must originate from proteins within the cells. A detailed assignment of these spectral bands can be found in **Table 4.1**.

These spectral changes suggest a clear modification in protein confirmation within the cells during PPT heating. It is likely that the local heat induced by the plasmonic excitation could perturb/denature the conformation of the protein corona around the nanoparticles as well as in their surrounding microenvironment so as to expose the hydrophobic amino acid residues to the nanoparticle plasmonic field.[57] The appearance of Raman vibrations mainly corresponding to phenylalanine after laser exposure (beginning around 5 min and steadily increasing) strongly supports this hypothesis. Combined with the reduction in the intensity of vibrations corresponding to the disulfide (–S–S–) bonds appearing around 500 cm^{-1}, these features suggest rupturing of the disulfide bonds induced by the plasmonic heating. This is further support for protein denaturation in the AuNP microenvironment as these aromatic amino acids are highly hydrophobic and generally found buried within proteins,[58] shielding them from solvent exposure and, accordingly, from the plasmon field of the hydrophilic AuNPs.

Table 4.1 Assignment of SERS Spectral Bands

shift (cm^{-1})	component	SERS band assignment
495-510	protein	–S–S–
640-660	protein	–C–S–
820-850	lipid and protein	lipid symmetric –O–C–C–N– stretch and Tyr
1000-1010	protein	Phe ring breathing
1020-1030	protein	Phe C–H in-plane bending and Trp ring breathing
1120-1140	lipid and protein	C–N backbone and Lipid *trans*-conformations
1170-1190	protein	C–H bend, C–C stretch, Tyr
1200-1210	protein	C_6H_5–C stretch of Phe and Tyr
1215-1225	protein	Amide III (β-sheet)
1265-1300	protein	Amide III (α-helix)
1300-1325	protein & lipid	$–CH_2$ twist
1440-1460	protein & lipid	$–CH_2$ bending (protein and lipid) and methylene deformation
1584-1592	protein	Phe

The spectral changes resulting from PPT cell death noted above are seen in cells treated with 0.20 nM NT-AuNPs and exposed to the laser operating at both 6.2 mW (**Figure 4.3**) and 9.4 mW (**Figure 4.4**) intensity. While the initial and final spectra are similar in both cases, exposure to a higher laser intensity resulted in faster loss of protein structure, evident in the more rapid loss of the disulfide peak at ~500 cm^{-1}, the exposure of phenylalanine residues at 1001 cm^{-1}, and the increase in amide III β-sheet vibration

(along with Phe, Tyr, and lipid contributions) in the 1200–1220 cm^{-1} region, relative to the amide III α-helix vibrations in the 1275–1300 cm^{-1} region (**Figure 4.5**). These ratios illustrate the drastic changes that occur during PPT-induced cell death. With more intense laser exposure, these changes began immediately and occurred rapidly, following an exponential trend. This implies that, at high enough laser intensity (9.4 mW), protein and lipid structural features begin to denature upon laser exposure. However, at the intermediate intensity (6.2 mW), an induction period was observed. Initially, the structural changes occur very slowly, but begin to increase over time, following a sigmoidal trend commonly observed in dose response studies. This implies that at this intermediate laser intensity, heat is generated slightly faster than it dissipates, leading to a slower but increasing rate of protein denaturation, while at higher intensity, these changes occur immediately.

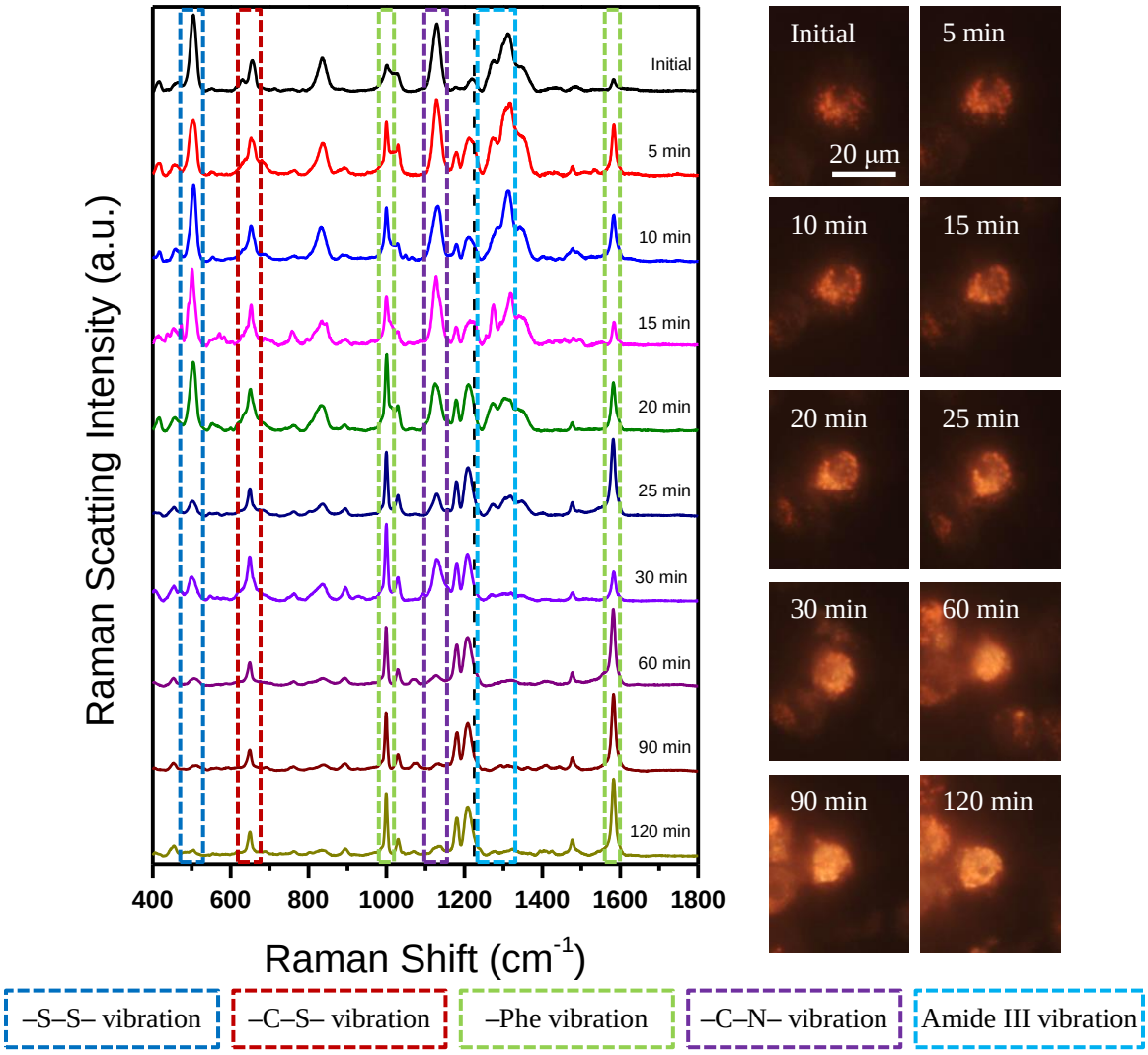

Figure 4.4 Time-dependent SERS spectra collected from a single HSC-3 cell during PPT cell death induced by continuous laser exposure at higher power (9.4 mW). The vertical line at 1225 cm^{-1} again serves as a visual guide to highlight the shift in this vibrational peak from the amide III β-confirmation to the aromatic amino acid residue peaks at 1209 cm^{-1}, which in conjunction with the disappearance of additional vibrations around 500 cm^{-1} and in the 1250–1350 cm^{-1} range signals cell death. Corresponding dark-field images for each spectrum are also shown.

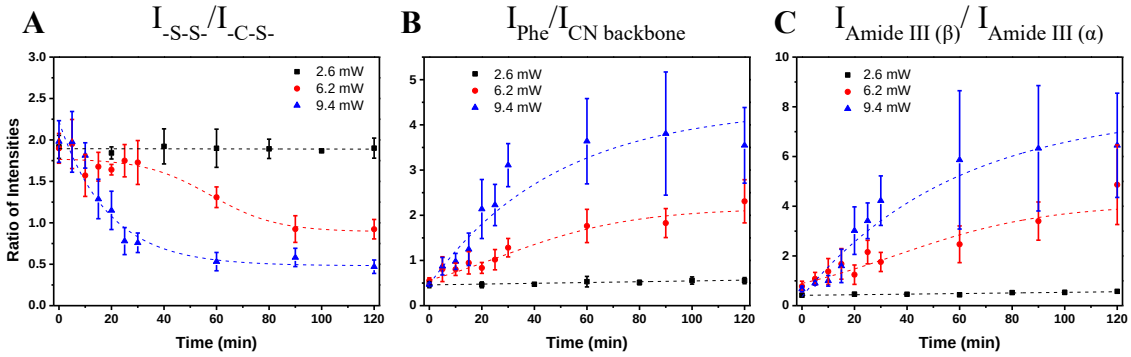

Figure 4.5 Plot showing changes in the SERS intensities for the ratio of the –S–S– and –C–S– vibrations (A), 1000 and 1130 cm^{-1} vibrations (B), and amide III β and α confirmations (C) during PPT heating at the indicated laser powers (n=4 cells).

Additionally, at lower laser intensity (2.6 mW, **Figure 4.6**) or lower NT-AuNP concentration with higher laser intensity (0.10 nM, 9.4 mW, **Figure 4.7**), these spectral changes were not observed, and the ratios in **Figure 4.5** remain relatively unchanged. This indicates that there is a critical threshold of nanoparticle concentration and laser intensity (i.e., of heat) necessary to generate PPT-induced cell death. Below this threshold, heat is most likely dissipated more rapidly than it is generated, and no major spectral changes or cell death is observed. However, when the laser intensity and nanoparticle concentration are above this threshold, heat generation outpaces heat dissipation, which results in PPT-induced cell death. It should be noted that this critical threshold for cell death is likely dictated by the number of nanoparticles internalized within the cell and degree of localization, which depends on their surface chemistry and the AuNPs absorption properties, which are primarily dictated by the size, shape, and the degree of aggregation of the nanoparticles.

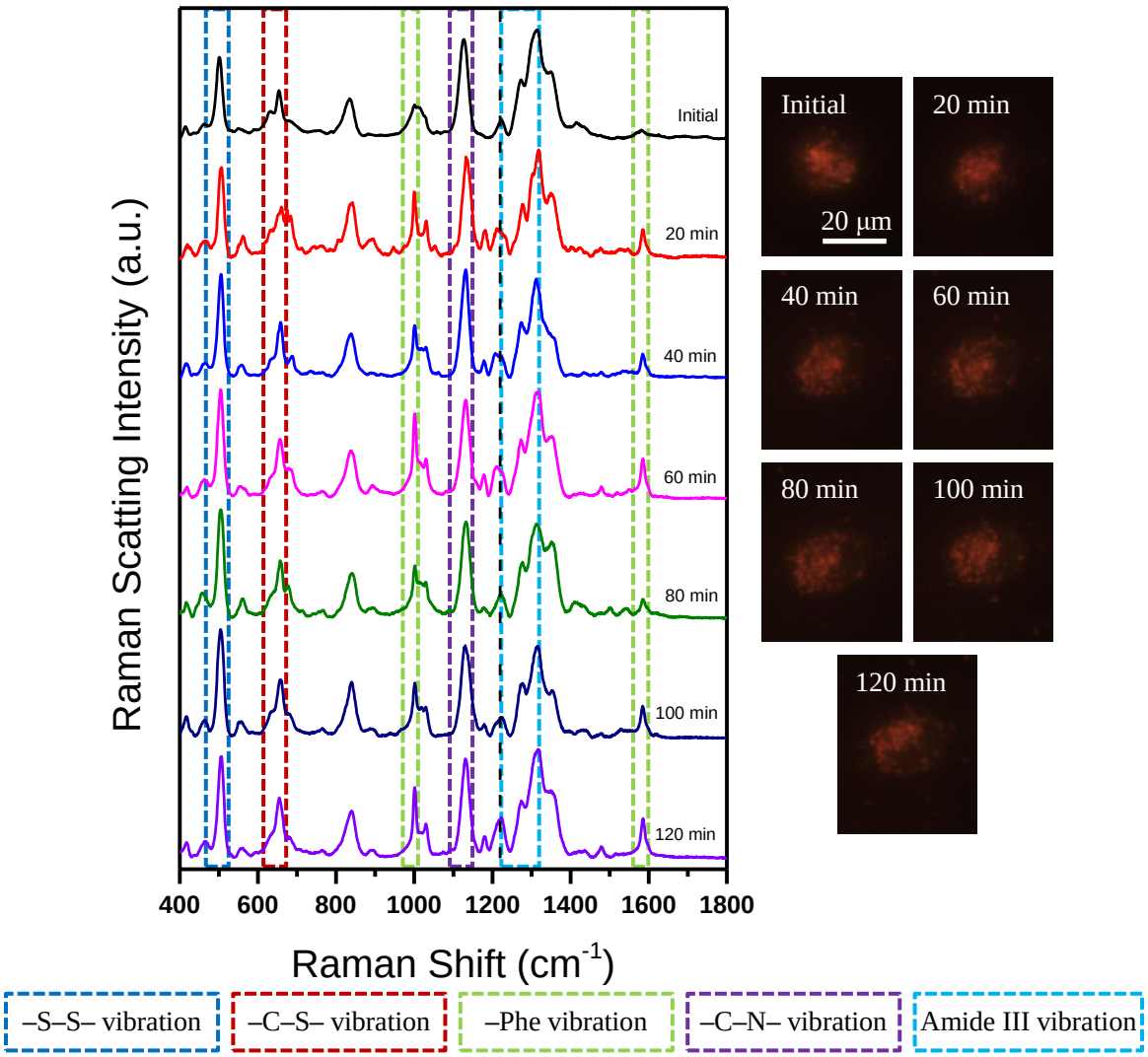

Figure 4.6 Time-dependent SERS spectra collected from a single HSC-3 cell incubated with 0.20 nM NT-AuNPs showing no PPT cell death induced by continuous laser exposure at lower power (2.6 mW). The vertical line at 1225 cm^{-1} highlights the vibrational peak from the amide III β-confirmation, which does not shift during laser exposure at low power, indicating a lack of cell death. Corresponding dark-field images for each spectrum are also shown.

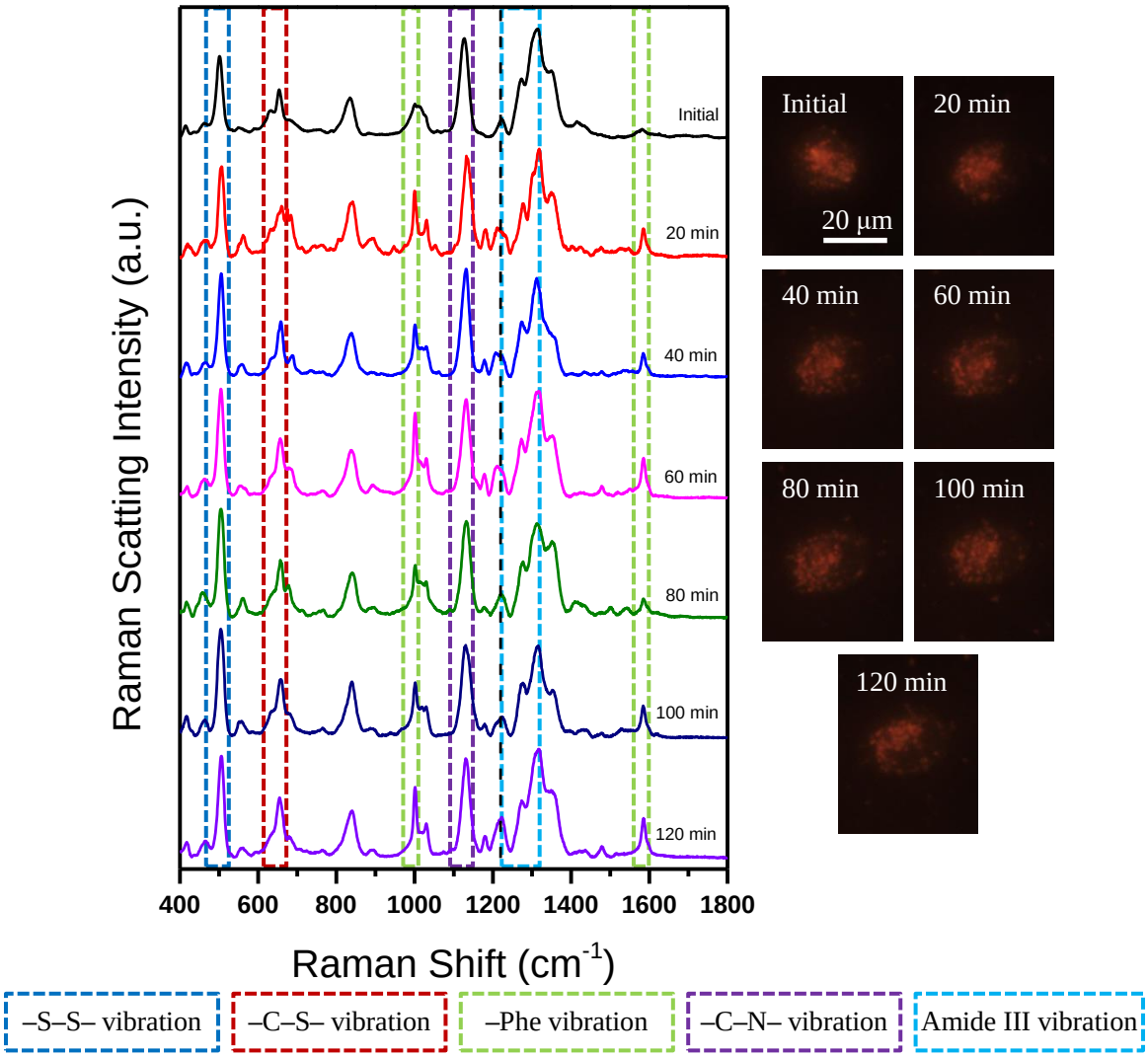

Figure 4.7 Time-dependent SERS spectra collected from a single HSC-3 cell incubated with 0.10 nM NT-AuNPs showing no PPT cell death induced by continuous laser exposure at higher power (9.4 mW). The vertical line at 1225 cm^{-1} highlights the vibrational peak from the amide III β-confirmation, which does not shift during laser exposure when lower nanoparticle concentration is used, indicating a lack of cell death. Corresponding dark-field images for each spectrum are shown.

The same spectral changes arising from PPT induced cell death can be observed by using smaller (15 nm) AuNPs modified with the same active targeting ligands (NT-

sAuNPs, **Figure 4.8**). Cell death is observed after incubation with 0.20 nM NT-sAuNPs upon exposure to both the lower (6.2 mW, **Figure 4.9**) and higher (9.4 mW, **Figure 4.10**) laser intensities previously observed to induce cell death in **Figure 4.3** and **Figure 4.4** using the larger 30 nm AuNPs. The initial SERS spectra, as well as the final spectra after 120 min laser exposure, are nearly identical to those obtained using the larger NT-AuNPs. The same vibrational peaks are also observed to change throughout the PPT heating, including loss of the –S–S– vibration at ~500 cm^{-1}, the loss of protein and lipid structural features observed at 1130 cm^{-1} and in the 1275 cm^{-1} to 1350 cm^{-1} region, the shift of the 1225 cm^{-1} vibration due to amide III β-conformation in the initial spectra toward 1209 cm^{-1} vibration of phenylalanine, and the drastic increase in aromatic amino acid vibrational peaks at 1180, 1001, and 1584 cm^{-1}. The observation of the same spectral changes with different laser intensities and different nanoparticle sizes shows the reproducibility of this technique to induce and monitor PPT cell death with actively targeted AuNPs on the single cell level. This also supports the theory that there is a critical threshold of nanoparticle concentration and laser intensity (i.e., photothermal energy) necessary to induce cell death, which occurs through the denaturation of proteins and lipids in the nanoparticles' microenvironment. Moreover, using the highly focused laser of our Raman microscope results in single-cell irradiation and cell death without affecting adjacent cells, as can be clearly seen in **Figure 4.11**. After incubation with either the smaller or larger AuNPs, only the cell of interest displays the distinct morphological changes indicative of cell death, including cell shrinkage and increased light scattering. Surrounding cells, some within a few microns of the cell being irradiated,

appear unchanged even at the highest laser intensity used in this study, confirming the single cell specificity of our technique.

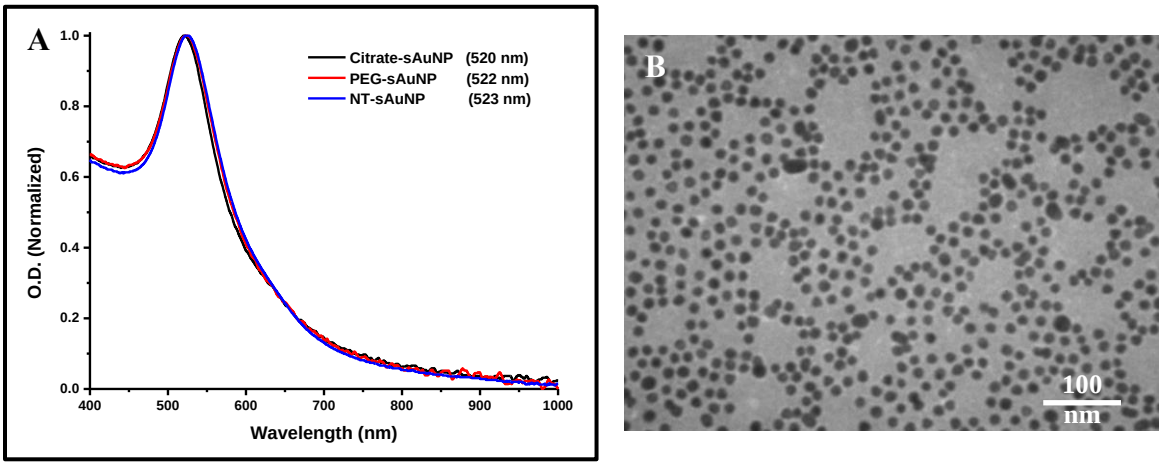

Figure 4.8 Characterization of smaller nuclear-targeted AuNPs (NT-sAuNPs). UV–Vis spectra of sAuNPs before (black) and after conjugation with PEG (red), and RGD and NLS peptides (blue) in aqueous solution. The red shift in the plasmon peak indicates successful conjugation. (B) A TEM micrograph of the 15 nm citrate stabilized sAuNPs.

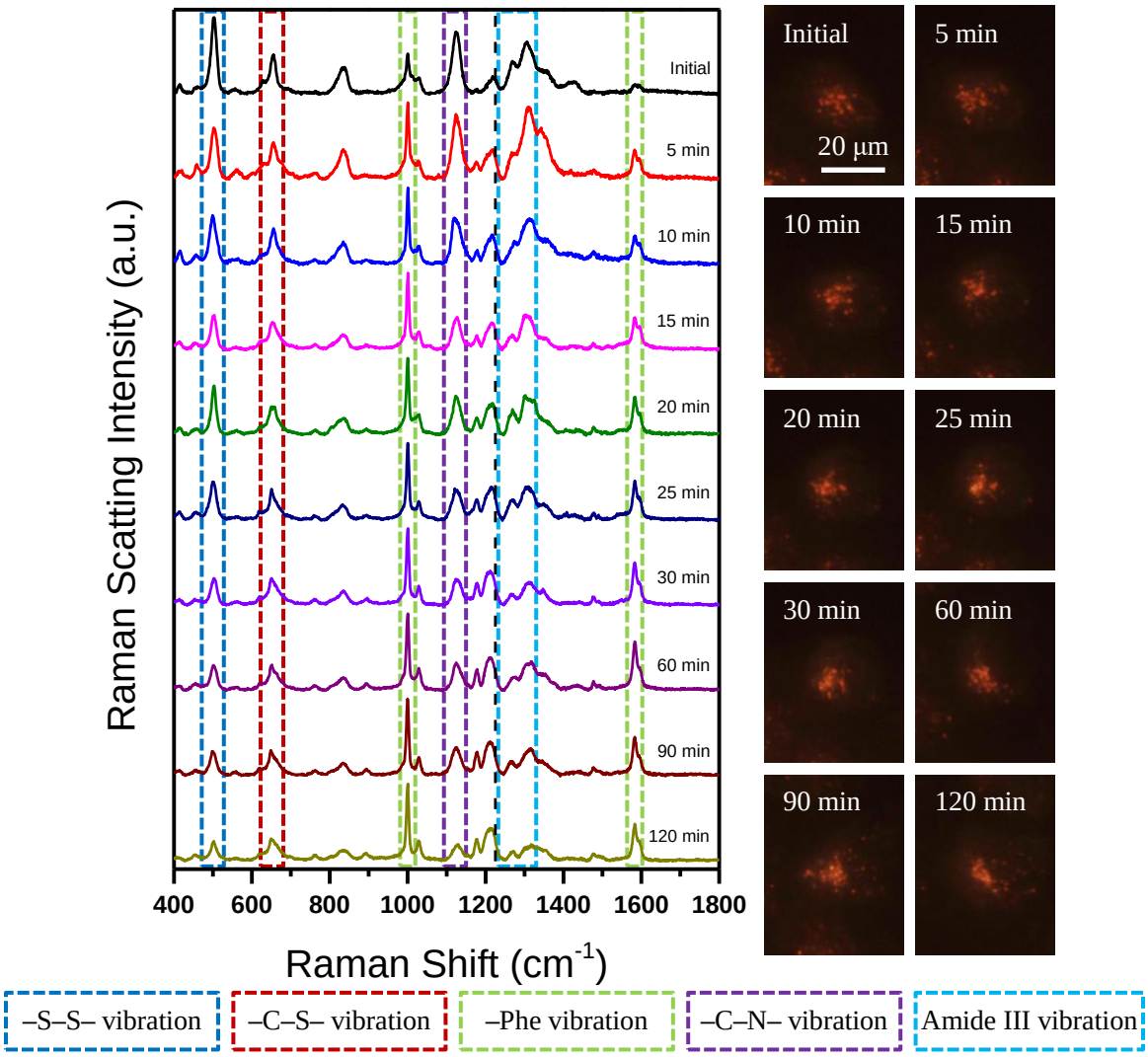

Figure 4.9 Time-dependent SERS spectra collected from a single HSC-3 cell incubated with 0.20 nM NT-sAuNPs during PPT cell death induced by continuous laser exposure at lower power (6.2 mW). The vertical line at 1225 cm^{-1} highlights the shift in this vibrational peak from the amide III β-confirmation to the aromatic amino acid peaks at 1209 cm^{-1}, which in conjunction with the disappearance of vibrations around 500 cm^{-1} and in the 1250–1350 cm^{-1} range signals cell death. Corresponding dark-field images for each spectrum are also shown.

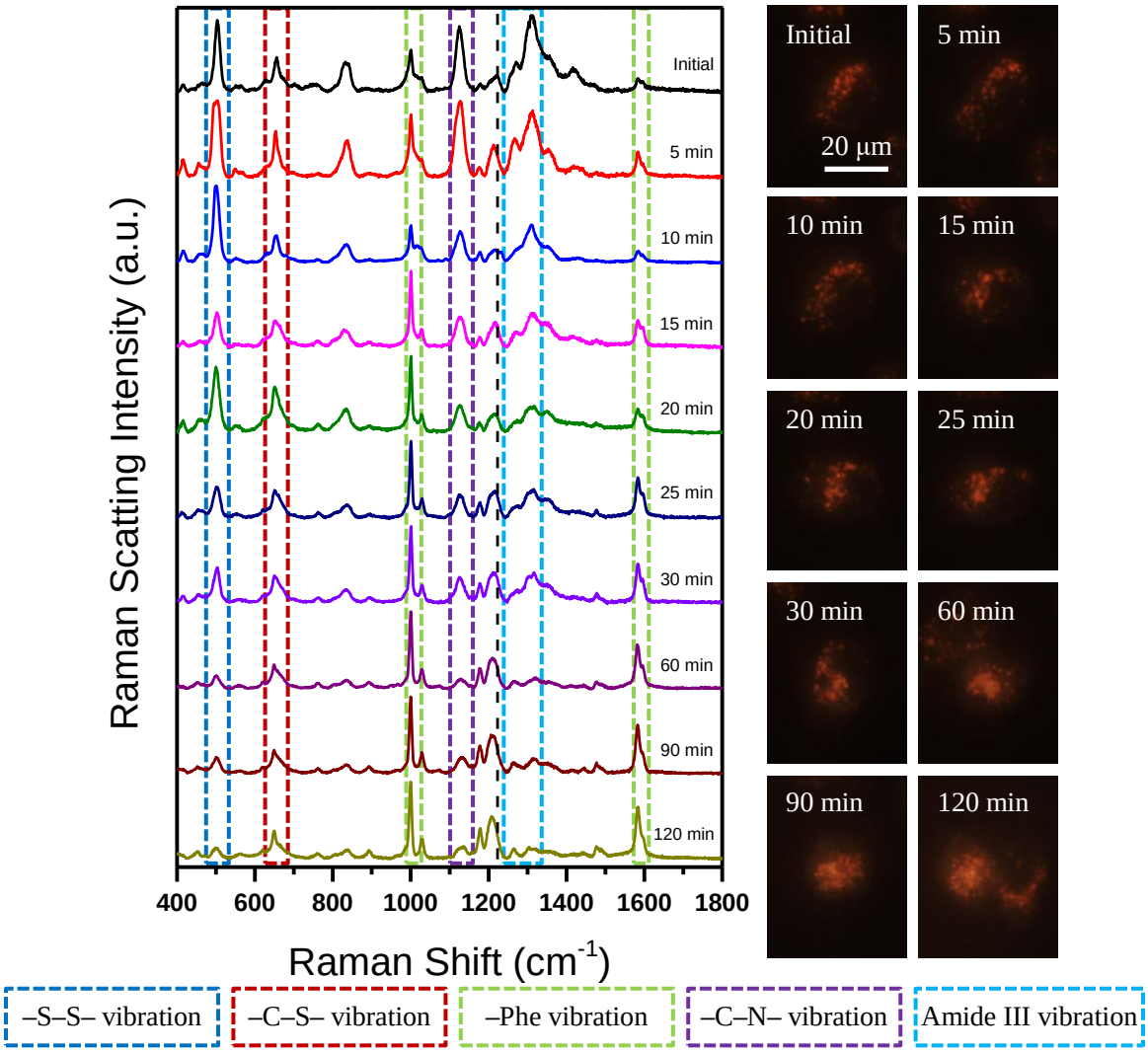

Figure 4.10 Time-dependent SERS spectra collected from a single HSC-3 cell incubated 0.20 nM NT-sAuNPs during PPT cell death induced by continuous laser exposure at higher power (9.4 mW). The vertical line at 1225 cm^{-1} highlights the shift in this vibrational peak from the amide III β-confirmation to the aromatic amino acid peaks at 1209 cm^{-1}, which in conjunction with the disappearance of additional vibrations around 500 cm^{-1} and in the 1250–1350 cm^{-1} range signals cell death. Corresponding dark-field images for each spectrum are also shown.

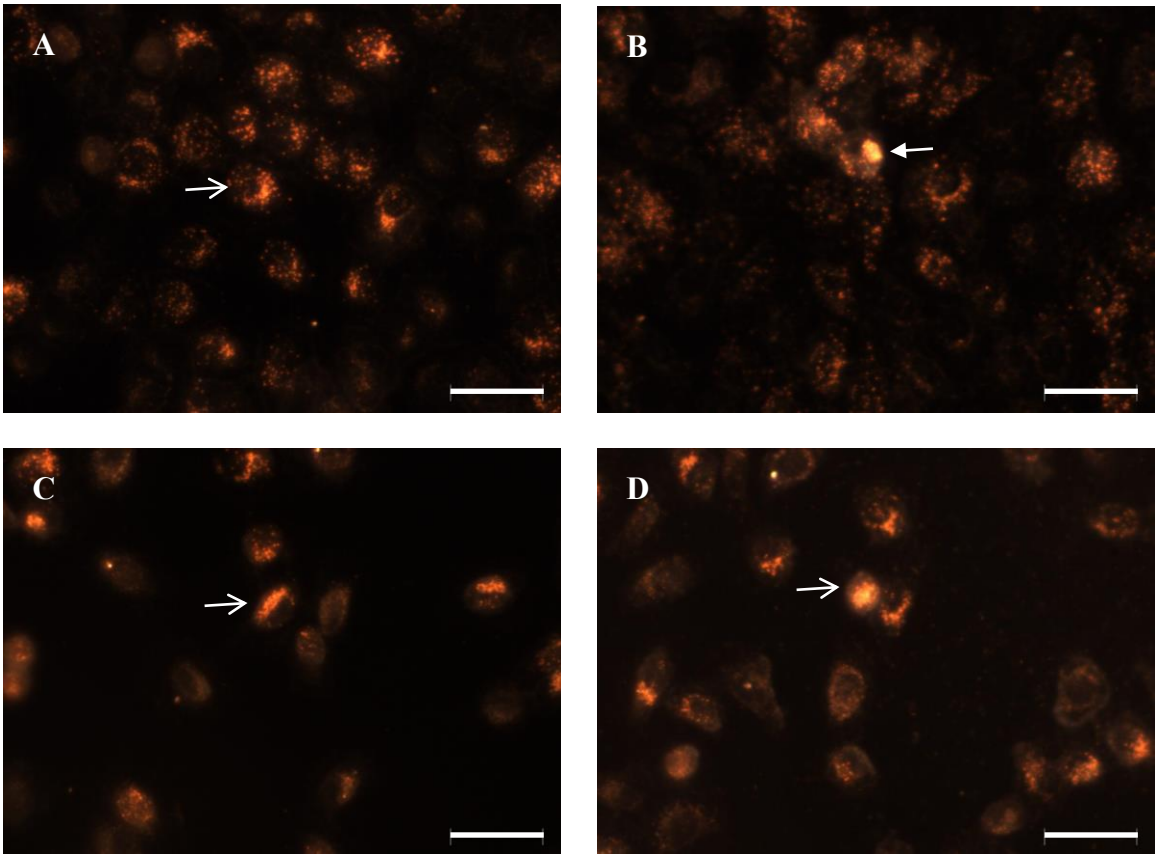

Figure 4.11 Representative dark-field scattering images of cells incubated with (A,B) 0.2 nM NT-AuNPs or (C,D) 0.20 nM NT-sAuNPs before (A,C) and after (B,D) continuous laser exposure (2 hours, 9.4 mW). White arrows denote the cell of interest. The images illustrate the single cell specificity of this method, as only the cell of interest is irradiated and displays morphological changes while surrounding cells are relatively unchanged and continue to move freely on the coverglass. The scale bar in each image is 50 μm.

Additionally, cells were incubated with 0.10 nM NT-AuNPs, and SERS spectra were collected before (**Figure 4.12A**) and after (**Figure 4.12B**) oven heating at 100 °C for 7 min. The initial spectra before oven heating were nearly identical to those obtained before PPT heating, highlighting the reproducibility of our technique across individual cells. The protein and lipid structural vibrations are again observed in the healthy cells before heating, with little contribution from the aromatic amino acid residue peaks.

However, the structural vibrations of both proteins and lipids are no longer seen after oven heating, and the aromatic amino acid vibrations again dominate the SERS spectra, which were nearly identical to the final spectra obtained after PPT-induced cell death.

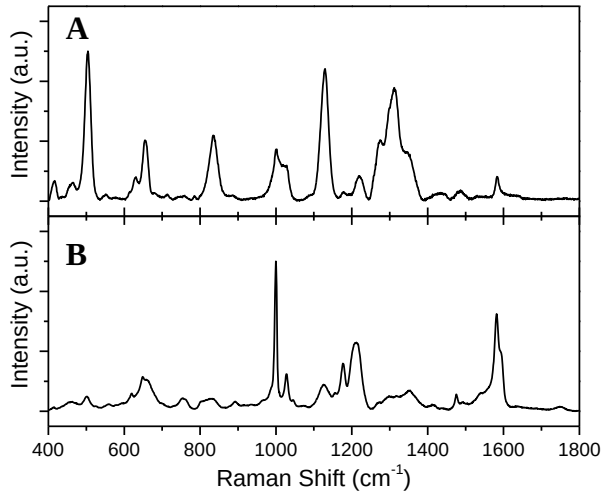

Figure 4.12 SERS spectra of HSC-3 cells incubated with 0.10 nM NT-AuNPs before (A) and after (B) oven heating at 100°C for 7 min. The spectrum shown in **part B** is consistent with those shown in **Figure 4.3** and **Figure 4.4**, displaying characteristics attributed to cell death.

To confirm cell death, we also performed flow cytometric analysis on cells incubated with 0.10 nM NT-AuNPs before (**Figure 4.13A**) and after oven heating (**Figure 4.13B**). A PI dye was used to tag necrotic cells, which have diminished membrane integrity, allowing the otherwise membrane impermeable dye to enter the necrotic cells. A FITC conjugated Annexin-V antibody was used to differentiate apoptotic cells due to its strong affinity for phosphatidylserine serine, a phospholipid found on the outer membrane of apoptotic cells. The HSC-3 cancer cells incubated with 0.10 nM NT-AuNPs were healthy before oven heating, exhibiting over 90% viability. After heating,

over 95% of the cells were undergoing necrosis/late apoptosis, as evidenced by the large increase in fluorescence intensity from both the PI and FITC dyes, confirming cell death. The similarity between the SERS spectra of oven heated cells and the PPT treated cells, combined with the observed morphological changes in those cells, confirms the death of PPT treated cells.

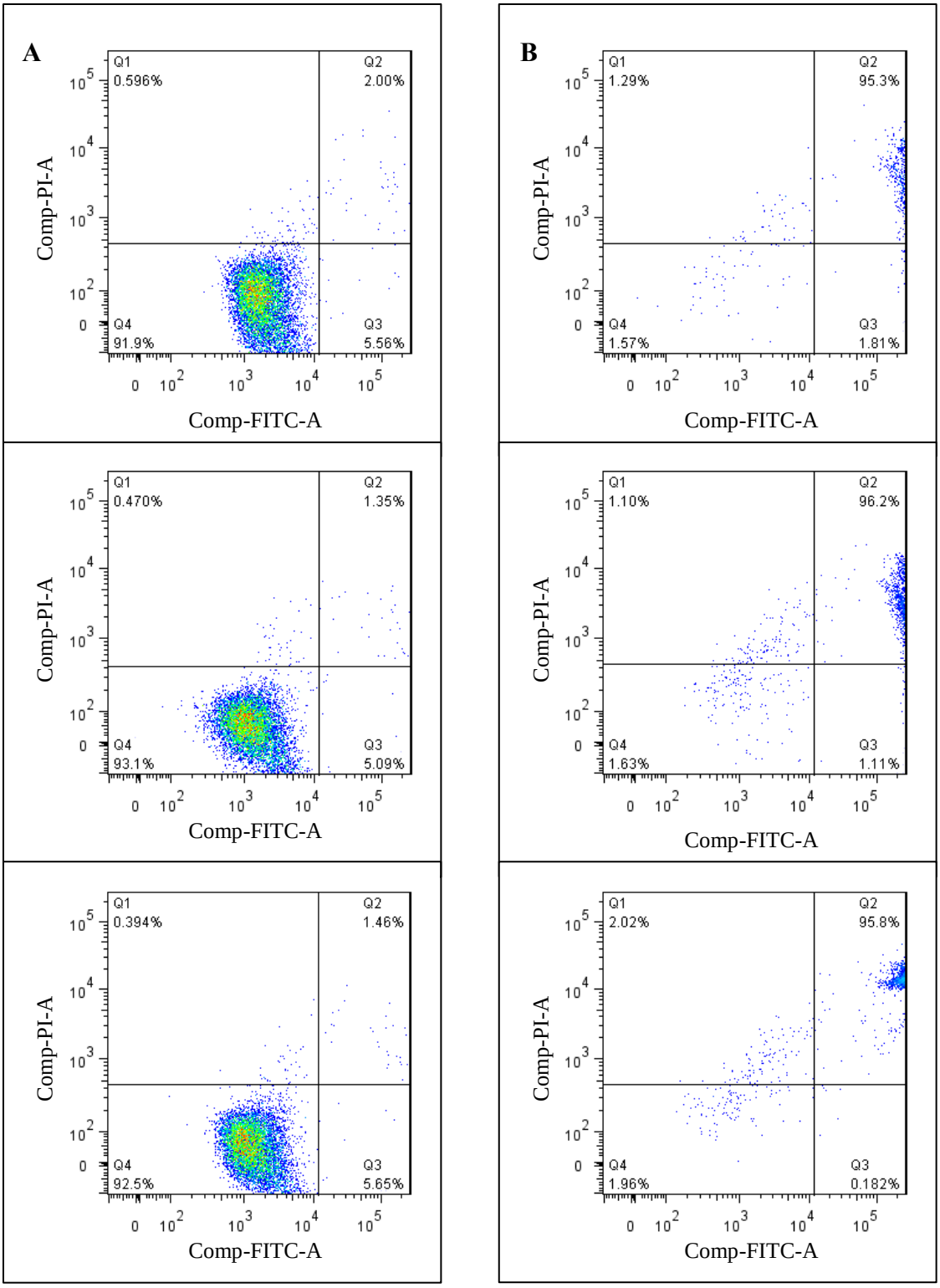
A
Q1
0.596%
Q2
2.00%
Q4
91.9%
Q3
5.56%
Comp-PI-A
Comp-FITC-A
B
Q1
1.29%
Q2
95.3%
Q4
1.57%
Q3
1.81%
Comp-PI-A
Comp-FITC-A
Q1
0.470%
Q2
1.35%
Q4
93.1%
Q3
5.09%
Comp-PI-A
Comp-FITC-A
Q1
1.10%
Q2
96.2%
Q4
1.63%
Q3
1.11%
Comp-PI-A
Comp-FITC-A
Q1
0.394%
Q2
1.46%
Q4
92.5%
Q3
5.65%
Comp-PI-A
Comp-FITC-A
Q1
2.02%
Q2
95.8%
Q4
1.96%
Q3
0.182%
Comp-PI-A
Comp-FITC-A

Figure 4.13 Flow cytometry data showing cells incubated with 0.10 nM NT-AuNPs are over 90% healthy before oven heating (A); after oven heating (B), over 95% of cells exhibit late apoptosis/necrosis as evidenced by the increase in both FITC and PI fluorescence.

4.4 Conclusion

We have used actively targeted AuNPs to induce PPT cell death upon laser exposure, and simultaneously monitor the corresponding molecular changes in real-time using SERS. We have found that continuous laser exposure of actively targeted nanoparticles internalized within cells leads to the modification of the protein and lipid structures, resulting in cell death. These alterations occur when the nanoparticle concentration/laser intensity (photothermal energy) reaches a minimum threshold. Above this critical point, cell death occurs through the same molecular changes, regardless of the nanoparticle size or laser intensity. It is important to note that cell death may still occur below this threshold, although not on the time scales studied herein. Additionally, the use of passively targeted nanoparticles would most likely result in different cell death mechanisms, as heat would be generated in the extracellular matrix surrounding the cell instead of from localized hotspots within it. Understanding the molecular mechanism of PPT cell death is crucial to understanding the treatment and optimizing its efficacy. We have presented a method to both induce and monitor this mechanism within single cells in real-time using actively targeted AuNPs.

4.5 References

(1) Aioub, M.; El-Sayed, M. A. A Real-Time Surface Enhanced Raman Spectroscopy Study of Plasmonic Photothermal Cell Death Using Targeted Gold Nanoparticles. *J. Am. Chem. Soc.* **2016,** *138*, 1258-1264.

(2) Jain, P. K.; Huang, X. H.; El-Sayed, I. H.; El-Sayed, M. A. Noble Metals on the Nanoscale: Optical and Photothermal Properties and Some Applications in Imaging, Sensing, Biology, and Medicine. *Acc. Chem. Res.* **2008,** *41*, 1578-1586.

(3) Dreaden, E. C.; Alkilany, A. M.; Huang, X. H.; Murphy, C. J.; El-Sayed, M. A. The Golden Age: Gold Nanoparticles for Biomedicine. *Chem. Soc. Rev.* **2012,** *41*, 2740-2779.

(4) Lane, L. A.; Qian, X.; Nie, S. Sers Nanoparticles in Medicine: From Label-Free Detection to Spectroscopic Tagging. *Chem. Rev.* **2015,** *115*, 10489-10529.

(5) Yang, X.; Yang, M.; Pang, B.; Vara, M.; Xia, Y. Gold Nanomaterials at Work in Biomedicine. *Chem. Rev.* **2015,** *115*, 10410-10488.

(6) O'Brien, M. N.; Jones, M. R.; Brown, K. A.; Mirkin, C. A. Universal Noble Metal Nanoparticle Seeds Realized through Iterative Reductive Growth and Oxidative Dissolution Reactions. *J. Am. Chem. Soc.* **2014,** *136*, 7603-7606.

(7) Jain, R. K.; Stylianopoulos, T. Delivering Nanomedicine to Solid Tumors. *Nat. Rev. Clin. Oncol.* **2010,** *7*, 653-664.

(8) Link, S.; El-Sayed, M. A. Spectral Properties and Relaxation Dynamics of Surface Plasmon Electronic Oscillations in Gold and Silver Nanodots and Nanorods. *J. Phys. Chem. B* **1999,** *103*, 8410-8426.

(9) Kelly, K. L.; Coronado, E.; Zhao, L. L.; Schatz, G. C. The Optical Properties of Metal Nanoparticles: The Influence of Size, Shape, and Dielectric Environment. *J. Phys. Chem. B* **2003,** *107*, 668-677.

(10) Link, S.; El-Sayed, M. A. Shape and Size Dependence of Radiative, Non-Radiative and Photothermal Properties of Gold Nanocrystals. *Int. Rev. Phys. Chem.* **2000,** *19*, 409-453.

(11) Aioub, M.; Kang, B.; Mackey, M. A.; El-Sayed, M. A. Biological Targeting of Plasmonic Nanoparticles Improves Cellular Imaging via the Enhanced Scattering in the Aggregates Formed. *J. Phys. Chem. Lett.* **2014,** *5*, 2555-2561.

(12) Kang, J. W.; So, P. T. C.; Dasari, R. R.; Lim, D. K. High Resolution Live Cell Raman Imaging Using Subcellular Organelle-Targeting SERS-Sensitive Gold Nanoparticles with Highly Narrow Intra-Nanogap. *Nano Lett.* **2015,** *15*, 1766-1772.

(13) Meyers, J. D.; Cheng, Y.; Broome, A. M.; Agnes, R. S.; Schluchter, M. D.; Margevicius, S.; Wang, X. N.; Kenney, M. E.; Burda, C.; Basilion, J. P. Peptide-Targeted

Gold Nanoparticles for Photodynamic Therapy of Brain Cancer. *Part. Part. Syst. Char.* **2015,** *32*, 448-457.

(14) Dreaden, E. C.; Mwakwari, S. C.; Sodji, Q. H.; Oyelere, A. K.; El-Sayed, M. A. Tamoxifen-Poly(Ethylene Glycol)-Thiol Gold Nanoparticle Conjugates: Enhanced Potency and Selective Delivery for Breast Cancer Treatment. *Bioconjugate Chem.* **2009,** *20*, 2247-2253.

(15) Dhar, S.; Daniel, W. L.; Giljohann, D. A.; Mirkin, C. A.; Lippard, S. J. Polyvalent Oligonucleotide Gold Nanoparticle Conjugates as Delivery Vehicles for Platinum(IV) Warheads. *J. Am. Chem. Soc.* **2009,** *131*, 14652-14653.

(16) Huang, X. H.; El-Sayed, I. H.; Qian, W.; El-Sayed, M. A. Cancer Cell Imaging and Photothermal Therapy in the near-Infrared Region by Using Gold Nanorods. *J. Am. Chem. Soc.* **2006,** *128*, 2115-2120.

(17) O'Neal, D. P.; Hirsch, L. R.; Halas, N. J.; Payne, J. D.; West, J. L. Photo-Thermal Tumor Ablation in Mice Using Near Infrared-Absorbing Nanoparticles. *Cancer Lett.* **2004,** *209*, 171-176.

(18) Perez-Hernandez, M.; del Pino, P.; Mitchell, S. G.; Moros, M.; Stepien, G.; Pelaz, B.; Parak, W. J.; Galvez, E. M.; Pardo, J.; de la Fuente, J. M. Dissecting the Molecular Mechanism of Apoptosis During Photothermal Therapy Using Gold Nanoprisms. *ACS Nano* **2015,** *9*, 52-61.

(19) Albanese, A.; Tang, P. S.; Chan, W. C. W. The Effect of Nanoparticle Size, Shape, and Surface Chemistry on Biological Systems. *Annu. Rev. Biomed. Eng.* **2012,** *14*, 1-16.

(20) Perrault, S. D.; Walkey, C.; Jennings, T.; Fischer, H. C.; Chan, W. C. W. Mediating Tumor Targeting Efficiency of Nanoparticles through Design. *Nano Lett.* **2009,** *9*, 1909-1915.

(21) Ghosh, P.; Han, G.; De, M.; Kim, C. K.; Rotello, V. M. Gold Nanoparticles in Delivery Applications. *Adv. Drug Delivery Rev.* **2008,** *60*, 1307-1315.

(22) Huang, X. H.; Kang, B.; Qian, W.; Mackey, M. A.; Chen, P. C.; Oyelere, A. K.; El-Sayed, I. H.; El-Sayed, M. A. Comparative Study of Photothermolysis of Cancer Cells with Nuclear-Targeted or Cytoplasm-Targeted Gold Nanospheres: Continuous Wave or Pulsed Lasers. *J. Biomed. Opt.* **2010,** *15*, 058002.

(23) Lowery, A. R.; Gobin, A. M.; Day, E. S.; Halas, N. J.; West, J. L. Immunonanoshells for Targeted Photothermal Ablation of Tumor Cells. *Int. J. Nanomed.* **2006,** *1*, 149-154.

(24) Rengan, A. K.; Bukhari, A. B.; Pradhan, A.; Malhotra, R.; Banerjee, R.; Srivastava, R.; De, A. In Vivo Analysis of Biodegradable Liposome Gold Nanoparticles as Efficient Agents for Photothermal Therapy of Cancer. *Nano Lett.* **2015,** *15*, 842-848.

(25) Burke, A. R.; Singh, R. N.; Carroll, D. L.; Wood, J. C. S.; D'Agostino, R. B.; Ajayan, P. M.; Torti, F. M.; Torti, S. V. The Resistance of Breast Cancer Stem Cells to Conventional Hyperthermia and Their Sensitivity to Nanoparticle-Mediated Photothermal Therapy. *Biomaterials* **2012,** *33*, 2961-2970.

(26) Chen, J. Y.; Glaus, C.; Laforest, R.; Zhang, Q.; Yang, M. X.; Gidding, M.; Welch, M. J.; Xia, Y. N. Gold Nanocages as Photothermal Transducers for Cancer Treatment. *Small* **2010,** *6*, 811-817.

(27) Tong, L.; Zhao, Y.; Huff, T. B.; Hansen, M. N.; Wei, A.; Cheng, J. X. Gold Nanorods Mediate Tumor Cell Death by Compromising Membrane Integrity. *Adv. Mater.* **2007,** *19*, 3136-3141.

(28) Kneipp, K.; Wang, Y.; Kneipp, H.; Perelman, L. T.; Itzkan, I.; Dasari, R.; Feld, M. S. Single Molecule Detection Using Surface-Enhanced Raman Scattering (SERS). *Phys. Rev. Lett.* **1997,** *78*, 1667-1670.

(29) Nie, S. M.; Emory, S. R. Probing Single Molecules and Single Nanoparticles by Surface-Enhanced Raman Scattering. *Science* **1997,** *275*, 1102-1106.

(30) Turkevich, J.; Stevenson, P. C.; Hillier, J. A Study of the Nucleation and Growth Processes in the Synthesis of Colloidal Gold. *Discuss Faraday Soc.* **1951**, 55-75.

(31) Frens, G. Controlled Nucleation for Regulation of Particle-Size in Monodisperse Gold Suspensions. *Nat., Phys. Sci.* **1973,** *241*, 20-22.

(32) Xue, H.; Atakilit, A.; Zhu, W. M.; Li, X. W.; Ramos, D. M.; Pytela, R. Role of the αvβ6 Integrin in Human Oral Squamous Cell Carcinoma Growth in Vivo and in Vitro. *Biochem. Biophys. Res. Commun.* **2001,** *288*, 610-618.

(33) Aioub, M.; Austin, L. A.; El-Sayed, M. A. Determining Drug Efficacy Using Plasmonically Enhanced Imaging of the Morphological Changes of Cells Upon Death. *J. Phys. Chem. Lett.* **2014,** *5*, 3514-3518.

(34) Zitzmann, S.; Ehemann, V.; Schwab, M. Arginine-Glycine-Aspartic Acid (RGD)-Peptide Binds to Both Tumor and Tumor-Endothelial Cells in Vivo. *Cancer Res.* **2002,** *62*, 5139-5143.

(35) Tkachenko, A. G.; Xie, H.; Liu, Y. L.; Coleman, D.; Ryan, J.; Glomm, W. R.; Shipton, M. K.; Franzen, S.; Feldheim, D. L. Cellular Trajectories of Peptide-Modified Gold Particle Complexes: Comparison of Nuclear Localization Signals and Peptide Transduction Domains. *Bioconjugate Chem.* **2004,** *15*, 482-490.

(36) Jain, P. K.; El-Sayed, M. A. Surface Plasmon Coupling and Its Universal Size Scaling in Metal Nanostructures of Complex Geometry: Elongated Particle Pairs and Nanosphere Trimers. *J. Phys. Chem. C* **2008,** *112*, 4954-4960.

(37) Huang, D.; Byers, C. P.; Wang, L. Y.; Hoggard, A. L.; Hoenee, B.; Dominguez-Medina, S.; Chen, S. S.; Chang, W. S.; Landes, C. F.; Link, S. Photoluminescence of a Plasmonic Molecule. *ACS Nano* **2015,** *9*, 7072-7079.

(38) Vanwart, H. E.; Lewis, A.; Scheraga, H. A.; Saeva, F. D. Disulfide Bond Dihedral Angles from Raman Spectroscopy. *Proc. Natl. Acad. Sci. U.S.A.* **1973,** *70*, 2619-2623.

(39) Vanwart, H. E.; Scheraga, H. A. Raman-Spectra of Strained Disulfides - Effect of Rotation About Sulfur-Sulfur Bonds on Sulfur-Sulfur Stretching Frequencies. *J. Phys. Chem.* **1976,** *80*, 1823-1832.

(40) Kang, B.; Austin, L. A.; El-Sayed, M. A. Observing Real-Time Molecular Event Dynamics of Apoptosis in Living Cancer Cells Using Nuclear-Targeted Plasmonically Enhanced Raman Nanoprobes. *ACS Nano* **2014,** *8*, 4883-4892.

(41) Ding, F.; Jha, R. K.; Dokholyan, N. V. Scaling Behavior and Structure of Denatured Proteins. *Structure* **2005,** *13*, 1047-1054.

(42) Maiti, N. C.; Apetri, M. M.; Zagorski, M. G.; Carey, P. R.; Anderson, V. E. Raman Spectroscopic Characterization of Secondary Structure in Natively Unfolded Proteins: Alpha-Synuclein. *J. Am. Chem. Soc.* **2004,** *126*, 2399-2408.

(43) Panikkanvalappil, S. R.; Hira, S. M.; Mahmoud, M. A.; El-Sayed, M. A. Unraveling the Biomolecular Snapshots of Mitosis in Healthy and Cancer Cells Using Plasmonically-Enhanced Raman Spectroscopy. *J. Am. Chem. Soc.* **2014,** *136*, 15961-15968.

(44) Asher, S. A.; Johnson, C. R.; Ludwig, M. UV Resonance Raman Studies of Aromatic-Amino-Acids and Proteins. *Biophys. J.* **1986,** *49*, A331-A331.

(45) Willets, K. A. Surface-Enhanced Raman Scattering (SERS) for Probing Internal Cellular Structure and Dynamics. *Anal. Bioanal. Chem.* **2009,** *394*, 85-94.

(46) Thomas, G. J. Raman Spectroscopy of Protein and Nucleic Acid Assemblies. *Annu. Rev. Biophys. Biomol. Struct.* **1999,** *28*, 1-27.

(47) Wei, F.; Zhang, D. M.; Halas, N. J.; Hartgerink, J. D. Aromatic Amino Acids Providing Characteristic Motifs in the Raman and Sers Spectroscopy of Peptides. *J. Phys. Chem. B* **2008,** *112*, 9158-9164.

(48) Premasiri, W. R.; Lee, J. C.; Ziegler, L. D. Surface-Enhanced Raman Scattering of Whole Human Blood, Blood Plasma, and Red Blood Cells: Cellular Processes and Bioanalytical Sensing. *J. Phys. Chem. B* **2012,** *116*, 9376-9386.

(49) Zheng, R.; Zheng, X. J.; Dong, J.; Carey, P. R. Proteins Can Convert to Beta-Sheet in Single Crystals. *Protein Sci.* **2004,** *13*, 1288-1294.

(50) Wu, H. W.; Volponi, J. V.; Oliver, A. E.; Parikh, A. N.; Simmons, B. A.; Singh, S. In Vivo Lipidomics Using Single-Cell Raman Spectroscopy. *Proc. Natl. Acad. Sci. U.S.A.* **2011,** *108*, 3809-3814.

(51) Puppels, G. J.; Demul, F. F. M.; Otto, C.; Greve, J.; Robertnicoud, M.; Arndtjovin, D. J.; Jovin, T. M. Studying Single Living Cells and Chromosomes by Confocal Raman Microspectroscopy. *Nature* **1990,** *347*, 301-303.

(52) Lippert, J. L.; Peticolas, W. L. Laser Raman Investigation of Effect of Cholesterol on Conformational Changes in Dipalmitoyl Lecithin Multilayers. *Proc. Natl. Acad. Sci. U.S.A.* **1971,** *68*, 1572-1576.

(53) Premasiri, W. R.; Moir, D. T.; Klempner, M. S.; Krieger, N.; Jones, G.; Ziegler, L. D. Characterization of the Surface Enhanced Raman Scattering (SERS) of Bacteria. *J. Phys. Chem. B* **2005,** *109*, 312-320.

(54) Asher, S. A.; Ianoul, A.; Mix, G.; Boyden, M. N.; Karnoup, A.; Diem, M.; Schweitzer-Stenner, R. Dihedral Psi Angle Dependence of the Amide III Vibration: A Uniquely Sensitive UV Resonance Raman Secondary Structural Probe. *J. Am. Chem. Soc.* **2001,** *123*, 11775-11781.

(55) Rygula, A.; Majzner, K.; Marzec, K. M.; Kaczor, A.; Pilarczyk, M.; Baranska, M. Raman Spectroscopy of Proteins: A Review. *J. Raman Spectrosc.* **2013,** *44*, 1061-1076.

(56) Stone, N.; Kendall, C.; Smith, J.; Crow, P.; Barr, H. Raman Spectroscopy for Identification of Epithelial Cancers. *Faraday Discuss.* **2004,** *126*, 141-157.

(57) Pustovalov, V. K.; Smetannikov, A. S.; Zharov, V. P. Photothermal and Accompanied Phenomena of Selective Nanophotothermolysis with Gold Nanoparticles and Laser Pulses. *Laser Phys. Lett.* **2008,** *5*, 775-792.

(58) Schlamadinger, D. E.; Gable, J. E.; Kim, J. E. Hydrogen Bonding and Solvent Polarity Markers in the UV Resonance Raman Spectrum of Tryptophan: Application to Membrane Proteins. *J. Phys. Chem. B* **2009,** *113*, 14769-14778.

CHAPTER 5. PLATINUM-COATED GOLD NANORODS: EFFICIENT REACTIVE OXYGEN SCAVENGERS THAT PREVENT OXIDATIVE DAMAGE TOWARD HEALTHY, UNTREATED CELLS DURING PPT [1]

(Adapted with permission from Aioub, M.; Panikkanvalappil, S. R.; El-Sayed, M. A. Platinum-Coated Gold Nanorods: Efficient Reactive Oxygen Scavengers That Prevent Oxidative Damage toward Healthy, Untreated Cells During Plasmonic Photothermal Therapy. *ACS Nano* **2017,** *11,* 579-586. Copyright 2017 American Chemical Society.)

As a minimally invasive therapeutic strategy, gold nanorod (AuNR) -based plasmonic photothermal therapy (PPT) has shown significant promise for the selective ablation of cancer cells. However, the heat stress experienced by cells during the PPT treatment produces significant amounts of reactive oxygen species (ROS), which could harm healthy, untreated tissue near the point of care by inducing irreversible damage to DNA, lipids, and proteins, potentially causing cellular dysfunction or mutation. In this study, we utilized biocompatible Pt-coated AuNRs (PtAuNRs) with different platinum shell thicknesses as an alternative to AuNRs often used for the treatment. We show that the PtAuNRs maintain the efficacy of traditional AuNRs for inducing cell death while scavenging the ROS formed as a byproduct during PPT treatment, thereby protecting healthy, untreated cells from indirect death resulting from ROS formation. The synergistic effect of PtAuNRs in effectively killing cancer cells through hyperthermia with the simultaneous removal of heat stress induced ROS during PPT was validated *in vitro* using cell viability and fluorescence assays. Our results suggest that the high photothermal efficiency and ROS-scavenging activity of PtAuNRs makes them ideal

candidates to improve the therapeutic efficacy of PPT treatment while reducing the risk of undesired side effects due to heat-stress-induced ROS formation.

5.1 Introduction

As biomedical applications of nanoparticles have increased greatly in recent years, plasmonic photothermal therapy (PPT)[2-3] has emerged as an effective and minimally invasive strategy to selectively target and kill malignant cells. PPT involves the delivery of plasmonic nanomaterials to the cancerous cells, where they absorb light and convert it into heat, greatly increasing the temperature at the nanoparticles' surface and within the local tumor microenvironment.[4-5] Gold nanoparticles (AuNPs) are among the most heavily studied PPT materials due to their strong optical absorption properties, the variety of chemical synthetic methods to produce well-controlled sizes and shapes, and their relatively low toxicity.[6-9] These properties have also led to many biomedical applications of AuNPs, including sensing,[10-12] optical[13-15] and acoustic imaging,[16-17] and drug delivery,[18-19] in addition to PPT[20-22] and photodynamic therapy, which often combines PPT with the use of photosensitizing agents or drugs.[23-24]

The optical properties of gold nanostructures arise from their localized surface plasmon resonance (LSPR), which can be easily tuned by adjusting the size and shape of the nanoparticle.[25-27] Significant efforts have gone into synthesizing nanoparticle geometries with LSPR bands in the near infrared (NIR) region, including nanorods,[2-3] nanoshells,[7, 28] nanocages,[29-30] and nanoprisms.[31-32] NIR absorption is highly desirable as biological tissue, specifically water and hemoglobin, display minimal light absorption within this region of the electromagnetic spectrum, often referred to as the "NIR

(biological) window". Gold nanorods (AuNRs), in particular, are considered an excellent candidate for PPT as they display an inherently high absorbance–to–scattering ratio, a prerequisite for efficient photothermal conversion, and their LSPR band is easily tunable for NIR absorption by simply adjusting the silver content during their synthesis.[2-3, 5, 33]

Despite the increasing utility of PPT as an effective cancer treatment, the interplay between thermally induced cell death and chemically induced cell death, through the formation of reactive oxygen species (ROS) during PPT treatment, has not been well studied. Oxidative stress has increasingly been implicated as a component of numerous degenerative diseases (*e.g.* Alzheimer's, autoimmune diseases such as RA, *etc.*) as well as progressive diseases such as cancer.[34-35] It has also been established that ROS can be produced in response to heat stress and during PPT treatment.[36-39] While ROS play a crucial role in endogenous processes, such as cell signaling and proliferation,[40] ROS can also potentially interact with neighboring healthy tissues, causing irreversible damage to DNA, proteins and lipids, leading to dysfunction and unwanted, off-target cell death.[41-42] Thus, introducing additional features to current PPT materials to maintain efficacy while minimizing potential side effects from ROS mediated cell death is highly desirable.

In this work, we address the utility of platinum-coated gold nanorods as a material for efficient PPT in cancer treatment that induces thermal cell death while simultaneously scavenging ROS. Platinum is one of the most common metals used to catalyze the reduction of oxygen, with applications ranging from fuel cells to the decomposition of peroxides. Platinum nanoparticles are also well-known for their antioxidant activity.[43-46] As a catalyst for oxygen reduction, a high surface-to-volume ratio is highly desirable to

maximize activity while minimizing metal loading. To this end, we synthesized small AuNRs and coated the tips with thin platinum shell layers following the method developed by Liz-Marzan *et al.*[47-48] Platinum-coated AuNRs (PtAuNRs) were synthesized with two different shell thicknesses to compare the effect of increasing platinum concentration on their biocompatibility and ability to scavenge ROS to reduce the potentially harmful side effects of the reactive oxygen species on healthy, untreated cells. Conjugation of poly(ethylene) glycol to the nanorods (NRs) mitigated their cytotoxicity and allowed for passive targeting of the nanocrystals. We also show that all NR compositions induce significant PPT cell death upon short, 1 min irradiation with an 808 nm NIR continuous wave (cw) laser. Within 30 s of irradiation, the temperature of all NR-containing solution surpassed 46°C, the temperature necessary to induce hyperthermia-mediated cell death.[49] The Pt shells successfully scavenged the ROS produced in response to the heat stress during PPT treatment. Upon addition of the PPT-treated media to healthy, untreated control cells, the solutions with PtAuNRs or without any NRs showed no toxicity, while the residual ROS from the AuNR-treated media induced cytotoxicity toward the healthy cells. Additionally, while the thicker platinum shell reduced ROS in both the laser-treated and untreated samples, the thinner shell did not alter basal ROS levels. These studies indicate the efficacy of PtAuNRs to induce hyperthermia-mediated cell death during PPT while reducing potential side effects on healthy cells from the ROS produced during treatment.

5.2 Methods

5.2.1 Materials

Gold(III) chloride trihydrate ($HAuCl_4 \cdot 3H_2O$), cetyltrimethylammonium bromide (CTAB), silver nitrate ($AgNO_3$), ascorbic acid, sodium borohydride ($NaBH_4$), potassium tetrachloroplatinate(II) (K_2PtCl_4), and 2,7-dichlorofluorescein diacetate (DCFDA) were purchased from Sigma-Aldrich. Methoxypoly(ethylene glycol)thiol (PEG, MW 5000) was purchased from Laysan Bio, Inc. Dulbecco's phosphate buffered saline (PBS), Dulbecco's modified Eagle's medium (DMEM), antibiotic/antimycotic solution, fetal bovine serum (FBS), and 0.25% trypsin/2.2 mM EDTA were purchased from VWR. The XTT cell viability assay kit was purchased from Biotium, Inc.

5.2.2 Instrumentation

Transmission electron microscope (TEM) images were taken using a JEOL 100CX-2 microscope. Average nanoparticle particle diameter was measured using ImageJ software. High-angle annular dark-field images and energy-dispersive X-ray spectroscopy (EDX) elemental line scans were obtained using an FEI Tecnai F30 TEM. UV–Vis spectra were collected using an Ocean Optics HR4000CG-UV-NIR spectrometer. Extinction coefficients were determined by inductively coupled plasma-atomic emission spectroscopy (ICP-AES) on a Varian Vista AX simultaneous spectrometer. An 808 nm cw laser (~5 W/cm^2) was used for PPT-heating experiments. The increase in solution temperature with PPT heating was measured by placing a 33 gauge thermocouple (OMEGA Engineering, Inc.) directly into the solutions. Fluorescence measurements were collected using a QuantaMaster 40 fluorimeter (Photon

Technology International). Zeta potentials of NR solutions in water were measured using a Malvern Zetasizer Nano Z.

5.2.3 Gold Nanorod Synthesis, Platinum Coating, and Functionalization

Gold nanorods (AuNRs) were synthesized following the seedless growth method by Samal *et al*.[50] A growth solution was first prepared with 100 mL of 100 mM CTAB, 4.25 mL of 10 mM $HAuCl_4$, 625 μL of 10 mM $AgNO_3$, and 675 μL of 100 mM ascorbic acid. After mixing, 1 mL of $NaBH_4$ (1 mM) was added and the solution was kept undisturbed at 25°C for 4 h. The AuNRs were used as prepared for further Pt coating experiments.

Pt-coated AuNRs (PtAuNRs) were prepared following the synthetic protocol developed by Liz-Marzan *et al.* with slight modification.[47-48] One milliliter of CTAB (100 mM) was added to 10 mL of the freshly prepared AuNR solution (~1.5 optical density (OD)). Next, 100 μL of 10 mM K_2PtCl_4 was added, followed by 200 μL of ascorbic acid (100 mM). The solution was kept at 40°C for 5 h, which resulted in the formation of $Pt_{13}Au_{87}$NRs (13% Pt, 87% Au as determined by ICP-AES). For $Pt_{20}Au_{80}$NRs, the solution was kept at 40°C for 12 h to obtain NRs with higher Pt content.

All NR solutions were purified by centrifugation for 10 min at 12000*g* and redispersed in deionized (DI) water twice to remove excess CTAB. The NRs were then conjugated with PEG to increase stability and biocompatibility.[51] A 1.0 mM aqueous solution of PEG was added at a 10000:1 molar ratio of PEG/NRs, and the PEG-NR solutions were shaken overnight at room temperature. NR solutions were again purified by centrifugation and redispersed in DI water, and PEG was added a second time at a

10000:1 molar ratio. The PEGylated NRs were centrifuged (12000*g*, 15 min) to remove unbound PEG molecules and dispersed in DI water.

5.2.4 Cell Culture

Human oral squamous carcinoma (HSC3) cells were used as our cancer model, and human keratinocytes (HaCat) cells were used as a healthy control. The cells were cultured in Dulbecco's modified Eagle's medium (DMEM) supplemented with 10% v/v FBS and 1% v/v antibiotic. Cell cultures were maintained in a humidified 37°C incubator with a 5% CO_2 atmosphere.

5.2.5 Photothermal Heating of NR Solutions

PEG-conjugated NRs (AuNRs, $Pt_{13}Au_{87}$NRs, or $Pt_{20}Au_{80}$NRs) were diluted to ODs of 0.5 in cell culture media. A 100 μL volume of NR solutions was then added to 96 well plates to mimic the cellular experiments. The NR solutions were then exposed to the 808 nm laser for increasing irradiation times and the temperature measured by directly placing a thermocouple into the solutions. To ensure uniformity, the initial temperature of all solutions was 35 ± 1 °C. Three independent experiments were performed and the mean ± s.d. of the thermal responses (over 5 min laser exposure) was fit using an exponential function.

5.2.6 Synthesis of 2,7 -Dichlorofluorescein (DCF):

DCF was prepared from 2,7-dichlorofluorescin diacetate (DCFDA) by mixing 0.5 mL of 1.0 mM DCFDA in methanol with 2.0 mL of 0.01 M NaOH. The solution was kept at 37°C for 30 min to deacetylate the DCFDA, producing the nonfluorescent

dichlorofluorescin (H_2DCF). The resultant mixture was then neutralized with 10 mL of 25 mM NaH_2PO_4 and stored in the dark at −20°C until use. In the presence of ROS, H_2DCF is oxidized to the fluorescent DCF molecule.

5.2.7 Cell Viability Assays and ROS Measurement

For PPT studies, the HSC3 cells were grown overnight in 96-well tissue culture plates. Upon reaching 70% confluence, the growth media was replaced with media containing PEG-conjugated NRs (AuNRs, $Pt_{13}Au_{87}$NRs, or $Pt_{20}Au_{80}$NRs) at optical densities of 0.5. After 1 h of incubation, the cells were exposed to the 808 nm laser for 1 min. The cells were incubated for another 30 min with the NR solutions and then the media was aspirated and replaced with culture media containing the XTT cell viability assay solution. The viability of the PPT treated HSC3 cells was then determined according to the manufacturer's protocol.

Following PPT treatment, the ROS levels in cell culture media were determined by incubating HSC3 cells with culture media containing NRs and exposing the samples to the NIR laser as previously described. After PPT treatment, the laser treated media was removed from the cells and centrifuged at 20000*g* to pellet the NRs. Then, 300 μL of the cell media supernatant solution was added to 100 μL of H_2DCF (1 mM) and 1.1 mL of PBS. The solutions were incubated in the dark for 30 min at room temperature, and the fluorescence of the oxidized DCF was measured using an excitation wavelength of 495 nm and emission of ~525 nm.

Finally, the toxicity of the PPT-treated cell culture media on healthy (untreated) cells was determined. HaCat cells were seeded in 96 well culture plates for a final

confluence of 70% and allowed to adhere overnight. Following PPT treatment of the HSC3 cells described previously, the aspirated media was centrifuged at 20000*g* to remove the NRs. The HaCat culture media was then replaced with the aspirated laser-treated media and incubated for 24 h. The laser-treated media was then replaced with cell culture media containing the XTT solution, and the viability of the HaCat cells was determined as before.

5.2.8 Nanorod Uptake Assay

The % of NRs taken up by HSC3 cells was determined as previously reported.[13] Briefly, cells were seeded in 96-well tissue culture plates and allowed to adhere overnight. The growth media was then replaced with culture medium containing PEG-conjugated NRs (AuNRs, $Pt_{13}Au_{87}$NRs, or $Pt_{20}Au_{80}$NRs) at optical densities of 0.5. After 2 h of incubation with the NRs, the nanoparticle culture medium was removed to a new microplate and the optical density measured at the LSPR peaks of the NR solutions (768 nm, 820 nm, or 879 nm). The OD of the NR solutions was then subtracted from that initially added to the cell culture to determine cellular uptake and converted to a percentage of that initially added.

5.2.9 Statistical Analysis

Results are expressed as the average ± standard deviation of 3-5 independent experiments. Statistical significance was calculated using a t-test or analysis of variance (ANOVA) calculator (GraphPad Software, Inc.) and denoted by a * ($p < 0.05$).

5.3 Results and Discussion

PPT using AuNPs as NIR light absorbers is increasingly studied as a potential cancer therapeutic strategy. The absorbed light is rapidly converted to heat, leading to large increases in temperature around the AuNPs, inducing cell death from hyperthermia. AuNRs are heavily studied due to their extremely high absorption cross section and easily tunable LSPR band, which can be shifted within the NIR by simply adjusting the NR aspect ratio (AR). Passive targeting using the enhanced permeability and retention (EPR) effect results in accumulation of the AuNRs within tumors.[52] The AuNRs are then exposed to NIR light, the intensity and duration of which, along with the NR optical properties (*i.e.*, absorption cross section), dictate the mechanism of cell death from PPT treatment. During PPT treatment, significant amounts of ROS are produced, which can damage DNA, proteins, and lipids in nearby healthy, untreated cells, resulting in the death of healthy tissues. In order to address this issue, we developed a PPT platform which utilizes hybrid nanorods prepared by depositing thin Pt shells on the tips of AuNRs. We show that PtAuNRs retain similar photothermal properties as the parent AuNRs, inducing cell death from hyperthermia, while effectively scavenging the ROS that are produced during PPT treatment. We compared the heating efficiency of AuNRs to PtAuNRs with increasing shell thicknesses and found that the Pt coating on the AuNRs surface did not significantly reduce their photothermal efficiency. Importantly, the reduction of ROS produced during PPT treatment mitigates the toxicity of the laser-treated culture media toward healthy, untreated cells.

Small AuNRs, generally synthesized through seedless techniques, have previously been shown to be more efficient PPT agents than larger NRs synthesized through the

more common seeded growth methods.[4] Accordingly, small AuNRs were synthesized for this study using the seedless method reported by Samal *et al*.[50] The AuNRs displayed an LSPR band at 766 nm (**Figure 5.1**) with a length of 25.6 ± 4.0 nm and width of 6.9 ± 1.1 nm (AR of 3.7 ± 0.4), as shown in **Figure 5.2A** and outlined in **Table 5.1**. In order to investigate the formation of ROS and the role of PtAuNRs in scavenging ROS formed during PPT-induced cell death, the tips of the AuNRs were coated with thin Pt shells by modifying the method of Liz-Marzan *et al*. The platinum salt was added to the as-prepared AuNRs, followed by the reducing agent, ascorbic acid, and the solutions were heated to 40°C.

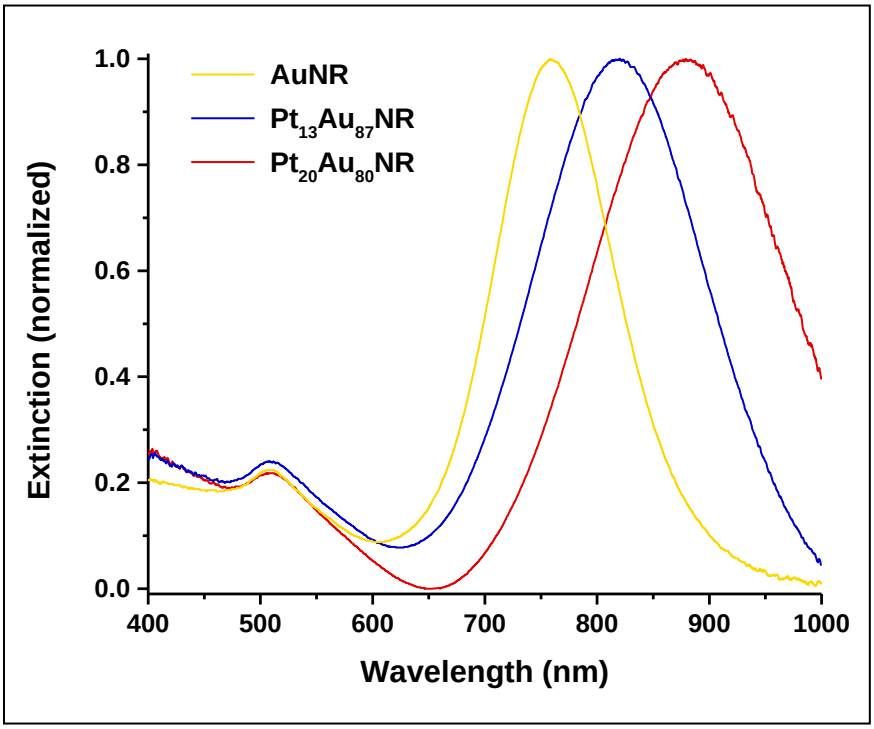

Figure 5.1 Vis–NIR extinction spectra of AuNRs before (yellow) and after coating with thin (blue, $Pt_{13}Au_{87}$NRs) and thick (red, $Pt_{20}Au_{80}$NRs) platinum shells.

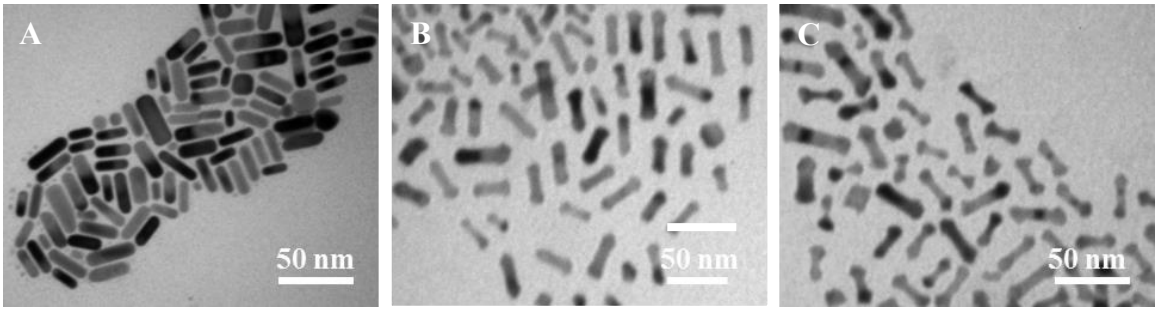

Figure 5.2 TEM of (A) AuNRs, (B) $Pt_{13}Au_{87}$NRs, and (C) $Pt_{20}Au_{80}$NRs.

Table 5.1 Dimensions and Optical Properties of NRs before and after Coating the Tips with Different Pt Shell Thicknesses.

Pt content (mol %)	length (L, nm)	middle width (W_m, nm)	tip width (W_t, nm)	aspect ratio (L / W_m)	LSPR λ (nm)	ε λ_{max} (M^{-1} cm^{-1})
0	25.6 ± 4.0	6.9 ± 1.1	6.9 ± 1.1	3.7 ± 0.4	768 nm	(2.33 ± 0.16) × 10^8
13	28.0 ± 4.1	6.8 ± 1.1	8.4 ± 1.3	4.1 ± 0.5	820 nm	(1.93 ± 0.14) × 10^8
20	28.8 ± 4.2	6.9 ± 1.2	9.3 ± 1.2	4.2 ± 0.6	879 nm	(1.58 ± 0.20) × 10^8

Addition of Pt to the AuNRs was found to red-shift the LSPR band to longer wavelengths while also broadening the band due to the changes in nanorod geometry and aspect ratio and the increased dephasing of the plasmon at the Au–Pt interface, respectively. Reduction of the Pt salt for 5 h resulted in the growth of a ~1.5 nm thick Pt shell on the AuNR tips, increasing the NR length to 28.0 ± 4.1 nm and the width of the

NR tips to 8.4 ± 1.3 nm (AR = 4.1 ± 0.5). These NRs contained a mole ratio of 13% Pt and 87% Au ($Pt_{13}Au_{87}$NRs), as determined by inductively coupled plasma – atomic emission spectroscopy (ICP-AES), and displayed an LSPR peak at 820 nm. Increasing the time allowed for reduction of the platinum salt resulted in the growth of a larger platinum shell on the AuNR tips of ~2.4 nm thickness. This increased the length of the NRs to 28.8 ± 4.2 nm and the width of the NR tips to 9.3 ± 1.2 nm (AR = 4.2 ± 0.6). These thicker nanorods contained a mole ratio of 20% Pt and 80% Au ($Pt_{20}Au_{80}$NRs) and displayed a further redshift in the LSPR band to 879 nm (see **Figure 5.1** and **Figure 5.2** and **Table 5.1**). The width at the middle of the NRs did not increase significantly with platinum deposition, while the tip width increased by ~1.5 – 2.5 nm (**Table 5.1**). Additionally, an energy-dispersive X-ray spectroscopy (EDX) elemental line scan analysis showed platinum at the NR edges (**Figure 5.3**), indicating that the platinum shell grew primarily on the tips of the AuNRs, which is in agreement with the growth reported by Liz-Marzan and others.[47-48, 53-54]

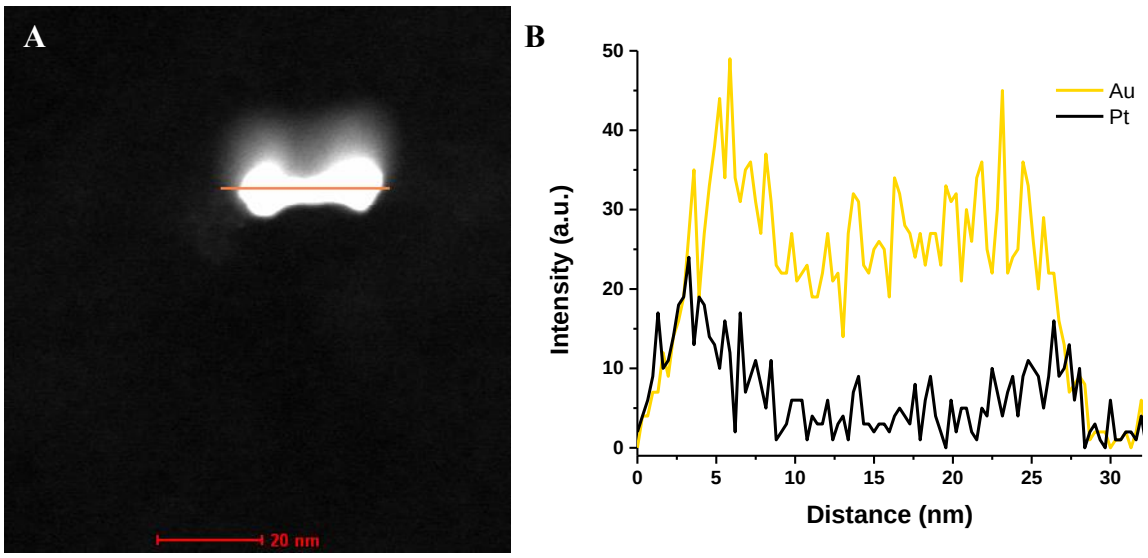

Figure 5.3 (A) HAADF-STEM image of a single $Pt_{20}Au_{80}$NR. (B) EDX line-scan analysis of the $Pt_{20}Au_{80}$NR along the line in A, showing the location of platinum primarily on the NR tips.

To increase the stability and biocompatibility of the NRs and prevent cellular internalization, a 5000 MW methoxypoly(ethylene) glycol thiol (PEG) polymer was conjugated to passivate the NR surface through the formation of the well-characterized Au–S bond.[55] Successful conjugation of PEG is evident in the slight red-shift (8–12 nm) of the LSPR bands to longer wavelengths (**Figure 5.4**) and in the decrease of the zeta potentials of the NR solutions after PEGlyation (**Table 5.2**). The stability of the NRs was confirmed by diluting the suspensions in cell culture media and incubating at 37°C. After 24 h, the NR solutions were exposed to NIR laser irradiation for 5 min. The solutions were then centrifuged to remove the cell culture media and dispersed in deionized (DI) water. Vis–NIR spectra of the NRs showed no significant changes before or after incubation and laser treatment (**Figure 5.5**), confirming the stability of the NRs.

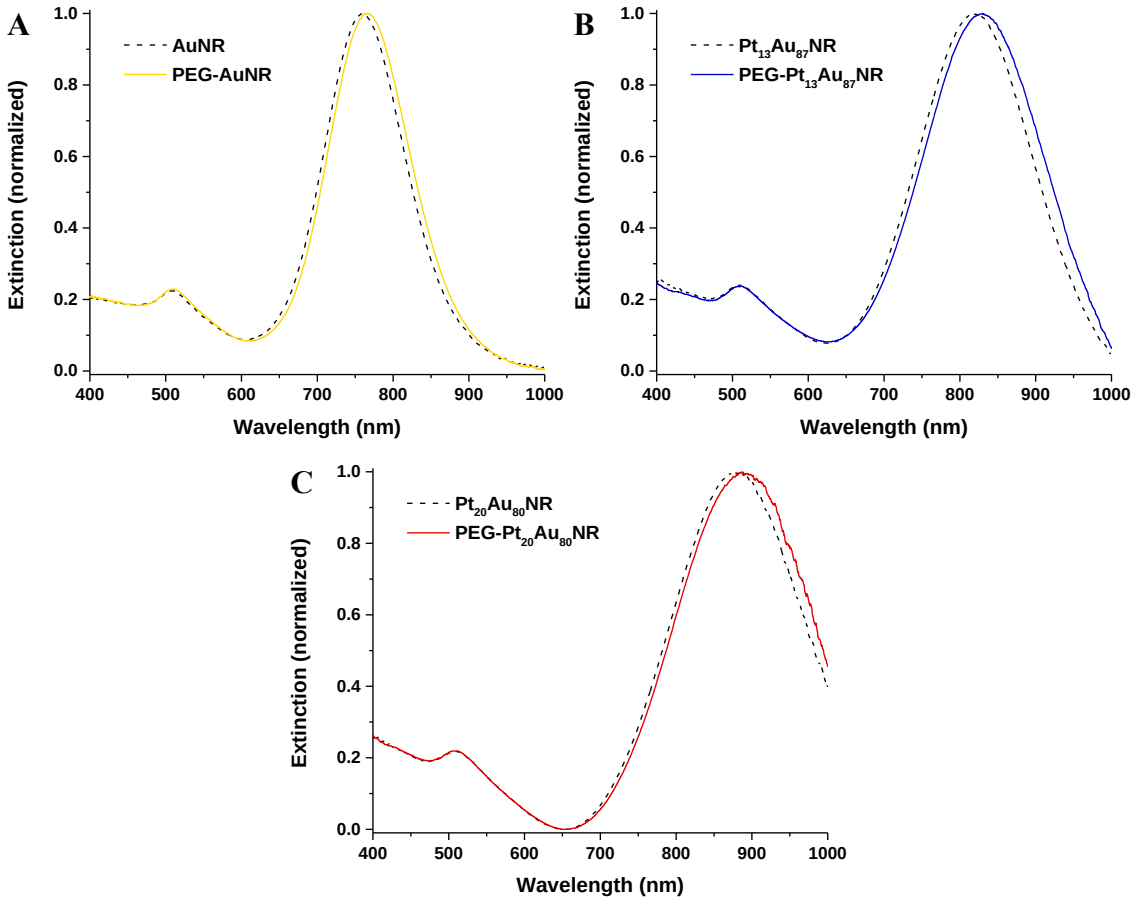

Figure 5.4 Vis-NIR extinction spectra of (A) AuNRs, (B) $Pt_{13}Au_{87}$NRs, and (C) $Pt_{20}Au_{80}$NRs before and after PEG conjugation. The redshift in the longitudinal LSPR bands is indicative of successful conjugation.

Table 5.2 Zeta potential of NR solutions before (left) and after (right) PEG conjugation. The decrease in zeta potential confirms successful conjugation of PEG to the nanorods surface.

	zeta potential (mV)		zeta potential (mV)
AuNRs	40.7 ± 1.9	PEG-AuNRs	5.1 ± 1.4
$Pt_{13}Au_{87}$NRs	42.0 ± 1.6	PEG- $Pt_{13}Au_{87}$NRs	4.9 ± 0.8
$Pt_{20}Au_{80}$NRs	42.6 ± 2.3	PEG- $Pt_{20}Au_{80}$NRs	5.7 ± 1.0

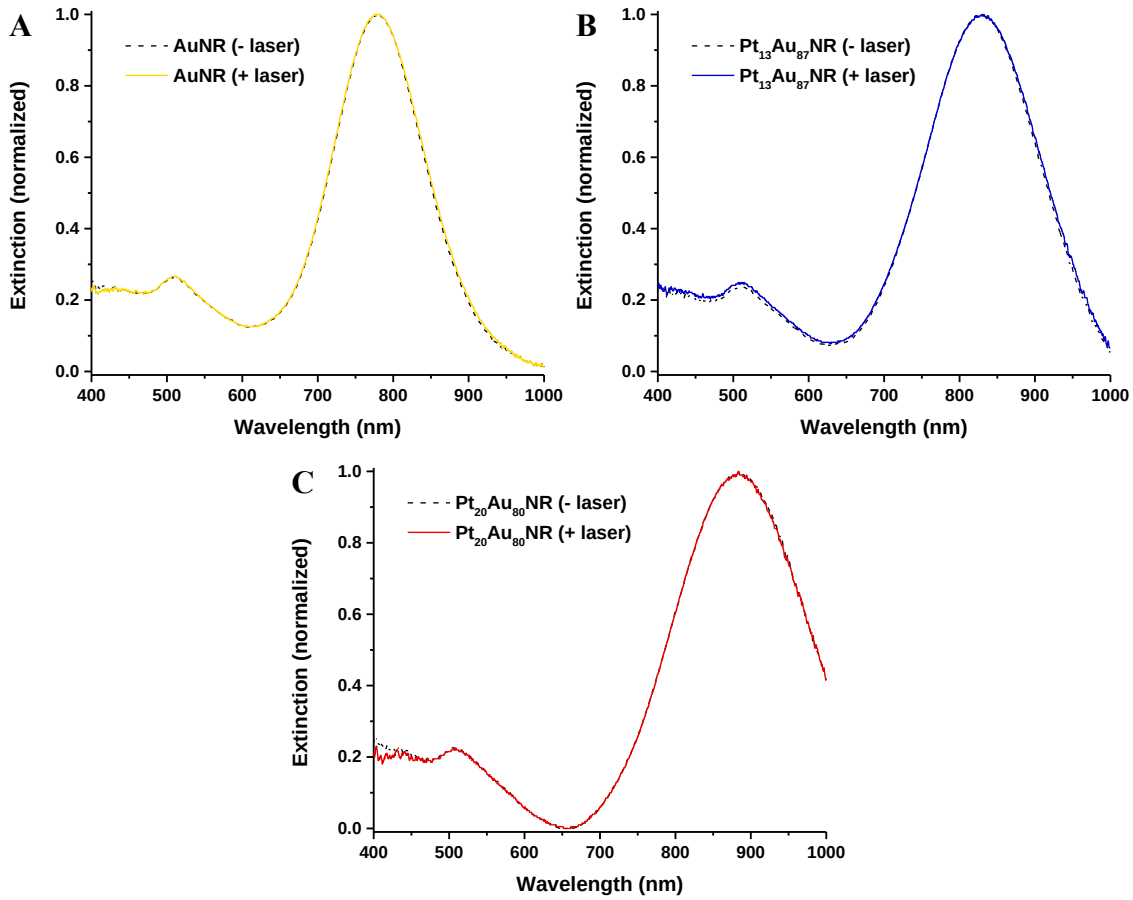

Figure 5.5 Vis–NIR spectra of (A) AuNRs, (B) $Pt_{13}Au_{87}$NRs, and (C) $Pt_{20}Au_{80}$NRs in cell culture medium show no significant changes before (solid lines) and after (dashed lines) 808 nm laser exposure (5 min), indicative of NR stability. Spectra are normalized to account for concentration differences due to evaporation of media during photothermal heating.

The heating efficiency of the NRs was first compared to determine the effect of platinum coating on the AuNRs absorption properties. Suspensions of the NR solutions were diluted to maximum optical densities (ODs) of 0.5 in culture media to mimic the conditions during cellular experiments. The thermal response of the NR solutions during 808 nm laser irradiation at ~5 W/cm^2 was measured directly in the cell culture media. As shown in **Figure 5.6**, the NR suspensions exhibited rapid temperature increases, with all

three NR solutions exceeding 46°C, the temperature required to induce hyperthermia,[49] within 30 s of irradiation. Within 1 min, the AuNR solution reached ~ 52°C, while both PtAuNR solutions exceeded 55°C, although no statistically significant difference was observed ($p > 0.1$). Upon increasing the exposure time to 5 min, the thermal response of AuNRs was found to reach a maximum of 57 ± 4°C. The $Pt_{20}Au_{80}$NRs reached a maximum temperature of 64 ± 2°C, while the $Pt_{13}Au_{87}$NRs reached a temperature of 66 ± 3°C. In comparison, the media without NRs showed a minimal thermal response, only reaching 37°C after 1 min and peaking at 39 ± 1°C. While all NR solutions displayed a strong thermal response, the differences in temperature were most likely due to the degree of overlap between the NRs LSPR bands and the NIR laser. The $Pt_{13}Au_{87}$NRs displayed the greatest overlap (> 98 %) between their LSPR band and the laser and accordingly had the strongest thermal response. However, the $Pt_{20}Au_{80}$NRs displayed a greater thermal response than the AuNRs despite having lower laser overlap (66 % vs 90%), likely due to the difference in NR concentration. Deposition of Pt on the NR tips led to a broadening of the LSPR bands, decreasing the extinction coefficient of the PtAuNRs. Since the thermal response was measured using NR solutions with the same OD of 0.5, the concentration of $Pt_{20}Au_{80}$NRs and $Pt_{13}Au_{87}$NRs was greater than that of AuNRs due to their lower extinction coefficients (**Table 5.1**), also contributing to the observed difference in thermal response.

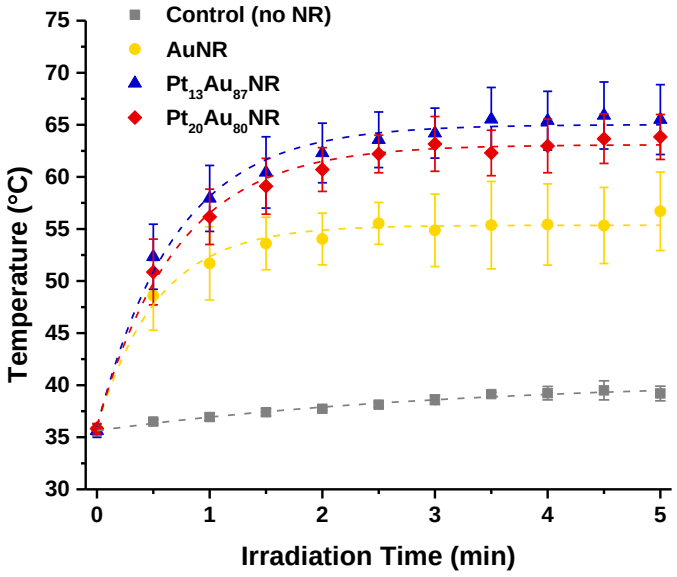

Figure 5.6 Temperature increase induced by PPT heating of NR solutions (OD = 0.5) upon exposure to 808 nm laser excitation. $Pt_{13}Au_{87}$NRs (blue) show the largest temperature increase to 58°C at 1 min (saturates at 65°C), followed by $Pt_{20}Au_{80}$NRs (red) at 56°C at 1 min (saturates at 63°C), and AuNRs (yellow) at 52°C at 1 min (saturates at 55°C). Control media without NRs only heat to 37°C at 1 min before saturating at 40.5°C. The temperature of all solutions was between 35 and 36°C before laser excitation.

The enhanced thermal response of PtAuNRs, relative to the traditional AuNRs, suggests the potential of these NRs as excellent PPT agents. Accordingly, we used human oral squamous carcinoma (HSC3) cells to compare the efficacy of the PtAuNR *in vitro* PPT treatment to that of the AuNRs. First, we confirmed that no significant cellular internalization was observed for any of the NRs studied (**Figure 5.7**) to mimic typical *in vivo* conditions for passively targeted PEG-AuNRs. Then, cancer cells were treated with the various NR solutions diluted to an OD of 0.5 in cell culture media for 1 h prior to NIR laser exposure. After 1 min exposure, the cells treated with the NR solutions displayed

significant cell death, as shown in **Figure 5.8**. Interestingly, while no statistically significant difference in cell death was observed between the NR treated samples, the AuNR- and $Pt_{13}Au_{87}$NR-treated cells displayed slightly lower cell viabilities (~65%) than the $Pt_{20}Au_{80}$NR-treated cells (~69%) after 1 min laser exposure. Cells exposed to the laser but without NR treatment, or treated with the NR solutions but without laser exposure, all displayed greater than 97% cell viability. This confirms the biocompatibility of the NR solutions, which do not induce cell death without laser exposure, and that cell death is due to PPT heating of the NR solutions. However, these results do not directly correlate to the thermal response measured for the NR solutions. While the $Pt_{13}Au_{87}$NRs showed the greatest heating efficiency, followed by the $Pt_{20}Au_{80}$NRs and then the AuNRs, the $Pt_{13}Au_{87}$NRs and the AuNRs induced slightly greater cell death than the $Pt_{20}Au_{80}$NRs. The disagreement between these findings further indicates that ROS play a significant role in cell death during PPT treatment as thermal effects alone would not account for the observed differences.

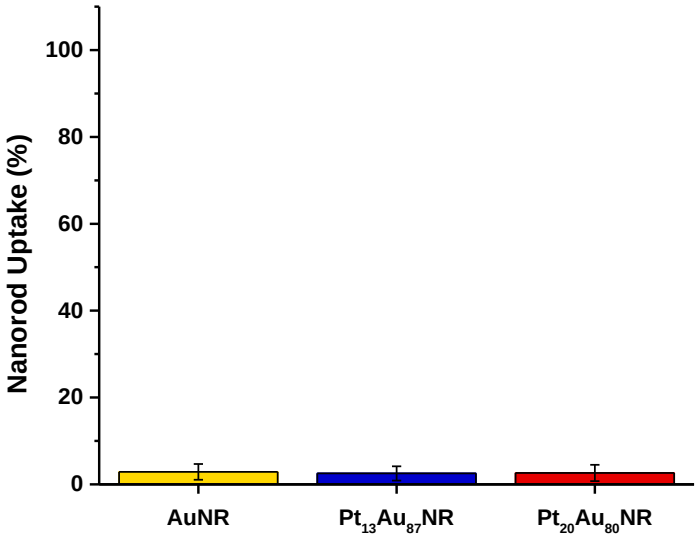

Figure 5.7 Cellular uptake of PEG conjugated NRs by HSC3 cells following 2 h of incubation, shown as the percentage of NR treatment solution internalized ± standard deviation. No statistically significant difference in uptake was observed between the NRs studied (p=0.91).

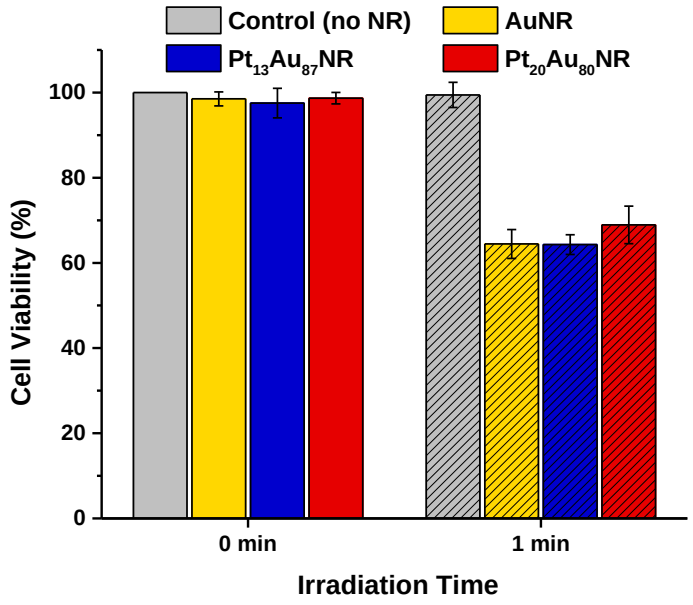

Figure 5.8 Cell viability for HSC3 cells treated with different NR solutions (OD = 0.5) and exposed to 808 nm laser to induce PPT cell death.

The role of ROS during PPT was then investigated using a fluorescent 2,7-dichlorofluorescein (DCF) assay to measure the reactive oxygen levels in cell culture media before and after treatment. For the DCF assay, we first synthesized the DCF from 2,7-dichlorofluorescin diacetate (DCFDA), a common ROS probe. The DCFDA was deacetylated under basic conditions to yield the nonfluorescent dichlorofluorescin (H_2DCF). The H_2DCF was then used to measure ROS as it was readily oxidized into the highly fluorescent DCF compound, which showed an excitation maximum at 495 nm and an emission maximum at ~525 nm (**Figure 5.9**).

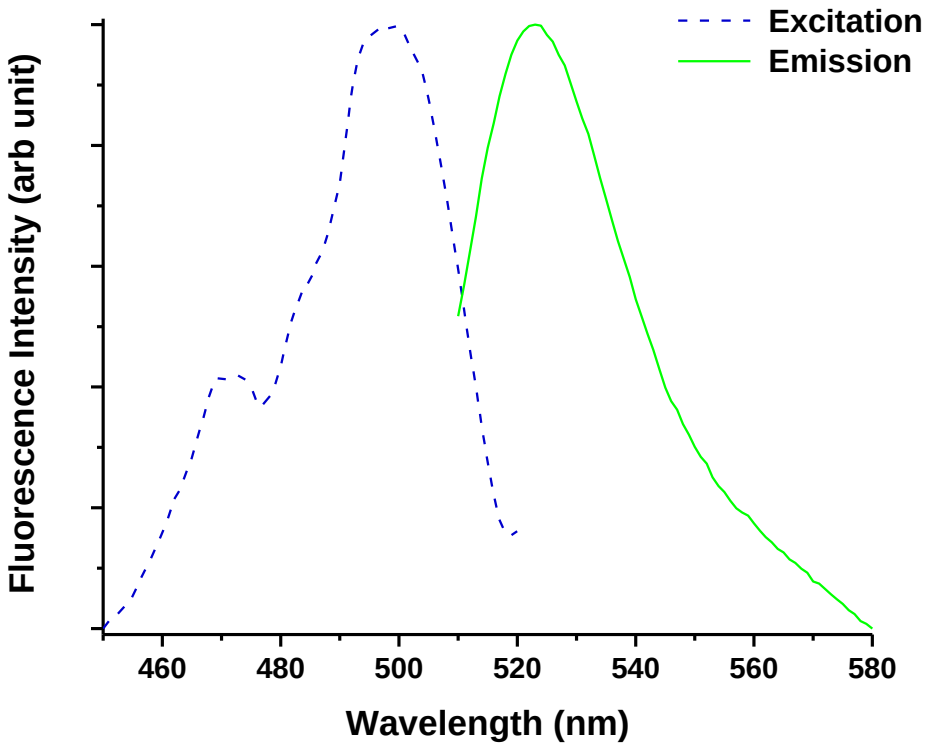

Figure 5.9 Excitation and emission spectra of 67 μM solution of 2,7 – Dichlorofluorescein (DCF) in phosphate buffered saline (PBS, pH = 7.4).

To investigate the ROS produced during PPT treatment, we again treated cancer cells with the solutions of the NRs in culture media. After 1 h of incubation, the cells were exposed to the NIR laser to induce hyperthermia and then incubated with the NR solutions for an additional 30 min to allow for the generation and potential reduction of ROS. Finally, the DCF assay was used to measure the amount of ROS present in the cell media before and after laser exposure. As shown in **Figure 5.10** and **Figure 5.11**, incubation of the cells with AuNRs or $Pt_{13}Au_{87}$NRs did not alter the amount of endogenous ROS present in the media before laser exposure. However, incubation with $Pt_{20}Au_{80}$NRs without laser exposure led to a highly significant ($p < 0.01$) reduction in ROS levels from the untreated control. While this demonstrates the successful ROS scavenging ability of the $Pt_{20}Au_{80}$NRs, prolonged exposure to these NRs has the potential to perturb normal cellular function as endogenous ROS serve an important role in many redox-based signaling pathways.[56-57] After laser exposure, the amount of ROS in culture media containing AuNRs displayed a highly significant increase in fluorescence, confirming the formation of ROS during PPT treatment. However, media without NRs or with PtAuNRs did not show any significant changes in fluorescence after laser exposure, indicating that the ROS formed during PPT treatment were reduced by the Pt shell on the AuNRs. The control cells, incubated with media without NRs, did not display a significant thermal response (**Figure 5.6**), so heat-stress induced ROS likely are not formed during PPT treatment and fluorescence is only detected from endogenous ROS. Additionally, the amount of ROS present in $Pt_{20}Au_{80}$NRs containing cell media was again lower than the control samples but did not change after laser exposure. These results again confirm the ROS scavenging ability of the PtAuNRs while accounting for the

discrepancy between the thermal response of the NRs and the cell viability assay. While AuNRs displayed the weakest thermal response to PPT treatment, significant amounts of ROS were produced during the treatment, likely resulting in some chemically induced cell death, through oxidative damage, in addition to the hyperthermia-induced toxicity. Accordingly, although the PtAuNRs displayed the strongest thermal response to PPT, they also reduced any ROS produced during the treatment before oxidative damage could occur, so the observed cell death resulted from hyperthermia.

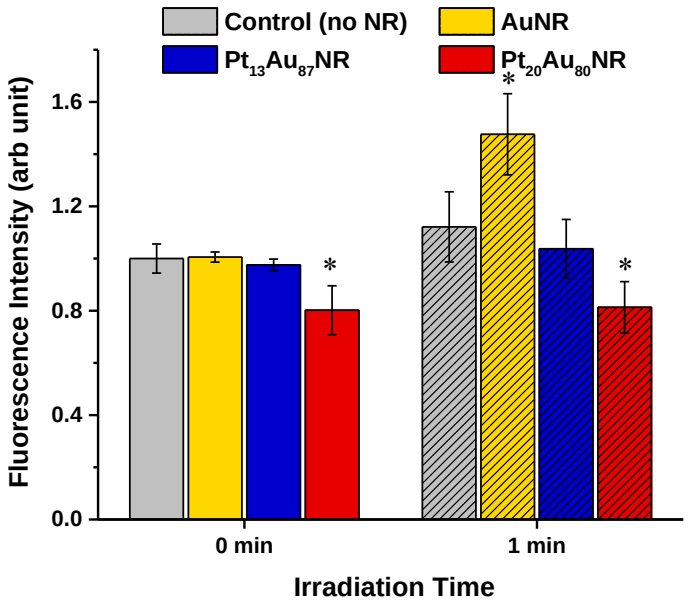

Figure 5.10 Levels of ROS in cell media before (0 min) and after (1 min) PPT heating. Before heating, $Pt_{20}Au_{80}$NRs show less ROS due to reduction of endogenous oxygen by Pt. After heating, AuNR-treated cells show significantly higher ROS levels due to heat stress. PtAuNRs do not show significant increases in ROS levels, indicating that the reactive species are reduced before cell damage can occur. Statistical significance ($p < 0.05$) is indicated by an asterisk.

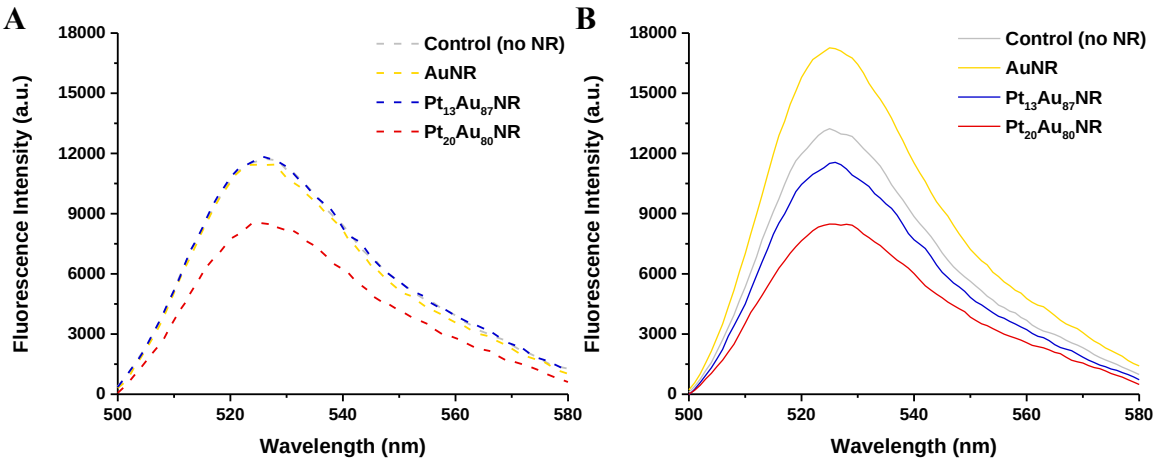

Figure 5.11 Example emission spectra of ROS present in cell culture medium containing NR solutions before (A) and after (B) laser exposure. Control samples (no NR), $Pt_{13}Au_{87}$NRs , and $Pt_{20}Au_{80}$NRs containing medium do not show significant changes in ROS levels before or after laser exposure, although incubation with $Pt_{20}Au_{80}$NRs reduces the level of endogenous ROS in both cases. AuNR containing medium shows no difference in ROS from endogenous levels before laser exposure, but shows a significant increase in ROS levels after exposure.

We then extended our study to determine the toxicity of the ROS produced during PPT treatment on healthy, untreated human keratinocyte (HaCat) cells. Cancer cells were again incubated with the NR solutions and exposed to the NIR laser to induce hyperthermia through PPT treatment. After laser exposure and incubation, the medium was aspirated and the NRs were removed through centrifugation. The laser-treated medium was then added to the HaCat cells and incubated for 24 h to determine the toxicity of the solutions after PPT treatment. Cells treated with fresh medium, without any exposure to the laser or cancer cells, were used as a control to normalize cell viability values. The healthy cells that were incubated with laser-treated media that previously contained PtAuNRs or did not contain any NRs but underwent NIR exposure showed no significant changes in cell viability ($p > 0.86$). However, the healthy cells incubated with

laser-treated media that had previously contained AuNRs did show a statistically significant decrease in viability ($p = 0.0036$), as seen in **Figure 5.12**. The toxicity of the laser-treated AuNR solution on healthy, untreated cells further supports the conclusion that ROS play a significant role during PPT treatment. Because of the similar thermal responses between the AuNRs and the PtAuNRs (**Figure 5.6**), comparable heat stress-induced ROS production, and accordingly cell death, would be expected between the NR treatments. However, the lack of cell death from the PtAuNR-treated samples further confirms the effective scavenging of ROS by the platinum shell.

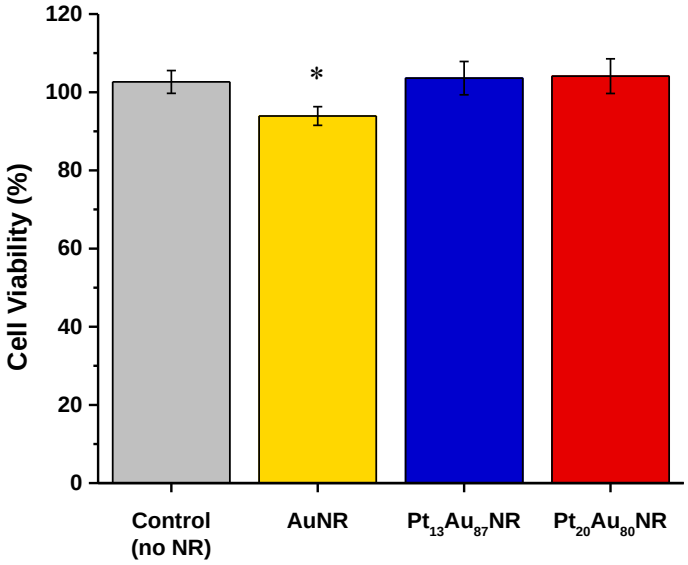

Figure 5.12 Viability of HaCat cells incubated with media from laser-treated HSC3 cancer cells. Cell media following AuNR PPT heating caused statistically significant ($p = 0.0036$, indicated by an asterisk) cell death, indicating the presence of harmful ROS remaining in solution. Solutions without NRs or with Pt-coated NRs show no significant decrease in cell viability ($p > 0.86$), indicating that ROS are reduced, mitigating side effects toward untreated cells.

5.4 Conclusion

We have shown the utility of PtAuNRs as efficient PPT agents that induce cell death through hyperthermia while scavenging the ROS produced during treatment. The optical properties of the NRs could be tuned by adjusting the thickness of the Pt shell on the NR tips and are not affected by interactions with complex cell culture media or during NIR laser exposure, confirming their stability. The Pt coating does not impair the thermal response of the NRs to laser exposure but instead enhances it slightly. The NR solutions do not induce cell death alone, confirming their biocompatibility, and induce cell death upon laser exposure, verifying their usefulness as PPT agents. The ROS scavenging ability of the PtAuNRs is also demonstrated through the fluorescent assays used to measure the reactive oxygen present in the NR solutions before and after PPT treatment. Laser exposure of AuNRs is shown to produce significant amounts of ROS, which have the potential to react with healthy tissue causing unwanted side effects and contribute to toxicity. PPT treatment of the AuNRs results in cell death through both hyperthermia and the formation of ROS, resulting in toxicity toward healthy, untreated cells. In contrast, the PPT treatment of PtAuNRs induces cell death solely through hyperthermia and no detectable changes are observed in ROS levels after laser exposure. The $Pt_{13}Au_{87}$NRs are the most promising nanoparticle studied for PPT treatment as they do not alter endogenous ROS levels and efficiently induce cell death through hyperthermia while scavenging the ROS produced during PPT to prevent unwanted death of healthy tissue.

5.5 References

(1) Aioub, M.; Panikkanvalappil, S. R.; El-Sayed, M. A. Platinum-Coated Gold Nanorods: Efficient Reactive Oxygen Scavengers That Prevent Oxidative Damage toward Healthy, Untreated Cells During Plasmonic Photothermal Therapy. *ACS Nano* **2017,** *11*, 579-586.

(2) Dickerson, E. B.; Dreaden, E. C.; Huang, X.; El-Sayed, I. H.; Chu, H.; Pushpanketh, S.; McDonald, J. F.; El-Sayed, M. A. Gold Nanorod Assisted Near-Infrared Plasmonic Photothermal Therapy (PPTT) of Squamous Cell Carcinoma in Mice. *Cancer Lett.* **2008,** *269*, 57-66.

(3) Huang, X.; El-Sayed, I. H.; Qian, W.; El-Sayed, M. A. Cancer Cell Imaging and Photothermal Therapy in the Near-Infrared Region by Using Gold Nanorods. *J. Am. Chem. Soc.* **2006,** *128*, 2115-2120.

(4) Abadeer, N. S.; Murphy, C. J. Recent Progress in Cancer Thermal Therapy Using Gold Nanoparticles. *J. Phys. Chem. C* **2016,** *120*, 4691-4716.

(5) Alkilany, A. M.; Thompson, L. B.; Boulos, S. P.; Sisco, P. N.; Murphy, C. J. Gold Nanorods: Their Potential for Photothermal Therapeutics and Drug Delivery, Tempered by the Complexity of Their Biological Interactions. *Adv. Drug Delivery Rev.* **2012,** *64*, 190-199.

(6) Dreaden, E. C.; Alkilany, A. M.; Huang, X. H.; Murphy, C. J.; El-Sayed, M. A. The Golden Age: Gold Nanoparticles for Biomedicine. *Chem. Soc. Rev.* **2012,** *41*, 2740-2779.

(7) Lal, S.; Clare, S. E.; Halas, N. J. Nanoshell-Enabled Photothermal Cancer Therapy: Impending Clinical Impact. *Acc. Chem. Res.* **2008,** *41*, 1842-1851.

(8) Albanese, A.; Tang, P. S.; Chan, W. C. W. The Effect of Nanoparticle Size, Shape, and Surface Chemistry on Biological Systems. *Annu. Rev. Biomed. Eng.* **2012,** *14*, 1-16.

(9) Jiang, W.; Kim, B. Y. S.; Rutka, J. T.; Chan, W. C. W. Nanoparticle-Mediated Cellular Response Is Size-Dependent. *Nat. Nanotechnol.* **2008,** *3*, 145-150.

(10) Byers, C. P.; Zhang, H.; Swearer, D. F.; Yorulmaz, M.; Hoener, B. S.; Huang, D.; Hoggard, A.; Chang, W. S.; Mulvaney, P.; Ringe, E.; Halas, N. J.; Nordlander, P.; Link, S.; Landes, C. F. From Tunable Core-Shell Nanoparticles to Plasmonic Drawbridges: Active Control of Nanoparticle Optical Properties. *Sci. Adv.* **2015,** *1*, 1-9.

(11) Li, M.; Kang, J. W.; Dasari, R. R.; Barman, I. Shedding Light on the Extinction-Enhancement Duality in Gold Nanostar-Enhanced Raman Spectroscopy. *Angew. Chem., Int. Ed.* **2014,** *53*, 14115-14119.

(12) Panikkanvalappil, S. R.; El-Sayed, M. A. Gold-Nanoparticle-Decorated Hybrid Mesoflowers: An Efficient Surface-Enhanced Raman Scattering Substrate for Ultra-Trace Detection of Prostate Specific Antigen. *J. Phys. Chem. B* **2014,** *118,* 14085-14091.

(13) Aioub, M.; Kang, B.; Mackey, M. A.; El-Sayed, M. A. Biological Targeting of Plasmonic Nanoparticles Improves Cellular Imaging via the Enhanced Scattering in the Aggregates Formed. *J. Phys. Chem. Lett.* **2014,** *5,* 2555-2561.

(14) Li, M.; Banerjee, S. R.; Zheng, C.; Pomper, M. G.; Barman, I. Ultrahigh Affinity Raman Probe for Targeted Live Cell Imaging of Prostate Cancer. *Chem. Sci.* **2016**, 6779-6785.

(15) Aioub, M.; Austin, L. A.; El-Sayed, M. A. Determining Drug Efficacy Using Plasmonically Enhanced Imaging of the Morphological Changes of Cells Upon Death. *J. Phys. Chem. Lett.* **2014,** *5,* 3514-3518.

(16) Comenge, J.; Fragueiro, O.; Sharkey, J.; Taylor, A.; Held, M.; Burton, N. C.; Park, B. K.; Wilm, B.; Murray, P.; Brust, M.; Levy, R. Preventing Plasmon Coupling between Gold Nanorods Improves the Sensitivity of Photoacoustic Detection of Labeled Stem Cells in Vivo. *ACS Nano* **2016,** *10,* 7106-7116.

(17) Jokerst, J. V.; Cole, A. J.; Van de Sompel, D.; Gambhir, S. S. Gold Nanorods for Ovarian Cancer Detection with Photoacoustic Imaging and Resection Guidance via Raman Imaging in Living Mice. *ACS Nano* **2012,** *6,* 10366-10377.

(18) Huschka, R.; Barhoumi, A.; Liu, Q.; Roth, J. A.; Ji, L.; Halas, N. J. Gene Silencing by Gold Nanoshell-Mediated Delivery and Laser-Triggered Release of Antisense Oligonucleotide and SiRNA. *ACS Nano* **2012,** *6,* 7681-7691.

(19) Vigderman, L.; Zubarev, E. R. Therapeutic Platforms Based on Gold Nanoparticles and Their Covalent Conjugates with Drug Molecules. *Adv. Drug Delivery Rev.* **2013,** *65,* 663-676.

(20) Aioub, M.; El-Sayed, M. A. A Real-Time Surface Enhanced Raman Spectroscopy Study of Plasmonic Photothermal Cell Death Using Targeted Gold Nanoparticles. *J. Am. Chem. Soc.* **2016,** *138,* 1258-1264.

(21) Bhana, S.; Lin, G.; Wang, L. J.; Starring, H.; Mishra, S. R.; Liu, G.; Huang, X. H. Near-Infrared-Absorbing Gold Nanopopcorns with Iron Oxide Cluster Core for Magnetically Amplified Photothermal and Photodynamic Cancer Therapy. *ACS Appl. Mater. Inter.* **2015,** *7,* 11637-11647.

(22) McGrath, A. J.; Chien, Y. H.; Cheong, S. S.; Herman, D. A. J.; Watt, J.; Henning, A. M.; Gloag, L.; Yeh, C. S.; Tilley, R. D. Gold over Branched Palladium Nano Structures for Photothermal Cancer Therapy. *ACS Nano* **2015,** *9,* 12283-12291.

(23) Vijayaraghavan, P.; Liu, C. H.; Vankayala, R.; Chiang, C. S.; Hwang, K. C. Designing Multi-Branched Gold Nanoechinus for NIR Light Activated Dual Modal

Photodynamic and Photothermal Therapy in the Second Biological Window. *Adv. Mater.* **2014,** *26*, 6689-6695.

(24) Fan, Z.; Dai, X. M.; Lu, Y. F.; Yu, E.; Brahmbatt, N.; Carter, N.; Tchouwou, C.; Singh, A. K.; Jones, Y.; Yu, H. T.; Ray, P. C. Enhancing Targeted Tumor Treatment by near IR Light-Activatable Photodynamic-Photothermal Synergistic Therapy. *Mol. Pharmaceut.* **2014,** *11*, 1109-1116.

(25) Jain, P. K.; Huang, X. H.; El-Sayed, I. H.; El-Sayed, M. A. Noble Metals on the Nanoscale: Optical and Photothermal Properties and Some Applications in Imaging, Sensing, Biology, and Medicine. *Acc. Chem. Res.* **2008,** *41*, 1578-1586.

(26) Link, S.; El-Sayed, M. A. Shape and Size Dependence of Radiative, Non-Radiative and Photothermal Properties of Gold Nanocrystals. *Int. Rev. Phys. Chem.* **2000,** *19*, 409-453.

(27) Lohse, S. E.; Murphy, C. J. The Quest for Shape Control: A History of Gold Nanorod Synthesis. *Chem. Mater.* **2013,** *25*, 1250-1261.

(28) Gobin, A. M.; Lee, M. H.; Halas, N. J.; James, W. D.; Drezek, R. A.; West, J. L. Near-Infrared Resonant Nanoshells for Combined Optical Imaging and Photothermal Cancer Therapy. *Nano Lett.* **2007,** *7*, 1929-1934.

(29) Chen, J. Y.; Wang, D. L.; Xi, J. F.; Au, L.; Siekkinen, A.; Warsen, A.; Li, Z. Y.; Zhang, H.; Xia, Y. N.; Li, X. D. Immuno Gold Nanocages with Tailored Optical Properties for Targeted Photothermal Destruction of Cancer Cells. *Nano Lett.* **2007,** *7*, 1318-1322.

(30) Wang, Y. C.; Black, K. C. L.; Luehmann, H.; Li, W. Y.; Zhang, Y.; Cai, X.; Wan, D. H.; Liu, S. Y.; Li, M.; Kim, P.; Li, Z. Y.; Wang, L. H. V.; Liu, Y. J.; Xia, Y. A. Comparison Study of Gold Nanohexapods, Nanorods, and Nanocages for Photothermal Cancer Treatment. *ACS Nano* **2013,** *7*, 2068-2077.

(31) Perez-Hernandez, M.; del Pino, P.; Mitchell, S. G.; Moros, M.; Stepien, G.; Pelaz, B.; Parak, W. J.; Galvez, E. M.; Pardo, J.; de la Fuente, J. M. Dissecting the Molecular Mechanism of Apoptosis During Photothermal Therapy Using Gold Nanoprisms. *ACS Nano* **2015,** *9*, 52-61.

(32) Ambrosone, A.; del Pino, P.; Marchesano, V.; Parak, W. J.; de la Fuente, J. M.; Tortiglione, C. Gold Nanoprisms for Photothermal Cell Ablation in Vivo. *Nanomedicine* **2014,** *9*, 1913-1922.

(33) Huang, X. H.; Neretina, S.; El-Sayed, M. A. Gold Nanorods: From Synthesis and Properties to Biological and Biomedical Applications. *Adv. Mater.* **2009,** *21*, 4880-4910.

(34) Uttara, B.; Singh, A. V.; Zamboni, P.; Mahajan, R. T. Oxidative Stress and Neurodegenerative Diseases: A Review of Upstream and Downstream Antioxidant Therapeutic Options. *Curr. Neuropharmacol.* **2009,** *7*, 65-74.

(35) Benz, C. C.; Yau, C. Ageing, Oxidative Stress and Cancer: Paradigms in Parallax. *Nat. Rev. Cancer* **2008,** *8*, 875-879.

(36) Slimen, I. B.; Najar, T.; Ghram, A.; Dabbebi, H.; Ben Mrad, M.; Abdrabbah, M. Reactive Oxygen Species, Heat Stress and Oxidative-Induced Mitochondrial Damage. A Review. *Int. J. Hypertherm.* **2014,** *30*, 513-523.

(37) Minai, L.; Yeheskely-Hayon, D.; Yelin, D. High Levels of Reactive Oxygen Species in Gold Nanoparticle-Targeted Cancer Cells Following Femtosecond Pulse Irradiation. *Sci. Rep.* **2013,** *3*, 2146.

(38) Fedyaeva, A. V.; Stepanov, A. V.; Lyubushkina, I. V.; Pobezhimova, T. P.; Rikhvanov, E. G. Heat Shock Induces Production of Reactive Oxygen Species and Increases Inner Mitochondrial Membrane Potential in Winter Wheat Cells. *Biochemistry-Moscow* **2014,** *79*, 1202-1210.

(39) Gao, H.; Liu, R.; Gao, F. P.; Wang, Y. L.; Jiang, X. L.; Gao, X. Y. Plasmon-Mediated Generation of Reactive Oxygen Species from near-Infrared Light Excited Gold Nanocages for Photodynamic Therapy in Vitro. *ACS Nano* **2014,** *8*, 7260-7271.

(40) Holmstrom, K. M.; Finkel, T. Cellular Mechanisms and Physiological Consequences of Redox-Dependent Signalling. *Nat. Rev. Mol. Cell Bio.* **2014,** *15*, 411-421.

(41) Schieber, M.; Chandel, N. S. ROS Function in Redox Signaling and Oxidative Stress. *Curr. Biol.* **2014,** *24*, R453-R462.

(42) Cervellati, F.; Cervellati, C.; Romani, A.; Cremonini, E.; Sticozzi, C.; Belmonte, G.; Pessina, F.; Valacchi, G. Hypoxia Induces Cell Damage Via Oxidative Stress in Retinal Epithelial Cells. *Free Radical Res.* **2014,** *48*, 303-312.

(43) Yoshihisa, Y.; Honda, A.; Zhao, Q. L.; Makino, T.; Abe, R.; Matsui, K.; Shimizu, H.; Miyamoto, Y.; Kondo, T.; Shimizu, T. Protective Effects of Platinum Nanoparticles against UV-Light-Induced Epidermal Inflammation. *Exp. Dermatol.* **2010,** *19*, 1000-1006.

(44) Hamasaki, T.; Kashiwagi, T.; Imada, T.; Nakamichi, N.; Aramaki, S.; Toh, K.; Morisawa, S.; Shimakoshi, H.; Hisaeda, Y.; Shirahata, S. Kinetic Analysis of Superoxide Anion Radical-Scavenging and Hydroxyl Radical-Scavenging Activities of Platinum Nanoparticles. *Langmuir* **2008,** *24*, 7354-7364.

(45) Panikkanvalappil, S. R.; Mahmoud, M. A.; Mackey, M. A.; El-Sayed, M. A. Surface-Enhanced Raman Spectroscopy for Real-Time Monitoring of Reactive Oxygen Species-Induced DNA Damage and Its Prevention by Platinum Nanoparticles. *ACS Nano* **2013,** *7*, 7524-7533.

(46) Collins, S. S. E.; Cittadini, M.; Pecharroman, C.; Martucci, A.; Mulvaney, P. Hydrogen Spillover between Single Gold Nanorods and Metal Oxide Supports: A Surface Plasmon Spectroscopy Study. *ACS Nano* **2015,** *9*, 7846-7856.

(47) Grzelczak, M.; Perez-Juste, J.; Rodriguez-Gonzalez, B.; Liz-Marzan, L. M. Influence of Silver Ions on the Growth Mode of Platinum on Gold Nanorods. *J. Mater. Chem.* **2006,** *16*, 3946-3951.

(48) Grzelczak, M.; Perez-Juste, J.; de Abajo, F. J. G.; Liz-Marzan, L. M. Optical Properties of Platinum-Coated Gold Nanorods. *J. Phys. Chem. C* **2007,** *111*, 6183-6188.

(49) Roti, J. L. R. Cellular Responses to Hyperthermia (40-46°C): Cell Killing and Molecular Events. *Int. J. Hypertherm.* **2008,** *24*, 3-15.

(50) Samal, A. K.; Sreeprasad, T. S.; Pradeep, T. Investigation of the Role of NaBH4 in the Chemical Synthesis of Gold Nanorods. *J. Nanopart. Res.* **2010,** *12*, 1777-1786.

(51) Ghosh, P.; Han, G.; De, M.; Kim, C. K.; Rotello, V. M. Gold Nanoparticles in Delivery Applications. *Adv. Drug Delivery Rev.* **2008,** *60*, 1307-1315.

(52) Agarwal, A.; Mackey, M. A.; El-Sayed, M. A.; Bellamkonda, R. V. Remote Triggered Release of Doxorubicin in Tumors by Synergistic Application of Thermosensitive Liposomes and Gold Nanorods. *ACS Nano* **2011,** *5*, 4919-4926.

(53) He, D. S.; Han, Y.; Fennell, J.; Horswell, S. L.; Li, Z. Y. Growth and Stability of Pt on Au Nanorods. *Appl. Phys. Lett.* **2012,** *101*, No. 113102.

(54) Fennell, J.; He, D. S.; Tanyi, A. M.; Logsdail, A. J.; Johnston, R. L.; Li, Z. Y.; Horswell, S. L. A Selective Blocking Method to Control the Overgrowth of Pt on Au Nanorods. *J. Am. Chem. Soc.* **2013,** *135*, 6554-6561.

(55) Love, J. C.; Estroff, L. A.; Kriebel, J. K.; Nuzzo, R. G.; Whitesides, G. M. Self-Assembled Monolayers of Thiolates on Metals as a Form of Nanotechnology. *Chem. Rev.* **2005,** *105*, 1103-1169.

(56) Thannickal, V. J.; Fanburg, B. L. Reactive Oxygen Species in Cell Signaling. *Am J Physiol-Lung C* **2000,** *279*, L1005-L1028.

(57) Rhee, S. G. H2O2, a Necessary Evil for Cell Signaling. *Science* **2006,** *312*, 1882-1883.